# FINAL REPORT

## Aromatic Radicals-Acetylene Particulate Matter Chemistry

SERDP Project WP-1575

DECEMBER 2011

Kenneth Brezinsky
**University of Illinois at Chicago**



SERDP
DOD ▪ EPA ▪ DOE

# REPORT DOCUMENTATION PAGE

*Form Approved*
*OMB No. 0704-0188*



**PLEASE DO NOT RETURN YOUR FORM TO THE ABOVE ORGANIZATION.**

| 1. REPORT DATE *(DD-MM-YYYY)* | 2. REPORT TYPE | 3. DATES COVERED *(From - To)* |
|---|---|---|
| 15-12-2011 | Final | July 2007 - December 2011 |

**4. TITLE AND SUBTITLE**
Aromatic Radicals-Acetylene Particulate Matter Chemistry

**5a. CONTRACT NUMBER**
W912HQ-07-C-0019

**5b. GRANT NUMBER**

**5c. PROGRAM ELEMENT NUMBER**

**6. AUTHOR(S)**
Dr. Kenneth Brezinsky

**5d. PROJECT NUMBER**
WP-1575

**5e. TASK NUMBER**

**5f. WORK UNIT NUMBER**

**7. PERFORMING ORGANIZATION NAME(S) AND ADDRESS(ES)**
University of Illinois
DBA: Office of Business and Financial Ser
809 S. Marshfield, RM 520, Chicago, IL 60612

**8. PERFORMING ORGANIZATION REPORT NUMBER**

**9. SPONSORING/MONITORING AGENCY NAME(S) AND ADDRESS(ES)**
USACE HUMPHREYS ENGR CTR SPT ACTIVITY
Attn: CECT-HC
7701 Telegraph Road
Alexandria, VA 22315-3860

**10. SPONSOR/MONITOR'S ACRONYM(S)**

**11. SPONSOR/MONITOR'S REPORT NUMBER(S)**

**12. DISTRIBUTION/AVAILABILITY STATEMENT**

**13. SUPPLEMENTARY NOTES**

**14. ABSTRACT**

In the present work the pyrolytic reactions of the phenyl radical in the presence of acetylene have been studied as a possible pathway to the formation of the second-ring species. In addition, the oxidation of m-xylene was investigated.
The experimental work has been conducted using the single-pulse high-pressure shock tube (HPST) at the University of Illinois at Chicago. A new experimental set-up, for use with the HPST, was studied and developed for accurate measurement of large compounds.
The experimental results were utilized to develop and validate comprehensive chemical kinetic models which constitute the base for the development of comprehensive soot models for predicting emissions in order to address regulatory/legislative concerns.
In addition, a theoretical study was performed using ab-initio quantum mechanics calculations which addressed the possible role of the radical/π-bond addition reactions in the formation of PAH compounds.

**15. SUBJECT TERMS**
Shock Tube, High Pressure, Chemistry, Polycyclic Aromatic Hydrocarbons, Soot, Kinetic Model, m-Xylene Oxidation, Phenyl + Acetylene, Phenyl Pyrolysis, Gas Chromatography, Potential Energy Surface, Ab-Initio Calculations.

| 16. SECURITY CLASSIFICATION OF: | | | 17. LIMITATION OF ABSTRACT | 18. NUMBER OF PAGES | 19a. NAME OF RESPONSIBLE PERSON |
|---|---|---|---|---|---|
| a. REPORT | b. ABSTRACT | c. THIS PAGE | None | 133 | Kenneth Brezinsky |
| | | | | | 19b. TELEPHONE NUMBER *(Include area code)* 312 996 9430 |

Reset

# TABLE OF CONTENTS

# LIST OF FIGURES

# LIST OF TABLES

# ACKNOWLEDGMENTS

We would like to take this opportunity to thank SERDP (Strategic Environmental Research and Development Program) for the financial support through Grant No. WP-1575.

The research was also supported in part by the National Science Foundation through TeraGrid resources provided by *www.ncsa.illinois.edu* under grant number TG-CHE100109 and TG-CHE110038.

# ABSTRACT

The formation of polycyclic aromatic hydrocarbons (PAHs), especially fused-ring compounds, represents an essential step in the mechanisms of soot formation. In particular the second-ring species, naphthalene, plays a key role as a building block for the subsequent growth to larger PAHs. Nevertheless the pathways leading to naphthalene are still uncertain requiring further experimental and theoretical investigations. In the present work the pyrolytic reactions of the phenyl radical in the presence of acetylene have been studied as a possible pathway to the formation of the second-ring species. In addition, the oxidation of m-xylene, an abundant single-ring component for typical fuels and surrogate mixtures, was investigated.

The experimental work has been conducted using the single-pulse high-pressure shock tube (HPST) at the University of Illinois at Chicago. A new experimental set-up, for use with the HPST, was studied and developed for accurate measurement of large compounds. The major stable species obtained from the experimental work, including the heavy polycyclic aromatic hydrocarbons, were identified and measured using gas chromatography/mass spectrometry techniques. The experiments were performed over a wide range of high-pressures (25 – 50 atm) and temperatures (900 – 1800 K) which encompass typical conditions in modern combustion chambers.

The experimental results on the phenyl pyrolysis (preliminary to the experiments with acetylene), the phenyl + acetylene reactions, and the m-xylene oxidation provide unique data about these reaction systems. In fact, for the first time, it has been possible to detect and accurately measure a variety of PAH compounds, including the fused-ring species, for which mole fraction profiles have been obtained. Such species profiles were utilized to develop and validate comprehensive chemical kinetic models which helped clarify aspects related to the mechanisms involved in the formation of large polycyclic aromatic hydrocarbons at high pressures.

In addition, in order to explore new possible pathways for the formation of condensed structures, a theoretical study of the radical/π-bond addition reactions between single-ring aromatic hydrocarbons was performed using ab-initio quantum mechanics calculations. Several pathways leading to the formation of PAH compounds have been addressed as potentially relevant for typical combustion environments, especially in relation to the formation of the second-ring aromatic hydrocarbon, naphthalene. The calculations are also supported by the experimental results obtained on the phenyl pyrolysis, which confirmed the presence of the non-conventional pathway to naphthalene involving the reaction between o-benzyne and benzene.

The calculations were also extended to a different radical/π-bond addition reaction between o-benzyne and cyclic C5 hydrocarbons, cyclopentadiene and cyclopentadienyl radical. The results indicated the presence of alternative pathwaya for the formation of another important building block for soot, indene.

The experimental, modeling, and theoretical work performed under the present program provided novel information about the processes involved in the incipient stages of soot formation. The chemical kinetic models developed and validated against the experimental results constitute the base for the development of comprehensive soot models for predicting emissions in order to address regulatory/legislative concerns.

# 1. BACKGROUND AND INTRODUCTION

The modern industrial economies, no matter how high-tech, are carbon-based economies; many of the human activities, from electricity generation to manufacturing, from residential and commercial heating/air conditioning to transportation, are mainly based on fossil fuel combustion. The combustion processes provide the energy necessary for the specific activity, but they also release numerous pollutants into the atmosphere. Particulate matter (soot), ozone, carbon monoxide, sulfur oxides, nitrogen oxides, and lead are representative harmful combustion products chosen by the US Environmental Protection Agency (EPA) as "criteria pollutants" from the definition of the National Ambient Air Quality Standards.

Among these pollutants, soot has recently received a lot of interest within the scientific community, especially after the discovery of the link between exposure to fine particles (<2.5 μm, referred to as $PM_{2.5}$) and adverse health effects. Epidemiological studies show that increased incidence of asthma and asthmatic symptoms are associated with increasing concentrations of $PM_{2.5}$ in the atmosphere[1]. In addition to acute respiratory problems, long-term effects include lung cancer and cardiopulmonary diseases, as studied by Pope at al. in collaboration with the American Cancer Society[2,3]. These studies show that every 10 $\mu g/m^3$ increase in the $PM_{2.5}$ concentration was linked to approximately a 6% and 8% increase in cardiopulmonary and lung cancer mortality respectively. Fine particles inhalation may also worsen underlying health problems such as ischemic heart disease, fatal arrhythmia, and congestive heart failure[4,5].

Strategies to reduce fine particulate matter (PM) formation include optimization of the design of the combustion systems, variation of the fuel composition or usage of appropriate fuel additives. These strategies have shown promise in reducing PM emissions significantly. However, in order to implement such PM mitigation strategies effectively, an accurate description of the fuel burning process is essential. It is clear that soot is a product of incomplete hydrocarbon combustion generated in regions of the flame where there is not enough oxygen to convert the fuel into carbon dioxide and water. In these regions the chemistry is driven by unburned or partially-burned hydrocarbons. Large polycyclic aromatic hydrocarbons (PAHs) are formed from primary aromatic species (first and second ring)[7-9]; PAHs dimerization, coagulation and chemical growth processes lead to the formation of soot precursor particles, characterized by a size of 5-10 nm[7,10-12]. These precursors undergo simultaneous coagulation, coalescence and surface growth to form the final aggregates[7,12]. The physico-chemical description of PM formation is reported schematically in Figure 1.

Within the complexity of the processes leading to soot, the limiting step in the overall chain is the formation of the primary aromatic species. Sometimes, these first and second ring compounds already present in large amounts in raw fuels are also formed during the combustion processes. Many theoretical and experimental studies have been performed on the formation of the first aromatic ring, as described in recent critical reviews[7-9]. On the other hand, the pathways leading to subsequent multi-ring compounds have not been so well studied and understood.

In particular, the recombination reactions between the phenyl radical ($C_6H_5$) with acetylene ($C_2H_2$) have not been well studied despite being hypothesized as important pathways to the formation of relevant multi-ring compounds as naphthalene ($C_{10}H_8$, second ring aromatic).

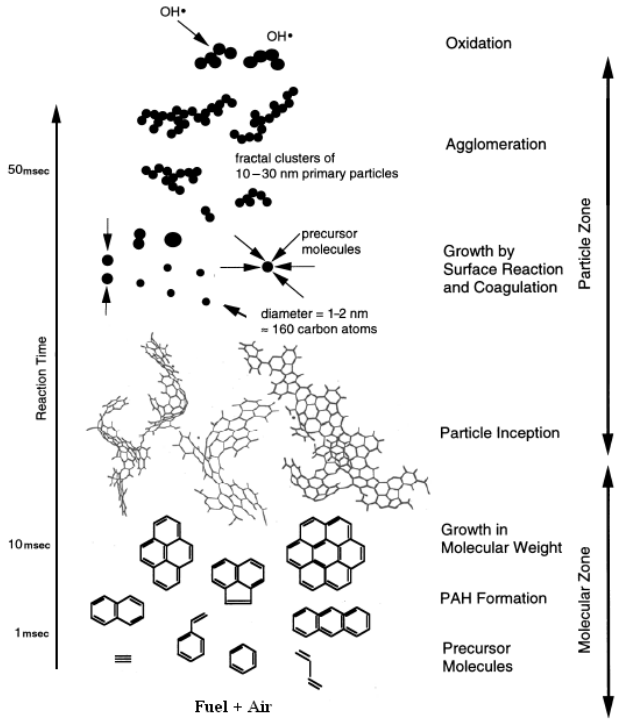


**Figure 1. Physico-Chemical Description of PM formation (based on Bockhorn[6]).**

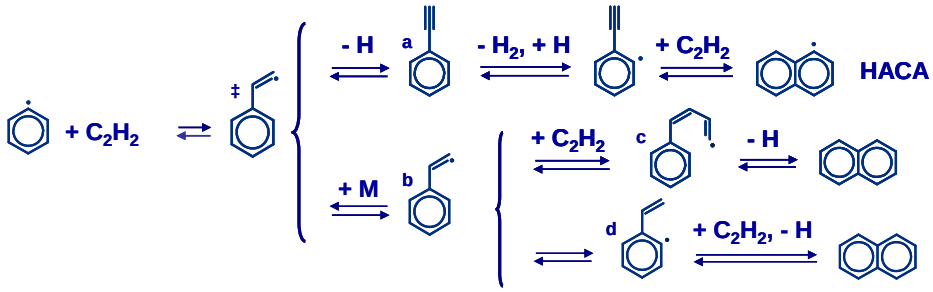


**Figure 2. Formation of naphthalene from phenyl + acetylene reaction.**

As mentioned, the reaction between phenyl and acetylene has been postulated to be the first major step in the formation of the second ring, naphthalene. This reaction could lead to the formation of an energized 2-phenylvinyl adduct (depicted with a dagger symbol in Figure 2) which can subsequently stabilize to either the 2-phenylvinyl radical ($C_6H_5CHCH$, compound "b") or decompose to phenylacetylene ($C_6H_5C_2H$, species "a") depending on the pressure and temperature conditions. Both species can lead to the formation of naphthalene, through addition of an additional acetylene to the radical site of the 2-phenylvinyl radical (forming first phenylbutadienyl radical, compound "c") or through the HACA (hydrogen abstraction $C_2H_2$ addition) mechanism[13,14] starting from phenylacetylene. Moreover 2-phenylvinyl radical could undergo an internal hydrogen abstraction from the ring forming 1-vinyl-2-phenyl radical (species "d"). Subsequent addition of acetylene to the radical site would lead to the second ring aromatic.

Prior experimental measurements on the total rate constant for the phenyl + acetylene reaction have been made by Fahr and Stein[15], who deduced an Arrhenius expression in a

temperature range between 1000 and 1330 K in experiments conducted in a Knudsen cell flow reactor operating at very low pressures (1-10 Torr). In a subsequent study Yu et al.[16] used cavity ring down spectrometry (CRDS) to obtain an estimate of the total addition rate constant at temperatures between 297 and 523 K. Yu et al.[16] performed an RRKM (Rice–Ramsperger–Kassel–Marcus) analysis of the reactions and were able to explain their data as well as prior high temperature experiments by Fahr and Stein[15]. At almost the same time Wang and Frenklach[17] studied the reaction as part of an attempt to characterize PAH growth up to the formation of pyrene (four fused rings species, $C_{16}H_{10}$, see nomenclature Figure 20 presented later) using semiempirical quantum-mechanical calculations and transition state theory and assessed pressure dependence by means of RRKM approach. Subsequent to these studies, Heckmann et al.[18] performed high temperature studies in their shock tube at pressure ~3 bars and reported the rate constant for $C_6H_5 + C_2H_2 \rightarrow C_6H_5C_2H + H$. In more recent works, Richter et al.[19] and Tokmakov and Lin[20] have performed additional theoretical studies in the attempt to improve the accuracy of the calculated rate constants based on the available experimental data[15,16,18]. Among the experimental measurements, only the Heckmann et al.[18] data were obtained at pressures above atmospheric, i.e. 3 bars. These data are clearly not sufficient to validate the theoretical models, especially in relation to pressure dependence effects and calculations of high-pressure limit rate constants. In addition, to the best of our knowledge there are no experimental investigations which provide a comprehensive speciation analysis of the products of the reaction between phenyl radical and acetylene, including measurement of the large PAH compounds which serve as soot precursors.

As described above, the formation of aromatic compounds, such as the phenyl radical, enhances soot formation. Aromatic compounds are not only formed as secondary products of the fuel decomposition, but are usually present in large amounts in the fuel itself. For example, alkylated aromatic hydrocarbons form major constituents of gasoline, diesel and jet fuels due to their high energy densities and resistance to autoignition[21-23]. The combustion of these aromatic based fuels is a serious emissions concern because of their enhanced capability to form polycyclic aromatic hydrocarbons, which ultimately lead to soot.

In view of these potential health and environmental hazards, it is important to identify the pathways leading to the soot formation from alkylated aromatic hydrocarbons. Previously, a high pressure oxidation and pyrolysis study of the monoalkylated aromatic, toluene, has been performed in our laboratory[24-25]. The corresponding double alkylated compound, m-xylene, has been studied in the past especially in relation to the formulation of surrogate mixtures.

| Measurement | Pressure/atm | Temperature/K | Reference |
|---|---|---|---|
| species profiles | 1 | ~1160 | 26 |
| species profiles | 1 | 1050-1400 | 27 |
| ignition delay times | 7-9 | 1336-1712 | 28 |
| ignition delay times | 9-45 | 941-1408 | 29 |
| ignition delay times | 20 | 600-900 | 30 |
| burning velocities | 3 | 450 | 31 |
| species profiles | 27-53 | 1024-1584 | current study |

**Table 1. Experimental conditions of the m-xylene studies available in literature.**

The m-xylene experimental data available in literature fall into three categories: species profiles obtained from reactors[26-27], ignition delay time measurements in shock tubes[28-29] and rapid compression machines[30] and laminar flame speeds[31]. The temperature and pressure ranges over which these experiments were performed are shown in Table 1**Error! Reference source not found.**. Despite the number of experimental studies conducted there is a lack of experimental data simultaneously at high temperature and high pressure conditions, which are characteristic of combustion environments.

**Goal and Technical Approach**

To address the lack of data, as well as the absence of chemical kinetic models validated at high temperature and pressure, the phenyl + acetylene reaction and the oxidation of m-xylene were studied using the high pressure shock tube present at the University of Illinois at Chicago. The decomposition of the phenyl radical prescursor was also investigated as a preliminary study for the subsequent experiments with added acetylene.

First, a new experimental set-up was studied and developed to address the problems, such as condensation and adsorption, which are typically encountered when large PAH compounds, including the ones which constitute the intermediate compounds for soot formation, are measured. Utilizing the new technique, valuable experimental data on key reactions for the formation of PAH species relevant to soot formation chemistry were obtained at pressures relevant to typical combustion chambers (25 - 50 atm) for a wide range of temperatures (900 - 1800 K) and for reaction times between 1.2 and 2 ms. Stable species profiles have been obtained by means of GC and GC-MS techniques, including profiles for the heavy multi-ring products.

Theoretical studies have been performed to estimate thermodynamic properties of the molecules involved in the reactions as well as estimate rate constants parameters for key reactions from analysis of potential energy surfaces. Finally, chemical reaction models have been developed to simulate the experimental data.

The comprehensive chemical kinetic models helped clarifying some of the aspects related to soot formation. The models provide the framework of detailed comprehensive models for the prediction of the morphology, size, and concentration of soot emission during combustion processes in modern high-pressure combustion chambers. Accurate predictions will lead to a better characterization of the optimal solutions to improve combustion performances and reduce soot emission.

# 2. PHENYL PYROLYSIS AND PHENYL + ACETYLENE REACTION

The development of chemical kinetic models able to accurately predict the formation of soot in combustion engines and turbines is strictly related to the accuracy in the description of the chemical mechanisms involved in the formation and growth of the polycyclic aromatic hydrocarbons (PAHs). Although several growth mechanisms have been proposed throughout the years, the multi-ring aromatic chemistry is far from being fully understood. The well-known HACA mechanism, Hydrogen-Abstraction/Carbon (acetylene)-Addition[33,13], is generally considered the principal pathway for the formation of large PAH compounds. The simplest system for which the HACA mechanism applies involves the reaction between phenyl radical and acetylene to form phenylacetylene and a subsequent additional HACA step which leads to the formation of the second-ring species. Among the competing pathways the so-called PAC mechanism (phenyl-addition/cyclization) has been proposed by Shukla and Koshi[34,35] as an efficient pathway for PAHs growth in benzene pyrolysis studies. In this case the phenyl radical adds directly to an aromatic molecule before undergoing cyclization to form larger intermediates. A comprehensive study on the phenyl + acetylene reaction and on the phenyl radical pyrolysis would clearly lead to a better understanding of the two mechanisms in relation to the formation of the primary PAH compounds which serve as building blocks for soot.

The radical-radical recombination between phenyl radicals has been studied in the past as main source of biphenyl[18,36], one of the most important intermediates for PAHs growth. In a recent paper, Tranter et al.[37] revisited the self-reaction of phenyl radicals based on low-pressure shock tube experiments and high-level theoretical calculations. The authors developed a chemical kinetic model which accurately simulates the laser schlieren experimental results. Nevertheless the model does not include a complete mechanistic description of the PAHs formation which is expected to be relevant at the high pressure conditions present in typical modern combustion devices. Several experimental and numerical studies have also been performed on the phenyl + acetylene reaction[15-20]. However to the best of our knowledge there are no experimental investigations which provide a comprehensive speciation analysis of the products of the title reaction, including measurement of the large PAH compounds.

The single-pulse high-pressure shock tube (HPST) present at the University of Illinois at Chicago has been used to perform experiments on the title reactions over a wide range of pressures (25 and 50 atm nominal pressures) and temperatures (900-1700 K) which encompass typical conditions in modern combustion devices.

## 2.1. Preliminary results

### 2.1.1. Traditional experimental set-up

The high-pressure shock tube present at the University of Illinois at Chicago is a well characterized experimental device for identification and measurement of the stable reaction products behind reflected shock waves. The apparatus has been described in detail in previous publications[38,39] and only the relevant features are reported here. A picture of the HPST and the analytical apparatus is shown in Figure 3.

**Figure 3. HPST and analytical equipment, traditional set-up.**

The HPST consists of a 2.97 m long driven section of 25.4 mm inner diameter (i. d.) and a driver section of 50.8 mm i. d. separated by a diaphragm section. The length of the driver section is varied by inserting metallic plugs in order to obtain constant reaction conditions as well as fast cooling of the reaction by the rarefaction wave. A dump tank placed just ahead of the diaphragm section on the driven side rapidly quenches the reflected shock wave, thereby permitting the shock tube to be operated in single pulse fashion. The apparatus is heated to 373 K to avoid condensation of reactant and product species.

The driven section is equipped with a set of seven high-frequency PCB piezoelectric pressure transducers, six positioned along the driven section and one located at the end-wall perpendicular to the flow. The pressure profiles from the six pressure transducers are used to obtain the incident shock wave velocities with an uncertainty ≤1%. Such velocities are experimentally related to the temperatures in the post-shock reaction by means of chemical thermometers[39]. Three chemical thermometers were used in the present investigation, cyclohexene[40] combined with 1,1,1-trifluoroethane[41] for the temperature range between 900 and 1362 K, and carbon disulfide[42] for temperatures between 1691 and 2000K. An interpolated calibration curve was used between 1362 K and 1691K. The maximum error in the post-shock temperature is around 1% for temperatures up to 1350 K, and 2% for temperatures higher than 1350 K. The pressure is measured directly from the pressure trace of the end-wall transducer while the reaction time is considered as the time between the arrival of the incident wave at the end-wall and the time when the pressure reaches 80% of its maximum value[43]. Uncertainty in the time measurement is no more than 5%.

Reagent mixtures consisting of phenyl iodide and acetylene, if any, diluted in argon (ultra high purity grade, 99.999%) were prepared manometrically in 42 liters vessels heated to 373 K and allowed to stand overnight before use. Phenyl iodide (Aldrich 98%) was degassed several times using a freeze/thaw procedure prior to use, while acetylene (BOC, grade 2.6) was purified using a Balston 95A filter. Neon was added as an internal standard to account for any dilution by the driver gas (helium).

In the traditional set-up, a sample of gas is withdrawn from the post-shock mixture through an automated sampling apparatus. The sample is stored at 373 K in electropolished, stainless steel vessels for subsequent analysis by gas chromatographic-mass spectrometric techniques. The analytical system consists of two Hewlett-Packard 6890 series gas chromatographs (GC's), the first equipped with a FID detector connected to a HP-1ms column for the measurement of phenyl

iodide and other heavy products, the second equipped with a FID (Flame Ionization Detector) detector and a TCD (Thermal Conductivity Detector) detector connected respectively to a HP-PLOT Q column for measurement of light species and to a HP-PLOT MoleSieve column for measurement of inert compounds (neon). A 5973 series mass spectrometer (MS) is also connected to the first GC for identification of unknown compounds in the mixtures. The GC calibration was mainly performed using certified gas mixtures as well as in-house prepared calibration mixtures. Typical errors in the GC measurements are around ±5%.

### 2.1.2. Traditional technique: experimental results

The initial experiments have examined nitrosobenzene ($C_6H_5NO$) and phenyl iodide ($C_6H_5I$) as phenyl radical sources for subsequent reactions with added acetylene.

Nitrosobenzene started decomposing around 950 K, while above approximately 1050 K it is completely gone, Figure 4A, presumably forming phenyl radical and NO. In order to determine if nitrosobenzene is a clean source of phenyl radicals, the GC apparatus was equipped with a Pulsed Discharge Detector (PDD) for NO measurement. The measured mole fraction of nitric oxide was found to be more than ten times the amount expected from a simple NO balance, suggesting that the quantification scheme for NO was not accurate. Moreover the nitric oxide profile showed a drop at high temperatures, indicating possible reactions of NO with the hydrocarbon products from the phenyl decomposition. Nitrosobenzene was abandoned as phenyl radical source.

Phenyl iodide showed, Figure 4B, a similar behavior to that for nitrosobenzene in that above a certain temperature, in this case approximately 1350K, all the phenyl iodide had disappeared presumably to phenyl radical and iodine. Figure 4 also indicates that the decomposition of phenyl iodide is pressure insensitive indicating that the decay is in the first order high pressure limit.

The main products of the phenyl iodide decomposition were acetylene, diacetylene, benzene, and phenylacetylene, measured using the FID detector coupled to the PLOT-Q column suitable for separation of light species. The additional FID coupled to the HP1-MS column was used for the quantification of phenyl iodide and the heavy species, i.e. naphthalene. Trace amounts of biphenyl were also observed, but could not be quantified. Subsequent studies showed that the quantitative measurement of heavy species using the traditional set-up was not accurate, due to inaccuracy of the calibration curves as well as condensation and adsorption of the heavy compounds onto the metallic vessel walls.

Figure 5 shows typical profiles for the main products of the phenyl iodide decomposition. Although acetylene and diacetylene start forming at around 1100K and 1300K respectively, the profiles show a steep increase only above 1400 K presumably in correspondence with the rupture of the aromatic ring. Benzene represents the major product of the reaction at intermediate temperatures. Small amounts of phenylacetylene were also measured.

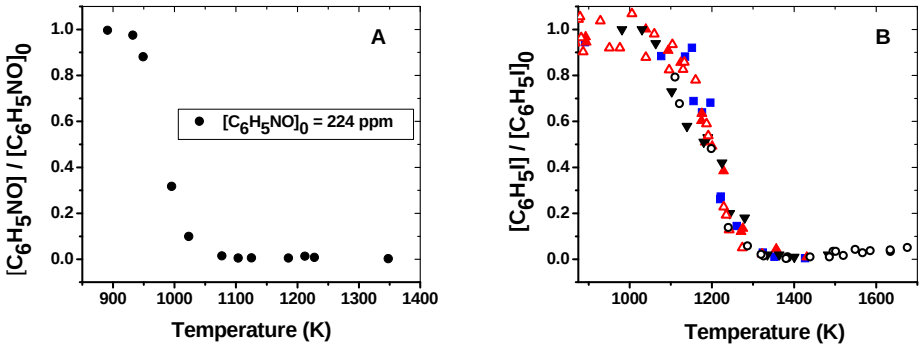


**Figure 4. Phenyl pyrolysis, traditional technique. A) Nitrosobenzene decomposition, 100 atm. B) Phenyl iodide decomposition; ■ $[C_6H_5I]_0 \approx 50$ ppm, 50 bar; ▲ $[C_6H_5I]_0 \approx 300$ ppm, 50 bar; ▼ $[C_6H_5I]_0 \approx 850$ ppm, 50 bar; Δ $[C_6H_5I]_0 \approx 200$ ppm, 25 bar; ○ $[C_6H_5I]_0 \approx 60$ ppm, 25 bar.**

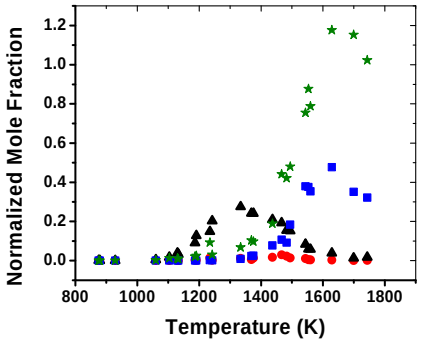


**Figure 5. Phenyl pyrolysis, traditional technique, main products. $[C_6H_5I]_0 = 61$ ppm, 25 bar. Black triangles: benzene; red circles: phenylacetylene; green stars: acetylene; blue squares: diacetylene.**

Phenyl iodide was subsequently used as a phenyl radical source for examination of reactions with acetylene. Different amounts of acetylene (50 and 240 ppm) were added to the initial mixture composed of around 100 ppm of phenyl iodide in argon. Experiments were conducted at nominal pressures of 25 and 50 atm over a range of temperatures between 1000 K and 1650 K. The phenyl iodide decomposition is shown in Figure 6. It is worth mention that neither the pressure nor the phenyl iodide/acetylene mixing ratio seem to have a noticeable effect on phenyl iodide consumption.

Besides the reactant molecule, several product species could be identified and measured. The corresponding mole fraction profiles for the experiments conducted with 50 ppm of acetylene are presented in Figure 7A. As for the phenyl radical pyrolysis, benzene is the major product at intermediate temperatures. Phenylacetylene is also produced in substantial amounts by the reactions between phenyl radicals and acetylene. Both benzene and phenylacetylene profiles peak at around 1300 K. At temperatures above 1400 K obviously decomposition reactions are dominating as indicated by the steep rise in acetylene and diacetylene concentrations. It is important to notice that both acetylene and diacetylene concentrations increase monotonically up to the temperature limit of the present experimental work (around 1600 K). There is a slight temperature shift in the profiles of these two species at the two different pressures which is not observed for benzene and phenylacetylene. Such a shift was not confirmed in the experimental

work conducted with an excess of acetylene in the initial mixture. Thus no definitive conclusions can be drawn on possible pressure-dependent mechanistic pathways which influence the formation of acetylene and diacetylene.

Figure 7B shows the results obtained with excess acetylene (240 ppm). The only substantial difference with the previous case is the increased formation of phenylacetylene. This result is in agreement with chemical intuition since at higher concentrations of acetylene more phenyl radicals are stabilized as phenylacetylene. Correspondingly, the phenylacetylene/benzene branching ratio increases from approximately ⅓ to 1 which corresponds as roughly to the variation in the phenyl iodide/acetylene ratio. Furthermore an interesting difference between the two sets of experiments is that, in case of the higher initial acetylene concentration, at high temperatures no further increase in the acetylene concentration could be detected but in contrast acetylene seems to be consumed. This might be due to the higher tendency for polymerization which leads to formation of larger polyacetylenes.

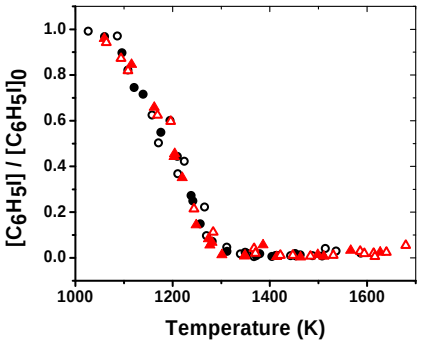


**Figure 6. Phenyl + acetylene, traditional technique, phenyl iodide decomposition. Solid symbols: nominal pressure = 25 atm; open symbols: nominal pressure = 50 atm. Circles: $[C_6H_5I]_0$ = 104 ppm, $[C_2H_2]_0$ = 50 ppm; triangles: $[C_6H_5I]_0$ = 118 ppm, $[C_2H_2]_0$ = 240 ppm.**

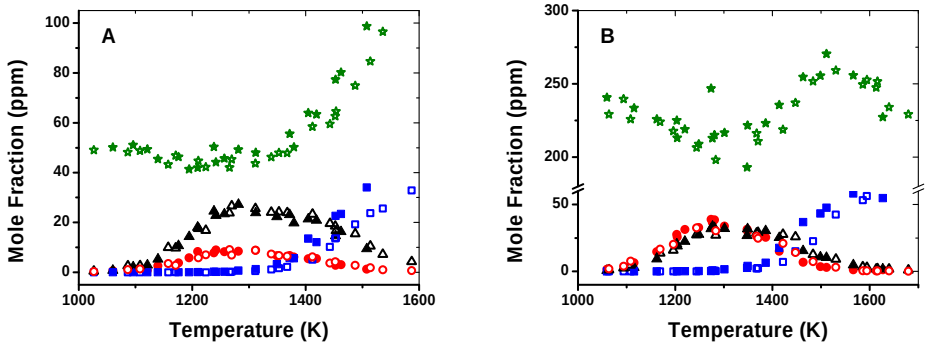


**Figure 7. Phenyl + acetylene, traditional technique, major products. A) $[C_6H_5I]_0$ = 104 ppm, $[C_2H_2]_0$ = 50 ppm. B) $[C_6H_5I]_0$ = 118 ppm, $[C_2H_2]_0$ = 240 ppm. Solid symbols: nominal pressure = 25 atm; open symbols: nominal pressure = 50 atm. Triangles: benzene; circles: phenylacetylene; stars: acetylene; squares: diacetylene.**

Although the experimental data presented in this section provide important information on the chemistry involved in the phenyl pyrolysis and in the phenyl + acetylene reactions, the

preliminary results are incomplete. In fact the experimental data show a drop in the carbon balance especially at high temperatures in correspondence with the formation of heavy semi- and non-volatile polycyclic hydrocarbons (i.e. naphthalene, biphenyl, phenanthrene, and so on) which are not analyzed (Figure 8). The profiles for the latter species are essential for the understanding of the reactions of the phenyl radical with acetylene as well as for the characterization of the pathways leading to naphthalene and other PAHs. The work reported in the following sections will describe the efforts done for defining an experimental procedure able to provide an accurate and reliable measurement of heavy semi- and non-volatile polycyclic hydrocarbons.

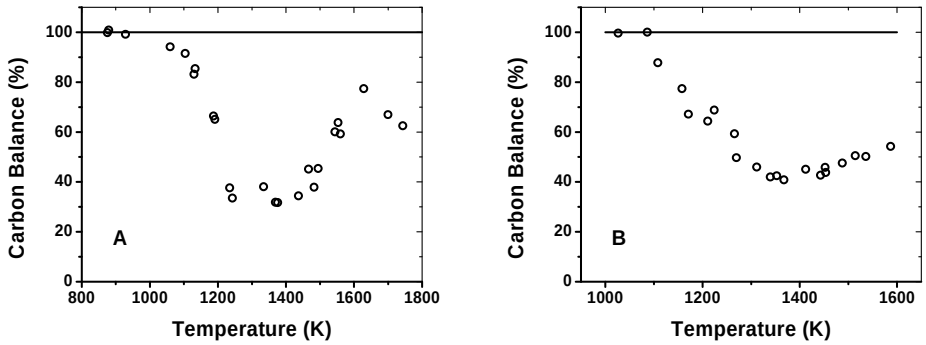


**Figure 8. Percentage of carbon recovery, traditional technique. A) $[C_6H_5I]_0$ = 61 ppm, 25 bar. B) $[C_6H_5I]_0$ = 104 ppm, $[C_2H_2]_0$ = 50 ppm, 50 atm.**

## 2.2.Online and offline experimental techniques for PAHs recovery and measurement

The condensation and/or adsorption of heavy semi-volatile and non-volatile compounds are common problems in many analytical systems, including among others, exhaust gas analysis apparatuses[44,45] and ambient air sampling analysis systems[46,47]. Alternatively, specific resins, such as Amberlite XAD-2 polymeric adsorbent have proven to be successful in many practical applications. The resins trap the gas-phase polycyclic aromatics (naphthalene and heavier compounds) present in the gas sample, for subsequent extraction with an appropriate solvent. However, the resin trapping technique is not suitable for systems where the sampling process involves high-speed or very fast (sometimes supersonic) flows, as in the case of high-pressure experimental apparatuses, since the resin can not guarantee the recovery of 100% of the PAH products. The resin trapping method thus can only provide a qualitative but not quantitative measure of the distribution of heavy compounds in the analyzed sample. Sometimes too, when the concentration of the PAHs in the sample is small, a rotary evaporator technique must be used to concentrate the solution obtained from the resin method to permit detection of the absorbed species. However, the experimental investigation by Cheng[48] has shown that the rotary evaporator technique leads to losses in the target species measurement which are molecular weight dependent as well as dependent on the required volumetric reduction in the sample size. Thus the sample concentration step of the resin trapping method not only greatly increases the time required to complete the experimental measurement but also provides an additional source

of uncertainty to the possible losses during the sampling as well as during the procedure aimed at extracting the heavy compounds from the resin.

This section presents the experimental investigation on alternative online and offline techniques for the recovery and measurement of the typical PAH compounds which constitute the building blocks for PM formation. In particular, the present techniques apply to all the experimental apparatuses where the conventional techniques which use resins and rotary evaporators fail to provide a complete recovery of the gas-phase semi-volatile and non-volatile components. Among such experimental apparatuses are shock tubes, such as the high-pressure shock tube present at the University of Illinois at Chicago[38], flow reactors, and furnace reactors, designed for the study of chemical reacting flows.

*Online vs. offline*. The traditional online techniques, which include well established method of time-of-flight (TOF) mass spectrometry, take advantage of the direct connection between the analytical apparatus and the instrumentation used to generate the gas sample which needs to be measured. This allows quick analysis of the sample, which results into the ability to detect short-lived species, such as radicals, and measure compounds which oxidize when stored or tend to condense/adsorb, such as large molecular weight species. Nevertheless, online techniques can not be implemented in those applications where the sample has a large volume or a very high pressure which can not be sustained by the specific analytical apparatus. In addition, the presence of solid particles (soot) in the sample could interfere with the analysis or even damage the analytical system. Another factor which plays a relevant role in the ability to implement the online techniques is the necessity to have the analytical apparatus available in-situ where the sample is generated. These limitations can be overcome by the use of offline techniques which allow the analysis of samples, such as the air samples[46,47], which are collected over relatively long times and in different geographical locations. Nevertheless, the use of offline techniques is limited to the measurement of stable compounds which can be easily stored. In particular, the measurement of heavy multi-ring species is possible only after the implementation of supplemental procedures such as the resin trap/rotary evaporator technique described above.

### 2.2.1. Offline technique

The GC/GC-MS offline measurement of light hydrocarbon compounds has been extensively used in our laboratory to measure stable products from high-pressure shock tube oxidative and pyrolytic experiments of PAH formation. Due to the high pressure reached during the experiments (up to 1000 atm, Ref. 38), instead of glass vessels, 150 cc stainless steel electropolished vessels are used to collect the gas sample withdrawn from behind the reflected shock wave during a 0.3 second time window. A portion of the stored sampled gas is subsequently injected into the gas chromatographic system for measurement of the stable species. Despite the success of this sampling procedure in our previous work[25,52,53] the experimental procedure had not been extended to the sampling of heavy multi-ring compounds. In order to establish a new experimental procedure aimed at extending the analytical capability to large molecules, a series of experiments were initiated using the traditional stainless steel electropolished vessels and naphthalene as representative test compound. The basic idea behind the new technique, which assumes that heavy multi-ring compounds will condense, is to analyze both the non-condensed gas phase species and the condensed components by a combination of gas phase and liquid injection GC analyses.

### *2.2.1.1. Preliminary experiments*

Before performing the experiments relevant to the determination of the optimal offline technique, several preliminary experiments were executed to test the uncertainties related to the various auxiliary experimental components.

The first important element to be evaluated when quantitative studies are performed is the uncertainty in the instrument calibrations as well as the linearity of the response. Several liquid solutions with different concentrations of naphthalene in methylene chloride were prepared and analyzed with both the mass spectrometer and the FID detector. The results, reported in Figure 9, clearly indicate that although the MS response is linear on a macroscopic scale, the detector loses sensitivity when the concentration drops below 1 μg/ml (Figure 9b). The difference between the calibration curves obtained fitting the data over the entire range (Figure 9a) or using only the data with concentrations below 1 μg/ml is around 12%. On the other hand, if we repeat the same test using the FID detector (Figure 9c and Figure 9d), the corresponding difference between the calibrations is only 3% which is within the experimental uncertainty of the measurements. Due to the improved linearity, the FID detector was utilized for analysis of liquid samples. Calibrations for other PAH components were obtained with a similar procedure used for Figure 9c and Figure 9d.

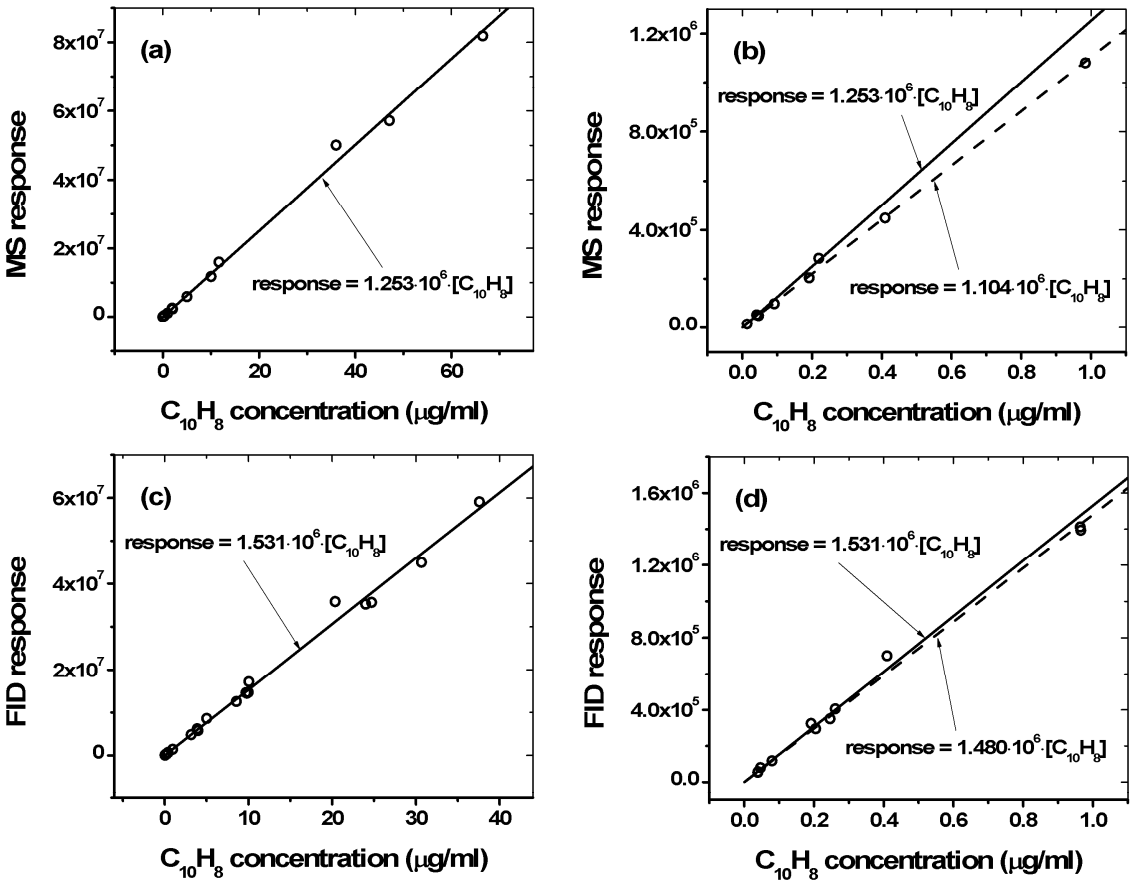


**Figure 9. MS [(a) and (b)] and FID [(c) and (d)] naphthalene calibrations using liquid injection port. (b) and (d) represent a zoom-in of the data in A and C respectively. ○ experiment; —— calibration curve; – – calibration curve considering only data with concentrations below 1 μg/ml.**

A second linear FID detector was used to measure the gas phase components. In this case the calibration was performed using a 250 cc glass vessel equipped with a septum. The vessel was heated to 150°C. Different solutions of naphthalene in methylene chloride were prepared and small amounts injected into the glass vessel, previously evacuated, using a syringe. The solution vaporizes immediately due to the high temperature and high vacuum. Using a mixing rig, the vessel is subsequently filled with argon to a determined pressure. Pressure and temperature are recorded and used subsequently to calculate the actual mole fraction of naphthalene in the gas phase mixture. The gas mixture is allowed to stand for around 10-15 minutes before injection into the GC (to guarantee homogeneity).

Figure 10a contains the experimental results obtained using a 10 µl syringe and different injection volumes. Although for each injection volume the response is linear, the calibration curve for naphthalene varies if obtained by injecting 1, 2, or 3 µl of solution into the glass vessel. In particular, the response becomes lower with increasing injection volume which suggests the presence of trapped sample in the syringe needle. In fact, from a logical point of view, the trapped sample is more relevant when low volumes are injected since the percentage of extra solution is greater. As shown in Figure 10b the use of a 5 µl syringe with plunger in the needle solves the dead volume problem. The experimental points lie on the same curve independently of the injection volume and the calibration curve is now self consistent. All the following experiments were performed using the 5 µl syringe with plunger in the needle. The gas phase calibrations for other species were obtained similarly to the case reported in Figure 10b.

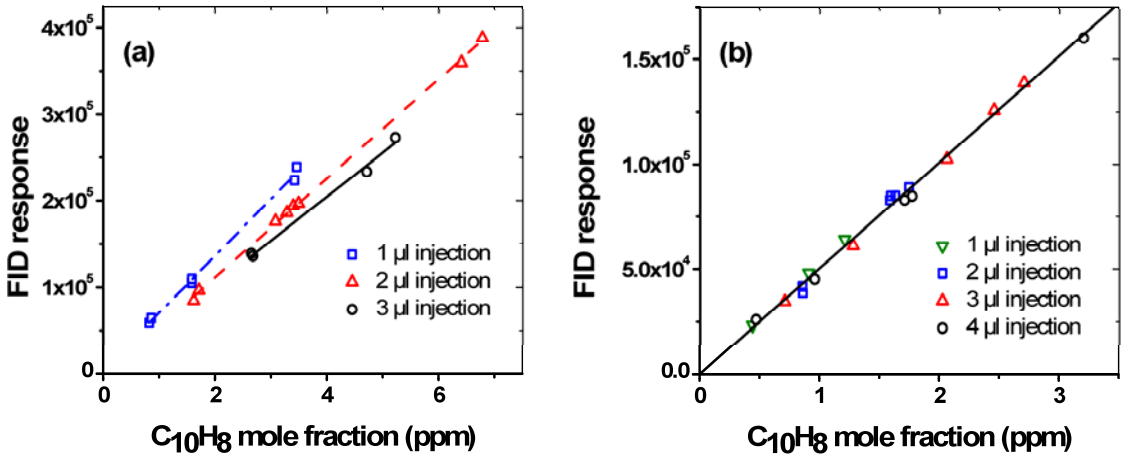


**Figure 10. FID gas calibrations. A) 10 µl syringe; B) 5 µl syringe with plunger in the needle.**

An additional possible source of uncertainty is related to the syringe calibration. Tests were performed to determine the magnitude of such uncertainty. Solutions of naphthalene in methylene chloride were prepared and the 5 µl syringe used to inject 5 µl of the solution into a measured volume of methylene chloride (dilution step). The diluted mixture is then analyzed and compared with the calculated value (from the measured masses of naphthalene and methylene chloride). The comparison provides a good estimate of the error associated with the use of the syringe. The results, reported in Table 2, indicate that the maximum uncertainty is around 2%,

which can be considered almost negligible compared to the uncertainty related to the preparation of the naphthalene and methylene chloride solution and to the GC calibrations.

| | measured [$C_{12}H_8$] (µg/mol) | calculated [$C_{12}H_8$] (µg/mol) | error (%) |
|---|---|---|---|
| **S1** | 1.43 | 1.42 | +0.7% |
| **S2** | 2.58 | 2.69 | -4.1% |
| **S3** | 1.26 | 1.29 | -2.3% |
| **S4** | 1.39 | 1.42 | -2.1% |
| **S5** | 1.43 | 1.45 | -1.4% |

**Table 2. Tests to evaluate the uncertainty in the syringe calibration.**

#### *2.2.1.2. Primary experiments*

The purpose of the present section is to provide a brief overview of the experimental work performed to determine an optimized procedure for the recovery of PAH compounds using gas phase and liquid injection GC techniques. The experimental set-up consists of a 150 cc stainless steel electropolished vessel connected one side to a septum and on the other to a stainless steel high-pressure valve (Figure 11). The connection section for the septum can be heated to 200-220 °C independently from the vessel body. The test mixture is prepared injecting into the heated connection section a specific volume of solution of naphthalene in methylene chloride. The flash vaporization of the injected solution is guaranteed by the high temperature of the connection section and by previous evacuation of the vessel. The injection volumes vary from 1 µl to 5 µl while the concentrations of the solutions from around 450 µg/ml to 2000 µg/ml. These values give a final naphthalene gas phase mole fraction between 1 and 10 ppm after dilution with argon (17 to 19 psi). The gas phase mixture simulates a gas sample withdrawn from an experimental apparatus or from the atmosphere containing a low concentration of target contaminant (1-10 ppm). This is definitely the most challenging situation especially if quantitative measurements are required but experiments similar to the ones presented here can be easily repeated using higher concentrations of naphthalene if necessary for the specific application.

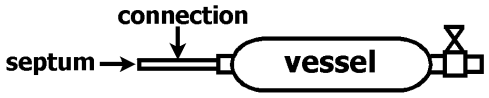


**Figure 11. Assembly for PAH recovery experiments.**

The first set of experiments has been conducted maintaining the vessel at room temperature during the entire analytical process. This technique represents the simplest solution since it does not require any additional instrumentation. After standing for at least 15 minutes to homogenize, the gas mixture is analyzed through the HP-1ms column. The mole fraction of naphthalene obtained from the analysis can be converted into actual µg of naphthalene using the ideal gas law (gas phase component). In the meantime, the vessel is flushed with methylene chloride. The volume of solvent used during the flushing procedure varied between 30 and 100 ml with no difference in the results. The resulting solution of naphthalene dissolved in methylene chloride is subsequently injected into the DB-17ms column. Multiplied by the measured volume of methylene chloride used in the flushing procedure, the concentration obtained from the analysis provides the condensed component of naphthalene in the sample. The sum of the gas phase and condensed components can be compared with the injected mass of naphthalene to obtain the percentage recovery for the specific experiment.

The results, presented in Table 3, are divided into two groups. The flushing procedure for the experiments from N1 to N4 was conducted introducing the methylene chloride into the vessel, closing the vessels, and shaking for 10 minutes. Within a 10% of discrepancy, the measured mass of naphthalene is higher than the actual mass introduced into the vessel. The reason for this unexpected result, confirmed also by tests conducted with lighter compounds as described later in the manuscript, is associated with the relatively high mole fractions of naphthalene in gas phase. Part of this gas phase component is clearly dissolved into the methylene chloride during the flushing procedure and thus it is counted twice both in gas and in liquid phase.

Improvement in the accuracy of the procedure was obtained by modifying the flushing technique (N5 to N8 in Table 3). The new flushing technique consists in introducing the solvent into the vessel and continuously rotating the open vessel for approximately 2 minutes. In this case the major part of the gas phase naphthalene is allowed to exit the vessel together with the methylene chloride vapor. After two minutes of rotation, the vessel is closed and subjected to the usual shaking for around 8 minutes. With the implementation of the new procedure the percentage of naphthalene recovered is closer to the desired 100% and only a couple of percentage points higher. Tests were also conducted to remove the gas component of the mixture using a gentle flow of argon through the vessel just before the flushing but the attempts resulted in lower recovery rates.

| | gas (µg) | condensed (µg) | total (µg) | injected (µg) | recovery (%) |
|---|---|---|---|---|---|
| **N1** | 2.70 | 2.69 | 5.39 | 5.06 | 106.5% |
| **N2** | 2.63 | 2.73 | 5.36 | 5.01 | 107.0% |
| **N3** | 5.56 | 4.95 | 10.51 | 10.00 | 105.1% |
| **N4** | 2.68 | 2.89 | 5.57 | 5.00 | 111.4% |
| **N5** | 2.71 | 2.43 | 5.16 | 5.00 | 103.2% |
| **N6** | 1.60 | 1.52 | 3.12 | 2.99 | 104.3% |
| **N7** | 0.82 | 1.15 | 1.97 | 1.92 | 102.6% |
| **N8** | 2.58 | 2.46 | 5.04 | 4.90 | 102.9% |

**Table 3. Experiments with vessel at room temperature.**

In order to further improve the recovery results eliminating the excess naphthalene, we started a series of experiments performing the entire analytical procedure with the vessel cooled to a temperature between -10 and -15 °C. Table 4 contains the related results. The recovery is accurate with an uncertainty of around 7% which is totally within the uncertainties associated with the preparation of the mixture and with the GC measurements. Since the gas phase component is small, no substantial differences were observed between the results obtained with the two flushing methods described above, i.e. the shaking (N9-N14) and the rolling techniques (N15-N17).

| | gas (µg) | condensed (µg) | total (µg) | injected (µg) | recovery (%) |
|---|---|---|---|---|---|
| **N9** | 0.46 | 4.47 | 4.93 | 5.06 | 97.4% |
| **N10** | 2.23 | 8.19 | 10.42 | 10.13 | 102.9% |
| **N11** | 0.27 | 4.40 | 4.67 | 5.01 | 93.4% |
| **N12** | 0.62 | 4.33 | 4.95 | 5.01 | 98.8% |
| **N13** | 0.74 | 4.00 | 4.74 | 4.90 | 96.7% |
| **N14** | 0.60 | 4.68 | 5.28 | 4.90 | 107.8% |
| **N15** | 0.35 | 4.41 | 4.76 | 4.90 | 97.1% |
| **N16** | 0.03 | 1.90 | 1.93 | 1.96 | 98.5% |
| **N17** | 1.63 | 3.50 | 5.13 | 4.90 | 104.7% |

**Table 4. Experiments with cooled vessel.**

Additional experiments were performed using a 500 cc stainless steel electropolished vessel to test possible dependence of the recovery results on the shape of the vessel, in particular on the ratio between surface area and volume. All the experiments were conducted cooling the vessel since this procedure showed slightly better recovery results compared to the procedure at room temperature. In this case solutions with naphthalene concentrations between 1800 and 9000 μg/ml and injection volumes between 1.5 and 8 μl were used to obtain a final argon-naphthalene mixture with a naphthalene mole fraction between 1 and 17 ppm. Similarly to the experiments reported in Table 4, the maximum error is around 7% (Table 5), becoming even smaller when relatively large masses of naphthalene are injected into the vessel (N26-N28). No difference between the shaking (N18-N24) and the rolling (N25-N28) flushing techniques is once again observable. The results confirm the excellent recovery rates obtained with the proposed analytical methodology and indicate that the specific shape of the vessel does not affect the accuracy of the procedure.

| | gas (μg) | condensed (μg) | total (μg) | injected (μg) | recovery (%) |
|---|---|---|---|---|---|
| **N18** | 4.19 | 5.56 | 9.75 | 9.67 | 100.8% |
| **N19** | 1.89 | 2.53 | 4.42 | 4.57 | 96.7% |
| **N20** | 1.53 | 2.68 | 4.21 | 4.57 | 92.1% |
| **N21** | 1.25 | 1.60 | 2.85 | 2.74 | 104.0% |
| **N22** | 2.09 | 2.59 | 4.68 | 4.57 | 102.4% |
| **N23** | 1.71 | 2.80 | 4.51 | 4.57 | 98.7% |
| **N24** | 1.59 | 10.08 | 11.67 | 10.91 | 107.0% |
| **N25** | 1.06 | 9.87 | 10.93 | 10.91 | 100.2% |
| **N26** | 1.48 | 26.78 | 28.26 | 27.42 | 103.1% |
| **N27** | 0.99 | 35.66 | 36.65 | 36.55 | 100.3% |
| **N28** | 2.01 | 52.94 | 54.95 | 54.83 | 100.2% |

**Table 5. Experiments with cooled 500 cc vessel.**

Before proceeding with the analysis of the recovery of compounds with different molecular weights and specific properties compared to naphthalene, the effect of the variation in the mixture pressure was also evaluated. As mentioned before, the results presented are referred to gas mixtures prepared at a total pressure between 17 and 19 psi, slightly above atmospheric pressure. Experiments were repeated using the 150 cc vessel and around 39 psi mixtures with the vessel at room temperature. Thus we would expect a recovery percentage between 102 and 110% as in the case of the experiments in Table 3. Surprisingly the results did not confirm the expectations. As shown in Table 6, although the experiments were conducted at room temperature, the recovery rate is low indicating a loss of naphthalene for both flushing procedures (N29-N31 shaking, N32-N33 rolling). This unexpected behavior could be a consequence of the quick release of the gas mixture, which largely exceeds atmospheric pressure for these experiments, when the vessel is opened to allow the introduction of the methylene chloride used for the flushing procedure. Part of the naphthalene condensed on the walls of the vessel could vaporize at the new low pressure conditions and not get dissolved in the methylene chloride. This is a very important point to consider when designing an experiment. In fact if the pressure of the gas withdrawn for analysis is too high, a low recovery rate as the one reported in Table 6 could be obtained. A solution to the problem could be an increased volume of the vessel so that the pressure is decreased to the atmospheric value in the vessel. The shape of the vessel does not influence accuracy of the recovery technique as discussed previously in the text.

| | gas (µg) | condensed (µg) | total (µg) | injected (µg) | recovery (%) |
|---|---|---|---|---|---|
| **N29** | 2.58 | 2.00 | 4.58 | 4.98 | 92.0% |
| **N30** | 2.37 | 1.85 | 4.22 | 4.90 | 86.1% |
| **N31** | 2.38 | 1.61 | 3.99 | 4.90 | 81.4% |
| **N32** | 2.27 | 1.89 | 4.16 | 4.98 | 83.5% |
| **N33** | 0.51 | 0.60 | 1.11 | 1.20 | 92.5% |

**Table 6. Experiments at higher pressures and vessel at room temperature.**

All the experiments reported in the previous paragraphs use naphthalene, the simplest among the multi-ring hydrocarbons, as reference compound. Species with larger molecular weights are expected to have lower vapor pressure than naphthalene, thus the recovery would be similar with the only difference being less of gas phase component compared to the solid condensed component. In order to test the recovery rates of the proposed technique for heavier species, the experiments with the 500 cc cooled vessel were repeated for biphenyl as a test compound using the rolling technique as the flushing procedure. The prepared gas mixtures in this case simulate a gas sample containing a mole fraction from 1 to 30 ppm of biphenyl. The results are reported in Table 7 and indicate an excellent recovery rate over the entire mass range. The excellent accuracy of the proposed method is again demonstrated for species like biphenyl which are practically non-volatile and have a very small vapor component.

| | gas (µg) | condensed (µg) | total (µg) | injected (µg) | recovery (%) |
|---|---|---|---|---|---|
| **B1** | 0.00 | 38.34 | 38.34 | 37.93 | 101.1% |
| **B2** | 0.15 | 21.66 | 21.81 | 21.07 | 103.5% |
| **B3** | 0.03 | 4.81 | 4.84 | 4.98 | 97.2% |
| **B4** | 0.01 | 114.64 | 114.65 | 115.81 | 99.0% |
| **B5** | 0.02 | 88.48 | 88.50 | 90.08 | 98.2% |
| **B6** | 0.02 | 65.01 | 65.03 | 64.34 | 101.1% |

**Table 7. Experiments for biphenyl recovery with cooled 500 cc vessel.**

Very different considerations apply for compounds having a smaller molecular weight than naphthalene but still sufficiently high to partially condense on the surface of the vessel. These compounds include for example small halogenated hydrocarbons and other semi-volatile compounds. Experiments have been conducted using iodobenzene as test species in order to determine if the procedure for the recovery of large PAH hydrocarbons is suitable also for lighter species. Of course the completely volatile compound can be easily measured with a simple gas analysis before the flushing procedure.

The preliminary experiments conducted using the procedures described above showed a percentage of recovery for iodobenzene much higher than 100% (around 130 to 140%). This is mainly due to the gas phase component which is predominant with respect to the condensed phase even when the 500 cc vessel is cooled to -15 °C. As, to a minor extent, for the naphthalene experiments at room temperature, part of the iodobenzene in gas phase is dissolved into the flushing solution, and thus measured twice in the total iodobenzene mass balance. This hypothesis was confirmed by blowing nitrogen through the vessel for 3-5 seconds right before the methylene chloride flushing. The results were accurate (error in the range between -9% to +2%) which indicate that the gas phase is responsible for the extra iodobenzene. On the other hand, as previously emphasized in the manuscript, this method of storing samples in a vessel is not suitable for the measurement of PAH compounds such as naphthalene.

Although the experiments for iodobenzene are clearly not satisfactory, a careful analysis of the results suggests a different approach to the problem. At a defined temperature the ratio between the amount of iodobenzene in gas phase and in condensed phase is almost constant. Experiments at room temperature were conducted to verify this hypothesis over a wide range of mole fractions (5 to 200 ppm) using both the 500 cc vessel and a new stainless steel electropolished 300 cc vessel. The results shown in Figure 12 indicate that the percentage of iodobenzene in gas phase is around 80% for the 500cc vessel and around 89% for the 300cc vessel. Excluding a few experiments, marked with a cross, which are clearly wrong possibly due to an error in the experimental procedure, all the condensed phase percentages lie close to the two fitting values within a 5-7% uncertainty. This uncertainty is similar to the one obtained for the recovery of naphthalene. Very interesting from an experimental point of view is the difference in average condensed phase percentages between the two vessels. The surface area to volume ratio clearly has a significant effect on the proportions between gas phase and condensed phase components. This suggests that new tests need to be repeated in case of the use of a different vessel. Once the average condensed phase percentage is obtained similarly to the case in Figure 12, this value can be used to scale the gas phase mole fraction. For example, if for a specific gas sample the gas phase mole fraction of iodobenzene is 100 ppm, the total iodobenzene mole fraction would be 125 ppm (100 divided by 0.8) and 112 ppm (100 divided by 0.89) in the case we used the 500 cc or the 300 cc vessel, respectively.

Finally, in order to evaluate the effect of the temperature on the percentage of iodobenzene in gas phase, a few experiments were also conducted with the 500cc vessel cooled to -12°C. The percentage dropped from an average value of 80% to values between 63% and 70% (mole fractions between 80 and 180 ppm, data not shown).

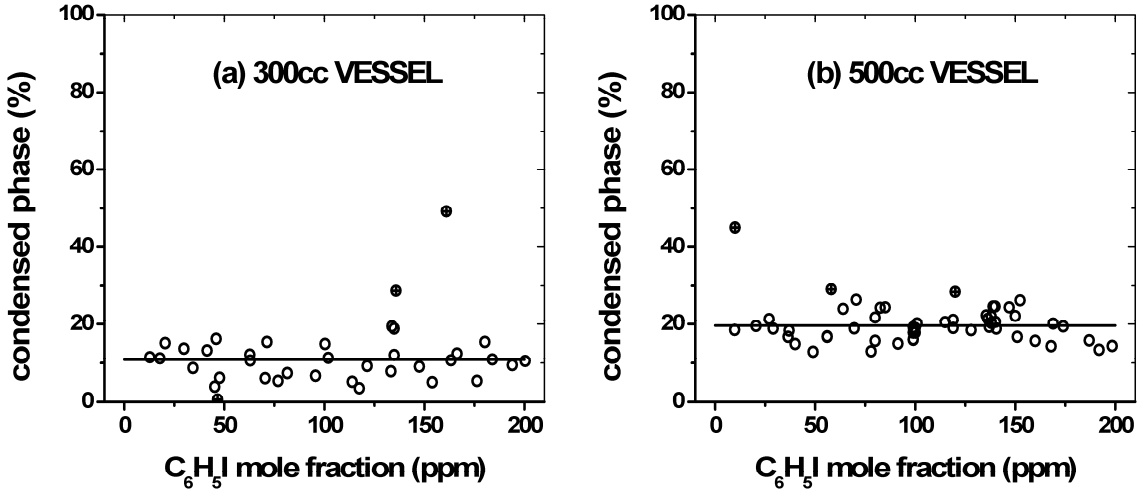


**Figure 12. Percentage of iodobenzene ($C_6H_5I$) in condensed phase. Vessel at room temperature.**

### *2.2.1.3. Optimal offline recovery technique*

Now that we have presented all the experimental results related to the recovery of semi- and non-volatile compounds, including PAH intermediates, a short paragraph which summarizes the main findings and suggests the optimal offline technique is provided. For the experimental results, the sample vessel can be maintained at room temperature during the collection of the gas

sample from a specific experimental apparatus, from automotive exhaust systems, or from the atmosphere. Once the sample is collected, gas injection into a GC column specifically suitable for the separation of light hydrocarbons, such as the HP-PLOT Q column, is required for the measurement of the gas phase volatile components of the mixture. The mole fraction of the semi-volatile species, such as iodobenzene, can be corrected by a factor that takes into account the component in condensed phase. After the injection for light species measurement, the vessel is cooled to ≈-15 °C and a new gas injection performed to measure the residual gas phase fraction of multi-ring compounds. The GC column in this case needs to be suitable for separation of heavy hydrocarbons (DB-17ms or HP-1ms). The sample vessel is subsequently flushed with methylene chloride and the solution injected into the GC for further analysis. The gas phase and liquid phase analyses done with the vessel cooled provide accurate quantitative measurements of heavy semi-volatile and non-volatile species (i.e. naphthalene, biphenyl, and so on). The expected error in the final recovery of the heavy components is around ±7%.

Before concluding it is worth mention that if a cooling apparatus is not available or if it is necessary to reduce the time of the experiment, the analyses of the PAH semi- and non-volatile components can be performed at room temperature. In this case the flushing technique should be modified to the rolling + shaking technique as described in the text. The performance of the technique is similar in terms of recovery of heavy non-volatile components, although for semi-volatile species such as naphthalene a small overestimation of the total mole fraction is expected.

### 2.2.2. Offline technique: experimental results

Experiments on the phenyl iodide pyrolysis as well as on the reactions between the phenyl radical and acetylene have been performed using the new offline experimental procedure. Similar conditions to the preliminary data reported in section 2.1.2 were used, with nominal pressure of 50 atm, temperature range between 900 K and 1850 K, and reaction times of 1.5-2 ms. The phenyl iodide in the initial mixture was around 45 ppm, with or without addition of 180 ppm of acetylene. The species profiles were consistent with the preliminary results obtained with the traditional technique for the lighter compounds (phenyl iodide, acetylene, diacetylene, benzene, phenylacetylene). The profiles are reported in Figure 13A and Figure 14A.

In addition to the compounds that could be measured with the traditional technique, profiles were obtained for naphthalene, biphenyl, phenanthrene, and diphenylethyne (chemical structures reported in Figure 20). In particular, Figure 13B shows the results for biphenyl which is the only PAH compound produced in substantial amounts from the phenyl radical self-reactions. On the other hand, several multi-ring compounds, including the major ones biphenyl and diphenylethyne, were identified in the study of the phenyl + acetylene reaction (Figure 14B). Small amounts of naphthalene and phenanthrene were also measured.

Although improvements were observed in the ability to collect and measure heavy polycyclic hydrocarbons, the carbon balance analyses still showed a drop at high temperatures (Figure 15). Although analyses were conducted to understand the causes of the drops, no plausible explanation could be found. Nevertheless, subsequent experimental tests on a different set-up showed that one of the seals of the automated valve had been destroyed, releasing pieces of graphite and powder in the vessels. The solid particles are chemically active and can easily adsorb PAH compounds from the gas phase. The recovery through the offline flushing technique was certainly influenced by the presence of particles in the system.

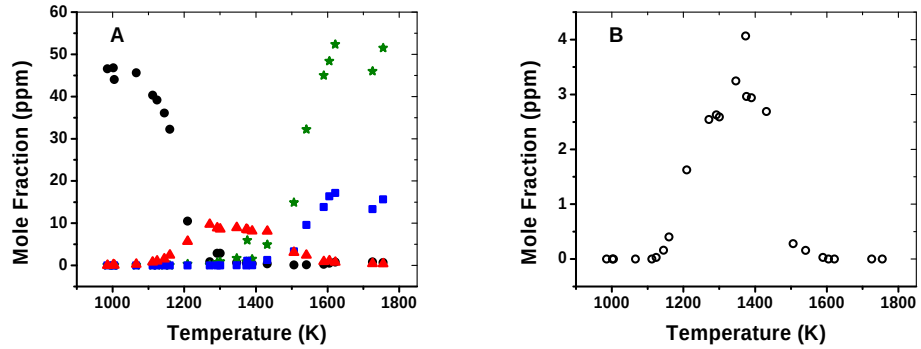


**Figure 13. Phenyl pyrolysis, flushing technique, $[C_6H_5I]_0$ = 46 ppm, 50 bar. A) Light hydrocarbons. Circles: phenyl iodide; triangles: benzene; stars: acetylene; squares: diacetylene. B) Biphenyl.**

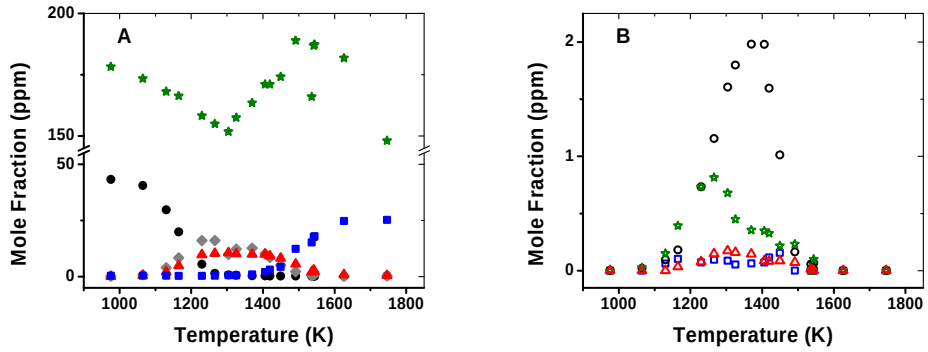


**Figure 14. Phenyl + acetylene, flushing technique, $[C_6H_5I]_0$ = 43 ppm, $[C_2H_2]_0$ = 178 ppm, 50 atm. A) Light hydrocarbons. Circles: phenyl iodide; triangles: benzene; rhombuses: phenylacetylene; stars: acetylene; squares: diacetylene. B) PAHs. Circles: biphenyl; stars: diphenylethyne; triangles: phenanthrene; squares: naphthalene.**

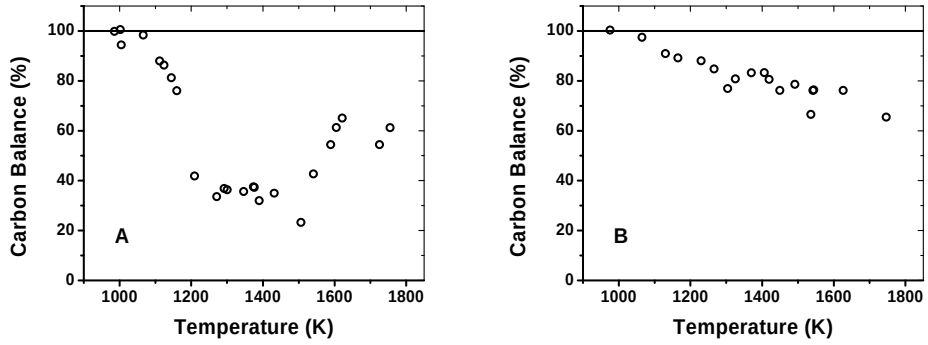


**Figure 15. Percentage of carbon recovery, flushing technique. A) $[C_6H_5I]_0$ = 46 ppm, 50 bar. B) $[C_6H_5I]_0$ = 43 ppm, $[C_2H_2]_0$ = 178 ppm, 50 atm.**

### 2.2.3. Online technique

The purpose of the present section is to provide an overview on the implementation of an online experimental set-up and methodology for measurement of heavy PAH gas phase compounds by conventional GC technique. The proposed technique combines the advantages of the conventional gas chromatography (sensitivity and ability to separate complex mixtures) with the simplicity in design and experimental procedure typical of the online techniques.

The GC apparatus described in the relative section was connected directly to the high-pressure shock tube present at the University of Illinois at Chicago[38] (Figure 16). A three-foot long, 1/4" OD tube connects the automated valve positioned at the end of the shock tube to the first GC. The gas is transferred to the GC injection valve through a 1/16" tube, fills the sample loop and flows to the second GC through a 1/8" tube. In this second GC, the gas fills in series two sample loops, before entering a sampling rig. The sampling rig is connected to an Edwards E2M1.5 rotary pump, a heated MKS capacitance manometer (type 631B, 1000 Torr full scale), a 150 cc reservoir, and a line for helium gas. Two additional lines are present, one connected to an exhaust line for safety purposes, the other available for connection of gas mixture bottles or vessels for calibration procedures. All the lines and connections present in the sampling section were built with treated stainless steel tubing, including the GC sample loops which were in-house cut using 1/16" tube. In addition, the lines are evenly wrapped with heavy insulated heating tapes of different width and watt density based on the thickness of the specific tube to be wrapped. Seven different heating zones are present, each associated with one type-J thermocouple. The temperature is set at 150 °C to avoid condensation of large molecules and is controlled by means of a multi-zone temperature controller by Omega (model CN1507-TC).

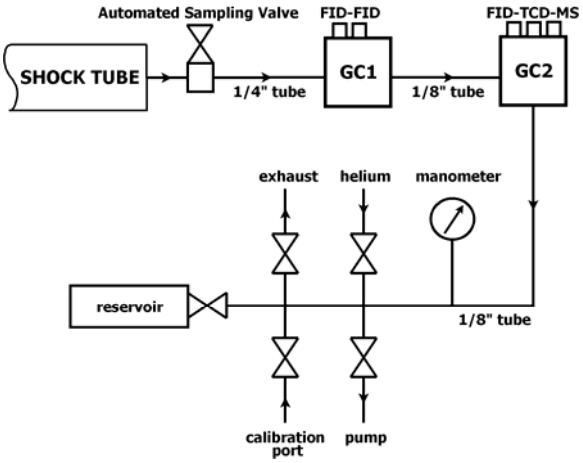


**Figure 16. Schematic of the online set-up.**

Particular attention was addressed to the choice of the optimal type of tubes used to build the entire sampling section. In order to avoid adsorption of species, first glass-lined tubes were considered. These tubes can be bent only at 800 °C. They are fragile and must be deactivated (if necessary). Thus they don't represent an easy solution to be implemented especially considering that in a complex sampling system the lines must usually be curvilinear. Excluding the glass-lined tubes if possible, other solutions include deactivated fused silica-lined tubing provided by Sigma-Aldrich. The internal wall of these tubes is covered by a thin layer of fused silica which is well known for its extremely low absorption characteristics and inertness to chemicals. Moreover

this kind of tube can be easily bent although, due to the specific manufacturing technique, only 1/16" and 1/8" OD tubes are commercially available. The size of these tubes would clearly constrain the gas flow downstream to the shock tube sampling valve (Figure 16) and would cause a withdrawal of too small of a gas sample for subsequent GC analyses, especially when low pressure experiments are conducted (low pressure in this case means 25 atm or less nominal pressure).

On the other hand, Restek provides treated stainless steel tubing specifically designated as inert with performances claimed to be as good as the ones from deactivated fused silica-lined tubing. Their 1/4" and 1/8" OD tubes are also electropolished for extreme inertness. In addition, Restek provides treated 1/16" tubes as well as tube connections and unions. The Restek solution was adopted to build the entire experimental sampling set-up.

The experimental procedure implemented for the collection and measurement of gas samples from the shock tube is relatively simple. After evacuation of the lines, the pump line is closed just before firing a shock. By controlling the exhaust line as well as the reservoir valve, it is possible to decrease/increase the pressure in the lines once the sample is collected from the tube (automatic valve opened for around 2 ms). In particular, it is important that the pressure does not reach very high values since the standard GC gas valves can only sustain pressures up to 300 psi, a relatively low value in relation to the shock tube experimental conditions. Once the pressure in the line is stabilized (usually in few seconds), gas injections into the two GCs are performed almost simultaneously. The lines are then flushed several times with helium to remove all the sample gas.

The separation of the gas sample is performed through a combination of columns/detectors specifically studied to identify and quantify all the components present even in the most complex mixtures. The first GC, utilized to measure heavy compounds, uses an FID coupled with a DB-17ms column while the second GC is used for measurement of light hydrocarbons (FID and HP-PLOT Q column) and inert species (TCD and HP-PLOT MoleSieve). The mass spectrometer present in the second GC can be connected for identification of unknown species if necessary. The GC calibration for the relatively light hydrocarbons can be performed using certified gas mixtures as well as in-house prepared calibration mixtures. Typical errors in the measurement of such species are around 5-10%. On the other hand, the calibration of large PAH compounds can not be performed in gas phase due to the difficulties associated with the preparation of appropriate gas phase calibration mixtures. The best solution to derive estimated calibration curves for heavy species is to use a combination of gas and liquid phase analyses as described next. In particular, the calibration curves can be deduced from the gas phase calibration curve for naphthalene based on the relative ratio between the corresponding liquid phase calibration curves. The gas phase calibration of naphthalene was obtained with accuracy using the experimental procedure described in the second part of the paper, related to the offline technique, while the liquid phase calibration curves can be obtained using certified solutions of PAHs in appropriate solvents (Sigma-Aldrich). The uncertainty in the calibration curves can be roughly estimated as proportional to the percentage difference between the molecular weights of the specific compound and the one of the reference species, naphthalene. Thus, the maximum uncertainty in the measurement of C12 hydrocarbons is estimated as 15-20%, of C14 compounds as 20-25%, and so on.

The online recovery technique has been tested on a relatively simple system, the decomposition of iodobenzene (phenyl iodide, $C_6H_5I$). The results, in terms of carbon recovery, were compared with similar experiments conducted using the traditional technique which

consisted of collecting the gas sample in electropolished stainless steel heated vessels for subsequent offline injection into the GC system (Figure 17). The experiments conducted with the traditional set-up show a substantial drop (down to 40%) in the carbon balance in correspondence with the formation of large PAH compounds which could not be measured. On the other hand, the results obtained with the online technique indicate an excellent performance of the new method, with an accuracy of ±10% in terms of carbon recovery.

The difference observed in Figure 17 between the results of the two techniques is mainly due to the ability to measure PAH compounds by the online technique. In fact, the species profiles for the light components are very similar in the two cases. A typical online gas chromatogram obtained with the FID detector coupled to the DB-17ms column is shown in Figure 18 where elution times for the major PAH groups (C12, C14, and so on) are indicated. Species profiles can be obtained for components with mole fractions down to sub-ppm levels, although products present in even smaller trace amounts can also be easily detected. Similar excellent recovery results were obtained for the pyrolytic and oxidative reactions of m-xylene[50] and n-propylbenzene[51].

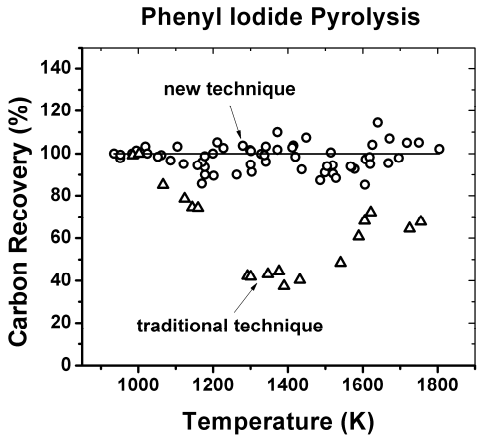


**Figure 17. Carbon recovery from phenyl iodide experiments; ○ online technique; Δ traditional technique. Adapted from Ref. 49.**

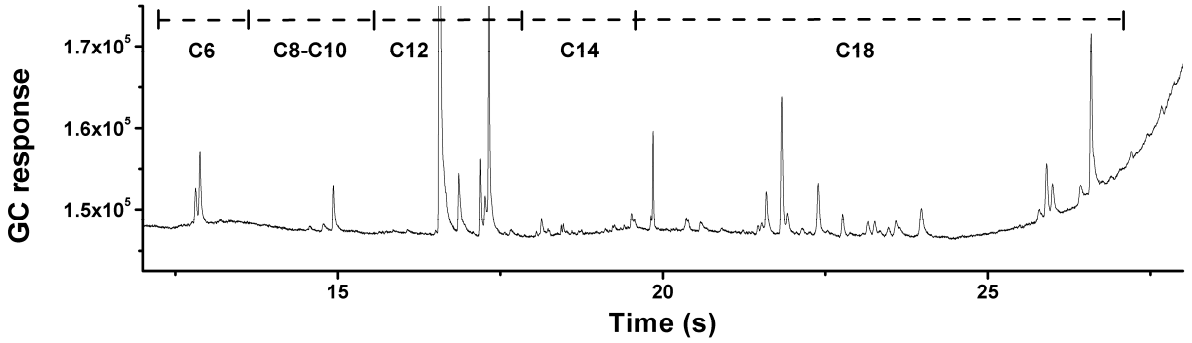


**Figure 18. Typical gas chromatogram (FID detector, DB-17ms column), online technique. Adapted from Ref. 49.**

The online technique described in detail in the previous paragraphs represents an excellent solution for identification and measurement of all components, including large PAH compounds, present in complex hydrocarbon gas mixtures. When possible from a logistical and experimental point of view, the implementation of this technique could lead to a substantial improvement in the experimental results extending the analytical capability to compounds which are usually barely detectable due to condensation and adsorption. However, in cases where soot is present in large amount in the sample, the direct transfer lines could become dirty (lose inertness) or get obstructed. This poses limitations in the possibility of using the online technique for some applications. A practical solution to the problem could be the use of particulate traps just at the entrance of the sampling system. New tests should be repeated to confirm that no losses of PAH compounds are present across the particulate trap, as well as to determine an optimal technique to recover all the heavy species contained on the particles surface.

## 2.3. Primary results

In order to fully analyze the reaction systems in consideration, several experimental sets were obtained by varying both the initial concentrations of the reactants and the nominal pressure. First the phenyl iodide decomposition has been investigated as a source of phenyl radicals for the subsequent experiments on the phenyl + acetylene reaction. Three experimental sets were conducted at a nominal pressure of 50 atm and initial phenyl iodide mole fraction of approximately 25, 50, and 100 ppm. One additional data set at 25 atm with approximately 50 ppm of reactant in the initial mixture was carried out to test possible pressure effects. The carbon balance for most of the experimental sets presents a maximum error of ~10% as shown in

Figure 19a which indicates efficient recovery of all the reaction products as well as reliability of the GC calibration curves. The only exception is constituted by the data set obtained using an initial phenyl iodide mole fraction of 100 ppm for which the carbon balance drops to 75% in the high temperature range. In this case the relatively large $C_6H_5I$ concentration leads to the formation of significant quantities of PAH intermediates. These intermediates could subsequently undergo processes such as aggregation or dimerization which lead to the formation of heavier PAHs and soot that can not be measured through gas phase GC technique.

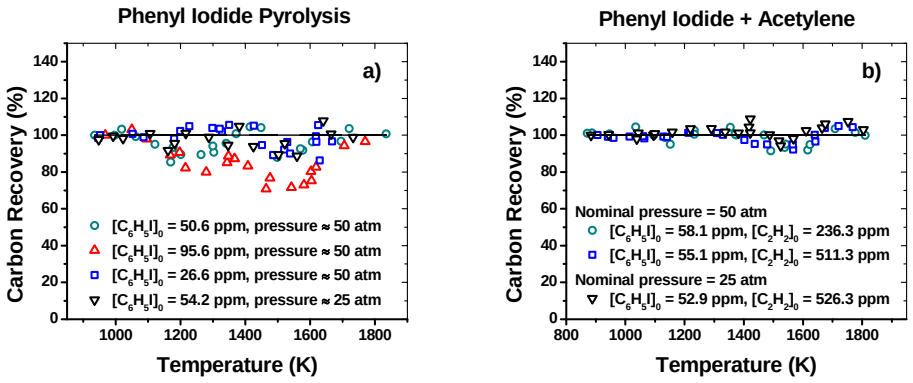


**Figure 19. Experimental carbon balance. a) Phenyl iodide decomposition; b) phenyl + acetylene reaction.**

Subsequent experimental work has been conducted in order to study the phenyl + acetylene reaction. In this case three experimental sets were obtained varying the initial acetylene mole fraction approximately from 250 ppm to 500 ppm with an initial phenyl iodide concentration of approximately 50 ppm. The carbon balance, as for the case of phenyl pyrolysis, indicates good recovery of the product species for all the data sets (Figure 19b).

A chemical kinetic model was developed to simulate the high-pressure experimental data on both the phenyl pyrolysis and the phenyl + acetylene reaction. Both the CHEMKIN 3.6.2[54] and the CHEMKIN 4.1.1[55] suite of programs were used to implement the model. For the modeling calculations, the exact reaction time, temperature and pressure were specified for each shock along with the initial mole fractions of the reactants. The simulations were performed assuming an adiabatic constant pressure process. As discussed in our previous publication addressing this issue[43], the adiabatic constant pressure process assumption leads to reasonable accuracy in predicting the stable species profiles.

The main reactions relevant to the formation and consumption of PAH compounds with associated reaction rate parameters are reported in Table 8. The thermochemical parameters for the species in the model were mainly taken from Burcat and Ruscic[56] and from chemical kinetic models available in literature[57,58]. The data not available in literature were estimated using the FITDAT data-fitting utility from the CHEMKIN 3.7.1 collection[59]. The enthalpies of the compounds, if not available on the NIST database, were calculated using the ring-conserved isodesmic reaction scheme[60]. The relative geometry optimizations and vibrational analyses were performed using the uB3LYP hybrid functional[61,62] with the Pople's valence triple-ζ basis set 6-311+G(d,p)[63]. For species containing iodine atoms, i.e. the iodobiphenyls, the DGDZVP basis set[64] was used. All of the calculations were carried out with the Gaussian 03 program package[65].

| Denomination | Reaction | A | n | Ea | Reference |
|---|---|---|---|---|---|
| | *Halogenated compounds* | | | | |
| R1 | $C_6H_5I \rightarrow C_6H_5+I$ | 1.374E+15 | 0.00 | 64406 | [67] |
| R2 | $C_6H_5+I \rightarrow C_6H_5I$ | 1.00E+13 | 0.00 | 0 | est., see text |
| R3 | $C_6H_5I \leftrightarrow o\text{-}C_6H_4+HI$ | 8.24E+13 | 0.00 | 64406 | see text |
| R4 | $C_6H_5I+H \leftrightarrow C_6H_5+HI$ | 8.73E+05 | 2.35 | -37.3 | [102][a] |
| R5 | $C_6H_5+HI \leftrightarrow C_6H_6+I$ | 3.00E+12 | 0.00 | 0 | est., see text |
| R6 | $C_6H_5I+C_6H_5 \leftrightarrow C_{12}H_{10}+I$ | 2.00E+12 | 0.00 | 11000 | [71] |
| R7 | $C_6H_5I+C_6H_5 \leftrightarrow o\text{-}C_{12}H_9I+H$ | 3.183E+11 | 0.00 | 4305 | see text |
| R8 | $C_6H_5I+C_6H_5 \leftrightarrow m\text{-}C_{12}H_9I+H$ | 3.183E+11 | 0.00 | 4305 | see text |
| R9 | $C_6H_5I+C_6H_5 \leftrightarrow p\text{-}C_{12}H_9I+H$ | 1.592E+11 | 0.00 | 4305 | see text |
| R10 | $o\text{-}C_{12}H_9+I \rightarrow o\text{-}C_{12}H_9I$ | 1.00E+13 | 0.00 | 0 | est. |
| R11 | $m\text{-}C_{12}H_9+I \rightarrow m\text{-}C_{12}H_9I$ | 1.00E+13 | 0.00 | 0 | est. |
| R12 | $p\text{-}C_{12}H_9+I \rightarrow p\text{-}C_{12}H_9I$ | 1.00E+13 | 0.00 | 0 | est. |
| R13 | $o\text{-}C_{12}H_9I \rightarrow o\text{-}C_{12}H_9+I$ | 1.374E+15 | 0.00 | 64406 | see text |
| R14 | $m\text{-}C_{12}H_9I \rightarrow m\text{-}C_{12}H_9+I$ | 1.374E+15 | 0.00 | 64406 | see text |
| R15 | $p\text{-}C_{12}H_9I \rightarrow p\text{-}C_{12}H_9+I$ | 1.374E+15 | 0.00 | 64406 | see text |
| R19 | $H+HI \leftrightarrow H_2+I$ | 3.98E+13 | 0.00 | 0 | [71] |
| | *Biphenyl and Benzene* | | | | |
| R20 | $C_6H_5+ C_6H_5 \leftrightarrow C_{12}H_{10}$ | 3.09E+12 | 0.036 | -1702 | [37] see text |
| R21 | $C_6H_5+ C_6H_5 \leftrightarrow o\text{-}C_6H_4+ C_6H_6$ | 8.52E-04 | 4.57 | -5735 | [37] see text |
| R22 | $C_6H_5+ C_6H_5 \leftrightarrow m\text{-}C_6H_4+ C_6H_6$ | 8.52E-04 | 4.57 | -5735 | [37] see text |
| R23 | $C_6H_5+ C_6H_5 \leftrightarrow p\text{-}C_6H_4+ C_6H_6$ | 4.26E-04 | 4.57 | -5735 | [37] see text |
| R24 | $o\text{-}C_6H_4 \leftrightarrow m\text{-}C_6H_4$ | 2.12E+14 | 0.00 | 73489.5 | [70] |

| | | | | | |
|---|---|---|---|---|---|
| R25 | m-$C_6H_4$ ↔ p-$C_6H_4$ | 2.83E+14 | 0.00 | 63045.7 | [70] |
| R26 | p-$C_6H_4$ ↔ z-$C_6H_4$ | 1.00E+13 | 0.00 | 17800 | see text |
| R27 | o-$C_6H_4$+$C_6H_5$ ↔ o-$C_{12}H_9$ | 1.00E+13 | 0.00 | 3720 | see text |
| R28 | m-$C_6H_4$+$C_6H_5$ → m-$C_{12}H_9$ | 1.00E+13 | 0.00 | 3720 | see text |
| R29 | p-$C_6H_4$+$C_6H_5$ → p-$C_{12}H_9$ | 1.00E+13 | 0.00 | 3720 | see text |
| R30 | m-$C_{12}H_9$ → m-$C_6H_4$+$C_6H_5$ | 2.223E+15 | 0.00 | 87232 | see text |
| R31 | p-$C_{12}H_9$ → p-$C_6H_4$+$C_6H_5$ | 2.223E+15 | 0.00 | 87232 | see text |
| R35 | o-$C_{12}H_9$+H ↔ $C_{12}H_{10}$ | 4.27E+13 | 0.338 | -158 | [37] |
| R36 | m-$C_{12}H_9$+H ↔ $C_{12}H_{10}$ | 1.25E+13 | 0.284 | -155 | [37] |
| R37 | p-$C_{12}H_9$+H ↔ $C_{12}H_{10}$ | 2.78E+13 | 0.185 | 15.3 | [37] |
| R38 | $C_6H_5$+ $C_6H_6$ ↔ $C_{12}H_{10}$+H | 9.55E+11 | 0.00 | 4305 | [74] |
| R44 | $C_6H_5$+H(+M) ↔ $C_6H_6$(+M) | 1.00E+14 | 0.00 | 0 | [73][b] |
| | *Terphenyls and Triphenylene* | | | | |
| R46 | $C_{12}H_{10}$+$C_6H_5$ ↔ o-TERPH+H | 6.367E+11 | 0.00 | 4305 | see text |
| R47 | $C_{12}H_{10}$+$C_6H_5$ ↔ m-TERPH+H | 6.367E+11 | 0.00 | 4305 | see text |
| R48 | $C_{12}H_{10}$+$C_6H_5$ ↔ p-TERPH+H | 3.183E+11 | 0.00 | 4305 | see text |
| R49 | o-$C_{12}H_9$+$C_6H_5$ → o-TERPH | 1.00E+13 | 0.00 | 0 | est. |
| R50 | m-$C_{12}H_9$+$C_6H_5$ → m-TERPH | 1.00E+13 | 0.00 | 0 | est. |
| R51 | p-$C_{12}H_9$+$C_6H_5$ → p-TERPH | 1.00E+13 | 0.00 | 0 | est. |
| R52 | o-TERPH → o-$C_{12}H_9$+$C_6H_5$ | 2.92E+15 | 0.00 | 109812 | see text |
| R53 | m-TERPH → m-$C_{12}H_9$+$C_6H_5$ | 2.92E+15 | 0.00 | 109812 | see text |
| R54 | p-TERPH → p-$C_{12}H_9$+$C_6H_5$ | 2.92E+15 | 0.00 | 109812 | see text |
| R55 | o-TERPH ↔ TRIPH+$H_2$ | 1.50E+15 | 0.00 | 84700 | see text |
| R56 | o-$C_{12}H_9$+o-$C_6H_4$ ↔ TRIPH+H | 1.00E+14 | 0.00 | 38000 | see text |
| R57 | $C_{12}H_8$+o-$C_6H_4$ ↔ TRIPH | 4.96E+09 | 0.827 | -1370 | see text |
| | *Biphenylene and Acenaphthylene* | | | | |
| R58 | o-$C_6H_4$+o-$C_6H_4$ ↔ $C_{12}H_8$ | 4.96E+09 | 0.827 | -1370 | [37] |
| R59 | o-$C_{12}H_9$ → BIPHENH | 5.00E+12 | 0.00 | 31056 | [79][c] |
| R60 | BIPHENH → o-$C_{12}H_9$ | 3.00E+13 | 0.00 | 19350 | [79] [c] |
| R61 | BIPHENH → $C_{12}H_8$+H | 5.00E+13 | 0.00 | 38223 | [79][c] |
| R62 | $C_{12}H_8$+H → BIPHENH | 4.00E+13 | 0.00 | 5972 | [79][c] |
| R63 | BIPHENH → BENZOH | 1.00E+13 | 0.00 | 31056 | [79][c] |
| R64 | BENZOH → BIPHENH | 1.00E+13 | 0.00 | 46345 | [79][c] |
| R65 | BENZOH → BENZO+H | 5.00E+13 | 0.00 | 41567 | [79][c] |
| R66 | BENZO+H → BENZOH | 1.00E+14 | 0.00 | 1911 | [79][c] |
| R67 | BENZOH → A2R5+H | 1.00E+13 | 0.00 | 44673 | [79][c] |
| R68 | $C_{12}H_{10}$ → $C_6H_5CHC_5H_4$ | 1.00E+14 | 0.00 | 109412 | [79][c] |
| R69 | $C_6H_5CHC_5H_4$ → $C_{12}H_{10}$ | 1.00E+13 | 0.00 | 76445 | [79][c] |
| R70 | $C_6H_5CHC_5H_4$ → BENZO+$H_2$ | 5.00E+13 | 0.00 | 56617 | [79][c] |
| R71 | $C_6H_5CHC_5H_4$ → A2R5+$H_2$ | 5.00E+13 | 0.00 | 60917 | [79][c] |
| R72 | $C_{12}H_8$ → $C_6H_4$oct | 6.152E+14 | 0.00 | 77387.6 | p.w. |
| R73 | $C_6H_4$oct → $C_{12}H_8$ | 7.482E+12 | 0.00 | 4059.6 | p.w. |
| R74 | $C_6H_4$oct → BENZOHyl | 1.205E+13 | 0.00 | 13712.9 | p.w. |
| R75 | BENZOHyl → $C_6H_4$oct | 5.321E+13 | 0.00 | 31139.8 | p.w. |
| R76 | BENZOHyl → BENZO | 1.941E+13 | 0.00 | 10615.0 | p.w. |
| R77 | BENZO → BENZOHyl | 4.188E+13 | 0.00 | 75265.9 | p.w. |
| R80 | BENZO → A2R5 | 4.699E+14 | 0.00 | 77831.2 | p.w. |
| R81 | $C_{10}H_7$-1+$C_2H_2$ ↔ A2R5+H | 1.87E+07 | 1.787 | 3262 | [**Error! Reference source not found.**] |
| | *Phenylacetylene* | | | | |
| R90 | $C_6H_5$+$C_2H_2$ ↔ $C_8H_6$+H | 1.00E+13 | 0.00 | 7648 | [**Error!** |

| | | | | | **Reference source not found.**] |
|---|---|---|---|---|---|
| R92 | $C_8H_6+H \leftrightarrow C_6H_4C_2H+H_2$ | 3.23E+07 | 2.095 | 15842 | [78] *1.5 |
| R95 | $o\text{-}C_6H_4+C_2H_2 \leftrightarrow C_8H_6$ | 2.00E+13 | 0.00 | 20000 | [99] |
| | *Diphenylethyne and Phenanthrene* | | | | |
| R96 | $C_8H_6+C_6H_5 \rightarrow DPE+H$ | 1.00E+13 | 0.00 | 7648 | see text |
| R97 | $DPE+H \rightarrow C_8H_6+C_6H_5$ | 4.00E+14 | 0.00 | 9691 | see text |
| R98 | $o\text{-}C_{12}H_9+C_2H_2 \leftrightarrow PHEN+H$ | 1.87E+07 | 1.787 | 3262 | [58] |
| R99 | $C_8H_6+C_6H_5 \leftrightarrow PHEN+H$ | 9.55E+11 | 0.00 | 4305 | [58] |
| R110 | $C_{12}H_{10}+C_2H_2 \rightarrow PHENH$ | 16.92 | 2.60 | 42193 | [105] |
| R111 | $PHENH \rightarrow PHEN+H_2$ | 4.73E+09 | 0.797 | 17176 | [105] |
| | *Naphthalene* | | | | |
| R146 | $o\text{-}C_6H_4+C_6H_6 \rightarrow BICYCLO$ | 1.1618E+04 | 2.526 | 5915.9 | [91] see text |
| R147 | $BICYCLO \rightarrow o\text{-}C_6H_4+C_6H_6$ | 4.910E+16 | 0.00 | 66811 | [91] see text |
| R148 | $BICYCLO \leftrightarrow C_{10}H_8+C_2H_2$ | 7.458E+14 | 0.0956 | 54780.1 | [91] |
| R149 | $C_6H_4C_2H+C_2H_2 \leftrightarrow C_{12}H_7\text{-}1$ | 1.87E+07 | 1.787 | 3262 | est.[d] |
| R151 | $C_{12}H_7\text{-}1+H(+M) \leftrightarrow C_{12}H_8(+M)$ | 1.00E+14 | 0.00 | 0 | est.[b] |
| | *Phenyl Decomposition* | | | | |
| R157 | $C_6H_5(+AR) \leftrightarrow o\text{-}C_6H_4+H(+AR)$ | 4.30E+12 | 0.62 | 77300 | [99][b] |
| R159 | $o\text{-}C_6H_4 \leftrightarrow C_4H_2+C_2H_2$ | 1.20E+18 | -0.34 | 87776 | [99] |
| R162 | $C_6H_2+H \leftrightarrow C_6H_3$ | 1.10E+30 | -4.92 | 10800 | [101] |
| R164 | $C_4H_2+ C_2H \leftrightarrow C_6H_2+H$ | 3.00E+13 | 0.00 | 0 | [99] |
| R167 | $z\text{-}C_6H_4+H \leftrightarrow C_6H_3+H_2$ | 1.33E+06 | 2.53 | 9240 | [57] |
| R191 | $C_2H+H_2 \leftrightarrow C_2H_2+H$ | 4.90E+05 | 2.50 | 560 | [57] |
| R193 | $C_2H+C_2H_2 \leftrightarrow C_4H_2+H$ | 9.60E+13 | 0.00 | 0 | [101] |

**Table 8. Chemical kinetic model, relevant reactions and associated reaction rate parameters. [a] modified within the uncertainty provided in ref. [102]; [b] reaction with fall-off parameters; [c] Ea from [79], A value estimated; [d] high-pressure limit for $C_{10}H_7+C_2H_2$ [19].**


naphthalene ($C_{10}H_8$)

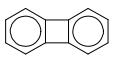
biphenylene ($C_{12}H_8$)


acenaphthylene (A2R5)

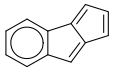
cyclopenta[a]indene (BENZO)

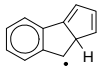
monohydrocyclo-penta[a]indene (BENZOH)

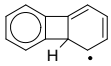
hydrobiphenylene radical (BIPHENH)

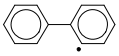
o-biphenyl radical ($o\text{-}C_{12}H_9$)

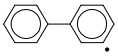
m-biphenyl radical ($m\text{-}C_{12}H_9$)

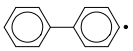
p-biphenyl radical ($p\text{-}C_{12}H_9$)

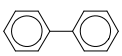
biphenyl ($C_{12}H_{10}$)

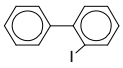
o-iodobiphenyl ($o\text{-}C_{12}H_9I$)

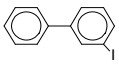
m-iodobiphenyl ($m\text{-}C_{12}H_9I$)

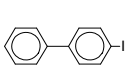
p-iodobiphenyl ($p\text{-}C_{12}H_9I$)

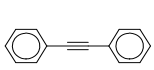
diphenylethyne (DPE)

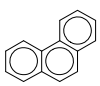
phenanthrene (PHEN)

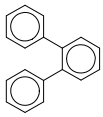
o-terphenyl (o-TERPH)

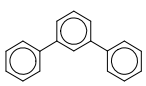
m-terphenyl (m-TERPH)

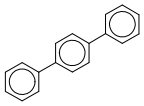
p-terphenyl (p-TERPH)


triphenylene

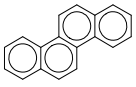
chrysene

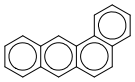
benzo[a]anthracene

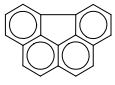
benzo[g,h,i]fluoran-

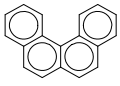
benzo[c]phenan-

| | | | |
|---|---|---|---|
| (TRIPH) | | thene | threne |

**Figure 20. Molecular structures of the major polycyclic aromatic hydrocarbons discussed in the text.**

In the following paragraphs the relevant results from the experimental work and from the modeling simulations will be discussed for both the phenyl pyrolysis and the phenyl + acetylene reaction. In order to facilitate the discussion, the molecular structures of the major polycyclic aromatic hydrocarbon products analyzed in this work are reported in Figure 20. Before proceeding with the discussion it is worth mentioning the fact that the model was optimized mainly based on the experimental sets having accurate carbon recovery (initial concentration of phenyl iodide around 50 ppm or lower). All the experimental results are reported in the supplemental material including for each experiment the actual conditions (pressure, temperature, and reaction time) as well as the mole fractions of the major products.

### 2.3.1. Phenyl Pyrolysis

A typical chromatogram obtained from the pyrolysis of phenyl iodide at a nominal pressure of 50 atm and initial mole fraction of 50.6 ppm is reported in Figure 21. The chromatogram clearly shows the complexity of the reaction system in consideration. Although only the major products are annotated, several additional peaks were detected. Such peaks correspond to compounds produced in trace amounts during the reaction, including among the others indene, di-iodobenzenes, fluorene, 1-iodonaphthalene, anthracene, phenanthrene, iodobiphenyls, 2-phenylindene, 1-phenylnaphthalene, 2-phenylnaphthalene, pyrene, and other unidentified C18 species. Although the formation of such compounds suggests the presence of several minor mechanistic pathways, from a practical point of view only the major products and the associated reactions were considered for the development of the chemical kinetic model. The main results are reported below.

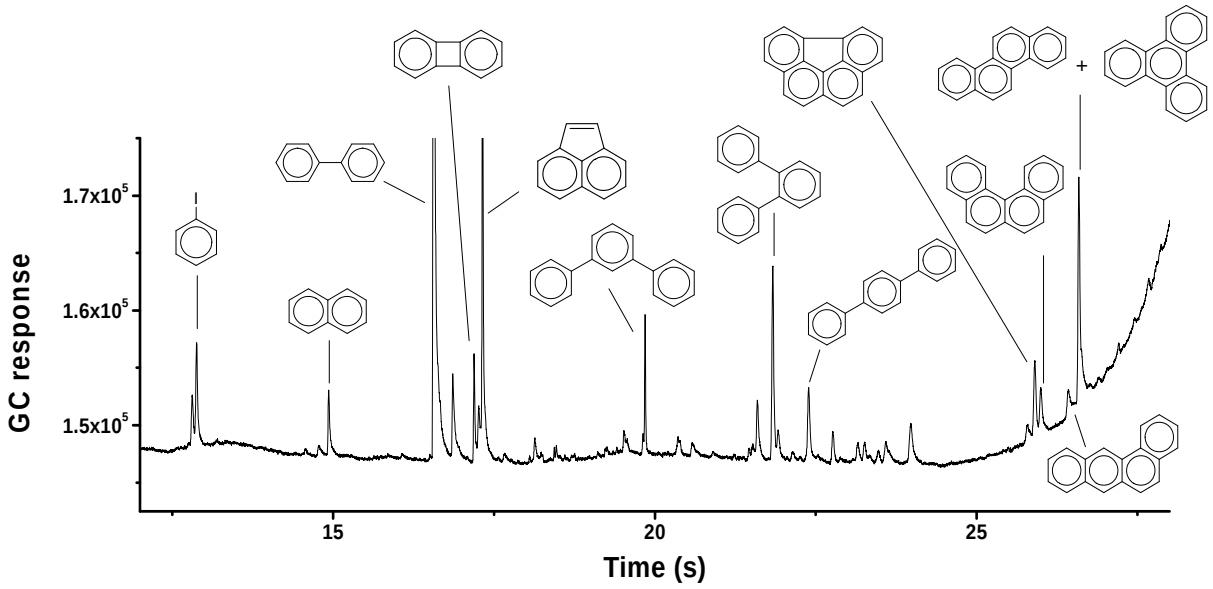

**Figure 21. Typical chromatographic signal for phenyl radical pyrolysis. FID detector, DB-17ms column.**

### *2.3.1.1. Phenyl Iodide Decomposition*

A comprehensive analysis of the C-I fission in phenyl iodide decomposition has been performed by Tranter et al.[37] in their recent investigation of the self-reaction between phenyl radicals. The authors compared the experimental data present in literature[66–69] with their experimental results as well as the reaction rate constants obtained with a Gorin model RRKM calculation. It is not the purpose of the present work to repeat a detailed analysis of the thermal decomposition of phenyl iodide. Thus, only a brief discussion of the main results obtained using the HPST is presented below.

The normalized profiles for the decomposition of phenyl iodide are reported in Figure 22a. The experiments do not indicate any significant dependence on the initial mole fraction of the reactant or on the reaction pressure. At the conditions of the present study the experimental decay of phenyl iodide is not only due to the C-I bond fission leading to the formation of phenyl radicals and iodine atoms, but it is also influenced by the secondary reactions of the phenyl iodide with different product species including phenyl radicals and hydrogen atoms when present in the system. Moreover the recombination reaction between phenyl radicals and iodine atoms to form $C_6H_5I$ will play a relevant role lowering the apparent decomposition rate. Thus the high-pressure conditions implemented in the present investigation do not allow the determination of the absolute rate constant for the phenyl iodide decomposition, although an apparent overall reaction rate constant can be derived from the Arrhenius plot presented in Figure 22b. The Arrhenius expression of the apparent reaction rate constant is $k \cong 3.24 \cdot 10^{10} \exp(-21797/T)$ ($s^{-1}$).

The high-pressure limit reaction rate constant for the C-I fission derived by Kumaran et al.[67] based on their low-pressure experiments best fits our experimental data although the phenyl iodide concentrations are slightly overpredicted by the model when the reverse reaction rate constant is calculated using the equilibrium constant. Better agreement between experiments and simulations was obtained assuming a temperature independent reaction rate constant $k_2$ for the recombination between phenyl radicals and iodine atoms (Table 8). In addition, as suggested by Tranter et al.[37], the branching ratio between the two main unimolecular decomposition channels forming respectively $C_6H_5$ + I and o-$C_6H_4$ + HI was assumed to be approximately 6%. The rate parameters for the two unimolecular decomposition reactions are reported in Table 8 (R1, R2, and R3). Figure 23 shows the excellent agreement between the phenyl iodide experimental profiles and the modeling results for the experiments conducted at nominal pressures of 25 and 50 atm and initial phenyl iodide mole fractions of around 25 and 50 ppm. Similar agreement was obtained for the data set at 50 atm and higher initial phenyl iodide mole fraction (95.6 ppm).

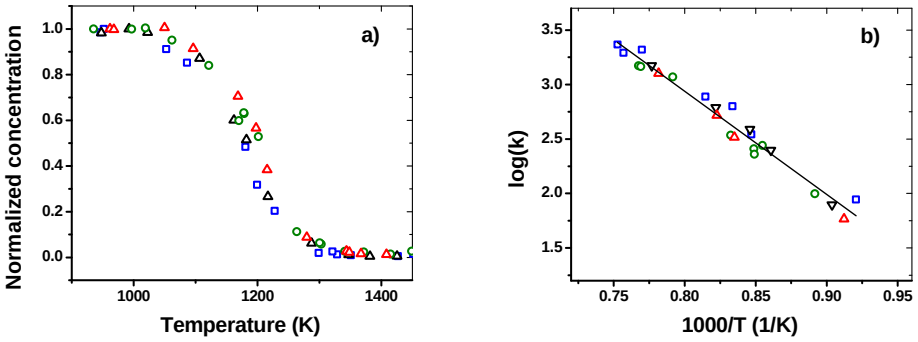


**Figure 22. a) Normalized phenyl iodide decomposition; b) Arrhenius plot of the measured apparent reaction rate constant for phenyl iodide decomposition between 1086 and 1328 K, k in $s^{-1}$. ○ $[C_6H_5I]_0$ = 50.6 ppm, p ~ 50 atm; Δ $[C_6H_5I]_0$ = 95.6 ppm, p ~ 50 atm; □ $[C_6H_5I]_0$ = 26.6 ppm, p ~ 50 atm; ∇ $[C_6H_5I]_0$ = 54.2 ppm, p ~ 25 atm; —— linear interpolation.**

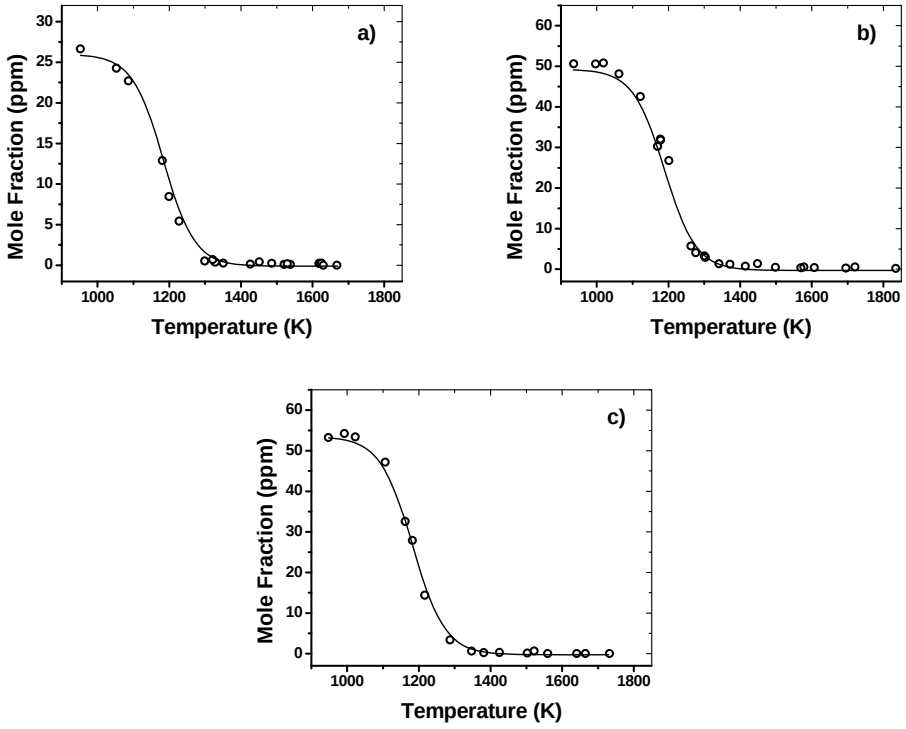


**Figure 23. Phenyl iodide decomposition. ○ experiments; —— simulations. a) $[C_6H_5I]_0$ = 26.6 ppm, p ~ 50 atm; b) $[C_6H_5I]_0$ = 50.6 ppm, p ~ 50 atm; c) $[C_6H_5I]_0$ = 54.2 ppm, p ~ 25 atm.**

### *2.3.1.2. Formation of Benzene, Biphenyl, and Substituted Biphenyls*

As already mentioned in the introduction, biphenyl is one of the most important building blocks for the formation of large PAH compounds and it constitutes the primary product of the radical-radical recombination between phenyl radicals[18,36]. If the only reaction channel available

for the self-reaction between phenyl radicals was the radical-radical recombination, biphenyl would be the major product of the phenyl iodide decomposition. Only small amounts of other stable compounds would be measured, including for example benzene from the recombination of the phenyl radicals with hydrogen atoms. Surprisingly the experiments indicated that a large amount of benzene is produced even at low temperatures where the hydrogen atoms are present in the system only in small concentrations. As shown in Figure 24a at temperatures between 1250 K and 1400 K around 25% of the phenyl radicals produced from the phenyl iodide decomposition is converted into benzene. The results presented in Figure 24a also indicate that the chemical mechanisms which lead to the formation/consumption of benzene are not dependent on either the initial phenyl iodide mole fraction or reaction pressure. Moreover the peculiar shape of the profiles, characterized by a rapid increase up to 1250 K in correspondence with the end of the phenyl iodide decay followed by a slight decrease up to 1450 K and a more rapid decrease at higher temperatures, suggests that at least two reaction mechanisms are responsible for the formation of benzene. The main mechanism was proposed and studied in detail by Tranter et al.[37] who highlighted for the first time the complexity of the self-reaction between phenyl radicals. The authors examined the different reaction channels by high-level computational methods and concluded that the reaction between phenyl radicals does not proceed only through recombination to form biphenyl, but also through hydrogen abstraction to form benzene and ortho-, meta-, and para-benzynes. The key role of the benzynes, in particular of o-benzyne, will be discussed later in the text in relation to the formation of terphenyls, biphenylene, acenaphthylene, naphthalene, and the four-ring compounds.

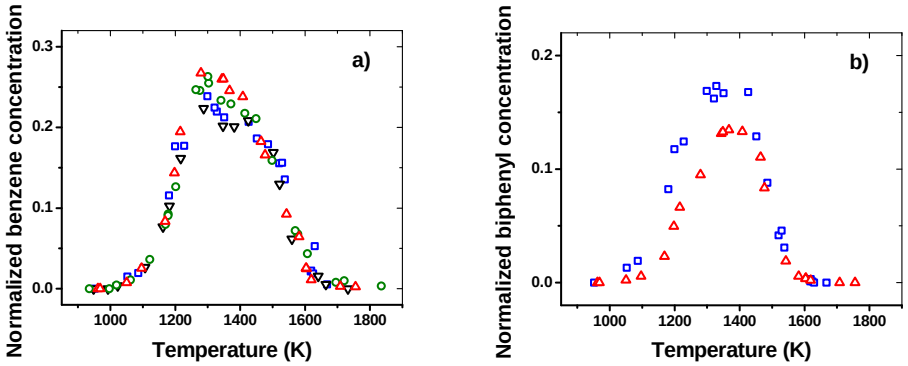


**Figure 24. a) Normalized benzene decomposition; b) normalized biphenyl decomposition. ○ $[C_6H_5I]_0$ = 50.6 ppm, p ~ 50 atm; Δ $[C_6H_5I]_0$ = 95.6 ppm, p ~ 50 atm; □ $[C_6H_5I]_0$ = 26.6 ppm, p ~ 50 atm; ∇ $[C_6H_5I]_0$ = 54.2 ppm, p ~ 25 atm.**

The reaction rate constants associated with the two competing channels for the self-reaction between phenyl radicals, i.e. the recombination channel and the hydrogen-abstraction channel, were calculated by Tranter et al.[37] using high-level theoretical calculations and transition state theory. As suggested by the authors, the branching ratio for the three hydrogen abstraction channels leading to o-benzyne + benzene, m-benzyne + benzene, and p-benzyne + benzene was estimated as 0.40-0.40-0.20 and the corresponding reaction rate constants taken as the high-pressure limit expressions calculated in [37] reduced, within the stated error limits, by a factor of two (reactions R21–R23, Table 8). A similar reduction, within the error limits, in the corresponding low-pressure expressions was applied by Tranter et al. in order to improve the

agreement between the simulations and the low-pressure experiments suggesting that the rate constant may be off by a factor of two across the entire pressure range. The isomerization between the three benzyne isomers has been studied theoretically by Moskaleva et al.[70] who derived reaction rate constant expressions utilized in the present work (R24 and R25). The p-benzyne can also easily undergo a Bergman decyclization to form 1,5-hexadiyn-3-ene. The corresponding reaction rate constant was estimated based on a reaction barrier of 17.8 kcal/mol as calculated in Ref. [70] (R26). Finally the reaction rate constant for the recombination reaction was reduced by a factor of two compared to the expression derived by Tranter et al.[37] for a pressure of 100 atm (R20). This modification, within the estimated uncertainty provided by the authors, lead to the improvement of the modeling results not only for biphenyl but also for other intermediates such as the terphenyls.

We mentioned earlier the fact that the benzene profiles in Figure 24a suggest the relevance of a second reaction mechanism which lead to the formation of benzene. Such a mechanism involves the reaction between phenyl radical and hydrogen iodide to form benzene and iodine atoms. Hydrogen iodide derives mainly from the direct decomposition of $C_6H_5I$ into o-$C_6H_4$ + HI as described in section 2.3.1.1 and at later times in the reaction by the abstraction reaction between phenyl iodide and hydrogen atoms (R4 in Table 8). Thus although the phenyl iodide is usually considered as a clean source of phenyl radicals its chemical properties lead to the formation of halogenated species, in this case HI, which can subsequently influence the formation of the intermediates of interest, in this case benzene, derived from the reaction of the phenyl radicals.

An estimated temperature-independent rate constant for the reaction between $C_6H_4$ and HI has been used in the present model (reaction R5, Table 8). In view of the decreased reactivity of the phenyl radical compared to the hydrogen atom, $k_5$ is an order of magnitude lower than the reaction rate constant for reaction R19, H + HI → $H_2$ + I (Ref. [71]), although nearly twice the value extrapolated from the expression derived by Rodgers et al.[72] who experimentally investigated the title reaction at relatively low temperatures (648–773 K).

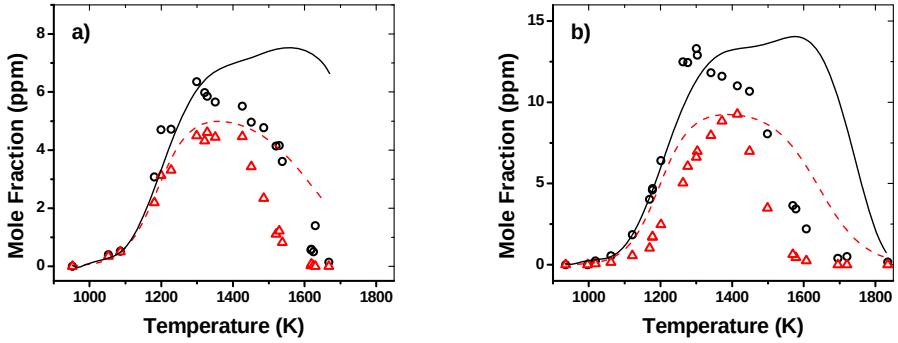

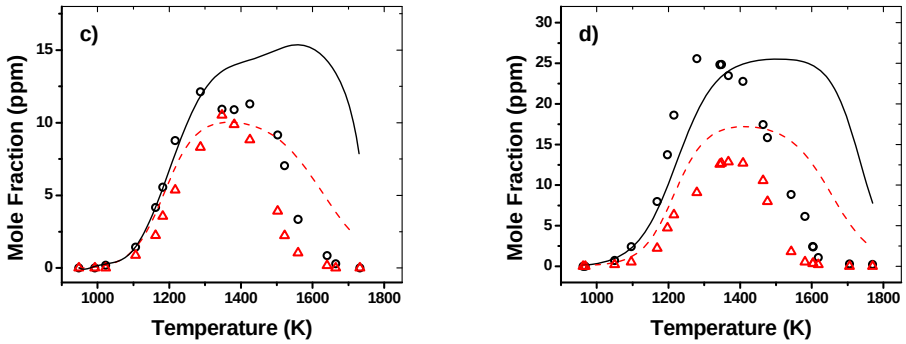


**Figure 25. ○ Benzene experiments; —— benzene simulations; Δ biphenyl experiments, – – biphenyl simulations; a) $[C_6H_5I]_0$ = 26.6 ppm, p ~ 50 atm; b) $[C_6H_5I]_0$ = 50.6 ppm, p ~ 50 atm; c) $[C_6H_5I]_0$ = 54.2 ppm, p ~ 25 atm; d) $[C_6H_5I]_0$ = 95.6 ppm, p ~ 50 atm.**

The model simulates with good accuracy the profiles of biphenyl for the experiments conducted at 50 atm with initial $C_6H_5I$ mole fraction of 26.6 ppm and at 25 atm with 54.2 ppm of reactant (Figure 25a and c). Above 1450 K the biphenyl concentrations are overpredicted by the model, but as discussed later in the text this discrepancy is mainly due to the fact that the model is not able to correctly predict the chemistry relevant to high-temperature conditions. The remaining $C_{12}H_{10}$ profiles (Figure 25b and d) are overestimated by the model even at low temperatures, in particular in the case presented in Figure 25d (initial mole fraction of 95.6 ppm). The drop in the relative carbon balance described above in relation to Figure19a suggests the presence of pathways for the formation of larger compounds which are not measured in the present study. Such pathways could be responsible for the consumption of biphenyl at relatively high phenyl radical concentrations. Such hypothesis is supported by the comparison between the normalized experimental profiles for biphenyl in the case of initial phenyl iodide mole fraction of 26.6 and 95.6 ppm at a nominal pressure of 50 atm (Figure 24b). In contrast with the case of benzene where no dependence on the pressure and the initial $C_6H_5I$ mole fraction was observed (Figure 24a), the normalized profiles show a significant drop in the biphenyl concentrations at higher phenyl iodide mole fractions.

Different considerations apply for the simulation of the benzene profiles. As shown in Figure 25 the initial slope of formation is well reproduced by the model for most of the experimental sets with the exception of the set conducted with initial phenyl iodide mole fraction of 95.6 ppm for which the initial slope is underpredicted. The rate of production analysis performed at 1217 K and 29.1 atm with initial mole fraction of 54.2 ppm shows that at the beginning the formation of benzene is mainly influenced by the abstraction channel between phenyl radicals with smaller contributions from the reaction between phenyl and hydrogen iodide and from the recombination between phenyl and hydrogen[73] (Figure 26a). In Figure 26a the lines for the ortho- and meta-benzyne channels are superimposed. As the reaction progresses, the reaction $C_6H_5$ + HI becomes the predominant pathway for the formation of benzene. Its contribution is essential for the accurate description of the benzene profiles in the low-temperature range of the present study as shown in Figure 27 where the modeling results from the complete model are compared to the results obtained when the reaction $C_6H_5$ + HI ↔ $C_6H_6$ + I is removed (experimental set with initial concentration of 54.2 ppm and nominal pressure of 25 atm). Similar reactions between $C_6H_5$ and HX could also be relevant when a generic $C_6H_5X$ precursor is utilized, i.e. $C_6H_5Cl$ or

$C_6H_5Br$. In these cases the reaction rate constants are expected to be lower than $k_5$ since in general the H-X bond would be stronger than the H-I bond.

While the benzene profiles are well reproduced for temperatures below 1350 K, at higher temperatures the model fails to simulate accurately the decay observed in the experimental data. In particular, above 1450 K where the experimental concentrations drop rapidly the model predicts an increase in the benzene mole fraction up to around 1600 K. As indicated in Figure 26b which shows the rate of production analysis performed at 1502 K the formation of benzene is still mainly due to the hydrogen-abstraction channel. In comparison to the low temperature case, the contributions provided by the reaction R5 and R44 are only minor. In order to understand if other reaction rate parameters could be responsible for the overestimation observed at high temperatures, the sensitivity analysis was also performed at the same conditions which confirmed the importance of the above mentioned reactions (Figure 28). The sensitivity analysis also indicates a strong dependence on the rate parameters of reaction R20, the recombination between phenyl radicals to form biphenyl. The modification of the related reaction rate parameters within the corresponding uncertainties does not lead to a substantial improvement of the benzene profile at high temperatures without affecting the accuracy of the predictions for other compounds, i.e. biphenyl and benzene at low temperatures. This is clearly an indication that the model is not complete and requires the addition of reaction pathways which reduce the predicted formation of benzene at high temperatures. We will analyze this issue in more detail later in the manuscript in correspondence with the discussion about the formation of the light hydrocarbons (section 2.3.1.7).

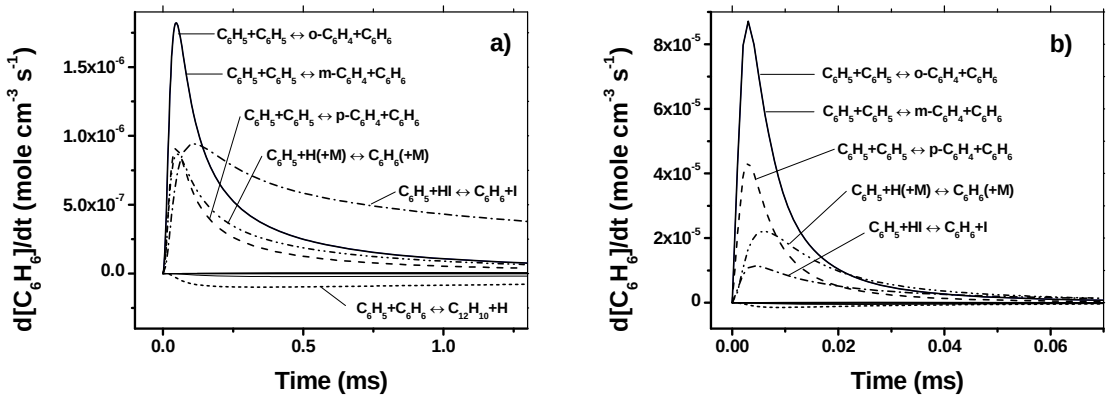


**Figure 26. Benzene, rate of production analysis, $[C_6H_5I]_0$ = 54.2 ppm. a) T = 1217 K, p = 29.1 atm; b) T = 1502 K, p = 25.3 atm.**

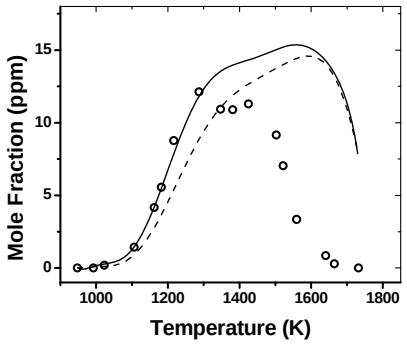


**Figure 27. Benzene, $[C_6H_5I]_0$ = 54.2 ppm, p ~ 25 atm. ○ experiments; —– model in Table 8; – – model in Table 8 omitting $C_6H_5 + HI \leftrightarrow C_6H_6 + I$.**

In addition to benzene and biphenyl, iodobiphenyls have been measured in the low temperature range of our experiments. Once again the measurement of halogenated species indicates that the phenyl iodide is not an ideal source of phenyl radicals. Although the study of the iodobiphenyls chemistry is not the focus of the present work, it is essential to include the corresponding reactions in the chemical kinetic model in order to obtain a better agreement between simulations and experimental results for the low temperature profiles of several species, including benzene, biphenyl, and the terphenyls. The experimental measurement of the three iodobiphenyl isomers is also important to define the primary products of the addition between the phenyl radical produced by decomposition of the phenyl iodide precursor and the precursor itself. Such addition process becomes relevant at the high pressures implemented in the present study or at low pressures when large concentrations of the precursor are utilized. A brief analysis of the main experimental and modeling results regarding the iodobiphenyls is provided below which can serve as reference for future investigations on the decomposition of phenyl radical precursors and the related chemistry.

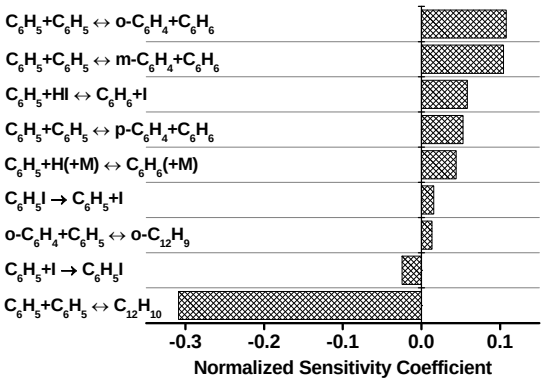


**Figure 28. Sensitivity analysis for benzene. $[C_6H_5I]_0$ = 54.2 ppm, T = 1502 K, p = 25.3 atm, t = 1.68 ms.**

As soon as the phenyl iodide starts decomposing, iodobiphenyls are produced indicating a strong correlation between the two processes. In fact the three isomeric forms are mainly

generated from the reaction between $C_6H_5I$ and $C_6H_5$ in a similar fashion as the reaction between phenyl radical and benzene leads to the formation of biphenyl and hydrogen[74]. The pre-exponential factors of the corresponding reaction rate constants have been adjusted based on the multiplicity of the specific reaction pathway (R7–R9, Table 8). Once produced, the iodobiphenyls can dissociate to form biphenyl radicals and iodine atoms (R10–R15). The dissociation and recombination reaction rate constants have been assumed similar to the ones relative to the phenyl iodide decomposition, i.e. R1 and R2.

The experimental profiles are well reproduced by the model as shown in Figure 29. In particular, for the sets in Figure 29a and Figure 29c both the shapes of the profiles and the maximum mole fractions are accurately predicted. The m-iodobiphenyl is the isomer present in larger amounts in these experiments, while the p-iodobiphenyl shows the lowest concentrations. It is important to notice how the model correctly replicates such hierarchy. When we analyze the experimental results obtained with higher concentrations of phenyl iodide (Figure 29b and d), we notice that the o-iodobiphenyl is the most abundant among the three isomers. This indicates the presence of alternative pathways for the formation or consumption of the iodobiphenyls compared to the cases shown in Figure 29a and b. Although the shapes of the profiles are well reproduced by the model, the calculated mole fractions are overestimated compared to the experiments, especially when 95.6 ppm of phenyl iodide are pyrolyzed (Figure 29d), thus we can hypothesize that additional consumption reactions should be added to the model. Such reactions include for example the reactions between the iodobiphenyls and $C_6H_5$ or H.

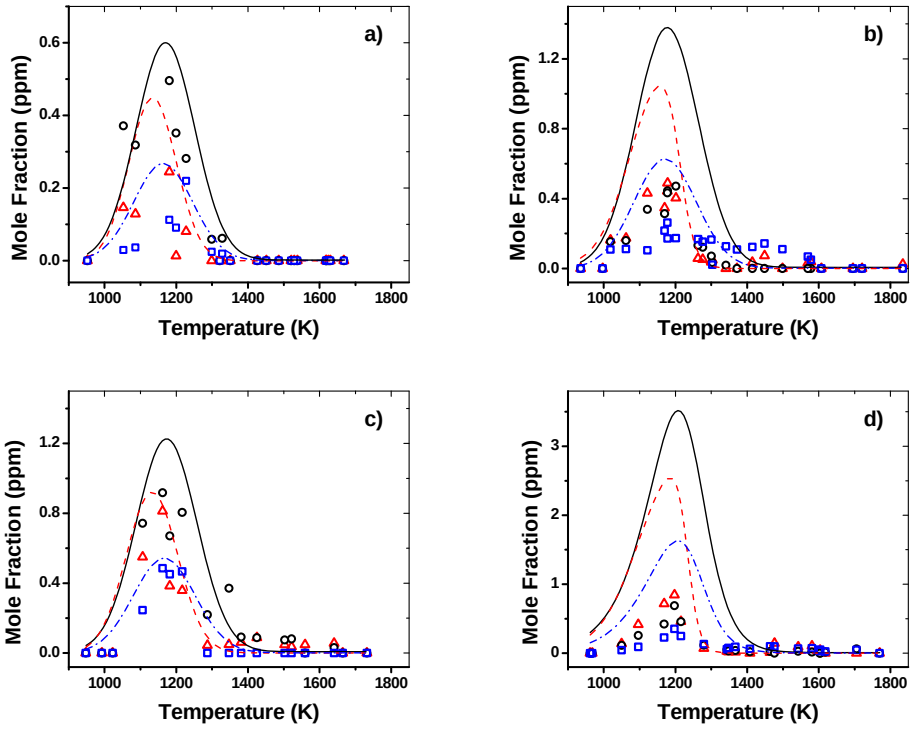


**Figure 29. Δ o-Iodobiphenyl exp., – – o-iodobiphenyl sim.; ○ m-iodobiphenyl exp., —– m-iodobiphenyl sim.; □ p-iodobiphenyl exp., – · – p-iodobiphenyl sim. a) $[C_6H_5I]_0$ = 26.6 ppm, p ~ 50 atm; b) $[C_6H_5I]_0$ = 50.6 ppm, p ~ 50 atm; c) $[C_6H_5I]_0$ = 54.2 ppm, p ~ 25 atm; d) $[C_6H_5I]_0$ = 95.6 ppm, p ~ 50 atm.**

### *2.3.1.3. Terphenyls*

The obvious step in the growth towards larger PAH compounds which follows the formation of biphenyl is the subsequent addition of a phenyl radical to form the terphenyls. The mechanism of phenylation of biphenyl to form o-, m-, and p-terphenyls was proposed by Brooks et al.[75] who measured trace amounts of these polyphenyls in their study on benzene pyrolysis at relatively low temperatures (873–1036 K). The o-, m-, and p-terphenyls are well separated by the GC method implemented in the present study as shown in Figure 21 and mole fraction profiles could be obtained for all three isomers (Figure 30). The experimental profiles reach a maximum around 1275–1300 K with the m-terphenyl being the most abundant among the isomers. The mole fraction of o-terphenyl is lower not only compared to the mole fraction of m-terphenyl but also compared to the mole fraction of p-terphenyl. This experimental finding is surprising since from a simple analysis of the multiplicity of the specific reaction pathways for the addition between biphenyl and phenyl we would expect similar yields of the o- and m-terphenyls, in proportion twice the yield of p-terphenyl. The experimental results clearly suggest that o-terphenyl is consumed by reactions which does not involve the other isomers or that additional reaction pathways are involved in the formation of the three terphenyls. Both hypotheses are in principle correct, although only one has a substantial impact in the modeling results as discussed below.

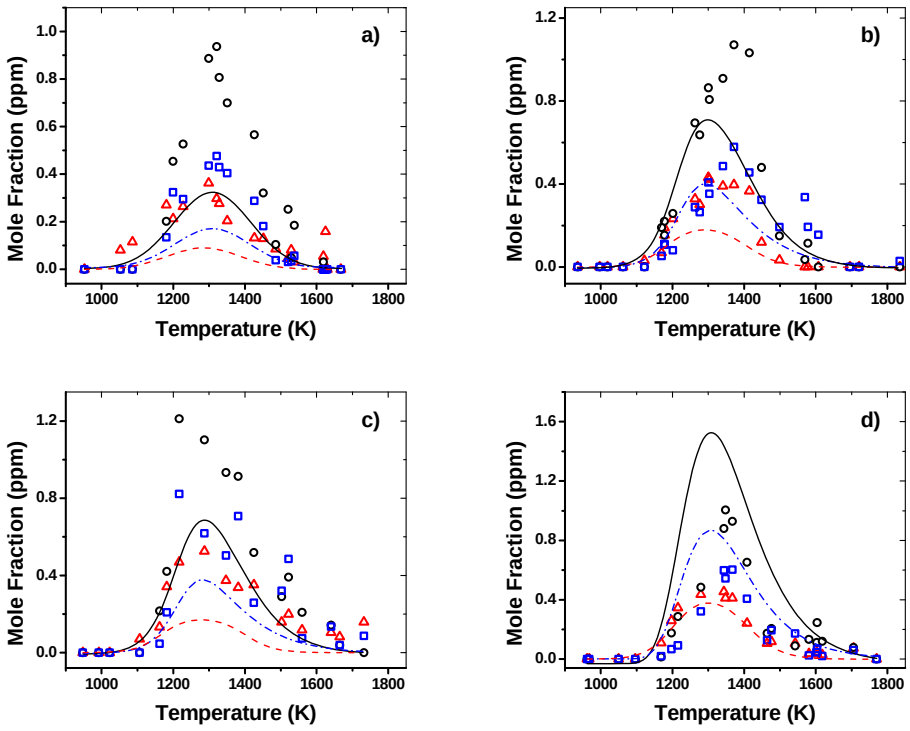


**Figure 30. Δ o-Terphenyl exp., – – o-terphenyl sim.; ○ m-terphenyl exp., —— m-terphenyl sim.; □ p-terphenyl exp., – · – p-terphenyl sim. a) $[C_6H_5I]_0$ = 26.6 ppm, p ~ 50 atm; b) $[C_6H_5I]_0$ = 50.6 ppm, p ~ 50 atm; c) $[C_6H_5I]_0$ = 54.2 ppm, p ~ 25 atm; d) $[C_6H_5I]_0$ = 95.6 ppm, p ~ 50 atm.**

o-Terphenyl can undergo a cyclodehydrogenization process to form triphenylene (R55 in Table 8). The corresponding reaction rate constant has been estimated based on the rate constant

proposed by Zhang et al.[76] for the cyclodehydrogenization of cis-1,2-diphenylethene to form phenanthrene. Due to the high activation energy involved in the process (84.7 kcal/mol) its contribution is not sufficient to justify the significant difference between the experimental o- and m-terphenyls mole fractions especially in consideration of the temperature range of the present study.

Let's now consider alternative pathways for the formation of the terphenyls which could explain the discrepancy between the expected concentrations and the experimentally observed ones. As discussed in the previous section, the decomposition of the iodobiphenyls leads to the formation of biphenyl radicals and iodine atoms. Even more significant for the formation of the o- and m-biphenyl radicals are the reactions of phenyl radical with o-benzyne and m-benzyne, respectively (R27 and R28). The corresponding reaction for the formation of the p-$C_{12}H_9$ radical (R29) does not play an important role in the modeling results since the p-benzyne radical quickly isomerizes to form 1,5-hexadiyn-3-ene (R26) and is not available for reaction with phenyl. Once produced the three biphenyl radicals can recombine with an additional phenyl radical to form directly the terphenyls (R49–R51).

We discussed in generic terms about additional pathways to the terphenyls, but we did not explain how these pathways could address our initial question about the unexpected relatively low o-terphenyl concentrations. The explanation is found in the fact that the pathway for the formation of o-terphenyl from o-$C_{12}H_9$ (Figure 20) + $C_6H_5$ is not as effective as the corresponding ones for m- and p-terphenyls even though o-$C_6H_4$ is the most abundant among the benzyne isomers which implies an relatively high concentration of o-biphenyl radicals compared to the m- and p- ones. In fact the o-biphenyl radical can isomerize and form the hydrobiphenylene radical (R59, see Figure 20 for chemical structure) reducing the concentration of o-$C_{12}H_9$ available for recombination with phenyl. We will discuss this reaction in the section relative to acenaphthylene formation (section 2.3.1.4). On the other hand, the m-$C_{12}H_9$ and the p-$C_{12}H_9$ are mainly consumed by reaction with $C_6H_5$ to form m- and p-terphenyls. In addition we need to consider that o-benzyne not only reacts with phenyl to form the o-biphneyl radical but is also consumed by other reactions involved in the formation of different PAH compounds, i.e. biphenylene, naphthalene, and the four-ring species. Such reactions will be discussed later in the manuscript in the corresponding sections.

To the best of our knowledge, no previous investigation has studied or proposed reaction rate constants for the steps involved in the formation of the terphenyls. Consequently, the corresponding parameters have been estimated as reported in Table 8. In particular, the activation energy for the recombination reactions between the benzynes and the phenyl radical (R27–R29) has been estimated as similar to the barrier calculated by Tokmakov and Lin[20] for the reaction between phenyl radical and acetylene forming the 2-phenylvinyl radical. The approximated reaction rate parameters for the dissociation reactions R30 and R31 respectively for m-$C_{12}H_9$ and p-$C_{12}H_9$ are analogous to the parameters for the reverse of reaction R27 for which the thermochemical parameters are well established. Likewise the reactions for the decomposition of the terphenyls into biphenyl radicals + phenyl radicals (R52–R54) are analogous to the reverse of $C_6H_5 + C_6H_5 \leftrightarrow C_{12}H_{10}$. Finally the reaction rate constants for $C_6H_5$ + $C_{12}H_{10}$ forming terphenyls and H atoms (R46–R48) have been estimated based on the reaction rate constant for $C_6H_5 + C_6H_6$ forming biphenyl + H[74]. The corresponding pre-exponential factors were adjusted based on the multiplicity of the specific pathway.

As shown in Figure 30 the simulation results reproduce the shape of the terphenyl profiles with very good accuracy in particular in relation to the estimated temperature range where the

profiles reach the maximum value. It is also noticeable how the relative concentrations between the three isomers are in good agreement with the experiments, with m-terphenyl produced in larger amounts compared to p-terphenyl and o-terphenyl.

The results presented in the current section indicate that in order to have an accurate representation of the phenyl radical chemistry it is necessary to consider the detailed pathways involved in the formation of the terphenyls. A particularly important role is played by the presence of the o- and m-benzynes as primary reactants involved in the formation of the biphenyl radicals which serve as building blocks for the terphenyls. We will discuss in the next sections how the benzyne chemistry influences the formation of other PAH compounds relevant for the formation of soot.

#### *2.3.1.4. Biphenylene and Acenaphthylene*

In view of the formation of substantial amounts of o-benzyne radicals by the decomposition of the phenyl iodide (R3), by the H-abstraction between phenyl radicals (R21), and by the isomerization of m-benzyne (R24), we would expect biphenylene to be among the major stable products of the decomposition of phenyl iodide. Once again the experimental results do not reflect the expectations. As shown in Figure 31 less than 1 ppm of biphenylene is produced even with initial phenyl iodide mole fraction equal to 95.6 ppm. The production of small amounts of biphenylene is a confirmation of the fact that o-benzynes are consumed by other reactions, i.e. the reaction with phenyl radical to form o-$C_{12}H_9$ described in the previous section. Figure 31 also indicates that the production of biphenylene is proportional to the initial concentration of the fuel, in agreement with the fact that biphenylene derives from the recombination between o-benzyne radicals whose formation is directly linked to the fuel or its primary products as described above. The high-pressure limit reaction rate constant for the recombination between the benzyne radicals has been recently calculated by Tranter et al.[37] and utilized in the present model without any adjustment (R58).

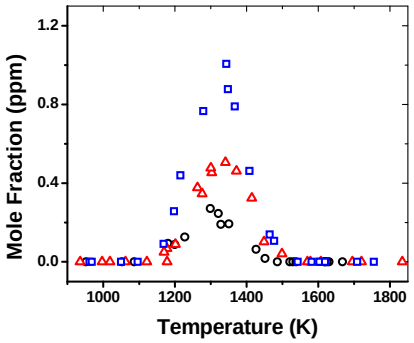


**Figure 31. Biphenylene experimental concentrations at p ~ 50 atm. ○ $[C_6H_5I]_0$ = 26.6 ppm; Δ $[C_6H_5I]_0$ = 50.6 ppm; □ $[C_6H_5I]_0$ = 95.6 ppm.**

While the formation of biphenylene is at least from a descriptive point of view simple, the mechanisms involved in the formation of acenaphthylene are more complex and still not well clarified. Our discussion starts with the simple experimental observation of the fact that acenaphthylene is produced in considerable amounts during the pyrolysis of the phenyl radical. The experimental profiles are reported in Figure 32 and indicate as expected that acenaphthylene

is not a primary product of the recombination between phenyl radicals. In fact its formation does not occur in the low temperature range of our experiments. As shown in Figure 32 acenaphthylene profiles are characterized by a rapid increase starting at around 1250 K which is typical of an isomerization process with relatively high pre-exponential and activation energy or of a process involving secondary products. The profiles reach the maximum at around 1500 K before dropping rapidly at higher temperatures.

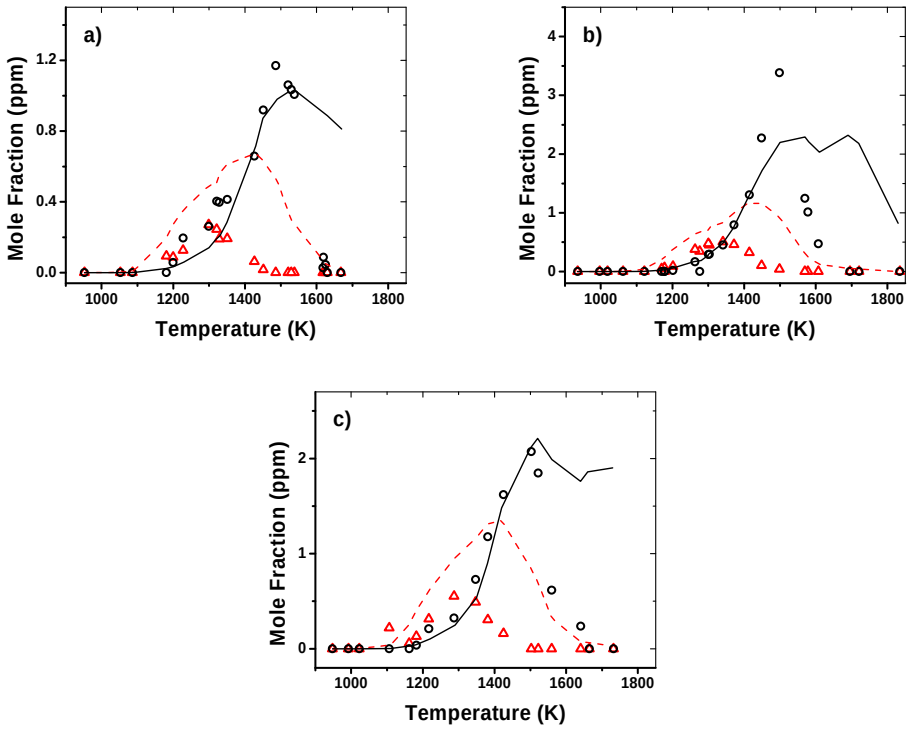


**Figure 32. Δ Biphenylene exp., – – biphenylene sim.; ○ acenaphthylene exp., —— acenaphthylene sim. a) $[C_6H_5I]_0$ = 26.6 ppm, p ~ 50 atm; b) $[C_6H_5I]_0$ = 50.6 ppm, p ~ 50 atm; c) $[C_6H_5I]_0$ = 54.2 ppm, p ~ 25 atm.**

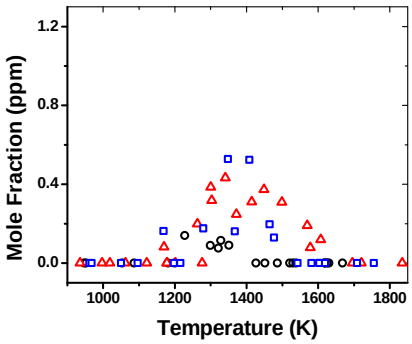


**Figure 33. Phenylacetylene experimental concentrations at p ~ 50 atm. ○ $[C_6H_5I]_0$ = 26.6 ppm; Δ $[C_6H_5I]_0$ = 50.6 ppm; □ $[C_6H_5I]_0$ = 95.6 ppm.**

The conventional formation pathway for acenaphthylene involves the well studied reaction between naphthyl radical and acetylene[19,77]. Naphthyl radicals are generally formed through the HACA mechanism[33,13] starting from phenyl and acetylene through the phenylacetylene intermediate. Thus the whole process requires the addition of three acetylene molecules to a phenyl radical with an intermediate H-abstraction from the phenylacetylene. The present experiments are performed without acetylene in the initial mixture, and although acetylene is produced at high temperatures we can exclude the naphthyl + acetylene reaction as relevant to the formation of acenaphthylene. A good proof for this hypothesis is provided by the measurement of the intermediate phenylacetylene. As shown in Figure 33 phenylacetylene is produced in trace amounts even when large concentrations of phenyl iodide are pyrolyzed. In addition as discussed in the second part of the paper the presence of much larger concentrations of acetylene would not be sufficient to justify the high mole fractions of acenaphthylene reported in Figure 32.

Richter et al.[78] reported the presence of large amounts of acenaphthylene in their benzene flame experiments. The authors hypothesized that acenaphthylene is produced through the formation of the hydrobiphenylene radical (Figure 20 for chemical structure) from the addition between biphenylene and hydrogen, followed by isomerization to acenaphthylene. The proposed pathway is part of a more complex potential energy surface which has been recently studied in details by Shukla et al.[79] using ab-initio calculations. The authors explored the possible pathways involved in the isomerization of biphenyl and o-biphenyl radical in relation to the formation of several stable compounds including among the others acenaphthylene.

The theoretical results presented in Ref. [79] have been included in the model (R59–R71). Due to the complexity of the problem in consideration few assumptions were made. First of all only the more stable compounds were considered as possible final products of the isomerization processes. These compounds include biphenylene, acenaphthylene, and cyclopenta[a]indene (benzopentalene, BENZO in Figure 20 and Table 8). The activation energies of the elementary reactions are assumed as equal to the relative theoretical barriers. The corresponding pre-exponential factors are estimated based on the values for similar reactions. When a global step is considered, a similar approach was used considering the barrier between the reactants and the maximum energy of the specific path as the activation energy. The pre-exponential was estimated based on the reaction constituting the limiting step in the global process.

The reaction pathway which involves the isomerization of biphenyl (R68–R71) does not play a significant role at the temperature conditions implemented in the present study although biphenyl is formed in large amounts. In fact the entrance barrier of almost 110 kcal/mol is too high to allow a significant flux to enter the potential energy surface. Even a ten-fold increase in the estimated pre-exponential factor does not lead to a significant change in the modeling results. On the other hand, the energy required for the isomerization of the o-biphenyl radical is much lower as the corresponding barrier is equal to around 31 kcal/mol (R59). Considering the fact that o-biphenyl radicals are formed in considerable amounts by the recombination between phenyl and o-benzyne radicals (R27) as discussed in the previous section, we expect the corresponding isomerization (R59) to occur even in the temperature range of our experiments. Thus we have to discuss in more details the reaction scheme utilized in the present model which is based on the potential energy surface investigated by Shukla et al.[79]

The entrance reaction step involves the isomerization of o-biphenyl radical into hydrobiphenylene radical (R59 and R60). Hydrobiphenylene radical can isomerize to form monohydrocyclopenta[a]indene (BENZOH in Figure 20 and in Table 8) or undergo a hydrogen-

loss process to biphenylene + H. Although the latter pathway (R61 and R62) is favorable from an entropic point of view, the corresponding barrier is around 7 kcal/mol higher than the barrier for the isomerization to monohydrocyclopenta[a]indene (R63 and R64). As also suggested by Shukla et al.[79] the isomerization pathway is favorable at relatively low temperatures as also confirmed by the low concentrations of biphenylene observed in the experiments (Figure 31). Once formed, the monohydrocyclopenta[a]indene intermediate can undergo a hydrogen-loss process to form cyclopenta[a]indene + H (R65 and R66) or proceed through a series of isomerization reactions followed by a hydrogen-loss to form acenaphthylene + H (R67). Clearly the former pathway is favorable due to the entropy contribution and due to the fact that it is constituted by a single elementary step.

Figure 34a shows the modeling results for acenaphthylene and cyclopenta[a]indene from the scheme described in the previous paragraph. The pathway leading to cyclopenta[a]indene is clearly predominant and the experimental profile for acenaphthylene is substantially underestimated. At this point it is important to underline the fact that although cyclopenta[a]indene was not measured in the experiments we cannot exclude its formation just on the basis of the experimental observations as cyclopenta[a]indene dimerizes quickly even at room temperature. Previous studies indicate that in order to obtain n.m.r. spectra for this species the analyses had to be run at -70 ºC[80,81]. Thus we have to base our considerations about cyclopenta[a]indene formation exclusively on the theoretical study by Shukla et al.[79]

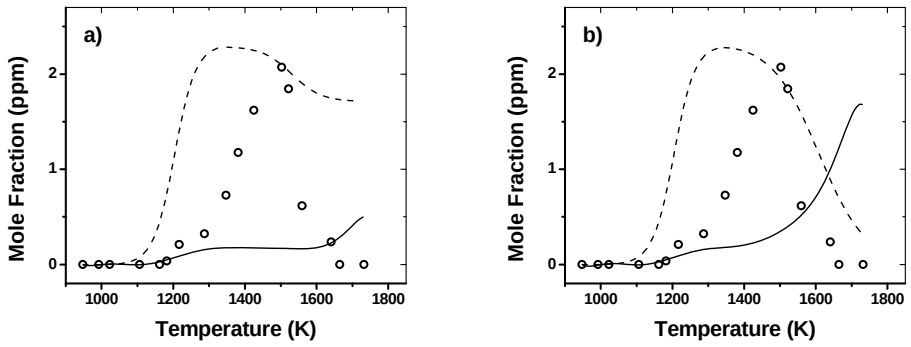


**Figure 34. ○ Acenaphthylene exp.; ── acenaphthylene sim.; – – cyclopenta[a]indene sim. a) model in Table 8 omitting reaction R80; b) model in Table 8 with $k_{80}$ calculated from [83]. $[C_6H_5I]_0$ = 54.2 ppm, p ~ 25 atm.**

The results presented in Figure 34a suggest the possibility of an isomerization pathway between cyclopenta[a]indene and the more stable acenaphthylene. Such pathway has experimental evidence in the work performed by Brown et al.[80,81] and by Wiersum and Jenneskens[82] on the formation of ring-contracted aromatic hydrocarbons, including acenaphthylene, starting from diradical compounds. Blake et al.[83] used ab-initio calculations to investigate the potential energy surface for the isomerization of the biphenyl diradical into acenaphthylene through the formation of the stable cyclopenta[a]indene.

The results in Ref. [83] were used to calculate the reaction rate constants for relevant isomerization reactions. Conventional transition state theory (TST)[84–86] with rigid rotor harmonic oscillator assumptions and estimated tunneling effects[87] was used to evaluate the high-pressure limit reaction rate constants from the quantum chemical calculations. Only the contributions from the low frequency torsional modes, if any, were calculated using free rotor approximation.

In particular, the isomerization between cyclopenta[a]indene and acenaphthylene was treated as a single step reaction (R80) with rate constant equal to the one for the limiting step in the global process which in reality is composed by several isomerization steps. The Arrhenius expression of the reaction rate constant calculated based on the molecular properties from [83] is $k_{80} \cong 2.704 \cdot 10^{14} \exp(-43866.5/T)$ ($s^{-1}$). The modeling results obtained using such expression are reported in Figure 34b. The acenaphthylene profile is still underestimated by the model. Clearly the activation energy is too high to allow the isomerization process to occur in the temperatures range where the experimental acenaphthylene concentration starts increasing (1300–1500 K).

In order to improve the agreement between experimental and modeling profiles for acenaphthylene we derived an expression for the isomerization between cyclopenta[a]indene and acenaphthylene based on the experimental profiles for acenaphthylene. Such estimate is based on the assumption that acenaphthylene is mainly produced through the above mentioned isomerization process. This assumption should be sufficiently accurate since the conventional formation pathway for acenaphthylene can not play a significant role as discussed earlier in the text. The expression used to evaluate the reaction rate constant is the following:

$$k = \frac{-\ln\left(\frac{[BENZO]_0 - \Delta[BENZO]}{[BENZO]_0}\right)}{t}$$

where $[BENZO]_0$ is the initial concentration of cyclopenta[a]indene as estimated by the model ignoring reaction R80, $\Delta[BENZO] = [BENZO]_0 - [BENZO]_t \cong [A2R5]_t$, and $t$ is the reaction time. $[A2R5]_t$ is the experimental concentration of acenaphthylene at the reaction time $t$.

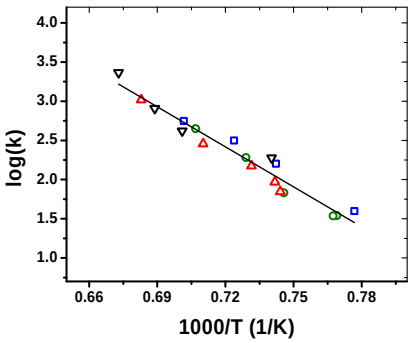


**Figure 35. Arrhenius plot of the measured reaction rate constant for isomerization of cyclopenta[a]indene into acenaphthylene between 1287 and 1486 K, $k$ in $s^{-1}$. ○ $[C_6H_5I]_0$ = 50.6 ppm, p ~ 50 atm; Δ $[C_6H_5I]_0$ = 95.6 ppm, p ~ 50 atm; □ $[C_6H_5I]_0$ = 26.6 ppm, p ~ 50 atm; ∇ $[C_6H_5I]_0$ = 54.2 ppm, p ~ 25 atm; —— linear interpolation.**

The Arrhenius plot of the reaction rate constant for R80 is reported in Figure 35. The linear interpolation of the experimental results provides the expression for the reaction rate constant for the isomerization of cyclopenta[a]indene into acenaphthylene, which is equal to

$k_{80} \cong 4.699 \cdot 10^{14} \exp(-39192.3/T)$. The pre-exponential factor is slightly higher than the one obtained above from the calculations based on the results from Ref [83] but within a two-fold factor. On the other hand, the activation energy is around 9 kcal/mol lower than the theoretical one. Further theoretical calculations performed with multireference methods will clarify if the discrepancy between the theoretical and the experimental activation energies is due to inaccuracy in the theoretical methods implemented in [83] or to the presence of additional lower energy isomerization pathways. It is important to mention that the experimentally derived rate expression is function of the parameters of a complex model which includes among the others the estimated reaction rate parameters for the formation of cyclopenta[a]indene (R59–R67) as well as the reaction rate parameters for the formation of o-biphenyl radical, R27. Thus its accuracy depends also on the accuracy of such relevant parameters in the model.

The results obtained including the experimental $k_{80}$ expression into the model are shown in Figure 32. The formation of acenaphthylene is well reproduced by the model in terms of shape of the curve as well as mole fraction levels. In the high temperature range of our study, above 1500 K where the experimental profiles drop, the concentrations are overestimated by the model. We can attribute this discrepancy to the absence of reaction pathways forming lighter compounds as we will discuss later in the appropriate section. Similar results were obtained for the experimental set conducted at nominal pressure equal to 50 atm with 95.6 ppm initial $C_6H_5I$ mole fraction.

In Figure 32 the profiles of biphenylene are also reported. The simulations predict the experimental profiles accurately in the low temperature range up to 1300 K where the formation of biphenylene is mainly driven by the recombination reaction between o-benzyne radicals (R58). At higher temperatures where the experimental profiles decay the modeling results do not follow the experimental trends so accurately. Above 1300 K the contribution from the isomerization reaction from hydrobiphenylene radical to biphenylene + H (R61 and R62) becomes relevant and causes the mentioned discrepancy. Thus the experimental profiles indicate that such reaction pathway could be even less relevant than estimated. On the other hand, additional channels which consume biphenylene could be important especially in the high temperature range of our study.

In order to test this hypothesis, a series of theoretical calculations were initiated. The model includes the results of such theoretical study performed to analyze possible biphenylene isomerization pathways (R72–R77). In particular, the study was inspired by the experimental investigations by Wiersum and Jenneskens[82] and by Brown et al.[80,81] as well as by the study by Scott[88] which indicate that biphenylene is a precursor of cyclopenta[a]indene and consequently of acenaphthylene. This possibility was investigated. The geometry optimizations and vibrational analyses were performed using the uB3LYP hybrid functional[61,62] with the Pople's valence triple-ζ basis set 6-311+G(d,p)[63]. The energetics of the optimized structures were refined by single point energy calculations performed with coupled-cluster method using both single and double substitutions and including triple excitations (CCSD(T))[89] with Dunning's correlation consistent polarized double-ζ basis set (cc-pVDZ)[90]. Frozen-core (FC) assumption was also used. All of the calculations were carried out with the Gaussian 03 program package[65].

The results of the theoretical investigation are shown in Figure 36. The pathway identified in the present study involves the formation of a benzocyclooctatetraene-like structure ($C_6H_4$oct) (see Figure 36 for chemical structure) and subsequent reorganization to form a cyclopenta[a]indene-like radical (BENZOHyl) (Figure 36). Since the calculations were performed on spin-singlet structures, hydrogen-transfer processes are favorable compared to

hydrogen-loss processes. As expected the BENZOHyl radical isomerizes to form cyclopenta[a]indene. Among the species in Figure 36 the only one which showed diradical character is BENZOHyl. The relative energy was estimated as

$$E = E(CCSD(T)) + E(uB3LYP) - E(rB3LYP)$$

where *E(uB3LYP)* and *E(rB3LYP)* are the energies of the diradical and closed-shell compounds estimated respectively by uB3LYP/6-311+G(d,p) and rB3LYP/6-311+G(d,p) methods.

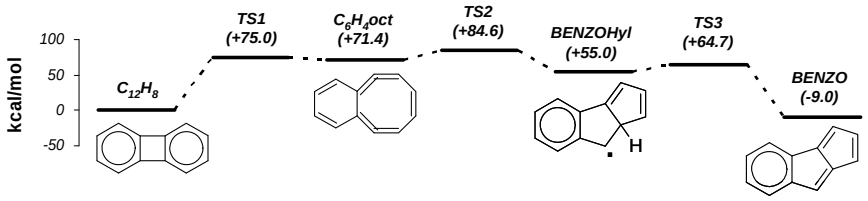


**Figure 36. Potential energy surface for the isomerization of biphenylene into cyclopenta[a]indene. uB3LYP/6-311+G(d,p) optimized structures. CCSD(T)/cc-pVDZ energies in kcal/mol, including ZPVE.**

Reaction rate constants for the elementary steps involved in the isomerization process were calculated using conventional TST and rigid rotor harmonic oscillator assumptions. The rate parameters are reported in Table 8 (R72–R77). No adjustments to the reaction rate constants were made. Clearly biphenylene is a very stable compound and its dearomatization can occur only at relatively high temperatures. Only above 1500 K the contribution of the proposed pathway becomes relevant for both the consumption of biphenylene and the formation of acenaphthylene through the cyclopenta[a]indene intermediate. Further considerations on the necessity of further studies on the biphenylene isomerization are dependent on the accuracy of the rate parameters of the reactions involved in the formation of biphenylene as well as on the understanding of the mechanisms which leads to the formation of the light hydrocarbons discussed later in the manuscript.

#### *2.3.1.5. Naphthalene*

The presence of fused-ring structures formed during the pyrolysis of the phenyl radical is definitely the most surprising and challenging experimental finding in the present investigation. We already discussed about the formation of acenaphthylene and its modeling. Naphthalene, the simplest among the condensed compounds, was also measured although in lower concentrations compared to acenaphthylene. The experimental profiles are shown in Figure 37. In particular, it is interesting to notice how naphthalene is produced as soon as the phenyl iodide starts decaying suggesting a link between the formation of the second-ring species and the primary products of the phenyl iodide decomposition.

Clearly the HACA mechanism[33,13] can not be responsible for the experimental formation of naphthalene since acetylene is not present in the reactant mixture or produced in large amounts at low temperatures. Comandini and Brezinsky[91] studied the radical/π-bond addition between single-ring aromatics and concluded that the reaction between o-benzyne and benzene leads mainly to the formation of naphthalene and acetylene through a two-step process involving the 1,4-cycloaddition between o-benzyne and benzene and the subsequent fragmentation of the

intermediate. Similar results were reported by Shukla et al.[79] Both benzene and o-benzyne are formed as primary products of the decomposition of the phenyl iodide and reaction between phenyl radicals, thus the proposed pathway was included in the model (R146–R148). The reaction rate constant $k_{147}$ was calculated based on the structures and energetics provided in Ref. [91] using conventional TST. In addition the reaction rate constant for the entrance reaction, the 1,4-cycloaddition, was multiplied by a factor of two within the uncertainty provided by the authors. For consistency $k_{147}$ was also multiplied by a two-fold factor.

The results of the simulations are reported in Figure 37 and show an excellent agreement with the experiments not only in terms of profile shape but also in terms of concentrations. The experimental results confirm the relevance of the radical/π-bond addition between o-benzyne and benzene as source of the second-ring species in this kind of pyrolytic systems.

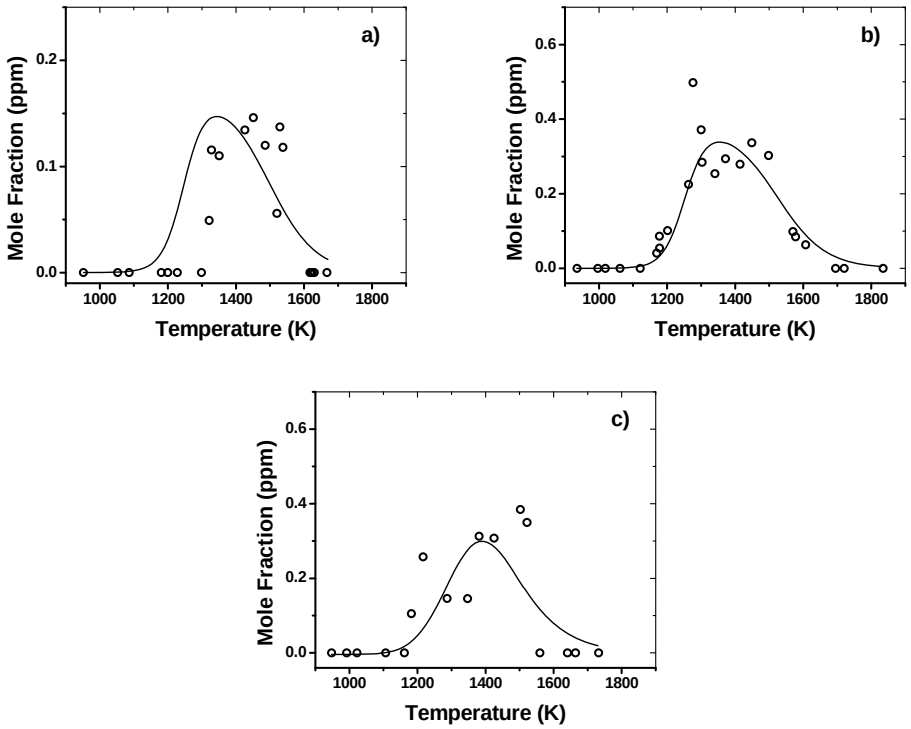


**Figure 37. ○ Naphthalene exp., —– naphthalene sim. a) $[C_6H_5I]_0$ = 26.6 ppm, p ~ 50 atm; b) $[C_6H_5I]_0$ = 50.6 ppm, p ~ 50 atm; c) $[C_6H_5I]_0$ = 54.2 ppm, p ~ 25 atm.**

### *2.3.1.6. Four-Ring Compounds*

Even more surprising than the formation of acenaphthylene and naphthalene was the identification and measurement of a variety of four-ring fused compounds including chrysene, triphenylene, benzo[a]anthracene, benzo[g,h,i]fluoranthene, and benzo[c]phenanthrene. An example of the profiles for these species is shown in Figure 38 for the experimental set conducted at a nominal pressure of 50 atm with an initial phenyl iodide mole fraction equal to 95.6 ppm for which the mole fractions of the four-ring compounds are maximum. The

experimental profiles provide critical information on how these large compounds could be formed.

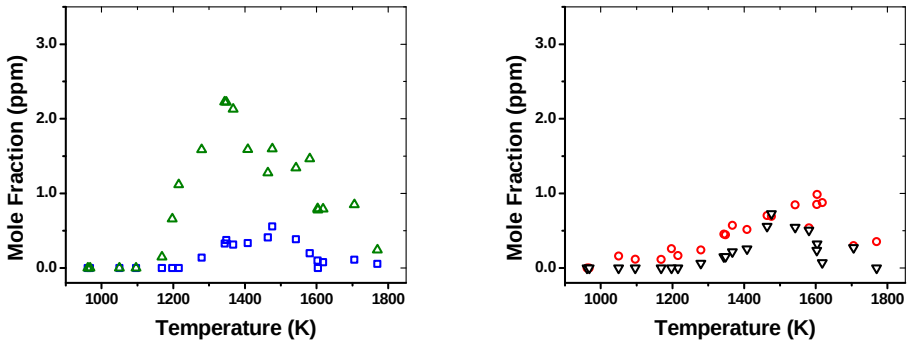


**Figure 38. Experimental mole fraction, $[C_6H_5I]_0$ = 95.6 ppm, p ~ 50 atm. Δ chrysene (~90%) + triphenylene (~10%); □ benzo[a]anthracene; ○ benzo[g,h,i]fluoranthene; ∇ benzo[c]phenanthrene.**

First of all it is important to notice that chrysene and triphenylene coelute in the present analytical set-up. In fact it is not possible to separate these two compounds using a (50%-Phenyl)-methylpolysiloxane phase column as the DB-17ms[92]. The LC-50 column, dimethyl-(50% Liquid Crystal), is not suitable for measuring the lighter PAH species, but it provides a good separation of heavy isomers, as for example triphenylene and chrysene. A series of relevant experiments were conducted with a LC-50 column attached to the second FID detector in parallel with the DB-17ms column, so that heavy species could be separated through the two different columns for better resolution. The results indicated that the peak area measured with the DB-17ms is constituted by 90% of chrysene and 10% of triphenylene. With this in mind, we can clearly state that the major four-ring compound produced in the pyrolysis of phenyl radical is chrysene. Only small amounts of the other isomers are produced.

Even more important from a mechanistic point of view is the fact that the chrysene is formed as soon as phenyl iodide starts decomposing. Conventional pathways for the formation of this compound include the HACA mechanism starting from phenanthrene. Since phenanthrene is only measured in trace amounts in the experiments and acetylene is not produced at low temperatures, the HACA mechanism can not be responsible for the formation of chrysene. Thus, such species must be produced by some sort of recombination between three single-ring aromatic compounds. On the other hand benzo[a]anthracene, benzo[g,h,i]fluoranthene, and benzo[c]phenanthrene are formed at higher temperatures, indicating that these isomers could derive from the isomerization of chrysene.

In order to understand the mechanisms of formation of chrysene we deconstructed its molecular structure into simpler components. The only reasonable pathway we were able to identify is the one reported in Figure 39. The primary reactants on the right of the figure are naphthyl vinyl radical and phenyl radical which can recombine to form an intermediate compound which undergoes ring closure and dehydrogenization to chrysene. This process is a sort of PAC mechanism of the naphthyl vinyl radical. The main problem with the proposed pathway is the fact that the naphthyl vinyl radical once formed would isomerize quickly to form acenaphthylene[77] and would not be available for the recombination reaction with the phenyl radical. A different mechanism must be responsible for the formation of chrysene.

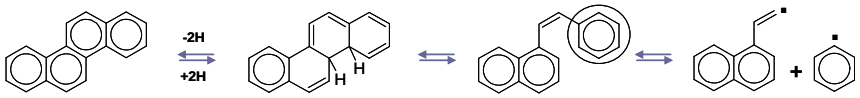


**Figure 39. Deconstruction of the molecular structure of chrysene.**

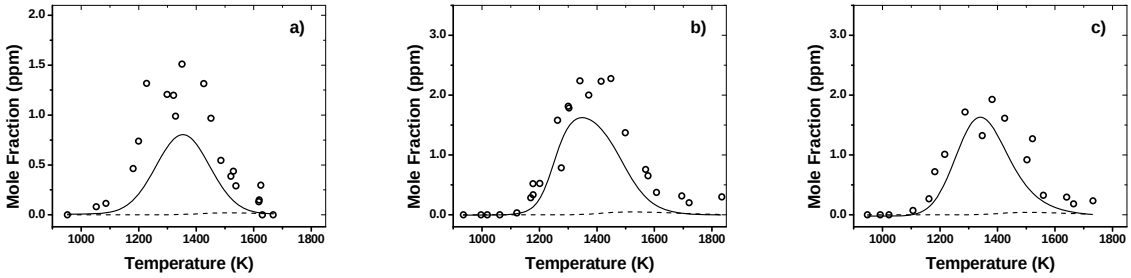


**Figure 40. ○ Sum four-ring compounds exp., —– triphenylene, model in** Table 8**; – – triphenylene, model in** Table 8 **omitting R57. a) $[C_6H_5I]_0$ = 26.6 ppm, p ~ 50 atm; b) $[C_6H_5I]_0$ = 50.6 ppm, p ~ 50 atm; c) $[C_6H_5I]_0$ = 54.2 ppm, p ~ 25 atm.**

Shukla and Koshi[34,35] identified the presence of triphenylene in their experimental work on benzene pyrolysis. Thus we can hypothesize that triphenylene is produced as the primary four-ring compound in our experiments too and that it subsequently undergoes isomerization to form chrysene. Since such an isomerization process is unknown, from a modeling point of view we will consider only the formation of triphenylene and compare the modeling results with the sum of the experimental mole fractions of all the four-ring species (Figure 40). The correspondence between the calculated triphenylene concentrations and the measured concentrations provides an estimate of the accuracy of the reaction pathways in the model keeping in mind the fact that triphenylene subsequently undergoes isomerization into chrysene and at higher temperatures into benzo[a]anthracene, benzo[g,h,i]fluoranthene, and benzo[c]phenanthrene too.

The formation of triphenylene is the prototype of the PAC mechanism[34,35]; Shukla and Koshi hypothesized that phenyl adds to biphenyl to form o-terphenyl which subsequently undergoes cyclodehydrogenization process to triphenylene. The latter step has always been controversial. Experimental studies on benzene pyrolysis[93] and on biphenylene pyrolysis[94] indicate that the cyclodehydrogenization process does not occur, although studies supporting the contrary are present in literature[75,95]. We will try to use our experimental results to clarify the point.

We have already discussed the formation of o-terphenyl in a previous section (section 2.3.1.3) and mentioned that from a modeling point of view its cyclodehydrogenization is energetically unfavorable due to its high activation energy (84.7 kcal/mol, R55). This consideration is based on estimated parameters which may not be very accurate, so we need to find a more convincing justification to rule out the cyclodehydrogenization process. Such justification derives from a simple empirical observation. The amount of o-terphenyl produced in the system (Figure 30) is not sufficient to justify the high mole fractions of four-ring compounds observed in the experiments even if o-terphenyl were entirely converted into triphenylene. Thus a different mechanism must be involved in the formation of the four-ring compounds.

Fields and Meyerson[96,97] reported the measurement of triphenylene in their pyrolytic studies on the reaction between o-benzyne and benzene. The authors hypothesized that the formation of triphenylene is mainly due to trimerization of o-benzyne radicals. Lindow and Friedman[94,98] investigated the liquid and vapor-phase pyrolysis of biphenylene and based on the distribution of the product species concluded that a relatively high concentration of the diradical species in Figure 41 is present especially in the high temperature range of their experiments (730 °C). Such diradical can react with o-benzyne and form triphenylene as shown in Figure 41. An important consideration reported by Lindow and Friedman is that naphthalene is not produced even when the experiments are conducted in benzene for which the estimated barrier is less than 7 kcal/mol[91]. This indicates that the reaction between the diradical intermediate and the o-benzyne radical must be very fast in order to justify the fact that all the o-benzyne radicals are consumed by the pathway in Figure 41 even when large concentrations of benzene are present. In order to account for such favorable trimerization process, we assumed that o-benzyne reacts directly with biphenylene with a reaction rate constant similar to the one used for the dimerization of o-benzyne radicals (R58).

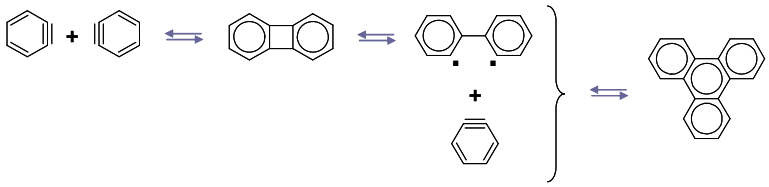

**Figure 41. o-Benzyne trimerization pathway.**

The results of the simulations are reported in Figure 40. The modeling profiles are in excellent agreement with the experiments not only for the general shape but also in terms of maximum mole fractions of the product species. This indicates that the proposed pathway is most likely correct although we need also to take into account the large uncertainty in the quantification of the four-ring species before drawing a conclusion on the accuracy of the estimated reaction constant $k_{57}$. For comparison the modeling results using only the PAC mechanism are also shown in Figure 40 (dashed lines). The results confirm the hypothesis that the PAC mechanism is not adequate to explain the formation of the four-ring compounds in the system in consideration.

Before concluding this section, we would like to mention that the diradical intermediate in Figure 41 can dimerize as shown in the previous studies on the biphenylene pyrolysis[94,98]. This process could be responsible for the discrepancy between experimental and modeling profiles for biphenylene reported in the corresponding section and in Figure 32. Such hypothesis requires additional theoretical validations.

#### *2.3.1.7. Light Hydrocarbons*

Although the main focus of the present investigation is to study the formation of polycyclic aromatic hydrocarbons and the relevance of the chemical mechanisms involved, several light hydrocarbons were measured including the major products benzene, acetylene, diacetylene, and triacetylene. Benzene formation has been already discussed earlier in the text in the corresponding section and no additional analyses are necessary for the purpose of the present investigation. The main consideration we need to keep in mind about the discussion on benzene

is the fact that although the low temperature profiles are well reproduced by the model the benzene concentrations in the high temperature range of our study are overestimated by the model (Figure 25). Overestimation of the experimental profiles at high temperatures has been also observed for other product species, i.e. biphenyl (Figure 25), biphenylene and acenaphthylene (Figure 32). Of course this means that the formation of other experimental compounds is underestimated. However before considering the modeling results we start as usual with the analysis of the experimental profiles of the remaining major compounds, i.e. acetylene, diacetylene, and triacetylene.

As expected, the formation of acetylene and polyacetylenes occurs in the high temperature range of our study mainly above 1400 K. Wang et al.[99] investigated the decomposition of the phenyl radical using ab-initio calculations and concluded that it proceeds through C-H fission to form o-benzyne (R157) which subsequently undergoes fragmentation into acetylene and diacetylene (R159). The derived reaction rate constants were included in the model used by the authors to accurately simulate the decomposition of benzene in shock-tube experiments where the polyacetylenes were measured[100]. Based on the mechanism proposed by Wang et al.[99], the formation of acetylene and diacetylene are strictly coupled and the corresponding concentrations should be very similar at least at low temperatures. As shown in Figure 42 the experimental profiles from the present study do not follow the expected behavior.

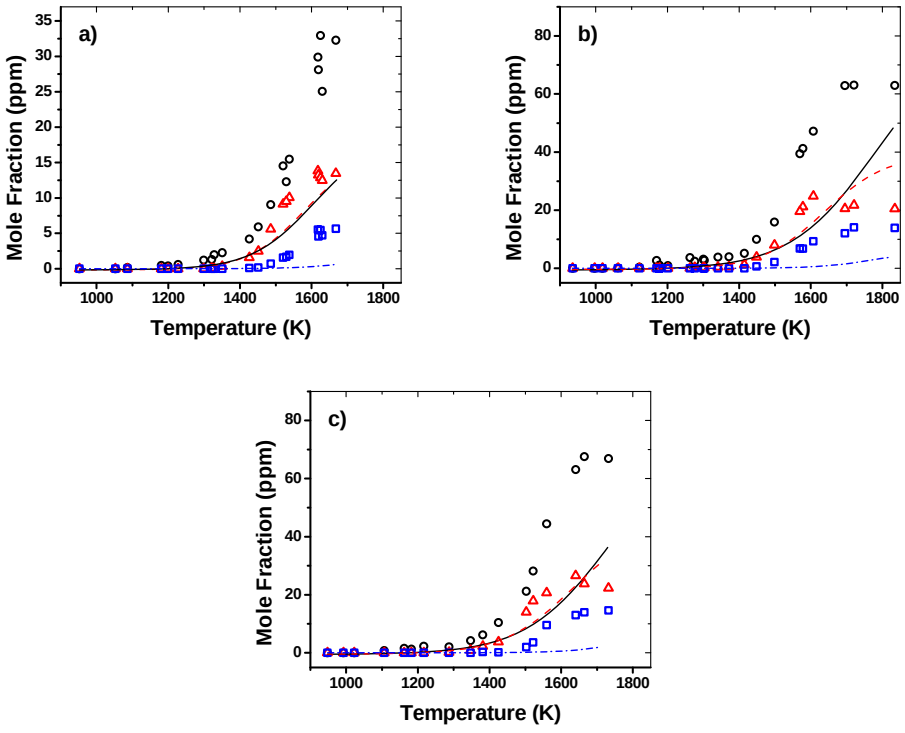


**Figure 42. ○ Acetylene exp., —— acetylene sim.; Δ diacetylene exp., – – diacetylene sim.; □ triacetylene exp., – · – tracetylene sim. a) $[C_6H_5I]_0$ = 26.6 ppm, p ~ 50 atm; b) $[C_6H_5I]_0$ = 50.6 ppm, p ~ 50 atm; c) $[C_6H_5I]_0$ = 54.2 ppm, p ~ 25 atm.**

The first obvious discrepancy between the experimental and the expected trends consists in the fact that acetylene is produced in much larger concentrations compared to diacetylene even at

the relatively low temperatures when the profiles starts to increase rapidly (1400 K). The second less evident difference between the acetylene and the diacetylene profiles is that acetylene is produced also below 1400 K although in small amounts (few ppm). These evidences suggest that there could be an additional low-energy reaction pathway which favors the formation of acetylene. The comparison between the experimental profiles for acetylene and diacetylene and the modeling results confirm such hypothesis (Figure 42). In fact, although the modeling profiles start increasing around 1400 K as the experiments indicate, the o-benzyne fragmentation pathway is not sufficient to justify the steep increase in the experimental mole fractions especially of acetylene. In addition the experimental profiles reach a sort of equilibrium at relatively low temperatures, around 1700 K for acetylene and 1600 K for diacetylene, while the modeling profiles do not reproduce such behavior. Finally no formation of acetylene is predicted at temperatures below 1400 K indicating that the model is not complete.

Different considerations apply for triacetylene. The corresponding experimental profiles have a similar trend to the profiles of acetylene and diacetylene with a relatively steep increase starting around 1450 K before reaching the equilibrium value around 1700 K. Of course the mole fractions of triacetylene are lower than the ones of acetylene and diacetylene. This is in agreement with the hypothesis that triacetylene could be mainly formed through polymerization.

The polymerization steps are included into the model but constitute only a minor pathway for the formation of triacetylene. Reaction pathway analysis indicates that triacetylene is mainly produced through decomposition of the $C_6H_3$ radical (reverse of R162, Ref. [101]) which is formed principally by reaction R167, z-$C_6H_4$+H $\leftrightarrow$ $C_6H_3$+$H_2$ (Ref. [57]). As already discussed, z-$C_6H_4$ is the product of the Bergman decyclization of p-benzyne (R26). As shown in Figure 42 the model significantly underestimates the concentrations of triacetylene. In particular, the polymerization mechanism should play a more relevant role for the formation of such polyacetylene as we will also discuss in the second part of the manuscript in relation to the phenyl + acetylene reaction.

The results reported in the present section indicate that although the formation of the PAH products is well simulated by the model, additional work is required in order to reach a similar accuracy with respect to the profiles of the light hydrocarbon compounds. On the other hand, the experimental results provide a very important benchmark for further development of the chemical kinetic model and for testing novel reaction pathways in particular in relation to the formation of acetylene. Possible pathways could involve the direct fragmentation of the large PAH compounds into small aliphatic hydrocarbons. A key role could be played by the presence of hydrogen atoms which could quite easily add to the various sites available in PAH compounds and allow the access into alternative potential surfaces. These hypotheses clearly require further theoretical validations.

#### *2.3.1.8. PAC, Benzyne Chemistry, and Polymerization*

Now that we presented a complete analysis of the experimental and modeling results on the pyrolytic reactions of the phenyl radical, we summarize the main findings in view of the initial purpose of the investigation, i.e. clarifying the role of the relevant reaction mechanisms. The considerations reported in this section apply specifically to the primary growth reaction steps up to the formation of the four-ring compounds. However, much of the present discussion can be extended to systems which involve reactions between even larger compounds.

First of all the experimental and modeling results indicate that for the system under consideration the PAC mechanism is not enough. In particular, the cyclization of o-terphenyl is

energetically unfavorable in the temperature range of this study, and the PAC mechanism alone is not sufficient to account for the formation of the large four-ring PAH compounds.

On the other hand, it is clear from the entire prior discussion that the presence of the benzynes enhances the formation of almost all the PAH compounds measured in the present investigation. While the p-benzyne undergoes rapid isomerization into 1,5-hexadiyn-3-ene (Bergman decyclization R26) and does not contribute to the growth process, the m-benzyne is the primary factor in the formation of the m-terphenyl. In fact it recombines with phenyl radicals to form m-$C_{12}H_9$ radicals (R28) which constitute the primary building block for the formation of the m-terphenyl through reaction R50. Nevertheless we focus our attention on the chemistry associated with the o-benzyne radical, the most abundant among the benzyne isomers and definitely the most influential intermediate in relation to PAHs formation.

o-Benzyne is mainly produced by three reaction pathways as shown in Figure 43a, i.e. the decomposition of phenyl iodide into o-benzyne and HI (R3), the H-abstraction between phenyl radicals (R21), and the isomerization of m-benzyne (R24). Once formed o-benzyne reacts with the most abundant radical intermediates present in the system, i.e. o-benzyne to form biphenylene (R58) and phenyl to form o-$C_{12}H_9$ (R27). In particular, o-biphenyl radical is a very important intermediate for the formation of PAH compounds as indicated in Figure 43b. In fact in addition to constituting the primary building block for the formation of o-terphenyl (R49) it can easily isomerize into the hydrobiphenylene radical (R59) which is the precursor for the formation of cyclopenta[a]indene, acenaphthylene, and biphenylene - to a minor extent. The reaction rate analysis in Figure 43b confirms that o-$C_{12}H_9$ is mainly formed by reaction between o-benzyne and phenyl radical. Moreover o-benzyne is also responsible for the formation of naphthalene through cycloaddition with benzene and subsequent fragmentation of the intermediate (R146–R148) and possibly for the formation of triphenylene through trimerization (R57).

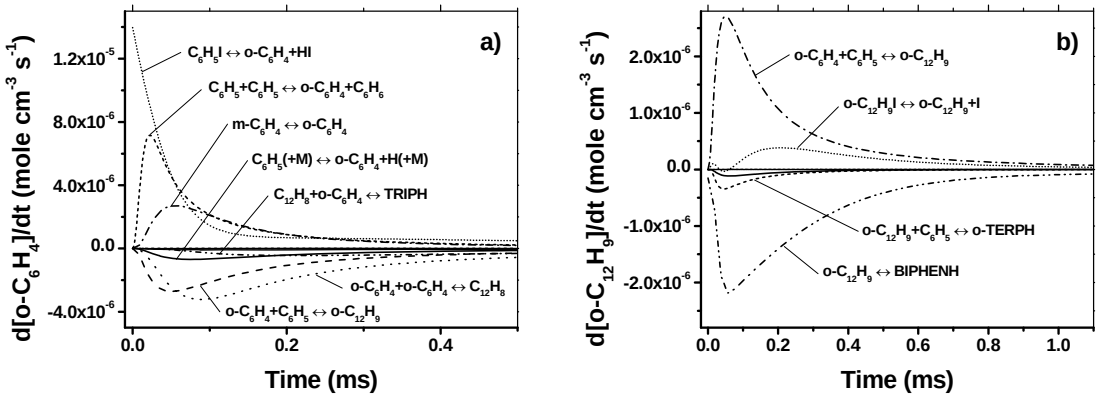


**Figure 43. Rate of production analysis, $[C_6H_5I]_0$ = 54.2 ppm, T = 1287 K, p = 28.3 atm. a) o-benzyne radical; b) o-biphenyl radical.**

The results summarized above not only highlight the importance of the o-benzyne chemistry for the formation of a variety of PAH components relevant to the formation of soot, but also draw attention to a wider category of compounds, the diradicals. In particular, at high-temperatures where the dehydrogenization or H-abstraction processes play a significant role the

presence of relatively high concentrations of diradical species could drive the growth to larger PAH compounds by cycloaddition or even more rapidly by diradical-diradical recombination. Clearly these processes would be in competition with the conventional growth mechanisms, i.e. the HACA mechanism or the PAC mechanism.

A final note regarding the formation of acetylene at relatively high temperatures and the consequent polymerization process: the experimental profiles indicate that below 1300–1400 K the formation of PAH compounds is the predominant pattern. All the polycyclic aromatic hydrocarbons but acenaphthylene have the highest concentrations in this temperature range after which the profiles drop. Above 1400 K the formation of acetylene becomes predominant together with the polymerization process to form the polyacetylenes. Further investigations are required in order to clarify the high-temperature mechanisms responsible from a theoretical point of view.

### 2.3.2. Phenyl + Acetylene Reaction

Now that the mechanisms which lead to the formation of PAH compounds from the pyrolysis of the phenyl radical have been studied in details both experimentally and theoretically we can move to the second part of our investigation which regards the reaction between the phenyl radical and acetylene. Just as for the phenyl pyrolysis study, we will present the major experimental and modeling results with particular attention to the specific mechanisms involved in the formation of the PAH products. The experimental and modeling results at 25 atm are very similar to the results obtained at 50 atm with higher acetylene concentrations and thus are not shown. It is worth mentioning that although not discussed in details trace amounts of several other PAH compounds were detected including most of the compounds shown in Figure 21. However, the pathways characteristic of the phenyl pyrolysis now play only a minor role.

#### *2.3.2.1. Phenyl Iodide Decomposition and Acetylene Profiles*

The mechanisms of decomposition of the phenyl radical precursor phenyl iodide are of course similar to the ones described for the phenyl pyrolysis study. The only major difference is the presence of hydrogen atoms in the system from the reaction between phenyl radical and acetylene to form phenylacetylene and H. The free hydrogen atoms can react with the phenyl iodide and abstract the iodine atom (reaction R4 in Table 8). This reaction was studied both experimentally and theoretically by Gao et al.[102] and the reaction rate constant derived by the authors was used in the present model within the given uncertainty limits. The experimental and modeling profiles for phenyl iodide are reported in Figure 44. Good agreement between experiments and simulations was obtained.

In these experimental sets, acetylene is also added as a reactant to the initial mixture. As we can observe in Figure 45 the acetylene profiles show similar trends for all sets. The trends are characterized by a drop in correspondence with the decay of the phenyl iodide, a recovery above 1300 K before a more consistent drop at higher temperatures (above around 1600 K). The model accurately predicts the experimental behavior of the acetylene profiles with regards to both the shape of the profiles and the concentrations. Clearly this indicates that the chemistry involved in the formation and consumption of acetylene is well represented by the model. Only at high temperatures does the model overestimate the experimental mole fractions. We will discuss the reason for such a discrepancy in the section related to the polyacetylenes (section 2.3.2.5).

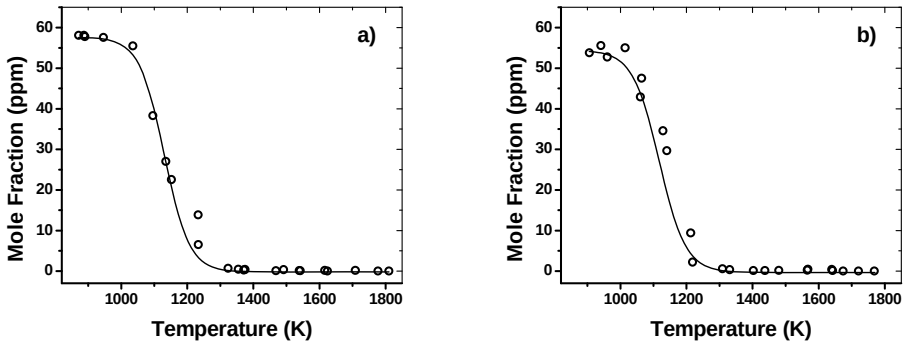


**Figure 44. Phenyl iodide decomposition. ○ exp.; —— sim. a) $[C_6H_5I]_0$ = 58.1 ppm, $[C_2H_2]_0$ = 236.3 ppm, p ~ 50 atm; b) $[C_6H_5I]_0$ = 55.1 ppm, $[C_2H_2]_0$ = 511.3 ppm, p ~ 50 atm.**

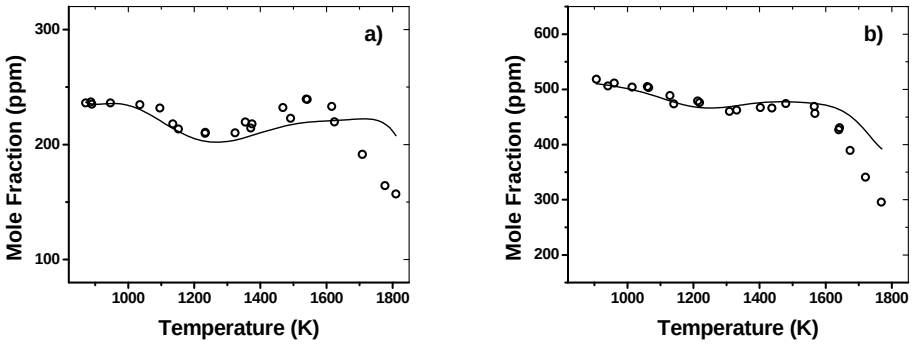


**Figure 45. Acetylene decomposition. ○ exp.; —— sim. a) $[C_6H_5I]_0$ = 58.1 ppm, $[C_2H_2]_0$ = 236.3 ppm, p ~ 50 atm; b) $[C_6H_5I]_0$ = 55.1 ppm, $[C_2H_2]_0$ = 511.3 ppm, p ~ 50 atm.**

#### *2.3.2.2. Phenylacetylene and Benzene*

Phenylacetylene is obviously the major product from the reaction between the phenyl radical and acetylene (R90). At low temperatures the process is mainly limited by the concentration of phenyl radicals in the system as indicated in Figure 46 where the experimental profiles for phenylacetylene are reported for the two sets conducted at a nominal pressure of 50 atm and with different initial amounts of acetylene (236.3 ppm and 511.3 ppm). In fact the initial slope for the formation of phenylacetylene is similar in both cases independently of the $C_2H_2$ mole fraction. Above 1175 K the experimental profiles start diverging and in the temperature range where the phenylacetylene profiles reach the maximum value (around 1275 K) the ratio between the phenylacetylene mole fractions is around 0.69, higher compared to the ratio between the acetylene concentrations (around 0.46). Thus, although the initial acetylene mole fraction does have an influence on the formation of phenylacetylene, the initial mole fraction of phenyl iodide is a limiting factor even at intermediate temperatures.

On the other hand, the experimental profiles for benzene indicate that the formation of this product is almost entirely dependent on the initial phenyl iodide concentration. In fact, as shown in Figure 46, the initial acetylene mole fraction does not have an influence on the concentration of benzene produced along the entire temperature range of our study. This is a clear indication

that the pathways for the formation of benzene are very efficient and involve reactions with very reactive compounds. This is indeed the case. As shown in Figure 47 the reactions responsible for the formation of benzene are the recombination between phenyl and H (R44) and the reaction between phenyl and HI (R5). The main difference with the experiments conducted without acetylene is the relevance of reaction R44 even at low temperatures due to the presence of large concentrations of H atoms from reaction R90. Reaction R5 still has a major influence on the ability to model the benzene formation. On the other hand, the hydrogen-abstraction channel between phenyl radicals (R21–R23) has a minor role due to the fact that the phenyl radicals are removed by the efficient reaction with acetylene and not available for self-reaction.

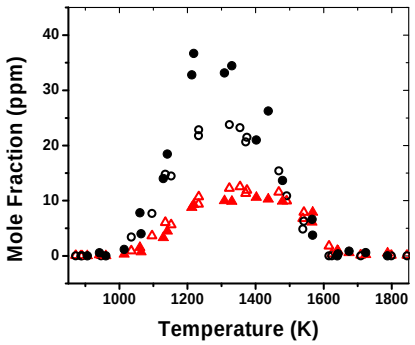


**Figure 46. Experiments, p ~ 50 atm. ○ phenylacetylene, $[C_6H_5I]_0$ = 58.1 ppm, $[C_2H_2]_0$ = 236.3 ppm; Δ benzene, $[C_6H_5I]_0$ = 58.1 ppm, $[C_2H_2]_0$ = 236.3 ppm; ● phenylacetylene, $[C_6H_5I]_0$ = 55.1 ppm, $[C_2H_2]_0$ = 511.3 ppm; ▲ benzene, $[C_6H_5I]_0$ = 55.1 ppm, $[C_2H_2]_0$ = 511.3 ppm.**

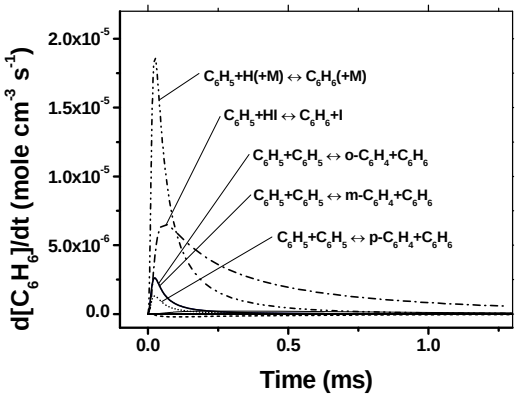


**Figure 47. Benzene, rate of production analysis. $[C_6H_5I]_0$ = 58.1 ppm, $[C_2H_2]_0$ = 236.3 ppm, T = 1233 K, p = 47.1 atm.**

The results of the simulations are reported in Figure 48. The model reproduces correctly the formation of both species for temperatures up to 1300 K. At higher temperatures, especially above 1400 K, the concentrations of benzene and phenylacetylene are overestimated. This behavior is similar to what we observed in the modeling results of the major species of the study on the phenyl pyrolysis. We can attribute this discrepancy to the same reason hypothesized in the

first part of the manuscript - that the model does not include relevant pathways which consume the intermediates forming smaller compounds, i.e. the polyacetylenes.

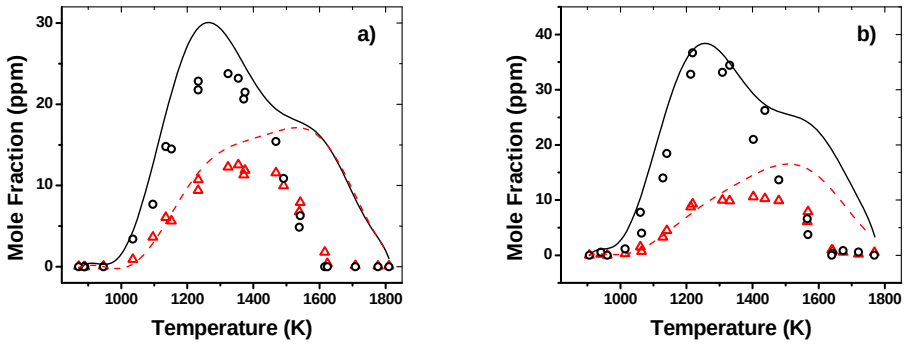


**Figure 48. ○ Phenylacetylene exp., —— phenylacetylene sim.; Δ benzene exp., – – benzene sim. a) $[C_6H_5I]_0$ = 58.1 ppm, $[C_2H_2]_0$ = 236.3 ppm, p ~ 50 atm; b) $[C_6H_5I]_0$ = 55.1 ppm, $[C_2H_2]_0$ = 511.3 ppm, p ~ 50 atm.**

### *2.3.2.3. Diphenylethyne and Phenanthrene*

If we compare the distribution of PAH products in the phenyl + acetylene system with the one observed for the phenyl pyrolysis study we would be surprised that not many additional product peaks were measured. The major difference in adding acetylene as an initial reactant consists in the presence of the C14 compounds, i.e. diphenylethyne and phenanthrene. The experimental profiles of these compounds are reported in Figure 49. The experiments indicate that the formation of diphenylethyne is slightly faster than the one of phenanthrene in the low temperature range of our study. In addition diphenylethyne concentrations reach slightly higher values compared to phenanthrene before decaying above 1250–1300 K.

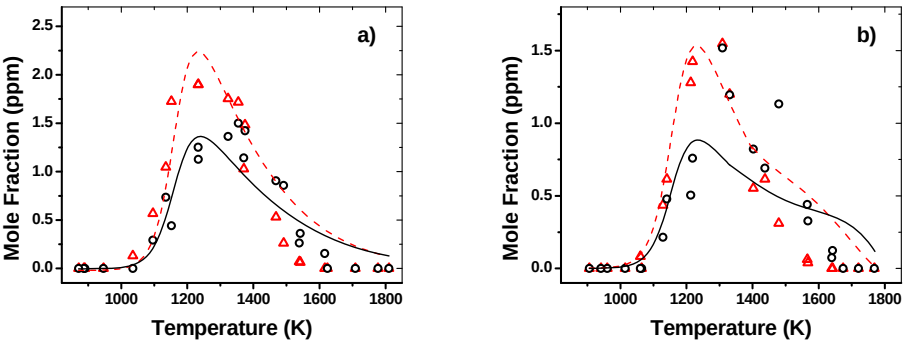


**Figure 49. ○ Phenanthrene exp., —— phenanthrene sim.; Δ diphenylethyne exp., – – diphenylethyne sim. a) $[C_6H_5I]_0$ = 58.1 ppm, $[C_2H_2]_0$ = 236.3 ppm, p ~ 50 atm; b) $[C_6H_5I]_0$ = 55.1 ppm, $[C_2H_2]_0$ = 511.3 ppm, p ~ 50 atm.**

The mechanisms of formation for phenanthrene are quite well known. The first relevant mechanism involves the reaction between o-biphenyl radical and acetylene forming phenanthrene + H (R98). At low temperature such reaction provides only a minor contribution to

the formation of phenanthrene for the case in consideration. In fact the major contribution derives from the reaction between phenyl radical and phenylacetylene. Such reaction has been investigated by Iparraguirre and Klopper[103] using ab-initio calculations but due to the complexity of the study we preferred to use for modeling purposes an estimated global reaction rate constant (R99) based on the model presented in Ref. [58].

On the other hand, to the best of our knowledge no previous studies have considered the formation of diphenylethyne although the potential energy surface proposed in Ref. [103] contains intermediate structures which could be precursors for diphenylethyne. In view of the structure of diphenylethyne and the system in consideration, finding the pathway for its formation becomes trivial. Clearly diphenylethyne is formed through addition between phenyl radical and phenylacetylene with subsequent hydrogen loss in a similar fashion as the reaction between $C_6H_5$ and $C_2H_2$ forming phenylacetylene + H. This is the reason why we considered the same reaction rate constant for both processes ($k_{96} = k_{90}$). The reaction rate constant for the reverse reaction (R97) was estimated based on the results by Hertzler and Frank[104] on the reaction between phenylacetylene and H. In particular, the pre-exponential factor was multiplied by a factor of two due to the multiplicity of the reaction pathway.

The results of the simulations show excellent agreement with the experiments especially for the profiles of diphenylethyne (Figure 49). The formation of phenanthrene at low temperatures is also well simulated by the model indicating that the corresponding reaction rate parameters in the model are appropriate. In particular, it is worth highlighting that the relative formation slopes are well reproduced. The major discrepancy between experiments and simulations consists in the fact that the phenanthrene experimental profiles obtained with higher $C_2H_2$ mole fractions reach higher concentrations than the modeling profiles. This is a consequence of the fact that the modeling profiles reach the maximum at around 1250 K in correspondence with the maximum $C_6H_5C_2H$ values while the maximum experimental value is obtained at higher temperatures (around 1350 K). Different alternative pathways for the formation of phenanthrene were considered including the Diels-Alder mechanism between biphenyl and acetylene studied by Kislov et al. (R110 and R111, Ref. [105]). No improvement in the modeling results could be obtained.

### *3.2.4. Biphenyl and Acenaphthylene*

The mechanisms of formation of biphenyl and acenaphthylene have been described in detail in the first part of the manuscript since both are produced in large concentrations by the pyrolytic reactions of the phenyl radical. The two C12 compounds are present also when acetylene is added in the initial mixture although in lower amounts as shown in Figure 50. In particular, biphenyl formation is significantly reduced due to the fact that phenyl radicals are removed by the reaction with acetylene and thus are not available for self-recombination.

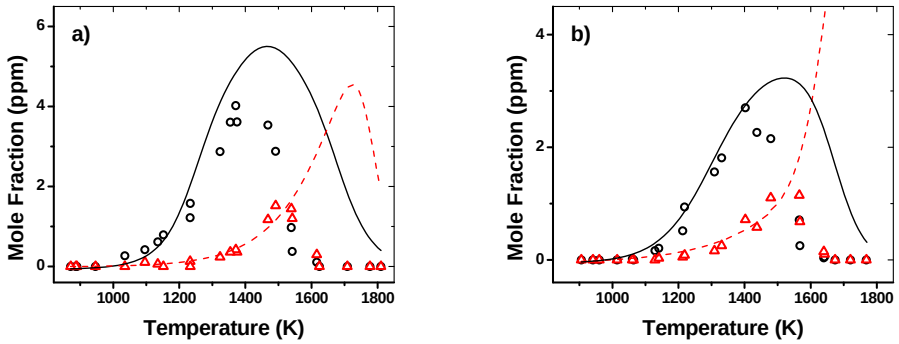


**Figure 50. ○ Biphenyl exp., ── biphenyl sim.; Δ acenaphthylene exp., – – acenaphthylene sim. a) $[C_6H_5I]_0$ = 58.1 ppm, $[C_2H_2]_0$ = 236.3 ppm, p ~ 50 atm; b) $[C_6H_5I]_0$ = 55.1 ppm, $[C_2H_2]_0$ = 511.3 ppm, p ~ 50 atm.**

A similar consideration applies for acenaphthylene although in this case the reduction is not as substantial as expected due to the fact that the HACA mechanism provides a significant contribution to the production of the species (R92 + R149 + R81). The relevance of the HACA mechanism of course depends on the initial concentration of acetylene. Figure 51 shows the results of the rate of production analyses for acenaphthylene conducted at similar temperature and pressure conditions but for different initial acetylene mole fractions. While the results in Figure 51a indicate that in the system with an initial acetylene concentration of 236.3 ppm the HACA mechanism competes with the alternative formation pathways which were found to be significant in the study conducted without acetylene, an increase in the acetylene concentration enhances the relevance of the hydrogen-abstraction acetylene-addition pathway (Figure 51b). In the latter case the HACA mechanism clearly dominates the acenaphthylene formation processes.

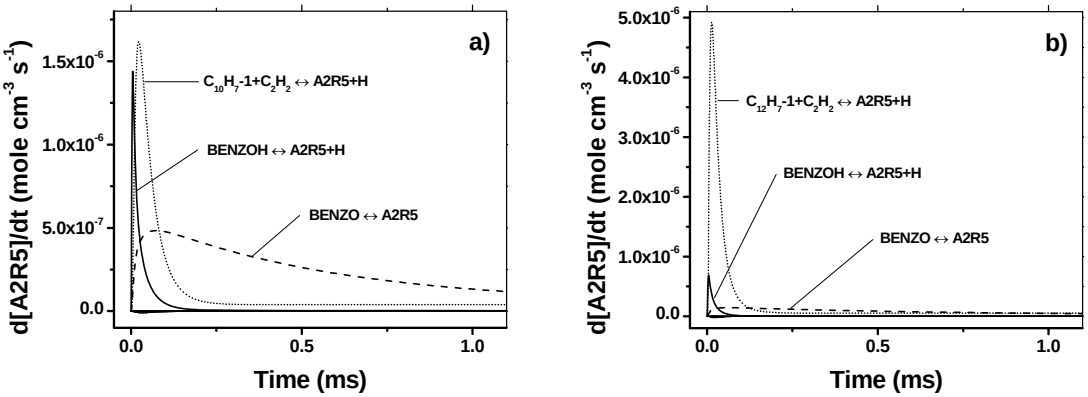


**Figure 51. Acenaphthylene, rate of production analysis. a) $[C_6H_5I]_0$ = 58.1 ppm, $[C_2H_2]_0$ = 236.3 ppm, T = 1491 K, p = 50.3 atm; b) $[C_6H_5I]_0$ = 55.1 ppm, $[C_2H_2]_0$ = 511.3 ppm, T = 1479, p = 51.1 atm.**

The modeling profiles are reported in Figure 50. The experimental profiles of biphenyl are well simulated by the model although overestimated at temperatures higher than 1400 K. The formation of acenaphthylene is also accurately predicted up to around 1500 K which confirms the accuracy of the reaction pathways considered in the present work. At higher temperatures the

experimental profiles drop rapidly while the simulated mole fractions increase up to 1725 K before decaying. This is another confirmation of the fact that the model is not complete but should include additional pathways which lead for example to the formation of light compounds.

#### *2.3.2.4. Naphthalene*

The analysis performed on acenaphthylene indicates that the HACA mechanism has a major role in the formation of such a compound. As is well known, one of the elementary steps of the HACA mechanism involves the formation of the naphthyl radical through reaction R149. Naphthyl radical could react with hydrogen atoms and lead to the formation of the second-ring species (R151). Thus it is interesting to understand if for the system under consideration naphthalene is produced in substantial amounts and how the formation of naphthalene compares with the results of the phenyl pyrolysis study (Figure 37).

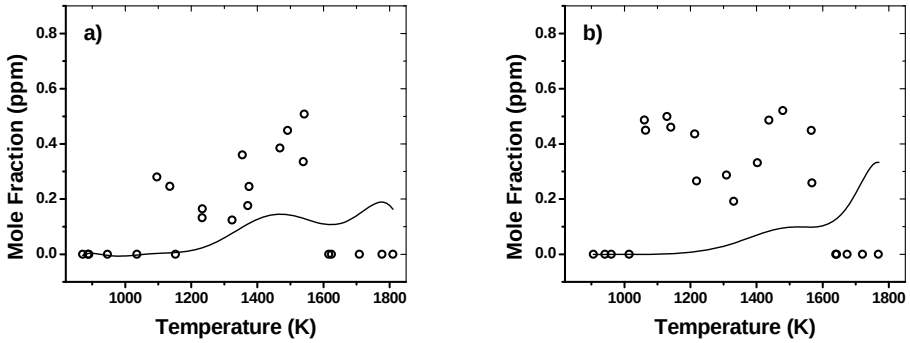


**Figure 52. ○ Naphthalene exp., —– naphthalene sim. a) $[C_6H_5I]_0$ = 58.1 ppm, $[C_2H_2]_0$ = 236.3 ppm, p ~ 50 atm; b) $[C_6H_5I]_0$ = 55.1 ppm, $[C_2H_2]_0$ = 511.3 ppm, p ~ 50 atm.**

The experimental results clearly show that the pathways previously identified as leading to naphthalene do not play a significant role at the conditions implemented in the present investigation (Figure 52). The amounts of naphthalene produced are indeed comparable with the ones observed in Figure 37. On the other hand, the profiles in Figure 52 have a very peculiar trend typical of a bimodal formation process. While the second rise starting at around 1300 K is at least from a qualitative point of view captured by the model, the first increase which seems instantaneous with respect to the phenyl iodide decomposition can not be explained by the model which includes the previously identified formation steps. The most reasonable explanation for such instantaneous formation of naphthalene is related to the possible stabilization of the phenylvinyl radical from the reaction between phenyl and acetylene[16] and the subsequent addition of a second acetylene molecule to form the second-ring species[8]. Although this pathway is not expected to be very favorable it could account for the small naphthalene production observed at low temperatures. However, it is not currently included in the model since the reaction between phenyl radical and acetylene to form phenylacetylene and atomic hydrogen treated as a single-step process has a reaction rate constant experimentally determined in Ref. [18] and which was sufficient for modeling our phenylacetylene results.

Before concluding the analysis on naphthalene, it is worth mentioning that the predicted formation of the second-ring compound around 1400 K is mainly due to the mechanism proposed in Ref. [91] involving the reaction between o-benzyne and benzene. The HACA

mechanism constitutes only a minor pathway since the naphthyl radicals produced are consumed quickly by reaction with acetylene to form acenaphthylene and thus are not available for recombination with H atoms to form naphthalene.

#### *2.3.2.5. Polyacetylenes*

Similarly to what we observed in the study on the phenyl pyrolysis, in the high temperature range of the present investigation the polyacetylenes become the main products while the PAH compounds are consumed. Figure 53 shows the comparison between the diacetylene and the triacetylene profiles for experiments conducted at nominal pressure of 25 atm with and without acetylene in the initial mixture. Clearly the presence of acetylene enhances the formation of the polyacetylenes supporting the hypothesis that the polymerization process plays a key role at high temperatures. In addition we can also notice that the profiles in Figure 53 start increasing all in the same temperature range (around 1400–1450 K) which suggests that the mechanistic pathways are common for the two cases presented.

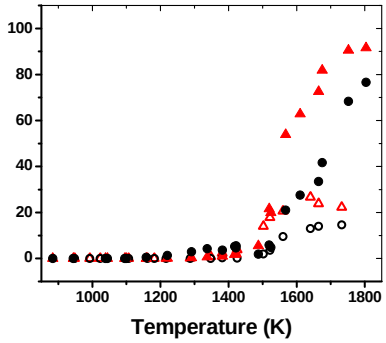


**Figure 53. Experiments, p ~ 25 atm. ○ triacetylene, $[C_6H_5I]_0$ = 54.2 ppm; Δ diacetylene, $[C_6H_5I]_0$ = 54.2 ppm; ● triacetylene, $[C_6H_5I]_0$ = 52.9 ppm, $[C_2H_2]_0$ = 526.3 ppm; ▲ diacetylene, $[C_6H_5I]_0$ = 52.9 ppm, $[C_2H_2]_0$ = 526.3 ppm.**

The experimental results as well as the modeling profiles for both diacetylene and triacetylene are shown in Figure 54. The most evident discrepancy consists in the substantial underestimation of the profiles for triacetylene. As also pointed out in the first part of the manuscript in relation to the results presented in Figure 42, the polymerization process responsible for the formation of triacetylene is clearly not described accurately by the model. On the other hand, we can notice that the triacetylene profiles show an early small increase between 1200 and 1400 K where the concentration of diacetylene is nearly zero. This could suggest that other pathways to the formation of triacetylene exist which do not involve the intermediate formation of diacetylene. Further studies are required to improve the accuracy of the mechanisms involved in the formation of diacetylene and triacetylene at high temperatures.

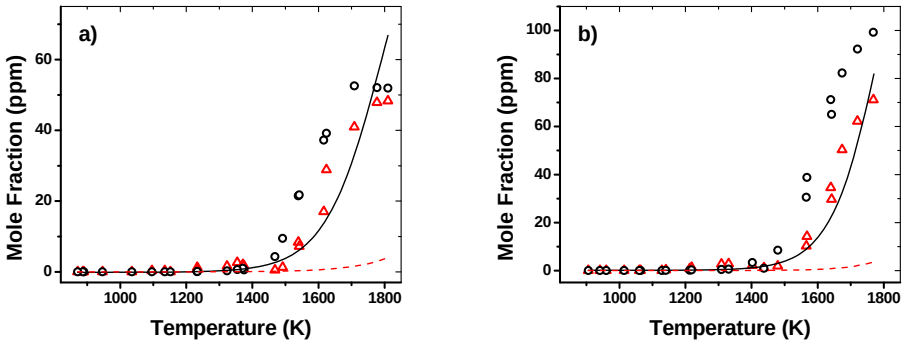


**Figure 54. ○ Diacetylene exp., —— diacetylene sim.; Δ triacetylene exp., – – triacetylene sim. a) $[C_6H_5I]_0$ = 58.1 ppm, $[C_2H_2]_0$ = 236.3 ppm, p ~ 50 atm; b) $[C_6H_5I]_0$ = 55.1 ppm, $[C_2H_2]_0$ = 511.3 ppm, p ~ 50 atm.**

### *2.3.2.6. Effects of Acetone Impurity*

Although the purity of the acetylene as stated by the supplier companies is 99.6% the relative level of acetone, used as a stabilizer for acetylene, can vary typically in the range between 1% and 2% when acetylene is withdrawn from the tank. Several studies have indicated that the acetone impurity does not affect significantly the experimental results on acetylene pyrolysis and oxidation[106] especially when small concentrations of acetylene are utilized. When acetylene is part of a multi-component reactant mixture for studies on acetylene-addition reactions such as in the present investigation the consequences of the acetone impurity are expected to be even less relevant since the chemistry is driven by the reactions with the most abundance among the components, i.e. acetylene. For this reason, in this kind of studies acetylene is usually not purified. However with the use of a Balston filter, small mole fractions of acetone were detected in the reactant mixtures and analyzed together with the relative products to estimate the actual magnitude of the uncertainty caused by the presence of such impurity.

First, a sub-mechanism for acetone chemistry was added to the chemical kinetic model. The sub-mechanism is based on the chemical kinetic mechanism used by Colket et al.[107] to accurately simulate experiments on acetylene pyrolysis in the presence of trace amounts of acetone. The reaction rate constants for the decomposition of acetone were updated based on the mechanism proposed by Dooley et al.[108] for the simulation of n-decane/iso-octane/toluene surrogate mixtures. The only modification in the rate constants is related to the H-abstraction reaction between acetone and H for which the estimated pre-exponential factor was multiplied by a factor of two in order to obtain a better agreement between experiments and simulations. Additional reactions relevant for the acetone chemistry include the reaction between acetone and phenyl radical studied by Choi et al.[109] and the reaction between $CH_3$ and HI to form $CH_4$ and I. The rate constant for the latter reaction was estimated based on the low-temperature work by Seetula et al.[110]

The experimental and modeling results for acetone and the major related products, i.e. methane and toluene, are presented in Figure 55 for the sets conducted at 50 atm. The decay of acetone and the formation of the intermediates are quite well reproduced by the model although at high temperatures methane mole fractions are overestimated. For the purpose of the present study no additional improvements are necessary since the model can already provide a good estimate of how the major stable products of the phenyl + acetylene reaction are affected by the acetone impurity. The comparison between the simulations conducted without and with acetone

in the initial reactant mixture is shown in Figure 56 for the compounds which are mostly affected by the impurity. Figure 56a, b, and c contain the profiles respectively for single-ring, C12, and C14 compounds for the experimental set conducted with an initial acetylene mole fraction equal to 236.3 ppm. The results clearly indicate that in this case the acetone impurity, around 1.5 ppm, does not significantly influence the formation of the intermediate compounds. The maximum error is around 2–4%. The error in the profiles of the species not shown which include phenyl iodide, acetylene, and the polyacetylenes is even smaller.

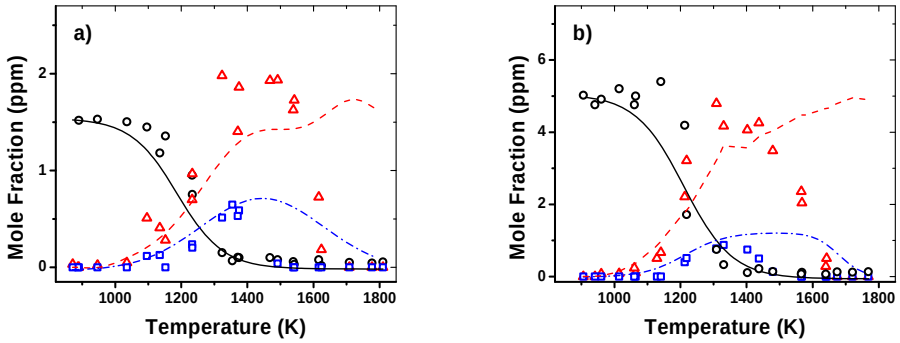


**Figure 55. ○ Acetone exp., —– acetone sim.; Δ methane exp., – – methane sim.; □ toluene exp., – · – toluene sim. a) $[C_6H_5I]_0$ = 58.1 ppm, $[C_2H_2]_0$ = 236.3 ppm, p ~ 50 atm; b) $[C_6H_5I]_0$ = 55.1 ppm, $[C_2H_2]_0$ = 511.3 ppm, p ~ 50 atm.**

The analyses performed on the experimental sets conducted with around 500 ppm initial acetylene mole fraction indicate the presence of larger relative amounts of acetone, around 1% of the acetylene in the mixture. As shown in Figure 56d, e, and f the effects of the acetone impurity in the profiles are larger than in the previous case but still below the uncertainty in the experimental measurements. The profiles for phenyl iodide, acetylene, and the polyacetylenes are almost unaltered by the presence of acetone. Thus we can conclude that the acetone impurity does not influence significantly the experimental profiles for the intermediate measured in the present work especially in relation to the experiments conducted with smaller amounts of initial acetylene in the reactant mixture.

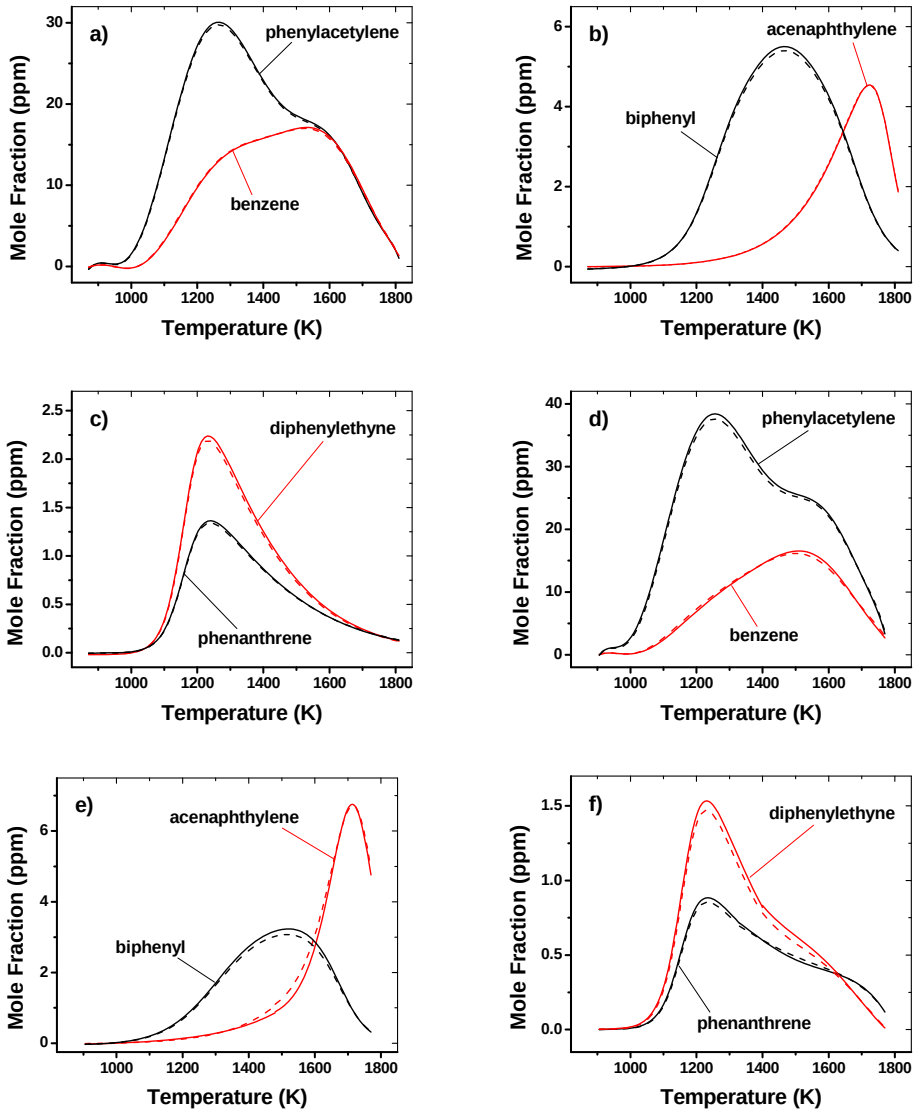


**Figure 56. Numerical simulations. a), b), and c) solid lines: $[C_6H_5I]_0$ = 58.1 ppm, $[C_2H_2]_0$ = 236.3 ppm, p ~ 50 atm; dashed lines: $[C_6H_5I]_0$ = 58.1 ppm, $[C_2H_2]_0$ = 236.3 ppm, $[CH_3COCH_3]_0$ = 1.5 ppm, p ~ 50 atm. d), e), and f) solid lines: $[C_6H_5I]_0$ = 55.1 ppm, $[C_2H_2]_0$ = 511.3 ppm, p ~ 50 atm; dashed lines: $[C_6H_5I]_0$ = 55.1 ppm, $[C_2H_2]_0$ = 511.3 ppm, $[CH_3COCH_3]_0$ = 5.0 ppm, p ~ 50 atm.**

#### *2.3.2.7. HACA, Addition between Single-Ring Aromatics, Benzyne Chemistry, and Polymerization*

Summarizing the main results on the experimental and modeling study of the phenyl + acetylene reaction we can state that the formation of multi-ring compounds is influenced by two main mechanisms, the HACA mechanism and the reaction between single-ring aromatics. In particular, the C14 compounds, i.e. phenanthrene and diphenylethyne, derive mainly from the reaction between phenyl radical and phenylacetylene, although especially at higher temperatures the contribution of the o-$C_{12}H_9$ + $C_2H_2$ for the formation of phenanthrene becomes important. Once again we need to remember that the o-benzyne radical plays a key role in the formation of o-$C_{12}H_9$ as discussed in the first part of the paper.

With regard to the formation of acenaphthylene the discussion is slightly more complex since the mechanisms involved differ based on the relative concentrations of the phenyl radicals and the acetylene in the system. For low acetylene mole fractions the HACA mechanism is one of the relevant pathways to acenaphthylene although not the dominant. In this case the isomerization of the o-biphenyl radical is still the most important pathway as in the study on the phenyl pyrolysis. Consequently o-benzyne becomes a key intermediate in the acenaphthylene formation. When acetylene concentration is increased the HACA mechanism is definitely the main source for acenaphthylene.

As in the phenyl pyrolysis study, above a certain temperature the polymerization process becomes dominant and the PAHs concentrations drop. The temperature range of maximum PAHs production is around 1300–1400 K after which the experimental profiles for diacetylene and triacetylene rapidly rise. The model does not accurately simulate the chemistry for the polymerization mechanism relevant to high temperature conditions indicating that additional studies are required to clarify this aspect of the problem. In this case the experimental results suggest that new pathways for the formation of triacetylene could be possible.

# 3. FORMATION OF NAPHTHALENE FROM THE RADICAL/π-BOND ADDITION BETWEEN SINGLE-RING AROMATIC HYDROCARBONS

Fine particles, $PM_{2.5}$, represent a major threat impacting not only the environment but also human health. Key steps in the formation of particulate matter include the formation of the first aromatic ring species, benzene, and the subsequent growth to naphthalene and larger polycyclic aromatic species (PAH's). Although formation of benzene is fairly well characterized[7-9], the pathways leading to the second-ring species are still not well understood. The experimental results on the phenyl pyrolysis reported in section 2.3.1 confirm that the conventional mechanisms for the formation of large polycyclic aromatic hydrocarbons[7-9] are not sufficient to explain the experimentally observed formation of the multi-ring fused compounds such as naphthalene.

The literature studies on naphthalene formation mainly focus on the addition of single-ring aromatics with small aliphatics. Examples of such addition pathways include the HACA mechanism (hydrogen abstraction acetylene addition)[33,13,14], the addition of vinylacetylene and 1,3-butadiene to phenyl radical[103,111,112], the reaction of 1,3-butadien-1-yl with benzene[112,113], and the addition of propargyl radical to phenyl and methylphenyl radicals[9]. Alternative mechanisms include the reaction between cyclopentadienyl radicals[114-116] and the addition between o-benzyne and benzene.

Benzyne radicals are members of a group of very reactive compounds known as arynes. In particular o-benzyne can undergo a variety of reactions involving the addition of linear or cyclic compounds to the triple bond of its structure. The review on the addition reactions of o-benzyne with heterocyclic compounds provided by Bryce and Vernon[117] contains an entire section focused on the reactions between o-benzyne and the six-membered ring azines, a class of organic compounds characterized by a ring structure like that of benzene but with one or more carbon atoms replaced by nitrogen atoms. Of even greater relevance for soot formation are the experimental studies of the benzene (deuterated and not) + o-benzyne reaction. This reaction was investigated for the first time by Miller and Stiles[118] as part of their pioneering experimental work on arynes compounds. In subsequent experimental investigations Fields and Meyerson[96,97,119] identified three main products of the reaction, i.e. biphenyl, naphthalene, and acetylene, along with small amounts of biphenylene and triphenylene. Friedman and Lindow[94] reexamined the reaction between o-benzyne and benzene (deuterated and not) and experimentally identified the additional products acenaphthylene and acenaphthene. The PAH compounds formed during the reaction consisted of naphthalene (80%), biphenyl (9%), acenaphthylene (6%) and acenaphthene (5%). Based on the relative abundance of the deuterated isomers, Friedman and Lindow hypothesized mechanistic pathways for the formation of each species (Figure 57). In particular naphthalene, by far the most abundant among the products, is expected to derive mainly from the insertion reaction of o-benzyne with benzene (1,4 cycloaddition) followed by thermal fragmentation of the intermediate compound benzobicyclo[2,2,2]octatriene. If we define the radical/π-bond addition as the addition of a radical site of a reactant species to any of the CC π-bonds of the other reactant, the experimental study from Friedman and Lindow clearly addressed the importance of such radical/π-bond addition (insertion reaction) in the formation of PAH compounds relevant to soot formation.

A different but related reaction system which proceeds through radical/π-bond addition is the benzene + phenyl reaction. This reaction was studied in the past both theoretically and experimentally as an important pathway for the formation of biphenyl, an intermediate species for PAH growth. The rate constants for both the forward and the reverse processes were measured using a combination of experimental techniques including the flash photolysis technique[120], the low-pressure Knudsen cell flow reactor-mass spectrometric technique[15], the single-pulse shock tube technique[121], and the cavity ringdown kinetic spectrometry (CRDS) technique[74]. In addition to the CRDS experiments, Park et al.[74] carried out a theoretical study on the radical/π-bond $C_6H_5$ + $C_6H_6$ addition reaction using DFT methods and RRKM calculations aimed to model the available experimental data on biphenyl formation. No alternative reaction pathways were investigated.

Besides the reactions between benzene and single-ring phenyl and o-benzyne radicals, the recent theoretical results by Tranter et al.[37] indicate that the self-reaction between phenyl radicals can proceed through radical/π-bond addition. Phenyl radicals play a relevant role in combustion processes because of their ability to recombine with small aliphatic species to form naphthalene[14,111-113]. Furthermore the radical-radical recombination between phenyl radicals leads to the formation of biphenyl as experimentally studied by Park and Lin[36] using the laser photolysis/mass spectrometry technique and by Heckmann et al.[18] in shock-tube experiments. Both studies focused on the direct radical-radical recombination of the reactant species to form biphenyl.

Tranter et al.[37] revisited the self-reaction of phenyl radicals based on low-pressure shock-tube experiments and high-level theoretical calculations. The study addressed for the first time the relevance of the abstraction channel leading to the formation of benzene and benzyne radicals. Above 1400 K the abstraction channel becomes dominant, while at low temperatures the radical-radical σ-recombination pathway to biphenyl prevailed. Besides the recombination and abstraction channels, the radical/π-bond addition reaction between phenyl radicals was partially investigated from a theoretical point of view as a minor path compared to two dominant channels described above. Due to the low stability of the complexes involved as well as the low-pressure conditions of the study, the authors hypothesized that most of the flux entering the radical/π-bond addition energy surface redissociates back to the reactants, while the remaining part yields biphenyl or biphenyl radical + H. Nevertheless the authors did not conduct a detailed theoretical study on the potential energy surface to confirm such hypothesis or define different pathways, relevant to higher pressures, for the radical/π-bond addition reaction.

The idea of a pivotal role of the π-bonds in combustion processes acquires even more relevance in consideration of the recent developments in the pioneering research on particle nucleation and growth. In his review paper presented at the 33rd International Symposium on Combustion[122], Wang proposed an innovative explanation for the unexpected experimentally observed features of nascent soot particles in premixed flames. These features include the presence of an aromatic core composed of stacked PAH compounds surrounded by an aliphatic shell[123]. Wang proposed that such a core-shell structure derives from π-electron interactions between aromatic π radicals and closed-shell aromatic compounds. Although the π-π bonding concept proposed by Wang certainly requires further validations, it confirms the scientific interest in the characterization of the effective role of the π-bonds in relation to unexplored chemical mechanisms relevant to soot formation.

Inspired by the numerous theoretical and experimental works described above, the present investigation focuses on the *theoretical* examination of radical/π-bond addition reactions

between aromatic compounds relevant to the formation of two-ring fused species. In particular, the addition between o-benzyne and benzene has been fully investigated for the first time from a theoretical point of view in order to test the pathways that Friedman and Lindow inferred from their experimental work. The theoretical study has been extended to the systems involving the radical/π-bond addition between benzene and phenyl radical and between phenyl radicals. Although these reactions are expected to lead mainly to the formation of biphenyl and biphenyl radical as described in the theoretical works by Park et al.[74] and by Tranter et al.[37], the unexplored possibility of additional pathways leading to the formation of fused PAH compounds, never before addressed, have been tested in the present investigation.

### 3.1. Computational Methods

All geometry optimizations and vibrational analyses were performed using the Becke three parameter hybrid method[61] with the Lee-Yang-Parr correlation functional approximation[62] with unrestricted open shell wave functions (uB3LYP) and Pople's valence triple-ζ basis set including diffuse and polarization functions (6-311+G(d,p))[63]. Structure optimizations of the local minima and saddle points (characterized by exactly one vibrational mode with imaginary frequency) were obtained using respectively the Berny geometry optimization algorithm[124] and the combined synchronous transit-guided quasi-Newton (STQN) method[125] as implemented by Gaussian 03 program package[65]. In addition to the vibrational analyses, intrinsic reaction coordinate (IRC) calculations[126] were carried out on the optimized transition state structures to confirm that each specific transition state is appropriate for the reaction path in consideration.

The energetics of the optimized structures were refined by single point energy calculations performed with coupled-cluster method using both single and double substitutions and including triple excitations (uCCSD(T))[89] with Dunning's correlation consistent polarized double-ζ basis set (cc-pVDZ)[90]. Frozen-core (FC) assumption was also used. All of the calculations were carried out with the Gaussian 03 program package[65].

Conventional transition state theory (TST)[84-86] was used to evaluate the high-pressure limit reaction rate constants from the quantum chemical calculations. The expression used to evaluate the reaction rate constants is

$$k_{\infty}(T) = \kappa(T) \cdot \frac{k_B T}{h} \cdot \frac{Q^{\ddagger}(T)}{\prod_{i=1}^{n} Q^{R_i}(T)} \cdot e^{-E_0/k_B T}$$

where $k_B$ is the Boltzmann's constant, $h$ the Planck's constant, $Q^{\ddagger}$ and $Q^{R_i}$ the partition functions of the activated complex and of the reactants respectively, $n$ the number of reactants, and $E_0$ the difference between the energies of the transition state and of the reactants, including the zero-point vibrational energies (ZPVE). The rotational partition functions include the symmetry number for the reactants and the transition states. The vibrational partition functions were calculated using rigid rotor harmonic oscillator assumptions. Only the contributions from the low frequency torsional modes were calculated using free rotor approximation. The transmission coefficient $\kappa(T)$ accounting for tunneling effects was estimated as[87]

$$\kappa(T) = 1 - \frac{1}{24} \cdot \left( \frac{h\upsilon^{\ddagger}}{k_B T} \right)^2 \cdot \left( 1 + \frac{RT}{E_0} \right)$$

where R is the universal gas constant and $\upsilon^{\ddagger}$ the imaginary frequency associated to the motion along the reaction coordinate.

## 3.2. Results and Discussions

### 3.2.1. Benzene + o-benzyne

The experimental work performed by Friedman and Lindow[94] on the relatively low-temperature pyrolysis of o-benzyne in benzene and benzene-d6 indicates that the products of the addition reaction consist mainly of naphthalene-d4 (80%). Considering the distribution of the remaining product species as well as the products of the pyrolysis of benzobicyclo[2,2,2]octatriene and benzocyclooctatetraene[94] (shown in Figure 57), we hypothesize that at least 70-75% of the $C_6H_6$ + o-$C_6H_4$ reaction proceeds through the benzobicyclo[2,2,2]octatriene intermediate (radical/π-bond insertion) to finally form naphthalene through fragmentation of the intermediate. On the other hand we can also hypothesize that the reaction will mainly occur on the singlet potential energy surface since the singlet spin-state o-benzyne molecule is more stable than the corresponding triplet configuration. Thus the radical/π-bond addition reaction between benzene and singlet o-benzyne could be the dominant pathway with naphthalene as major product. In order to test these hypotheses for the formation of the experimentally observed naphthalene, a series of theoretical calculations were initiated.

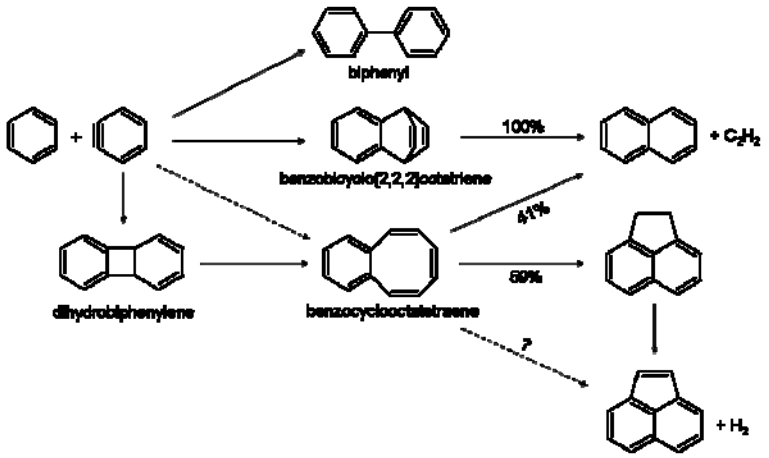


**Figure 57. Benzene + o-benzyne reaction, based on Friedman and Lindow[94].**

Figure 58 shows the results of the calculations performed on the potential energy surface for the singlet radical/π-bond addition reaction. The system proceeds along an unique channel leading to the formation of benzobicyclo[2,2,2]octatriene ($S1^s$) through an energy barrier of 6.8

kcal/mol (1,4 cycloaddition). Benzobicyclo[2,2,2]octatriene can easily dissociate into naphthalene and acetylene through TS2. The barrier for such dissociation process is 13.6 kcal/mol lower than the barrier for redissociation of $S1^s$ back to the reactants.

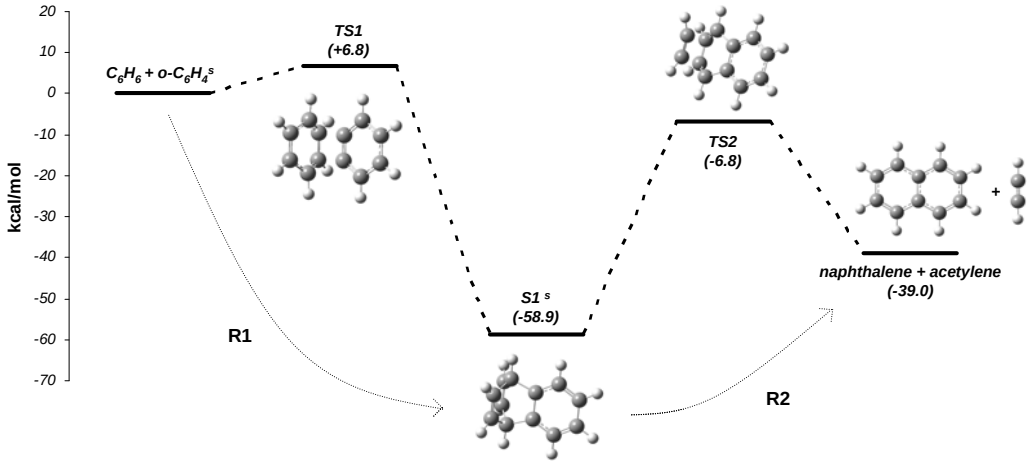


**Figure 58. Potential energy surface for benzene + singlet o-benzyne radical/π-bond 1,4 cycloaddition. uB3LYP/6-311+G(d,p) optimized structures. uCCSD(T)/cc-pVDZ relative energies in kcal/mol, including ZPVE.**

As already mentioned above, the experimental work on the reaction between benzene and o-benzyne indicates that the reaction leads not only to the formation of naphthalene but possibly also to the formation of other different PAH compounds including biphenyl, acenaphthylene and acenaphthene (Figure 57). Beno et al.[127] studied the initial step of the o-benzyne + benzene reaction in relation to the interaction between an o-benzyne molecule located inside a large host molecular structure and the host molecule. The authors performed calculations at the B3LYP/6-31G(d) level of theory and reported the presence of two transition states, the one corresponding to TS1 (Figure 58) and an additional transition state TS** as reported in Figure 59. TS** leads to the formation of a stable biphenyl-like compound (S** in Figure 59), which could isomerize to form biphenyl and/or benzocyclooctatetraene.

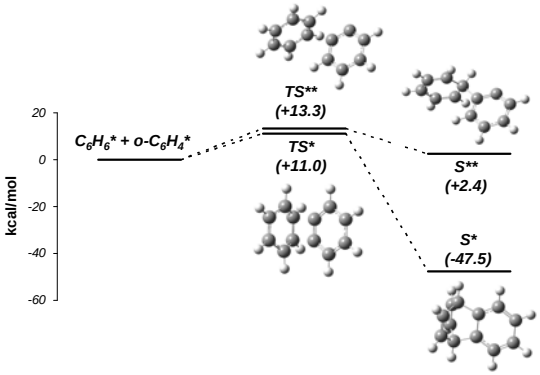


**Figure 59. Benzene + singlet o-benzyne radical/π-bond addition. uB3LYP/6-31G(d) optimized structures and energies, including ZPVE.**

We were able to reproduce the results by Beno et al.[127] using the same basis set they used. The results are reported in Figure 59. As discussed by the authors, the calculated energy difference between the two transition states is small, around 2 kcal/mol. Nevertheless the biphenyl-like complex S** is bound by only 10.9 kcal/mol with respect to TS** and a consistent part of the flux entering the channel will redissociate back to the reactants. Surprisingly we could not confirm the presence of TS** using our 6-311+G(d,p) basis set. Any attempt to identify such saddle point did not converge or converged but to a transition state structure similar to TS6 in Figure 62 not relevant to the specific case. At this point we can not draw a definitive conclusion on the presence and the relevance of the stepwise o-benzyne + benzene channel shown in Figure 59. If the stepwise channel exists as indicated by Beno et al.[127], we expect this channel to account for maximum 25-30% of the total reaction between o-benzyne and benzene.

Another important element that we need to take into consideration is the fact that the experimental work by Friedman and Lindow[94] is subject to uncertainties due to the nature of the pyrolytic study performed. As hypothesized by the authors, the observed C12 compounds could not be the result of chemical processes but they could possibly derive from catalytic mechanisms occurring on the surface of the fused quartz chips used in the experiments. This hypothesis is supported by a study conducted by Friedman[128] on the reaction between o-benzyne and benzene at 45 ºC in the presence of silver ions. The PAH products formed in the experiments conducted without silver ions in solution were composed almost entirely of naphthalene (88%) and biphenylene (11%). Increasing amounts of silver ions concentration were related to increased yields of biphenyl and benzocyclooctatetraene. A similar catalytic mechanism could be responsible for the formation of these products even at the higher temperatures of the study by Friedman and Lindow[94]. This means that the relative importance of the stepwise o-benzyne + benzene channel shown in Figure 59 which through isomerization of S** leads to biphenyl and benzocyclooctatetraene could be even lower than hypothesized at the beginning of the paragraph.

Calculations were also performed to try to identify a possible concerted 1,2 cycloaddition pathway in alternative to the 1,4 cycloaddition shown in Figure 58. No corresponding transition state could be identified. Depending on the initial guess for the transition state structure, the calculations either could not converge or converged to the 1,4 cycloaddition TS1 transition state presented in Figure 58.

At this point it is clear that both the experimental results by Friedman and Lindow[94] and the theoretical calculations indicate the presence of a reaction channel which leads to the formation of naphthalene and acetylene as shown in Figure 58. Due to the possibly important role of such route, the corresponding reaction rate constants have been estimated.

| Species | T1 Diagnostic |
|---|---|
| $C_6H_6$ | 0.010 |
| $C_6H_4^S$ | 0.012 |
| TS1 | 0.011 |
| $S1^S$ | 0.011 |
| TS2 | 0.011 |
| naphthalene | 0.010 |
| acetylene | 0.012 |

**Table 9. $T_1$ diagnostic for the calculations in Figure 58.**

First the $T_1$ diagnostic[129] was implemented to test the level of accuracy of the calculations presented in Figure 58. The results, reported in Table 9, are all below the 0.02 threshold for

closed shell species which indicates that the energy calculations do not suffer from a strong multi-reference character and provide reliable energy barriers for the elementary reactions. Thus high-pressure limit rate constants for $C_6H_6$ + o-$C_6H_4$[s] → S1[s] (R1) and S1[s] → $C_{10}H_8$ + $C_2H_2$ (R2) have been estimated based on the calculated properties of the species involved. The fitted modified Arrhenius expressions for R1 and R2 over a temperature range between 1000 K and 2000 K are

$$k_{R_1}(T) = 5.809 \times 10^3 T^{2.526} \exp(-2979.0/T) \ [\text{cm}^3\ \text{mol}^{-1}\ \text{s}^{-1}]$$
$$k_{R_2}(T) = 7.458 \times 10^{14} T^{0.0956} \exp(-27584.8/T) \ [\text{s}^{-1}]$$

The reaction rate constants calculated from TST for R1 and R2 are reported in **Error! Reference source not found.**. The error associated with these calculations is mainly due to the uncertainty in the reaction barriers. In particular the barrier for the entrance reaction R1 is expected to be over-estimated by the theoretical methods implemented in the present work, as also reported for the corresponding reactions for the benzene + phenyl and phenyl + phenyl systems. As described in the corresponding sections, the estimated entrance barrier for $C_6H_6$ + $C_6H_5$ is 2.4 kcal/mol higher than the optimal experimental value, while for the $C_6H_5$ + $C_6H_5$ reaction the barrier is around 4 kcal/mol higher than the value obtained from higher-level energy calculations. A 3 kcal/mol decrement in the R1 barrier would cause an increase of the rate constant value of around 2.1 times at 2000 K, 2.7 times at 1500 K, and 4.5 times at 1000 K.

| | Temperature (K) | | | | | |
|---|---|---|---|---|---|---|
| **reaction** | 1000 | 1100 | 1200 | 1300 | 1400 | 1500 |
| **R1** | 1.12 x $10^{10}$ | 1.86 x $10^{10}$ | 2.90 x $10^{10}$ | 4.30 x $10^{10}$ | 6.10 x $10^{10}$ | 8.37 x $10^{10}$ |
| **R2** | 1.54E x $10^{03}$ | 1.89 x $10^{04}$ | 1.53 x $10^{05}$ | 9.03 x $10^{05}$ | 4.14 x $10^{06}$ | 1.55 x $10^{07}$ |
| | **Temperature (K)** | | | | | |
| **reaction** | 1600 | 1700 | 1800 | 1900 | 2000 | |
| **R1** | 1.12 x $10^{11}$ | 1.45 x $10^{11}$ | 1.85 x $10^{11}$ | 2.31 x $10^{11}$ | 2.84 x $10^{11}$ | |
| **R2** | 4.91 x $10^{07}$ | 1.36 x $10^{08}$ | 3.37 x $10^{08}$ | 7.60 x $10^{08}$ | 1.58 x $10^{09}$ | |

**Table 10. Calculated TST rate constants for R1 in $cm^3$ $mol^{-1}$ $s^{-1}$ and for R2 in $s^{-1}$.**

The practical relevance of the singlet channel described in Figure 58 depends mainly on the concentration of o-benzyne in the reacting system, as benzene is usually present in large amounts. o-Benzyne radicals derive mainly from the dehydrogenization of phenyl radicals. The process involves an energy barrier of around 78 kcal/mol[130] , considerably lower than the overall energy necessary for the fragmentation of $C_6H_5$ into n-$C_4H_3$ + $C_2H_2$[17,99,131]. Thus o-benzyne is the main product of the thermal decomposition of the phenyl radical. At relatively high temperatures we expect high concentrations of phenyl radicals produced by dehydrogenization of benzene, thus the concentration of o-benzyne radicals should be substantial and the singlet channel of the radical/π-bond addition reaction with benzene could play a significant role in the formation of naphthalene. On the other hand the proposed pathway may not play a major role in combustion systems because it will be in competition with different other channels involving the consumption of o-benzyne. In particular the HACA mechanism[7-9] could represent the main

source of o-benzyne consumption through double addition of acetylene leading to the formation of naphthalene. Moreover o-benzyne can dissociate into acetylene and diacetylene as investigated both experimentally and theoretically[17,70,99,132].

The present study could be extended to systems involving different benzyne-like species. For example, in a recent paper García-Cruz et al.[133] showed that the dehydrogenization of pyrene to form the corresponding diradical species occurs with a lower barrier compared to the dehydrogenization of benzene to o-benzyne. Similarly to the o-benzyne radical, 1,2-didehydropyrene and 4,5-didehydropyrene (Figure 60) could react with benzene to form a 5-ring species through benzene insertion and subsequent fragmentation. Thus the radical/π-bond addition could contribute to the growth in the number of aromatic rings.

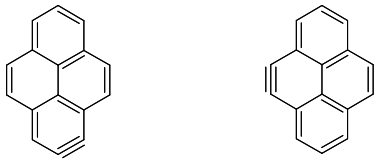

1,2-didehydropyrene 4,5-didehydropyrene

**Figure 60. Schematic representation of the molecular structures of 1,2- and 4,5-didehydropyrene.**

The results reported in the previous paragraphs indicate that the benzene + singlet o-benzyne proceeds mainly through 1,4 cycloaddition. Although the singlet o-benzyne radical is 31.9 kcal/mol more stable than the corresponding triplet configuration based on the CCSD(T) calculations, the triplet surface could be accessible, especially at high temperatures. Thus the possibility for additional channels through the benzene + triplet o-benzyne reaction was investigated.

The reaction between benzene and triplet o-benzyne proceeds through several channels (Figure 61 and Figure 62). The first channel involves the hydrogen abstraction from the benzene ring to form two phenyl radicals. The calculated barrier through TS3 is 8.2 kcal/mol.

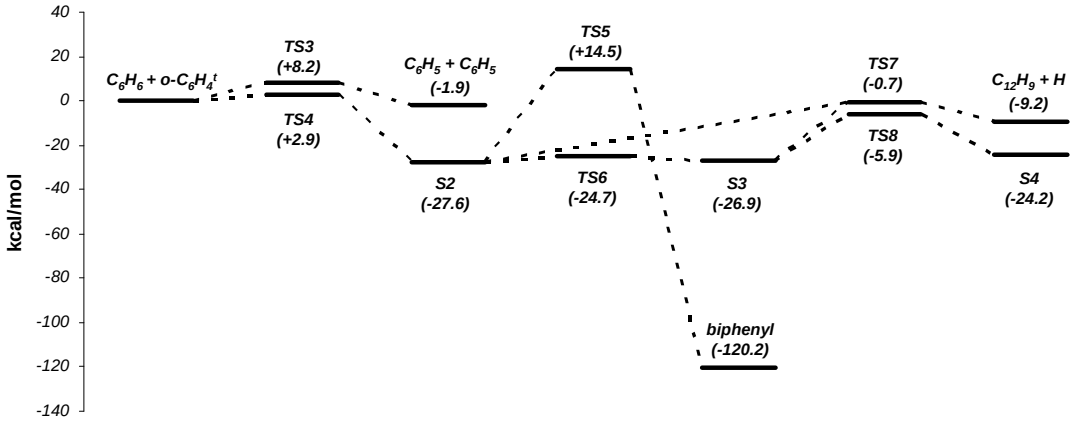


**Figure 61. Potential energy surface for benzene + triplet o-benzyne radical/π-bond addition. uCCSD(T)/cc-pVDZ relative energies in kcal/mol, including ZPVE.**

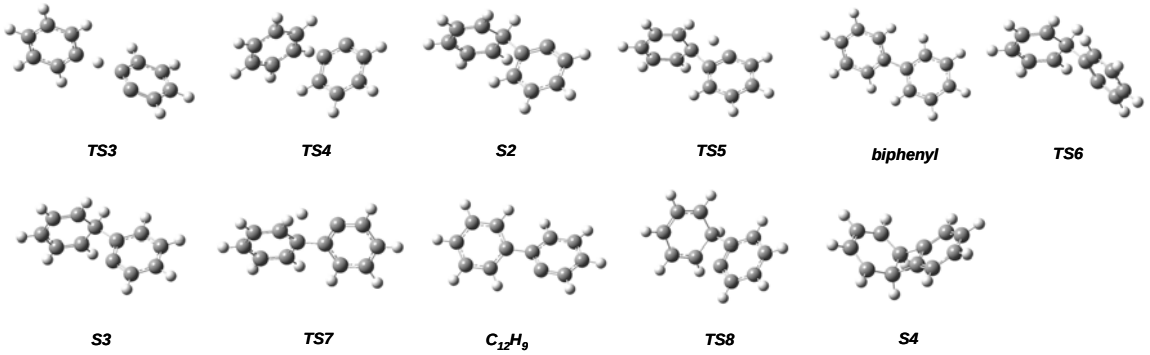


**Figure 62. Species on the potential energy surface for benzene + triplet o-benzyne radical/π-bond addition. uB3LYP/6-311+G(d,p) optimized structures.**

The second channel proceeds through the formation of a biphenyl-like species (S2) with an entrance barrier of 2.9 kcal/mol. The radical site can abstract the H atom from the second ring forming biphenyl. Nevertheless the barrier for such abstraction reaction is 11.6 kcal/mol higher than the barrier for redissociation back to the reactants, thus this channel is energetically unfavorable. On the other hand S2 can easily isomerize and form S3 through torsional motion around the C-C bond between the two rings. S3 is a biphenyl-like species characterized by several low frequency vibrational modes including the ones corresponding to the relative torsional motion between the two rings and to the bending motion of one ring towards the other. Along the torsional motion, the system can undergo isomerization to form dihydrobiphenylene (S4), reported as the intermediate species between reactants and benzocyclooctatetraene in Figure 57. Once formed, benzocyclooctatetraene can isomerize and lead to the formation of acenaphthylene and acenaphthene as hypothesized by Friedman and Lindow[94] based on their experimental work (Figure 57). Friedman and Lindow also reported the presence of biphenyl-d5 as a product of the reaction between o-benzyne and benzene-d6. The formation of biphenyl-d5 could be explained considering the pathway from S2 and S3 to $C_{12}H_9$ + H. In this case the energy barrier for the dissociation of S2 is 26.9 kcal/mol, while the corresponding barrier for S3 is 26.2 kcal/mol, 5.2 kcal/mol higher than the barrier for the formation of dihydrobiphenylene.

The present study on the triplet potential energy surface provides plausible pathways for the experimentally observed formation of biphenyl, acenaphthylene, and acenaphthene as products of the o-benzyne + benzene reaction. On the other hand a Boltzmann distribution of triplet states with excitation energy of 31.9 kcal/mol as calculated in the present work would lead to a very small population of triplet o-benzynes especially at the temperatures implemented in the experimental work by Friedman and Lindow[94] (690 ºC). Unless a transient nonequilibrium population of triplet state o-benzynes is present, the channels presented in Figure 61 cannot account for the formation of the C12 compounds observed experimentally.

### 3.2.2. Benzene + phenyl

The radical/π-bond addition reaction between benzene and phenyl radical (Figure 63 and Figure 64) involves the doublet electronic state. The entrance barrier has been calculated as 5.1 kcal/mol and the biphenyl-like species S5 is bound by 31.0 kcal/mol. The optimized structures for TS9 and S5 are similar to those obtained by Park et al.[74] since similar optimization methods

were used. On the other hand the relative energy levels of both the transition state and the $C_{12}H_{11}$ complex are different due to the CCSD(T) calculations implemented in the present work. In particular, the relative energy of TS9 lies between the value calculated by Park et al.[74] (7.93 kcal/mol) and the optimal value derived from the experimental work (2.70 kcal/mol). Thus the CCSD(T) calculations improve the accuracy of the entrance barrier, although the calculated barrier is still 2.4 kcal/mol higher than the optimal value. The higher-level calculations also provide a better estimate of the relative energy of the $C_{12}H_{11}$ complex.

We will now focus our attention on the possible reaction pathways to fused ring structures. Two possible channels lead to the formation of bicyclo-like species and both are associated with the low-frequency bending vibrational motion of the biphenyl-like complex S5. The first channel involves both a C-H fission and a hydrogen transfer process to form benzobicyclo[2,2,2]octatriene ($S1^s$). Since the relative energy of the corresponding transition state TS10 is 62.7 kcal/mol, such a path is energetically unfavorable. The second pathway proceeds through ring closure to form a bicyclo-like species (S6) which can subsequently undergo a C-H dissociation process to form $S1^s$. Once again the energies of the saddle points TS11 and TS12 are higher than the redissociation barrier by 12.0 kcal/mol and 25.1 kcal/mol respectively. Thus the only channel energetically available to the system is the path leading to the formation of biphenyl through C-H dissociation (TS13).

The relative energy level of the transition state TS13 lies once again between the calculated value from Park et al. and the optimal value. On the other hand the CCSD(T) calculations over-estimate by 8.7 kcal/mol the energy barrier for the addition reaction between biphenyl and H forming the S5 complex in comparison with the experimental value reported by Park et al.[74]. This discrepancy is not relevant for the purpose of the present study, and no additional analyses were performed.

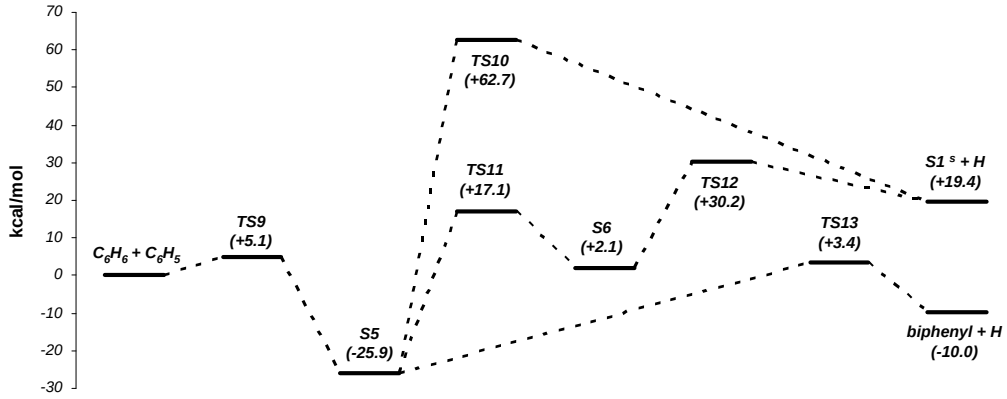


**Figure 63. Potential energy surface for benzene + phenyl radical/π-bond addition. uCCSD(T)/cc-pVDZ relative energies in kcal/mol, including ZPVE.**

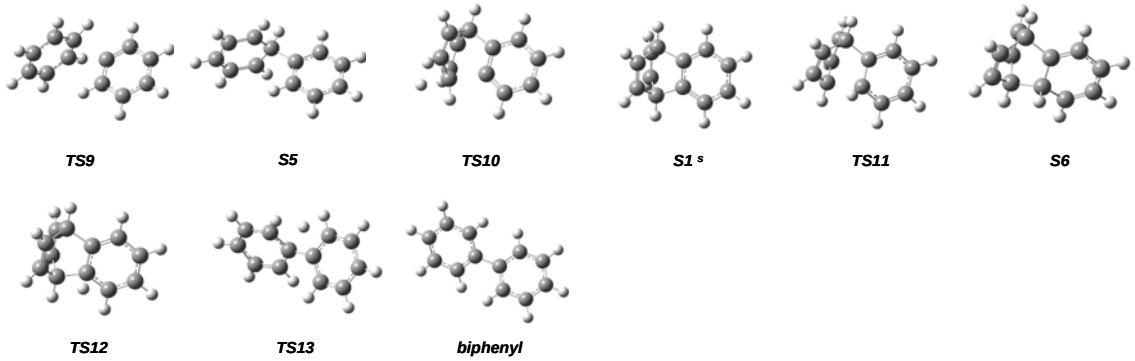


**Figure 64. Species on the potential energy surface for benzene + phenyl radical/π-bond addition. uB3LYP/6-311+G(d,p) optimized structures.**

To conclude, the results reported in the present section are in agreement with both the theoretical work from Park et al.[74] and the absence of any experimental evidence of the presence of fused ring species as products of the benzene + phenyl reaction. As expected, the radical/π-bond addition reaction between phenyl radical and benzene leads to the formation of biphenyl only.

### 3.2.3. Phenyl + phenyl

The radical/π-bond addition reaction between phenyl radicals proceeds along different pathways depending on the carbon atoms involved in the formation of the initial bond between the two aromatic rings (Figure 65). If the two radical sites are involved in the reaction (case 1), the system undergoes rapid reorganization to form biphenyl. In the other cases, the addition reaction produces a $C_{12}H_{11}$ biphenyl-like complex which can subsequently undergo several isomerization reactions. First consider case 2, where the initial bond involves the radical site of one phenyl and the carbon atom opposite to the radical site of the second phenyl radical.

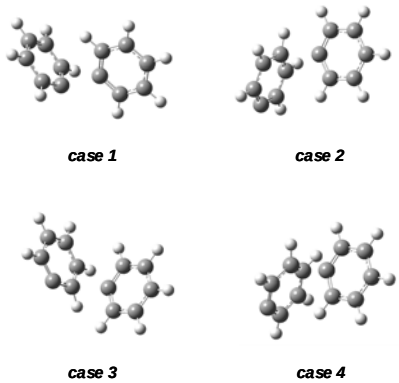


**Figure 65. Radical/π-bond addition reaction between phenyl radicals.**

In order to have a clear picture of the potential energy surface, the three different possible channels have been analyzed separately. All the channels include an initial common elementary

addition step which leads to the formation of the biphenyl-like species. As shown in Figure 66 and Figure 67 (potential energy surface and species for channel 1 of case 2), such an addition step could proceed through either a singlet or a triplet state saddle point ($TS14^s$ and $TS14^t$ respectively). $TS14^t$ is 2.2 kcal/mol more stable than $TS14^s$. Both entrance barriers are higher by around 4 kcal/mol with respect to the corresponding values calculated by Tranter et al.[37]. This discrepancy is mainly due to the different computational methods implemented for the energy calculations. The multi-reference second order perturbation theory (CASPT2) used by Tranter et al.[37] is expected to be more accurate than the single-reference methods such as CCSD(T). On the other hand the computational costs associated with the use of a multi-reference method would not be justified by the scope of the present study.

Due to the lower entrance barrier, the addition reaction will mainly proceed on the triplet surface to form the biphenyl-like species $S7^t$. Associated with the low-frequency bending mode, the system can undergo an isomerization process involving an hydrogen transfer to form spin-triplet benzobicyclo[2,2,2]octatriene ($S1^t$). The barrier for such isomerization on the triplet surface is 47.5 kcal/mol, higher than the barrier for the redissociation process back to the reactants (32.6 kcal/mol). Thus this pathway is energetically unfavorable. On the other hand the same isomerization process on the singlet surface would involve a transition state ($TS15^s$) characterized by a much lower energy. In such a case the calculated isomerization barrier is only 22.8 kcal/mol, 7.3 kcal/mol lower than the barrier for redissociation. Therefore the radical/π-bond addition pathway on the singlet surface leads to the formation of spin-singlet benzobicyclo[2,2,2]octatriene ($S1^s$) which can easily dissociate into naphthalene and acetylene (reaction R2 as marked in Figure 58).

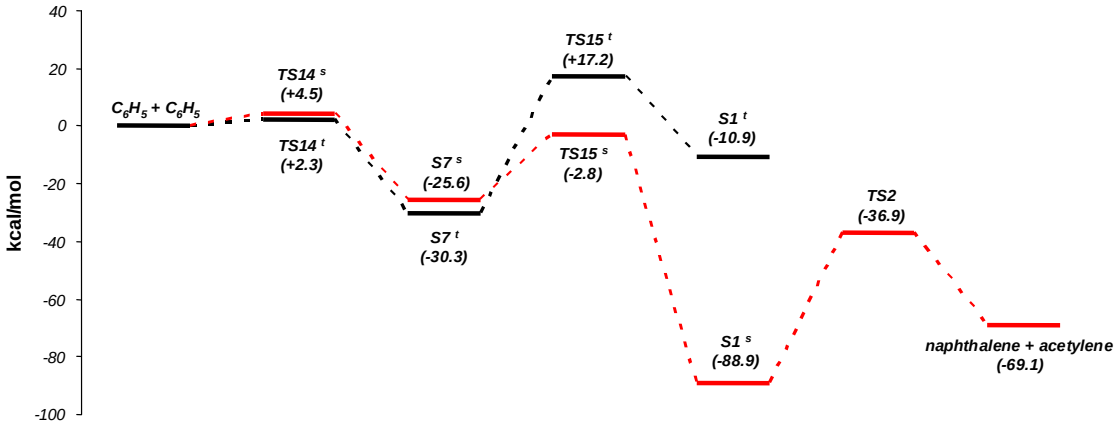


**Figure 66. Potential energy surface for phenyl + phenyl radical/π-bond addition, case 2, channel 1. uCCSD(T)/cc-pVDZ relative energies in kcal/mol, including ZPVE.**

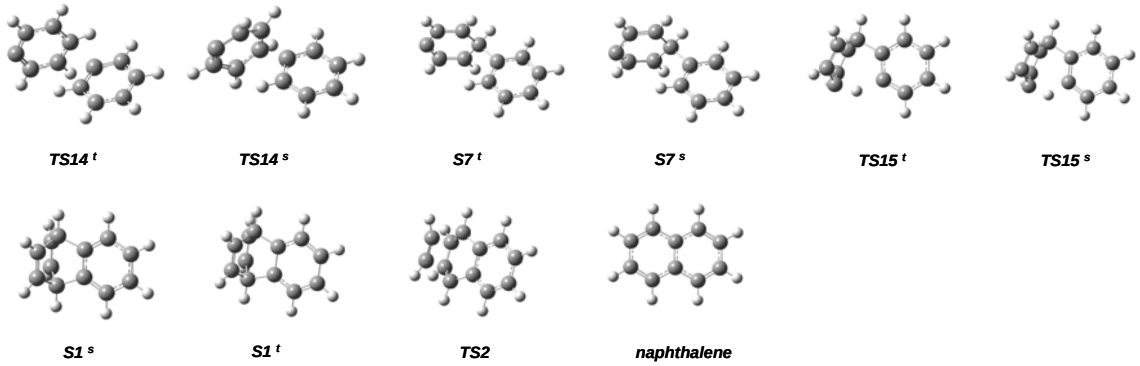


**Figure 67. Species on the potential energy surface for phenyl + phenyl radical/π-bond addition, case 2, channel 1. uB3LYP/6-311+G(d,p) optimized structures.**

Although as mentioned, the singlet pathway is in general energetically unfavorable compared to the triplet one, the accessibility to the singlet pathway is provided by the triplet-to-singlet intersystem crossing, as shown in Figure 66, during the isomerization process from the biphenyl-like species to benzobicyclo[2,2,2]octatriene. Such intersystem crossing forces the system towards the lower energy singlet path to form naphthalene and acetylene. Thus as in the benzene + o-benzyne system, the presence of a bond which involves the π-orbitals allows the system to proceed towards the formation of benzobicyclo[2,2,2]octatriene and the fused-ring naphthalene as a final product.

Other channels for the formation of two-ring fused species have been analyzed for case 2 (Figure 68 and Figure 69, channel 2). In this case $S7^s$ and $S7^t$ undergo ring closure along the low-frequency bending motion without involving the hydrogen transfer process. As for channel 1, the singlet saddle point ($TS16^s$) is more stable than the triplet one ($TS16^t$) and a triplet-to-singlet intersystem crossing, as shown, is possible. The isomerization process leads to the formation of bicyclo-like compounds ($S8^s$ and $S8^t$ for spin-singlet and spin-triplet states respectively). The energy for $S8^s$ has been estimated based on the CCSD(T) energy for $TS16^s$ and the difference between the B3LYP energies for $S8^s$ and $TS16^s$.

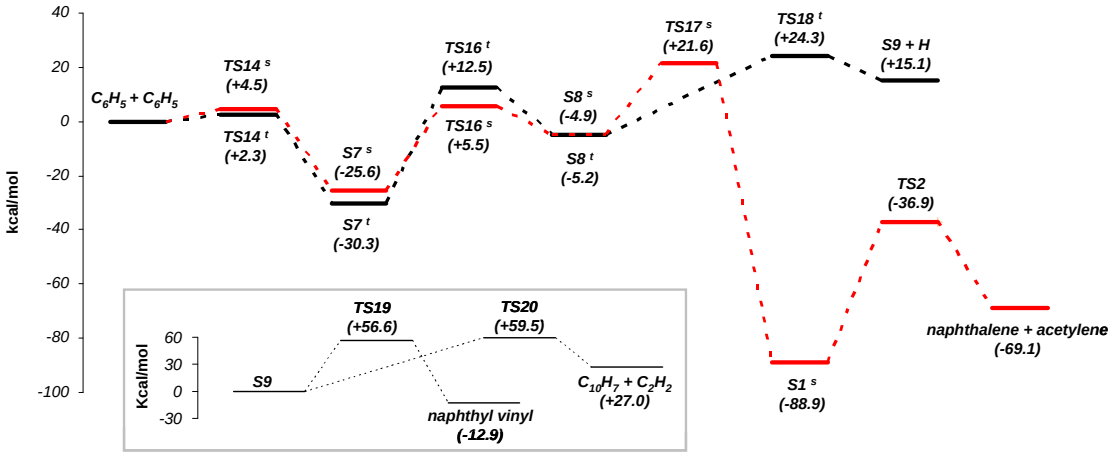


**Figure 68. Potential energy surface for phenyl + phenyl radical/π-bond addition, case 2, channel 2. uCCSD(T)/cc-pVDZ relative energies in kcal/mol, including ZPVE.**

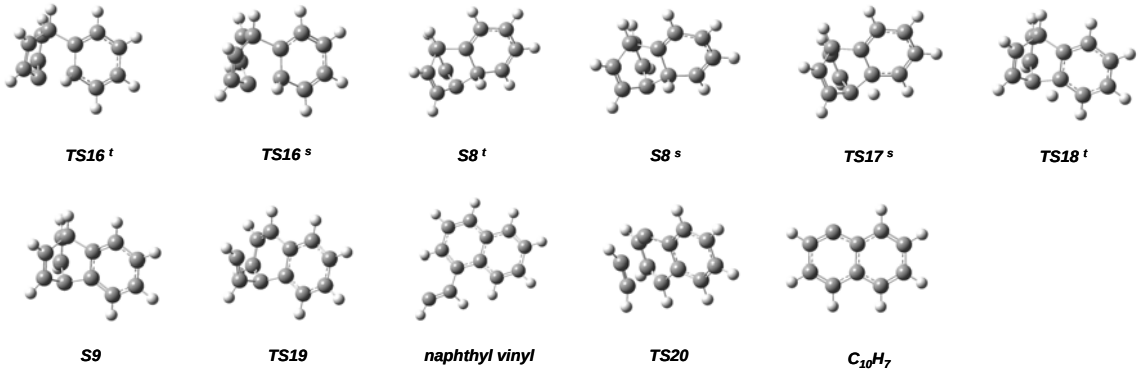


**Figure 69. Species on the potential energy surface for phenyl + phenyl radical/π-bond addition, case 2, channel 2. uB3LYP/6-311+G(d,p) optimized structures. Structures for TS14$^s$, TS14$^t$, S7$^s$, S7$^t$, S1$^s$, TS2, and naphthalene reported in Figure 67.**

Depending on the spin-state, the bicyclo-like compounds undergo different processes. A hydrogen transfer leads to the formation of benzobicyclo[2,2,2]octatriene (S1$^s$) from S8$^s$ (Figure 68). On the other hand S8$^t$ undergoes a C-H dissociation to form one of the possible isomers of the benzobicyclo[2,2,2]octatrienyl radical (S9). Such isomer is not only a possible source for naphthyl radical through fragmentation, but it can also isomerize to form naphthyl vinyl radical. Naphthyl vinyl radical is an important intermediate for the formation of acenaphthylene, as confirmed in previous theoretical and experimental investigations[17,19,77]. The energy barriers as well as the structures involved in the benzobicyclo[2,2,2]octatrienyl isomerization and fragmentation are shown in Figure 68 and Figure 69.

Although leading to the formation of two-ring fused compounds, the channels described in Figure 68 are energetically unfavorable. The lowest energy barrier for isomerization from biphenyl-like species to S8$^s$ and S8$^t$ is 1.0 kcal/mol higher than the redissociation barrier. Moreover S8$^s$ and S8$^t$ lie around 5 kcal/mol below the reactants energy. As a consequence, TS17$^s$ and TS18$^t$ energies are more than 20 kcal/mol higher than the reference energy of the reactants. The system is forced back towards the reactants.

In competition with the channels leading to the formation of bicyclo-like species and subsequently to the two-ring fused aromatic hydrocarbons, channel 3 of case 2 involves hydrogen transfer and/or C-H fission to form biphenyl and biphenyl radical (Figure 70 and Figure 71). Due to the carbene character of the species involved, the singlet channel proceeds through a series of hydrogen transfers to form biphenyl as hypothesized by Tranter et al.[37] The first transfer occurs with a barrier of only 20.9 kcal/mol, around 9 kcal/mol lower than the redissociation barrier. The following steps involve saddle points characterized by even smaller relative energies (TS24$^s$ and TS25$^s$). Thus the singlet path is forced towards the production of biphenyl. Although no transition state for the C-H dissociation was found on the singlet surface, the corresponding barrier is expected to be higher than the H-atom transfer barrier as for the case of benzene[134].

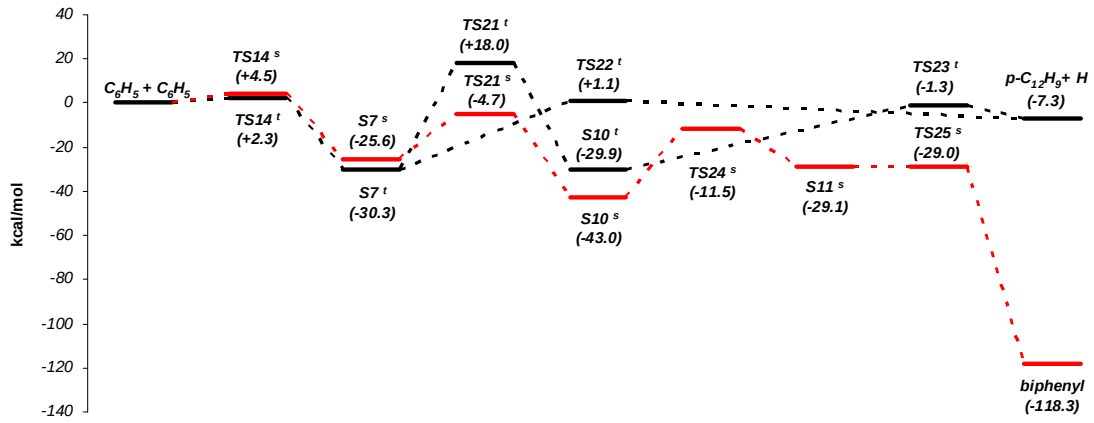


**Figure 70. Potential energy surface for phenyl + phenyl radical/π-bond addition, case 2, channel 3. uCCSD(T)/cc-pVDZ relative energies in kcal/mol, including ZPVE.**

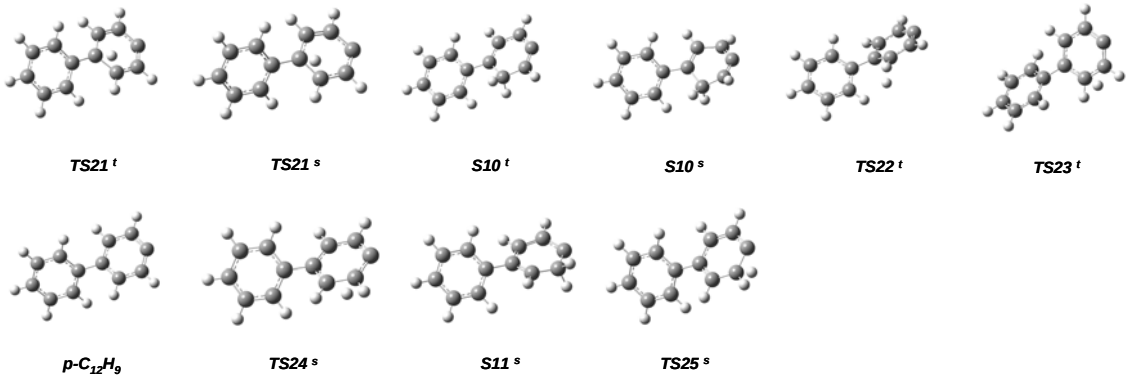


**Figure 71. Species on the potential energy surface for phenyl + phenyl radical/π-bond addition, case 2, channel 3. uB3LYP/6-311+G(d,p) optimized structures. Structures for TS14$^s$, TS14$^t$, S7$^s$, and S7$^t$ reported in Figure 67. Structure for biphenyl reported in Figure 64.**

For the triplet radical/π-bond addition the lowest energy path involves C-H fission through TS22$^t$ to directly form p-$C_{12}H_9$ radical and hydrogen. The barrier for such process is 31.4 kcal/mol, slightly lower than the redissociation barrier (32.6 kcal/mol). In addition to the dissociation reaction, S7$^t$ can undergo a hydrogen transfer to form S10$^t$ complex. However the barrier for such process is much higher than the dissociation barrier. These results are once again in agreement with the hypothesis by Tranter et al.[37]

Considering the fact that the phenyl + phenyl radical/π-bond addition proceeds mainly through the triplet surface, we would expect that channel 3 leads mainly to the formation of p-$C_{12}H_9$. On the other hand the triplet-to-singlet intersystem crossing could increase the importance of the low-energy singlet path towards biphenyl.

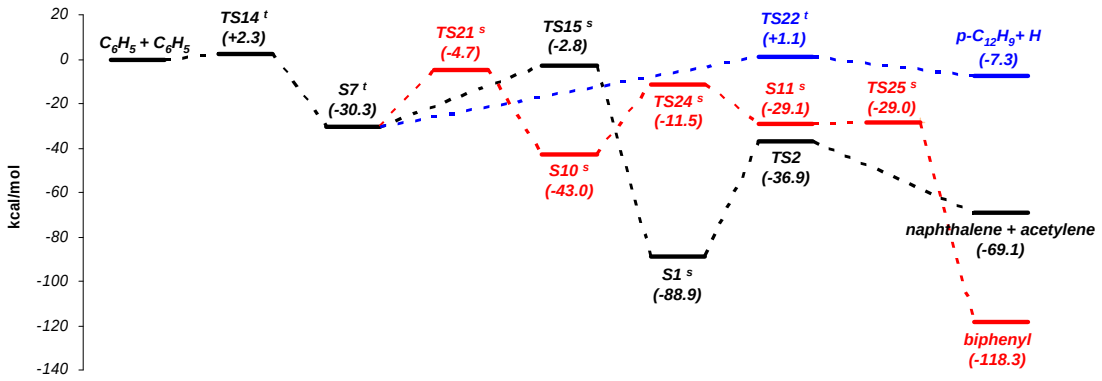


**Figure 72. Potential energy surface for phenyl + phenyl radical/π-bond addition, case 2, most favorable reaction channels. uB3LYP/6-311+G(d,p) optimized structures. uCCSD(T)/cc-pVDZ relative energies in kcal/mol, including ZPVE. Structures reported in Figure 67 and Figure 71.**

To summarize the results reported in Figure 66, Figure 68, and Figure 70, the phenyl + phenyl radical/π-bond addition in case 2 (Figure 65) proceeds towards two main processes, one leading to the formation of naphthalene + acetylene, the other to the formation of biphenyl and biphenyl radical (Figure 72). The relative importance of such competing channels could be determined by calculating the global reaction rate constants and the consequent branching ratio. However this examination would have only a minor impact on the ability to model actual combustion systems because either path shown in Figure 72 will be less favorable than the radical-radical recombination and the hydrogen abstraction channels shown by Tranter et al.[37] In addition, the results reported in Figure 72 require further validations using a more accurate multi-reference method such as the one implemented by Tranter et al.[37] in their recent investigation on the self-reaction of phenyl radicals. Nevertheless, the ab-initio theoretical results presented in this section address an alternative possible pathway leading to the formation of fused PAH compounds starting from a radical/π-bond addition.

In order to complete the detailed analysis of the potential energy surface of the phenyl + phenyl radical/π-bond addition, the present study has been extended to cases 3 and 4 presented in Figure 65. Since the results are very similar, only the calculations for case 3 are reported (Figure 73). Differently than in case 2, no singlet channels could be found. Thus we can assume that the reaction proceeds only on the triplet surface (similar results were obtained by Tranter et al.[37]).

The reaction proceeds similarly to the benzene + phenyl system. The entrance barrier for the formation of the biphenyl-like species is 2.6 kcal/mol, similar to the corresponding barrier observed in case 2. On the other hand the two pathways leading to the formation of bicyclo-like species are not energetically accessible. In fact the corresponding transition states (TS27 and TS28) lie 61.8 kcal/mol and 15.0 kcal/mol higher than the reactants energy level. Thus part of the entrance flux will redissociate back to the reactants, while part will undergo C-H fission or hydrogen transfer process to form biphenyl radical + hydrogen and biphenyl, respectively (pathways not shown).

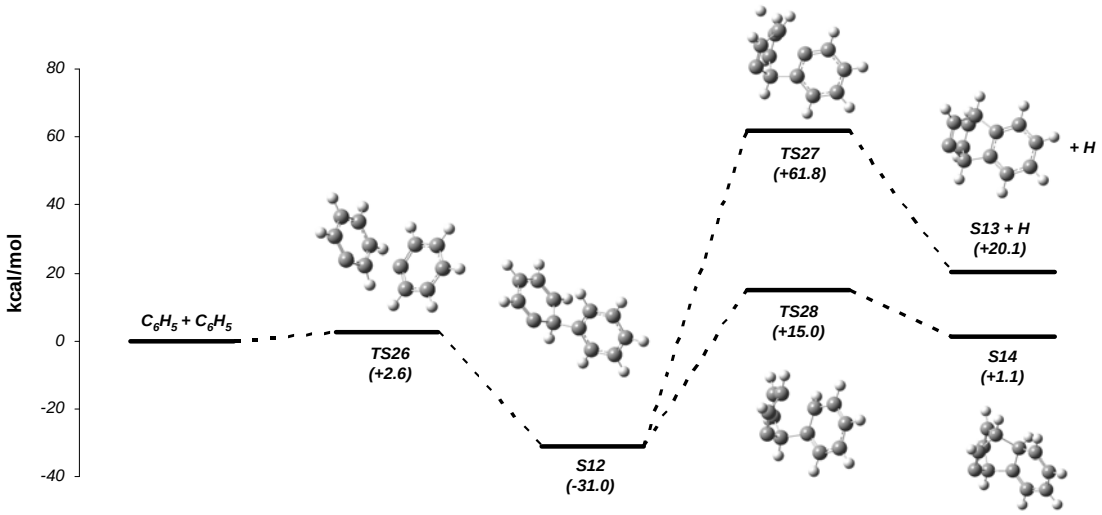


**Figure 73. Potential energy surface for phenyl + phenyl radical/π-bond addition, case 3. uB3LYP/6-311+G(d,p) optimized structures. uCCSD(T)/cc-pVDZ relative energies in kcal/mol, including ZPVE.**

# 4. RADICAL/π-BOND ADDITION BETWEEN o-BENZYNE AND CYCLIC C5 HYDROCARBONS

In chapter 3 we presented the theoretical investigation on the radical/π-bond addition between single-ring aromatic hydrocarbons as possibly relevant to the formation of fused-ring compounds[91]. In particular the potential energy surface for the reaction between o-benzyne and benzene contains a low-energy pathway leading to naphthalene and acetylene through the fragmentation of the bicyclo intermediate. The peculiar chemical structure of the o-benzyne reactant constitutes the key element in the process as it determines its high reactivity through cycloaddition reactions (Diels-Alder additions). The possibility of o-benzyne addition through concerted reactions, such as the Diels-Alder reactions, is of course not limited to the case studied in Ref. [91]. For example, the review article by Bryce and Vernon[117] includes a variety of literature studies on the addition reactions of the o-benzyne radical with single and multi-ring heterocyclic compounds. Not all of these reactions are significant for actual combustion systems as the species flow entering the specific potential energy surface depends on the concentrations of the intermediates involved in the reaction. However, among the major intermediate compounds common to most of the combustion applications are the cyclic C5 hydrocarbons.

Cyclopentadienyl radicals (CPDyl, c-$C_5H_5$) are mainly produced by the rapid decarbonylation of the phenoxy radical ($C_6H_5O$) into c-$C_5H_5$ and CO[135]. The phenoxy radical is an abundant intermediate in oxidation environments deriving from the reaction between the phenyl radical and $O_2$ to form $C_6H_5O$ and atomic oxygen[136]. The pyrolytic reactions involving both the cyclopentadienyl radicals and the corresponding closed-shell cyclopentadiene molecules (CPD, c-$C_5H_6$) have been extensively studied both experimentally and numerically in relation to the formation of various PAH compounds including naphthalene and indene (Ref. [137], [138], [139], and references therein). The reactions between the cyclic C5 hydrocarbons and other intermediate compounds have never been investigated in such detail although some studies have been conducted. In particular, the reaction between cyclopentadiene and o-benzyne was studied experimentally by Wittig and Knauss[140] in the late 1950s but few other investigations are present in literature[141]. The experimental results of Wittig and Knauss, as summarized by Meinwald and Gruber[142], indicate that the addition between o-$C_6H_4$ and CPD occurs only through 1,4-cycloaddition to form the bicyclo intermediate benzonorbornadiene[140] (see Figure 74 for chemical structure). No additional information is available. To the best of our knowledge no studies have ever been performed on the reaction between o-benzyne and the cyclopentadienyl radical.

The purpose of the present investigation is to explore the potential energy surface for the radical/π-bond addition between o-benzyne and the cyclic C5 hydrocarbons, i.e. cyclopentadiene and cyclopentadienyl radical, and test the possibility of low-energy pathways to the typical PAH compounds relevant to the formation of soot. The study will help clarify some aspects related to the chemistry of these important intermediates.

### 4.1. o-Benzyne + Cyclopentadiene

The first potential energy surface investigated in the present work is related to the reaction between spin-singlet o-benzyne radical and cyclopentadiene. The results of the calculations are

reported in Figure 74 while the corresponding transition state molecular structures are shown in Figure 75. In agreement with the experimental results described in the introduction[142] the lowest-energy entrance channel proceeds through 1,4-cycloaddition to form the bicyclo compound S1 (benzonorbornadiene). The entrance barrier is around 2 kcal/mol through the transition state TS1 (see Figure 75 for chemical structure). TS1 does not possess a structural symmetry which is characteristic of the corresponding transition state on the benzyne + benzene reaction studied in Ref. [91] and the structures of the two reactant molecules are almost unaltered when approaching the transition state configuration. This is due to the transition state been reached quite early in the cycloaddition process with a distance of around 2.53 Å between the two carbon atoms which create the first bond between o-$C_6H_4$ and c-$C_5H_6$.

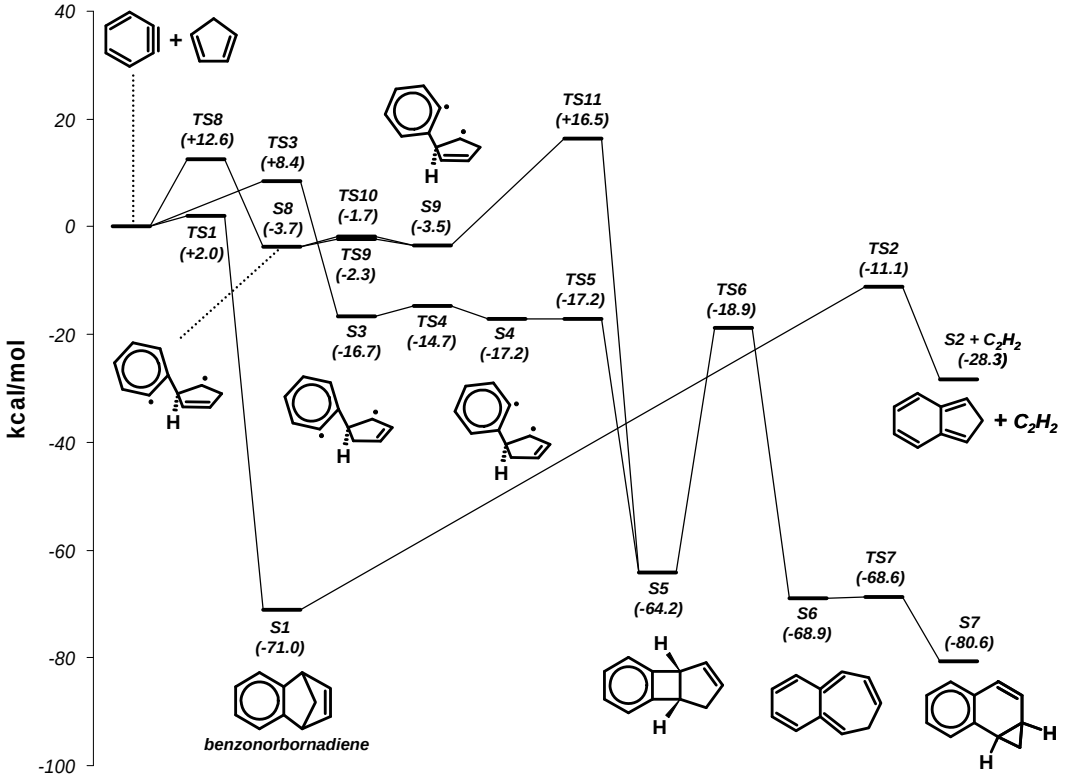


**Figure 74. Potential energy surface for the radical/π-bond addition between o-benzyne and cyclopentadiene. uB3LYP/6-311+G(d,p) relative energies in kcal/mol, including ZPVE.**

Based on the present calculations, the reaction rate constants for the entrance step can be calculated using transition state theory. The calculated values are well fitted by the following modified Arrhenius expression (in $cm^3mol^{-1}s^{-1}$).

$$k\left(o-C_6H_4+c-C_5H_6 \rightarrow S1\right)=37.89\cdot T^{2.996}\exp\left(-499/T\right)$$

The uncertainty in the above expression can be estimated as a factor of 3-4 mainly due to the uncertainty in the reaction barrier. The Arrhenius plot of the calculated reaction rate constant is reported in Figure 76 which also contains the *k* values for the similar 1,4-cycloaddition process between o-benzyne and benzene as calculated in Ref. [91]. The reaction between o-benzyne and cyclopentadiene is clearly faster at low temperatures due to the lower entrance barrier, the difference being around 5 kcal/mol. For temperatures above 1600 K the o-$C_6H_4$ + $C_6H_6$ reaction becomes faster due mainly to the higher multiplicity of the corresponding pathway. More generally, it is worth mentioning that the reaction rate constants for the two 1,4-cycloaddition processes reported in Figure 76 differ by less than a two-fold factor over the entire range between 1000 and 2000 K. This observation not only indicates that the two processes are similar but also suggests that the *k* values reported in Figure 76 could define the typical range for the reaction rate constants of most o-benzyne cycloaddition processes.

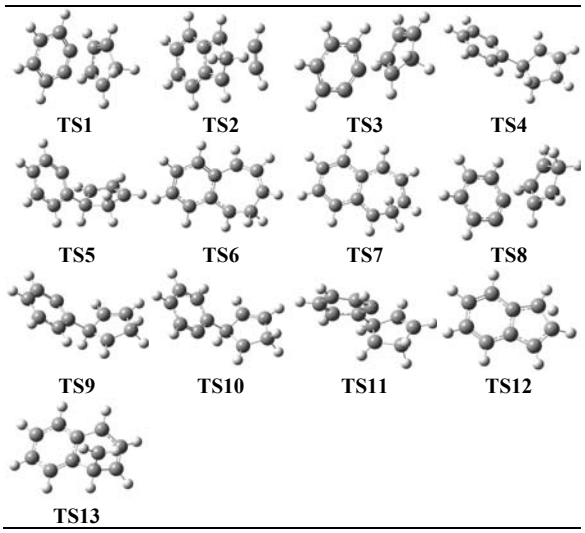


**Figure 75. uB3LYP/6-311+G(d,p) transition state structures for potential energy surfaces in Figure 74, Figure 77, and Figure 79.**

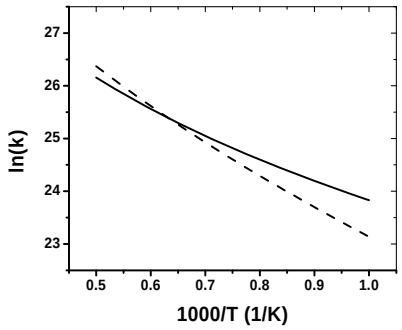


**Figure 76. Arrhenius plot of the calculated 1,4-cycloaddition reaction rate constant between o-benzyne and: —– cyclopentadiene (present work); – – benzene (Ref. [91]).**

Similarly to the reaction between o-benzyne and benzene for which the initial 1,4 adduct undergoes fragmentation to form naphthalene and acetylene, benzonorbornadiene can undergo a

similar process to form the stable S2 adduct and acetylene. S2 is an isomeric form of the more stable indene. As shown in Figure 77 the isomerization process between S2 and indene is very favorable as it proceeds through a reaction barrier of only 16.6 kcal/mol for the hydrogen-transfer process (see Figure 75 for the structure of the transition state TS12). Thus we can conclude that the 1,4-cycloaddition between o-benzyne and cyclopentadiene leads finally to the formation of indene and acetylene.

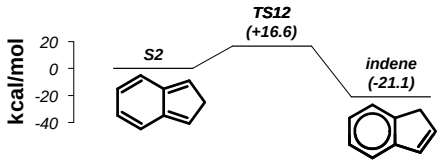


**Figure 77. Potential energy surface for the isomerization of indene. uB3LYP/6-311+G(d,p) relative energies in kcal/mol, including ZPVE.**

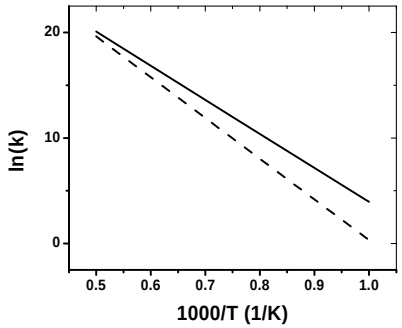


**Figure 78. Arrhenius plot of the calculated reaction rate constant for the fragmentation of benzonorbornadiene into: —— S2 + $C_2H_2$; – – o-$C_6H_4$ + $C_5H_6$.**

Benzonorbornadiene can also undergo fragmentation into the initial reactants, o-benzyne and cyclopentadiene, but the barrier for this process is around 13 kcal/mol higher compared to the fragmentation into S2 and acetylene described above. This difference in the reaction barriers determines the latter process to be the dominant one over the entire temperature range of the present study as indicated in Figure 78 (reaction rate constants calculated using transition state theory). In the high temperature range the difference between the reaction rate constants become smaller due to the higher entropy contribution in the case of formation of o-benzyne and benzene. The Arrhenius fit of the reaction rate constants in Figure 78 are provided below (in $s^{-1}$).

$$k\left(S1 \rightarrow o-C_6H_4 + c-C_5H_6\right) = 7.943 \cdot 10^{16} \cdot \exp\left(-38595.3/T\right)$$
$$k\left(S1 \rightarrow S2 + C_2H_2\right) = 5.272 \cdot 10^{15} \cdot \exp\left(-32268.4/T\right)$$

The radical/π-bond addition between spin-singlet o-benzyne and cyclopentadiene not only proceeds through concerted 1,4-cycloaddition but it can undergo a stepwise reaction to form a stable intermediate characterized by the two rings connected through a single C-C bond and the planes containing the rings positioned almost perpendicularly (S3 and S8 in Figure 74). Similar

stepwise reactions are also present in the potential energy surface for the radical/π-bond addition between singlet o-benzyne + benzene[35,127], triplet o-benzyne + benzene[91], phenyl radical + benzene[74,91], and between phenyl radicals[37,91]. In the specific case of the reaction studied in the present investigation between o-$C_6H_4$ and c-$C_5H_6$ four different carbon atoms are available on the cyclopentadiene molecular structure for the formation of the primary C-C bond with the o-benzyne radical site. Nevertheless the symmetry of the c-$C_5H_6$ molecule reduces the problem to only two different cases which will be discussed in the following paragraphs.

The lower-energy stepwise channel proceeds through the addition between one of the two radical sites in the o-benzyne molecule and the carbon atoms close to the $CH_2$ moiety in the cyclopentadiene molecule. The corresponding transition state (TS3 in Figure 75) is characterized by a distance of around 2.00 Å between the two reactant molecules which is relatively small compared to the case of the 1,4-cycloaddition presented above. Due to the smaller distance, the two molecular structures of o-$C_6H_4$ and c-$C_5H_5$ are in this case slightly distorted at the saddle point. Since the reaction barrier is around 6.4 kcal/mol higher compared to the concerted cycloaddition, the stepwise channel leading to the formation of the intermediate S3 is clearly less favorable compared to the concerted process to benzonorbornadiene (S1), in agreement with the experimental results available in literature[140-142]

Once formed, S3 can isomerize to form the S4 complex which has similar molecular structure but different torsional angle between the two rings. The torsional barrier is around 2 kcal/mol through the transition state TS4 (Figure 75). Due to the presence of the $CH_2$ moiety the molecular structure of S4 is characterized by a relatively small distance between the two radical sites present in the molecule. A simple bending motion between the two rings leads to the formation of a second C-C bond between the two radical sites. The bending barrier through TS5 is less than 0.05 kcal/mol thus the process can be considered barrierless based on the uncertainty of the implemented method. The resulting intermediate compound (S5) is bound by around 47 kcal/mol with respect to S4 and can isomerize through a ring expansion process to form S6 (Figure 74). The isomerization barrier through the transition state TS6 to form the ring-expanded intermediate S6 is only 1.7 kcal/mol lower than the barrier for the isomerization of S5 back to S4. On the other hand, once formed, S6 quickly isomerizes to form a new stable intermediate S7 through a barrier of only 0.3 kcal/mol. S7 (1,2-dihydro-1,2-methanonaphthalene) is the most stable compound on the potential energy surface with a relative energy equal to 80.6 kcal/mol thus it is possibly the final product of the stepwise addition process. 1,2-dihydro-1,2-methanonaphthalene is a stable compound which can be easily measured with traditional analytical techniques such as gas chromatography. Experimental studies on the reaction between o-benzyne and cyclopentadiene performed at different pressure and temperature conditions, which complement the results obtained by Wittig and Knauss[140], would clarify the actual role of the stepwise channel by comparing the yield of 1,2-dihydro-1,2-methanonaphthalene (S7) with those of benzonorbornadiene (S1) and indene from the 1,4-cycloaddition process. The latter products can also be measured with traditional analytical techniques.

Before proceedings with the discussion on alternative channels, it is worth mention that no transition state which connects the S4 adduct with benzonorbornadiene could be identified. A similar transition state is part of the potential energy surface for the reaction of the o-benzyne radical with benzene as studied by Shukla et al.[35] On the other hand, due to the $CH_2$ moiety on the cyclopentadiene molecule, the lower-energy o-$C_6H_4$ + c-$C_5H_6$ stepwise channel is forced towards the formation of the stable S5 intermediate as discussed above.

The second stepwise channel on the potential energy surface for the radical/π-bond addition between o-benzyne and cyclopentadiene is the least favorable. In this case the entrance step leads to the formation of a C-C bond between the o-benzyne radical site and one of the two carbon atoms not bonded to the $CH_2$ moiety in the cyclopentadiene molecule. The relative energy of the corresponding transition state (TS8 in Figure 75) is 12.6 kcal/mol while the resulting adduct (S8 in Figure 74) is only bounded by 16.3 kcal/mol. S8 can isomerize through torsional motion to form the intermediate S9. Depending on the direction of the torsional rotation (clockwise or counterclockwise), two different transition states were identified, TS9 and TS10 (Figure 75). The isomerization will occur almost indifferently through TS9 or TS10 since the two corresponding barriers (respectively 1.4 kcal/mol and 2.0 kcal/mol) are indeed very similar. The resulting S9 adduct can subsequently isomerize into S5 through the formation of a second C-C bond across the C6 and C5 rings. On the other hand, the energy barrier through TS11 (Figure 75) is around 4 kcal/mol higher than the dissociation barrier back to the reactants, thus the specific stepwise channel is not favorable.

Further analyses were performed to identify additional channels in particular for the isomerization of the benzonorbornadiene intermediate. In addition to the fragmentation of this intermediate to form the S2 indene-like compound and acetylene, the rupture of the $CH\text{-}CH_2$ bond in the benzonorbornadiene molecule could proceed through the transition state TS13 (see Figure 75 for molecular structure) to the formation of a possible alternative stable intermediate (at the moment unknown). On the other hand, we could not identify any corresponding stable product and the IRC calculation on TS13 does not support the hypothesis that TS13 is a direct transition state between benzonorbornadiene and the S7 adduct as depicted in Figure 79. At this point it is not clear if the transition state TS13 is relevant for the title reaction and consequently if the dashed pathway shown in Figure 79 is actually present on the potential energy surface.

The theoretical results described in this first part of the manuscript indicate that the potential energy surface for the radical/π-bond addition between o-benzyne and cyclopentadiene contains a favorable pathway which leads to the formation of indene and acetylene through the fragmentation of the 1,4-cycloadduct benzonorbornadiene. The practical relevance of this pathway depends definitely on the concentrations of o-benzyne and cyclopentadiene in the specific combustion system. As described in the introductory section, cyclopentadiene is generally an abundant intermediate in oxidative environments since its corresponding radical complex ($c\text{-}C_5H_5$) derives from the fast decarbonylation of the phenoxy radical. On the other hand, o-benzyne is produced mainly by dehydrogenization of the phenyl radical through an energy barrier of around 78 kcal/mol[130]. Abstraction of a hydrogen atom from the phenyl ring could provide additional pathways for the formation of o-benzyne at relatively low-temperatures. For example, the self-reaction between phenyl radicals investigated by Tranter et al.[37] does not proceeds only through recombination but also through hydrogen abstraction to form benzene and benzynes. The typical abundance of the single-ring aromatics could result in relatively high concentrations of the o-benzyne radical and as a consequence in the relevance of the proposed pathway. This hypothesis awaits further modeling and experimental validations.

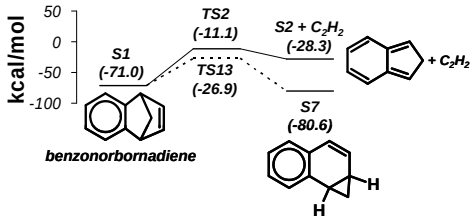


**Figure 79. Possible alternative pathway for the isomerization of benzonorbornadiene. uB3LYP/6-311+G(d,p) relative energies in kcal/mol, including ZPVE.**

## 4.2. o-Benzyne + Cyclopentadienyl Radical

The radical/π-bond addition between the o-benzyne radical and the cyclopentadienyl radical involves the doublet electronic state. Just as for the reaction between benzene and the phenyl radical which occurs on a doublet potential energy surface too[74,91], the o-$C_6H_4$ + c-$C_5H_5$ addition proceeds through a stepwise reaction which leads to the formation of a $C_{11}H_9$ intermediate (S10 in Figure 80). The radical/π-bond addition is almost barrierless since the transition state TS14 (Figure 81) is only 0.1 kcal/mol more stable than the reactants. On the other hand, the imaginary vibrational frequency of TS14 is very small (-12.78 $cm^{-1}$) making it difficult to determine with absolute certainty if such molecule is really a transition state which is present along the stepwise addition process. No concerted transition state could be identified as expected based on similarity with other previously studied reaction spin-doublet and triplet systems[37,74,91].

The S10 adduct can undergo a hydrogen transfer process to form the stable intermediate S12 through a barrier of around 30 kcal/mol (see Figure 81 for the molecular structure of the transition state TS16). Although this barrier is relatively small, it is definitely larger than the barrier for the torsional rotation of the $C_6H_4$ ring forming the complex S11 (Figure 80). More importantly the relative energy of TS16 is higher compared to the barriers for the isomerization of S11, thus the channel leading to the formation of S12 is energetically unfavorable.

The lowest energy and thus most favorable pathway proceeds indeed through the transition state TS17 starting from S11 with a barrier of around 10 kcal/mol (Figure 80 and Figure 81). In this case the coupled rotation and bending motions of the $C_6H_4$ ring towards the C5 ring leads to the formation of a second C-C bond between the radical site in S11 and the carbon close to the primary C-C bond between the two rings. The resulting adduct (S13 in Figure 80) is similar to the intermediate S5 described for the potential energy surface of the stepwise addition between o-benzyne and cyclopentadiene (Figure 74) although in this case S13 is a radical intermediate. On the other hand, the corresponding energy barriers through TS5 and TS17, respectively for S5 and S13, are quite different. Two are the possible reasons for such difference. The first obvious reason is that in the o-$C_6H_4$ + c-$C_5H_6$ reaction the second C-C bond leading to the formation of S5 occurs between two radical sites (Figure 74) while only one radical site is present in S11 (Figure 80). The second possible reason is due to the actual molecular structures of the species involved. We mentioned in the first part of the paper that the molecular structure of the adduct S4 in Figure 74 is strongly influenced by the presence of the $CH_2$ moiety in the C5 ring and how this peculiar feature favors the formation of S5. This is clearly demonstrated by the fact that the corresponding formation process through TS5 is barrierless. In the case of S11 the structure is

symmetric with respect to the $C_6H_4$ ring and the step which leads to S13 requires a consistent distortion of the lowest-energy configuration represented by S11.

The symmetry in the molecular structure which is characteristic of the S11 adduct is also responsible for the presence of an additional transition state which leads to the formation of the bicyclo benzonorbornadienyl radical (S14 in Figure 80). The corresponding reaction barrier through the TS18 transition state (Figure 81) is 22.4 kcal/mol which is 12.6 kcal/mol higher than the barrier for the isomerization of S11 into S13 described in the previous paragraph. Due to the spin-doublet character, benzonorbornadienyl radical does not undergo direct fragmentation but isomerizes to form the indenylvinyl radicals (S15, S16, and S17, Figure 80) through the rupture of a C-C bond on the C5 ring. The three isomers differ only by the torsional angle of the $C_2H_2$ moiety and are connected by low-barrier rotational transition states (TS20, TS21, and TS22 in Figure 81).

Depending on the specific isomer, the indenylvinyl radical undergoes different isomerization processes. As shown in Figure 80, the radical site on the $C_2H_2$ moiety can form an additional C-C bond starting from S15 and S16 to form a variety of stable adducts (S18, S19, S20, and S21). Among these isomerization steps, the lowest-barrier channel leads to the formation of S18 which is also the most stable among the above mentioned adducts. Differently than the other isomers, the S17 indenylvinyl radical can only fragment to form the indenyl radical + acetylene. The corresponding barrier through the transition state TS27 is relatively low (17.6 kcal/mol) but higher than the barrier for the isomerization of S15 into S18. Thus we can conclude that although the potential energy surface for the radical/π-bond addition between o-$C_6H_4$ and CPDyl contains a pathway for the formation of indene, such channel is unfavorable from an energetic point of view.

We previously mentioned that the lowest-energy pathway for the radical/π-bond addition between o-benzyne and cyclopentadienyl radical leads to the formation of the S13 adduct. On the other hand, S13 is definitely not the final product of the title reaction since it can undergo a relatively low-barrier (around 22 kcal/mol) ring expansion isomerization to form S23. The isomerization of the S23 adduct requires higher energies since the corresponding barriers are around 50 kcal/mol or higher.

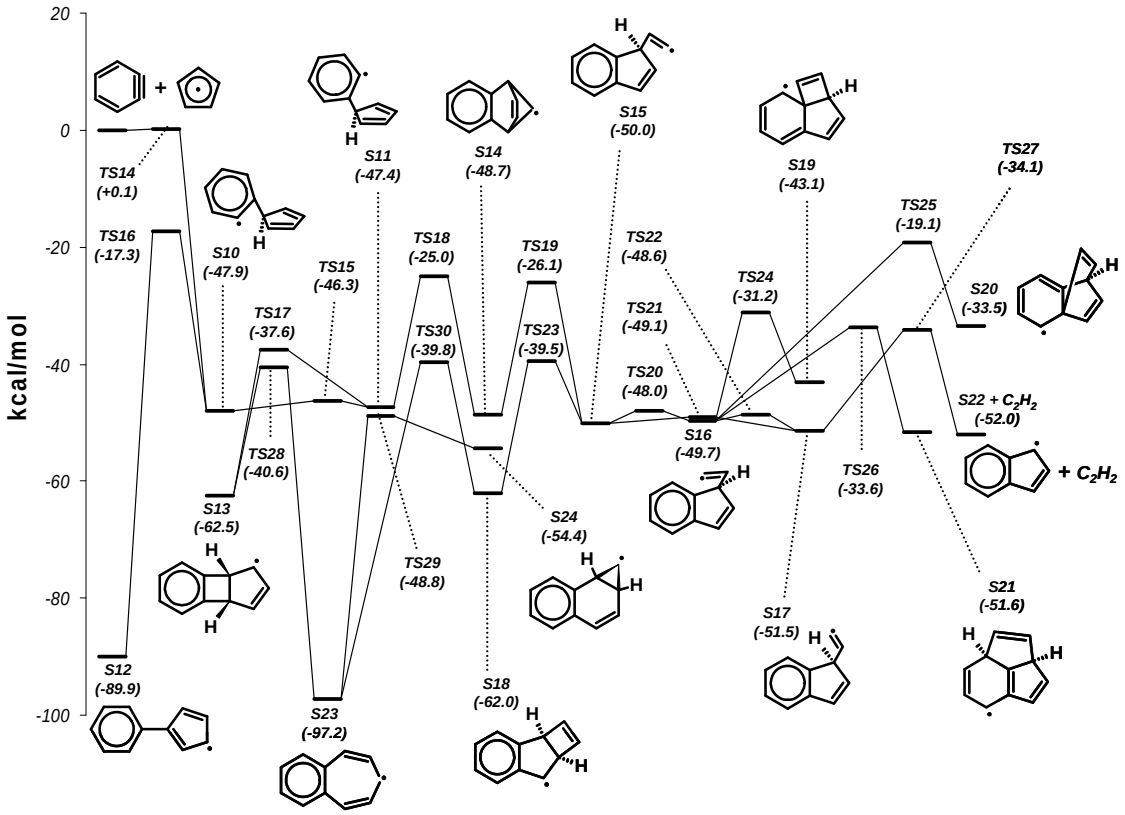


**Figure 80. Potential energy surface for the radical/π-bond addition between o-benzyne and cyclopentadienyl radical. uB3LYP/6-311+G(d,p) relative energies in kcal/mol, including ZPVE.**

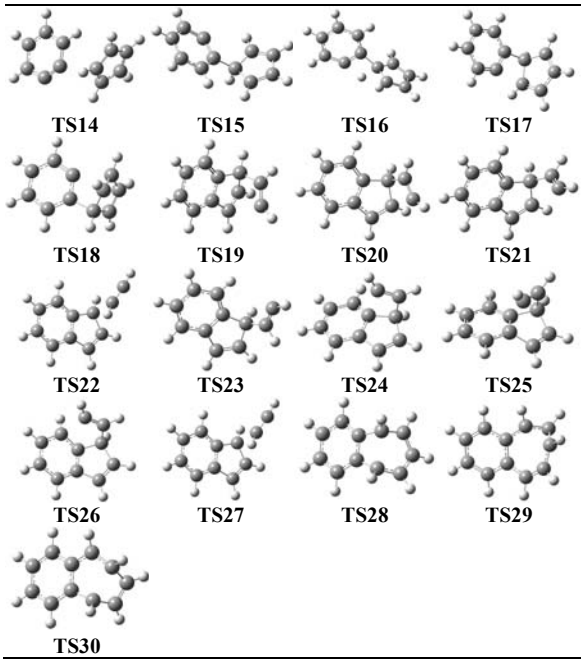


**Figure 81. uB3LYP/6-311+G(d,p) transition state structures for potential energy surfaces in Figure 80.**

The last aspect that we need to take into account on a doublet potential energy surface is the competition between the isomerization steps and the hydrogen-elimination processes which are energetically accessible and lead to the formation of spin-singlet adducts and hydrogen atoms. All the possible spin-singlet intermediates were considered although only the lower-energy elementary steps are summarized in Figure 82. The compound which can most favorably undergo the H-loss process is S21, to form the stable and potentially detectable species, S26, while the reaction of S23, the most stable adduct on the potential energy surface, to form S27 + H involves a barrier of around 85.6 kcal/mol. As shown in Figure 82, the reaction between S27 and H can be considered barrierless based on the corresponding uB3LYP/6-311+G(d,p) energies.

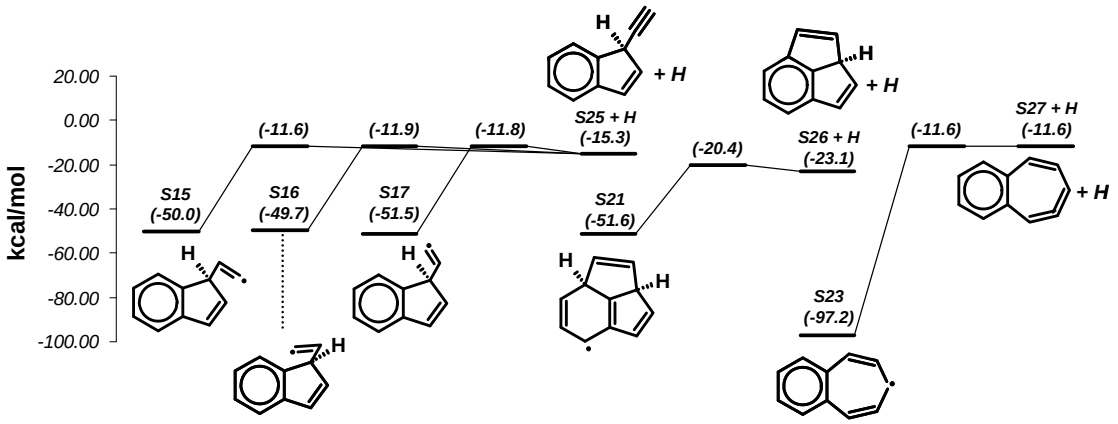


**Figure 82. Lower energy H-loss reactions on the potential energy surface for the radical/π-bond addition between o-benzyne and cyclopentadienyl radical. uB3LYP/6-311+G(d,p) relative energies in kcal/mol, including ZPVE.**

The complexity of the potential energy surface for the radical/π-bond addition between o-benzyne and cyclopentadienyl radical does not allow an immediate identification of the final product of the reaction. From a simple analysis of the pathways in Figure 80, we can hypothesize that at relatively low temperature the ring expanded S23 intermediate could be the major product due to its high stability and low-energy formation pathway. S23 is a radical, similarly to all the products and transition states on the potential energy surface of Figure 80. Thus, once formed, it will presumably react with other radicals present in the combustion system, including hydrogen atoms to form a stable ring-expanded intermediate. At higher temperatures, where S23 can isomerize, the system could proceeds through fragmentation to the formation of indenyl radical. Hydrogen-loss reactions (Figure 82) which could compete at high temperatures involve transition states with higher energies compared to the fragmentation pathway, thus are energetically unfavorable. Similarly to S23, indenyl radical will recombine with other radical in the system, including hydrogen atoms to form indene.

Further theoretical and experimental validations are required to verify these hypotheses. In particular, the use of experimental techniques able to detect and measure radicals, such as the time of flight mass spectrometry, would clarify which among the radicals in Figure 80 are produced by the radical/π-bond addition between o-benzyne and cyclopentadienyl radical or possibly identify the presence of additional pathways which have not been considered in the present work.

# 5. M-XYLENE OXIDATION

## 5.1. Experimental results

m-Xylene oxidation experiments were performed at fuel lean, stoichiometric and fuel rich conditions (Φ = 0.53, 1, 2.35), for a temperature range of 1024-1583 K. Experiments at fuel lean and fuel rich conditions were done at two nominal reflected shock pressures of 25 and 50 atm, where as all the experiments at stoichiometric conditions are at an average pressure of 51 atm. The diaphragm opening process causes minor variations (±20%) in the final pressure; consequently the experiments are referred to as being performed at "nominal" pressures as quoted above. The reaction times for these experiments are in the range of 1.5 ± 0.5 ms (again due to the shock conditions and the nature of shock quenching process). The exact reaction times and pressures are presented in the supplementary information and these have been used in the simulations done in this paper. Experiments were performed using dilute m-xylene mixtures with a maximum mole fraction of 102 ppm. Less than 200 ppm of the fuel was recommended to maintain isothermal conditions in the shock tube[43]. The low mole fractions minimize the temperature drop due to initial endothermic reactions and temperature rise due to later exothermic oxidation reactions, thereby maintaining isothermal conditions over the time range (1.5 – 2.0 ms) of the current experiments. However, to achieve good carbon totals (± 10%), an optimum concentration (100 ppm and lower) of the fuel was used, so that most of the polycyclic aromatic hydrocarbons could be measured and good carbon totals were obtained. Using higher concentration of the fuel would result in greater carbon losses.

### 5.1.1. Effect of pressure on m-xylene decay

The profiles of the fuel are shown as a function of temperature in Figure 83, for two different reflected shock pressures and similar equivalence ratios. Over the pressure and temperature range of the current experiments, no significant pressure dependence was seen for the decay of the fuel, oxidizer and for the formation of the intermediates.

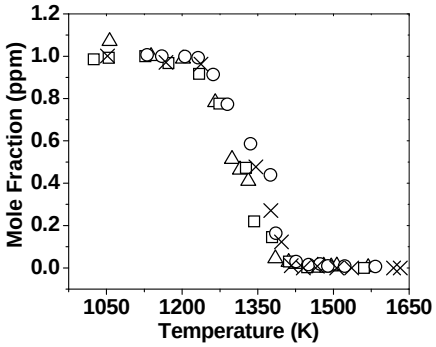


**Figure 83. m-Xylene decay, [Δ]-average P5 = 53 atm, Φ = 0.53, [□]-average P5 = 27 atm, Φ = 0.55, [o]-average P5 = 50 atm, Φ = 2.35, [X]- average P5 = 28 atm, Φ = 2.1, nominal reaction time = 1.5 ms.**

### 5.1.2. Effect of oxygen concentration on the fuel decay

As seen in Figure 83, for similar temperatures a lower amount of m-xylene is consumed at fuel rich conditions when compared to the fuel lean conditions. The species distribution also varied for different equivalence ratios with greater number of polycyclic aromatic hydrocarbons being formed for the experiments at fuel rich conditions when compared to the fuel lean and stoichiometric conditions. The structures of a few of these polycyclic aromatic hydrocarbons and other relevant species mentioned below can be found in Table 11 (T2) and Table 12 (T3). Note: Following the initial mention of species not thought to be of common knowledge a T2 or T3 is placed to provide the reader with a guide to location of the species structure.

| Species | Structure | Species | Structure |
|---|---|---|---|
| 3, 3'-Dimethylbibenzyl ($C_{16}H_{18}$) | 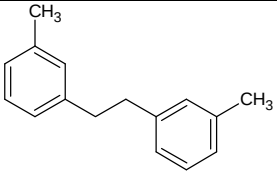 | di-m-Tolylmethane ($C_{15}H_{16}$) | 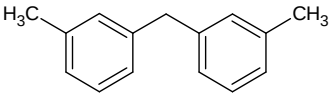 |
| m-Tolyl-p-tolylmethane ($C_{15}H_{16}$) | 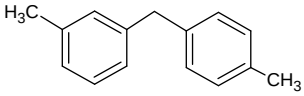 | Indene ($C_9H_8$) | 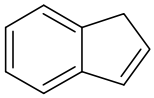 |
| Naphthalene ($C_{10}H_8$) | 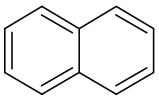 | Fluorene ($C_{13}H_{10}$) | 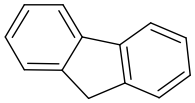 |
| Biphenylene ($C_{12}H_8$) | 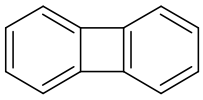 | Pyrene ($C_{16}H_{10}$) | 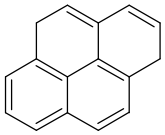 |
| Acenaphthylene ($C_{12}H_8$) | 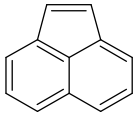 | Anthracene ($C_{14}H_{10}$) | 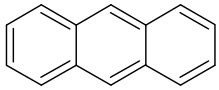 |

**Table 11. Structures of major polycylic aromatic hydrocarbons measured in the m-xylene oxidation experiments.**

| Species | Structure | Species | Structure |
|---|---|---|---|
| m-Xylene ($C_6H_4(CH_3)_2$) | 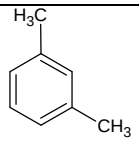 | 3,5-Dimethylphenoxy radical ($OC_6H_3(CH_3)_2$) | 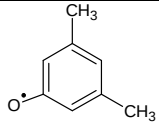 |
| m-Xylyl radical or m-methylbenzyl radical ($CH_3C_6H_4CH_2$) | 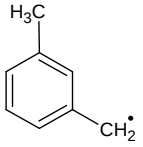 | 1,3-Dimethylcyclopentadiene ($C_5H_4(CH_3)_2$) | 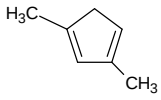 |

| | | | |
|---|---|---|---|
| m-Methylphenyl radical ($C_6H_4CH_3$) | 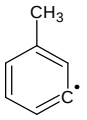 | 1-Methylcyclopentadienyl radical ($C_5H_4CH_3$) | 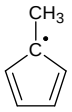 |
| Fulvenallene ($C_7H_6$) | 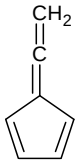 | 3-Methylbenzaldehyde ($CH_3C_6H_4CHO$) | 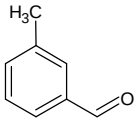 |
| p-Xylylene ($CH_2C_6H_4CH_2$) | 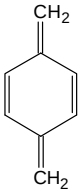 | 1-Ethynylcylcopentadiene ($C_5H_5C_2H$) | 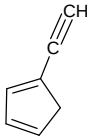 |
| m-Formylphenyl radical ($C_6H_4CHO$) | 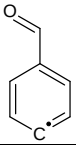 | Formyl cyclopentadiene ($C_5H_5CHO$) | 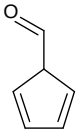 |

**Table 12. Structures of the species, whose reactions are discussed in this publication.**

### *5.1.2.1. Fuel lean oxidation (Φ = 0.53)*

Fuel lean oxidation experiments were performed for a temperature range from 1025 to 1560 K and nominal post reflected shock pressures of 25 and 50 atm.

Apart from the fuel and oxidizer, several other intermediates were also measured, among which the major small hydrocarbon intermediates formed were CO, $CO_2$, benzene ($C_6H_6$), toluene ($C_6H_5CH_3$), 3-methylbenzaldehyde ($CH_3C_6H_4CHO$)T3, methane ($CH_4$), acetylene ($C_2H_2$), and ethene ($C_2H_4$). Small amounts (<3 ppm) of 1-ethyl-3-methylbenzene ($CH_3C_6H_4C_2H_5$), styrene ($C_6H_5C_2H_3$), phenylacetylene ($C_6H_5C_2H$), 1, 3-cyclopentadiene ($C_5H_6$), vinylacetylene ($C_4H_4$), and ethane ($C_2H_6$) and trace amounts of allene ($C_3H_4$), propyne ($C_3H_4$), 1,3-butadiene ($C_4H_6$), 1,3-hexadiene ($C_6H_{10}$), p-xylene ($C_8H_{10}$), 1,3,5-cycloheptatriene ($C_7H_8$), 5-methylcylopentadiene ($C_5H_5CH_3$), benzaldehyde ($C_6H_5CHO$) and 1-ethenyl-4-methyl-benzene ($CH_3C_6H_4C_2H_3$) were also measured.

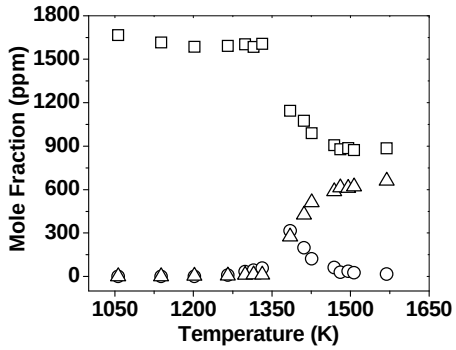


**Figure 84. m-Xylene oxidation species profiles , average P5 = 53 atm, Φ = 0.53, nominal reaction time = 1.5 ms , [□]-$O_2$, [o]-CO, [Δ]-$CO_2$.**

The major species profiles are shown in Figure 84 and Figure 85 as a function of temperature. Above 1350 K, $O_2$ decays rapidly and CO and $CO_2$ start to build up. The aliphatic and aromatic intermediates reach their peak concentrations around 1350 K.

Dimeric species like bibenzyl ($C_{14}H_{14}$), 3,3'-dimethylbibenzyl ($C_{16}H_{18}$)T2, di-m-tolylmethane ($C_{15}H_{16}$)T2 and m-tolyl-p-tolyl-methane ($C_{15}H_{16}$)T2 were also formed from the interactions of benzyl, methylbenzyl (m-xylyl) and methylphenyl radicals. It can be seen from Figure 86 that 3,3'-dimethylbibenzyl and bibenzyl reach their maximum concentrations around 1250 K, which corresponds to the temperature at which almost 25% of the fuel has decayed. This observation suggests since 3,3'-dimethylbibenzyl, for example, is a recombination product of m-xylyl radical, that the fuel decays primarily to m-xylyl radical at temperatures below 1300 K. Above 1300 K the methylphenyl radicals are formed leading to the formation of small amounts of di-m-tolylmethane and m-tolyl-p-tolylmethane.

Other multi-ring aromatic hydrocarbons which were measured include indene ($C_9H_8$)T2, naphthalene ($C_{10}H_8$)T2, fluorene ($C_{13}H_{10}$)T2 and biphenylene ($C_{12}H_8$)T2.

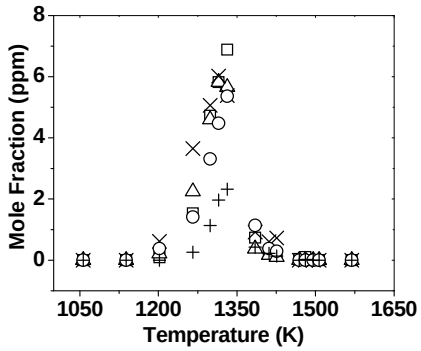


**Figure 85. m-Xylene oxidation species profiles, average P5 = 53 atm, Φ = 0.53, nominal reaction time = 1.5 ms, [□]-Benzene, [Δ]-Toluene, [X]- 3-Methylbenzaldehyde, [o]-Methane, [+]-Ethene.**

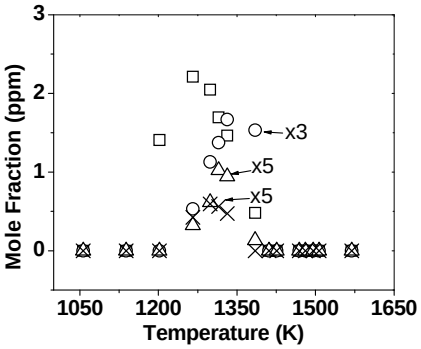


**Figure 86. m-Xylene oxidation species profiles, average P5 = 53 atm, Φ = 0.53, nominal reaction time = 1.5 ms [□]-3,3'-Dimethylbibenzyl, [o]-di-m-Tolylmethane, [Δ]-m-Tolyl-p-tolylmethane, [X]-Bibenzyl2.**

The carbon totals were calculated for this set of experiments and are shown in Figure 87. Almost 95 % of the carbon was recovered for this set of experiments.

Except for the oxygenated species like 3-methylbenzaldehyde and benzaldehyde, all the other aromatic and aliphatic species observed in this set of experiments were also measured in experiments at stoichiometric and fuel rich conditions.

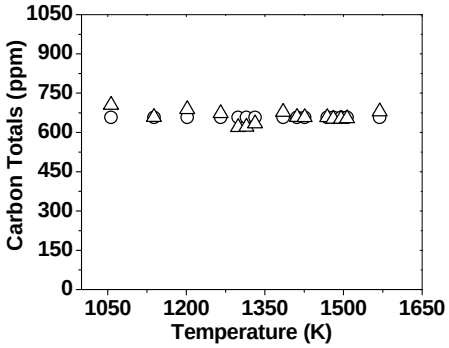


**Figure 87. m-Xylene oxidation carbon totals, average P5 = 53 atm, nominal reaction time = 1.5 ms, Φ = 0.53, [o]-Preshock carbon, [Δ]-Postshock carbon.**

### *5.1.2.2. Stoichiometric oxidation (Φ = 1.2)*

Stoichiometric oxidation experiments were performed for a temperature range from 1079 to 1514 K and an average post reflected shock pressure of 49 atm. New species which were measured in this set were diacetylene ($C_4H_2$), triacetylene ($C_6H_2$), 1-methylindene ($C_{10}H_{10}$), acenaphthylene ($C_{12}H_8$)T2, anthracene ($C_{14}H_{10}$)T2, 2-ethynylnaphthalene ($C_{12}H_8$), 4-methylfluorene ($C_{14}H_{12}$) and diphenylethyne ($C_{14}H_{10}$). The carbon totals for this set of experiments are similar to the ones in Figure 87.

### *5.1.2.3. Fuel rich oxidation (Φ =2.35)*

Fuel rich oxidation experiments were performed for a temperature range from 1079 to 1583 K and an average post reflected shock pressures of 28 and 50 atm at fuel rich conditions

Figure 88 shows the carbon totals as a function of temperature for this set of experiments. More than 95% of carbon is recovered for temperatures up to 1385 K which corresponds to the temperature for which almost 85% of the fuel is consumed. In between 1385 K and 1450 K about 86% of the carbon is recovered. For temperatures below 1385 K maximum mole fractions of the polycyclic aromatic hydrocarbon intermediates were formed, which explains the good carbon balance at these temperatures. Some of these PAH intermediates are shown in Figure 89 and Figure 90. At temperatures in between 1385 and 1450 K these intermediates decay, possibly forming heavier aromatics which were not identified in the present set up. Heavy aromatics up to pyrene ($C_{16}H_{10}$)T2 were measured in the current experiments. It was found to be important to measure even sub-ppm levels of these polycyclic aromatic hydrocarbons so as to attain better carbon recovery. The highest carbon number hydrocarbon measured for these sets of experiments was pyrene ($C_{16}H_{10}$); even 0.5 ppm of measured pyrene will have an 8 carbon count which accounts for 1% loss of carbon.

The pathways involving polyacetylenic species could be important in the decay and formation of polycyclic aromatic hydrocarbons 143. As shown in Figure 91, acetylene and diacetylene start building up around 1335 K and their maximum concentrations are attained at 1450 K, which is the same temperature window within which the maximum carbon loss is

observed. Polyacetylenes up to triacetylene ($C_6H_2$) were identified and quantified in the present experiments.

Most of the carbon was recovered at temperatures above 1450 K since all the carbon is converted to CO and $CO_2$ in the oxidation experiments.

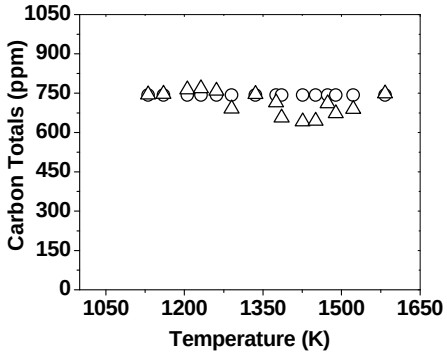


**Figure 88. m-Xylene oxidation carbon totals, average P5 = 50 atm, Φ = 2.35, nominal reaction time = 1.5 ms, [o]-Preshock carbon, [Δ]-Postshock carbon.**

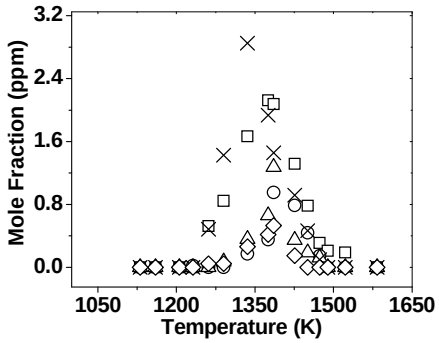


**Figure 89. m-Xylene oxidation species profiles, average P5 = 50 atm, Φ = 2.35, nominal reaction time = 1.5 ms, [□]-Naphthalene, [Δ]-Anthracene, [X]-Indene, [o]-Acenaphthylene, [◊]-Fluorene.**

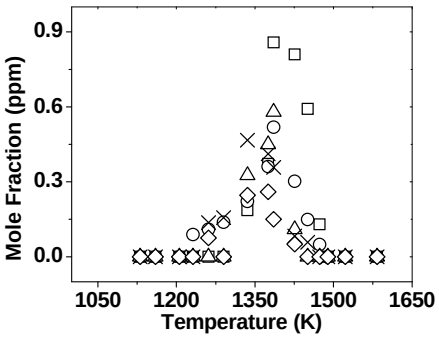


**Figure 90. m-Xylene oxidation species profiles, average P5 = 50 atm, Φ = 2.35, nominal reaction time = 1.5 ms, [□]-1-Methylindene [Δ]-1-Methylnaphthalene, [X]- 1,3,6-Trimethylnaphthalene, [o]-2-Methylanthracene, [◊]-2-Methylphenanthrene.**

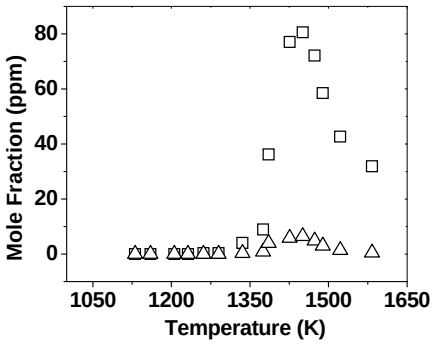


**Figure 91. m-Xylene oxidation, species profiles, average P5 = 50 atm, Φ = 2.35, nominal reaction time = 1.5 ms, [□]- Acetylene, [Δ]-Diacetylene.**

## 5.2.Modeling

As observed from the experiments, the oxidation of m-xylene produced both lower carbon number aromatics and aliphatics and higher carbon number aromatics than the fuel. This work discusses the modeling results up to the formation of the lower carbon number first aromatic ring. Future work is planned in order to include into the model the formation of higher carbon number multi-ring aromatic hydrocarbons from the fuel.

Three chemical kinetic models, the Gail and Dagaut model[28], the Battin-Leclerc et al. model[29], and Narayanaswamy et al. model[144] were initially used to simulate our experimental data. The Battin-Leclerc et al. model had been validated against their shock tube ignition delay experiments of the xylenes, spanning a temperature range from 1300 to 1800 K and pressures from 6.7 to 9 atm. The Gail and Dagaut model was developed to simulate their m-xylene oxidation data in an atmospheric jet stirred reactor. The Narayanaswamy et al. model was validated against the experimental data available in literature and this includes the flow reactor experiments, shock tube ignition delay experiments and laminar burning velocities of m-xylene. Both the CHEMKIN 3.6.2[54] and CHEMKIN 4.1.1[55] suite of programs were used to simulate our experimental data with these models. For the modeling calculations, the exact reaction time, temperature and pressure are specified for each shock along with the initial conditions of the fuel, oxidizer and the diluent. The simulations are performed assuming an adiabatic constant pressure process. As discussed in our previous publication addressing these issues[43], for shock tube experiments with less than 15% endwall pressure increase the adiabatic constant pressure process assumption leads to reasonable accuracy in predicting the stable species profiles. All the pressure profiles considered for these simulations had less than 15% endwall pressure increase. The influence of reactions occurring in the quenching period have insignificant effect on the concentration of the stable species, as discussed in our previous publication[43], hence the quench was not simulated.

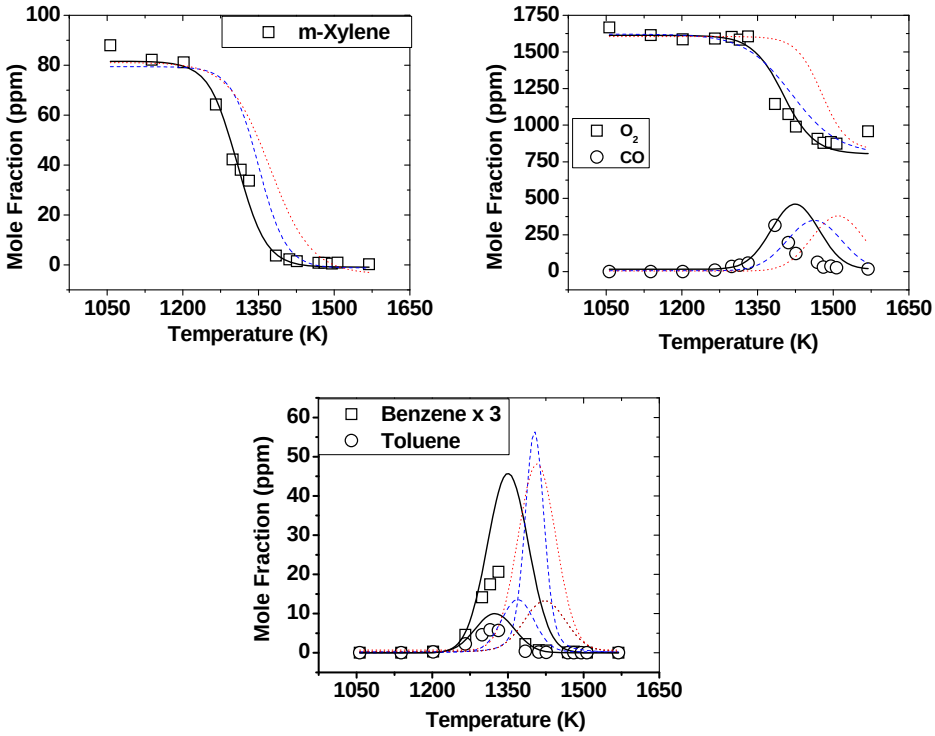


**Figure 92. Comparison of experimental and modeling profiles for m-xylene oxidation, average P5 = 53 atm, Φ = 0.53, nominal reaction time = 1.5 ms, [□]-Experiments, [-]-Battin-Leclerc et al. model [29], […]-Gail and Dagaut model [28], [---]-Narayanaswamy et al. model [144].**

The Battin-Leclerc et al. model provides a better fit to the experimental data than the Gail and Dagaut model and the Narayanaswamy et al. model but all the three of them fail to predict the experimental data accurately. The Gail and Dagaut model and the Narayanaswamy et al. model show lower consumption of the fuel and oxygen and formation of the intermediates. The Battin-Leclerc et al. model shows fairly good consumption of fuel and oxygen but shows displaced profiles for the formation and consumption of the intermediates, like CO, benzene and toluene as seen in Figure 92 and Figure 93. Improved agreement of the Battin-Leclerc et al. model with the experimental data can be achieved by modifying or including the reactions to which the fuel decay and formation of intermediates is sensitive. This model has been built in a hierarchical fashion and consists of their toluene, benzene and $C_0$-$C_5$ oxidation mechanisms. However, as a result of greater familiarity with and confidence in the authors' own high pressure toluene oxidation and pyrolysis models, an independent m-xylene oxidation model has been developed by us based on our previous work.

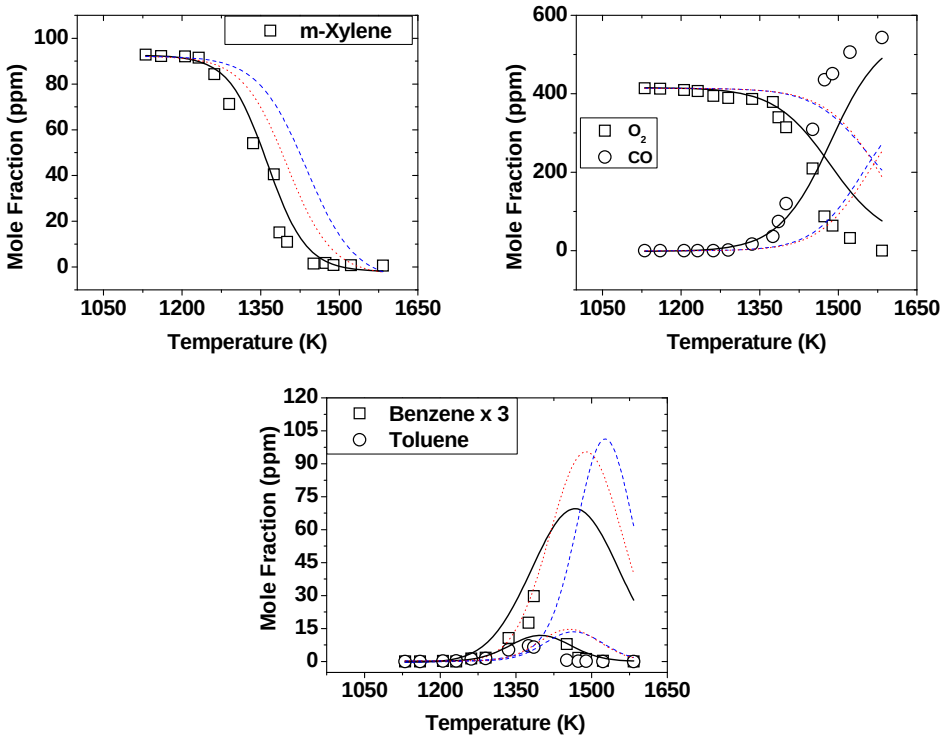


**Figure 93. Comparison of experimental and modeling profiles for m-xylene oxidation, average P5 = 51 atm, Φ = 2.35, nominal reaction time = 1.5 ms, [□]- Experiments, [-]-Battin-Leclerc et al. model [29], […]-Gail and Dagaut model [28], [---]-Narayanaswamy et al. model [144].**

### 5.2.1. The high pressure toluene oxidation model

The high pressure toluene oxidation model[Error! Reference source not found.24] was used as the base model in constructing the m-xylene oxidation model. Hence, it was important to update the rate parameters and include additional pathways as available from the literature. The rate constants for the pyrolytic steps of toluene, $CO/H_2$ oxidation and ethane oxidation were updated from the references[25-26,145,146], all of which have been works from our laboratory. In addition to this, rate constants for a few important reactions were updated based on the suggestions of Vasu et al.[147]. Recent experimental and modeling work have highlighted the dominance of a few pathways in toluene oxidation such as, the decomposition of the benzyl radical[148-149], the benzyl+$O_2$, methylphenyl+$O_2$ and benzyl+$HO_2$ pathways[150-153]. The benzyl radicals decays to form a seven carbon numbered intermediate, which has later been identified by theoretical calculations to be fulvenallene ($C_7H_6$)T3 by both Da Silva et al.[148] and Cavallotti et al.[149], and this further decays to form cyclopentadienyl radical and acetylene. Murakami et al.[154] investigated the potential energy surface for the reaction of benzyl radical with molecular oxygen, using ab initio calculations. Pressure dependent rate constants were calculated for the dissociation reactions of the benzylperoxy radicals, forming benzaldehyde and OH as the major products, along with minor amounts of phenoxy radical and formaldehyde. The addition of molecular oxygen to methyphenyl radicals forms methylphenoxy radical[155] and fulvene, propyne, CO, $CO_2$ and ethenyl radical as products[144]. All of the above reactions and subsequent reactions of fulvene

forming benzene, phenyl[134] and propargyl radicals[144] have been included in the updated toluene oxidation model. The rate constants of the modified reactions and included pathways are shown in Table 13.

| Reaction Number | Reaction[a] | A | n | $E_a$ | Reference |
|---|---|---|---|---|---|
| R1 | $C_6H_5CH_2+C_6H_5CHO=C_6H_5CH_3+C_6H_5CO$ | 2.18E+07 | 2.5 | 46045 | 147 |
| R2 | $C_6H_5CH_3+OH=C_6H_5CH_2+H_2O$ | 1.81E+05 | 2.39 | -602 | 147 |
| R3 | $C_6H_5CH_3+H=C_6H_5CH_2+H_2$ | 6.47E+00 | 3.98 | 3384 | 147 |
| R4 | $C_6H_5CH_3+H=C_6H_6+CH_3$ | 3.90E+08 | 1.25 | 2371 | 147 |
| R5 | $C_6H_4CH_3+O_2=OC_6H_4CH_3+O$ | 8.57E+20 | -2.27 | 7189.29 | 144 |
| R6 | $C_6H_5CH_2+HO_2=>C_6H_5CHO+H+OH$ | 3.67E+13 | 0 | 0 | Estimated |
| R7 | $C_6H_5CH_2+HO_2=>C_6H_5+CH_2O+OH$ | 1.17E+13 | 0 | 0 | Estimated |
| **R8** | **$C_6H_5CH_2=>C_7H_6+H$** | **6.28E+22** | **-2.056** | **93400** | **148** |
| **R9** | **$C_7H_6+H=>C_6H_5CH_2$** | **1.12E-06** | **6.25** | **6040** | **148** |
| **R10** | **$C_6H_5CH_2+O_2=>C_6H_5CH_2OO$** | **1.75E+09** | **-0.02** | **-7700** | **154** |
| **R11** | **$C_6H_5CH_2OO=>C_6H_5CH_2+O_2$** | **6.87E+11** | **0** | **17341** | **154** |
| **R12** | **$C_6H_5CH_2OO=C_6H_5O+CH_2O$** | **1.56E+07** | **0** | **33817** | **154** |
| **R13** | **$C_6H_5CH_2OO=C_6H_5CHO+OH$** | **1.65E+09** | **0** | **29040** | **154** |
| **R14** | **$C_6H_4CH_3+O=OC_6H_4CH_3$** | **1.00E+14** | **0** | **0** | **144** |
| **R15** | **$C_6H_4CH_3+OH=OC_6H_4CH_3+H$** | **3.00E+13** | **0** | **0** | **144** |
| **R16** | **$C_6H_4CH_3+HO_2=OC_6H_4CH_3+OH$** | **3.00E+13** | **0** | **0** | **144** |
| **R17** | **$C_6H_4CH_3+O_2=>C_5H_4CH_2+CO_2+H$** | **2.55E+13** | **-0.44** | **-1649.1** | **144** |
| **R18** | **$C_6H_4CH_3+O_2=>PC_3H_4+C_2H_3+2CO$** | **2.55E+13** | **-0.44** | **-1649.1** | **144** |
| **R19** | **$C_5H_4CH_2=C_6H_6$** | **2.95E+31** | **-4.97** | **175780** | **134** |
| **R20** | **$C_5H_4CH_2=C_6H_5+H$** | **8.51E+24** | **-2.505** | **225187** | **134** |
| **R21** | **$H_2CCCH+H_2CCCH=C_5H_4CH_2$** | **8.25E+46** | **-10.1** | **16959.9** | **144** |

a. $k = AT^n \exp(-Ea/RT)$: rate constant (units: mol, s, $cm^3$, cal).
Bolded reactions denote the reactions added to the model.

**Table 13. Modifications and additions to the High Pressure Toluene Oxidation model referred to as Updated Toluene Oxidation Model 1.**

The benzyl+HO2 chemistry has been accounted for previously in our High Pressure Toluene Oxidation model[24] by the global reactions, R6 and R7, as shown in Table 13. but were adjusted for the current work by being lowered by a factor of 10 when compared to the original High Pressure Toluene Oxidation Model. The updated High Pressure Toluene Oxidation Model consisting of all the changes mentioned in the above paragraphs is referred to as Updated Toluene Oxidation Model 1.

The high pressure toluene oxidation experimental data at $\Phi = 1$ and 543 atm[24] are compared against the original High Pressure Toluene Oxidation Model and the Updated Toluene Oxidation Model 1 in Figure 94. Both the models are also compared against ignition delay data of Vasu et al.[147], in Figure 95. The Updated Toluene Oxidation Model 1 does a fairly good job in predicting the ignition delay times, when compared to the original High Pressure Toluene Oxidation Model.

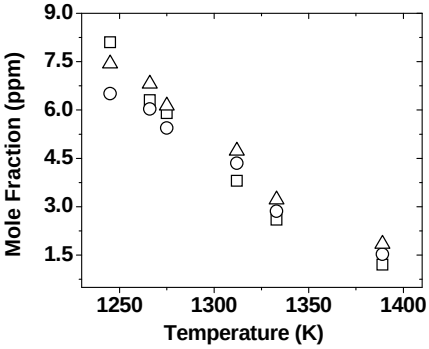


**Figure 94. Comparison of the experimental data and the modeling results for toluene oxidation [24], average P5 = 543 atm, Φ = 1, nominal reaction time = 1.4 ms, [□]- Experiments, [Δ]-High Pressure Toluene Oxidation Model [24], [o]-Updated Toluene Oxidation Model 1.**

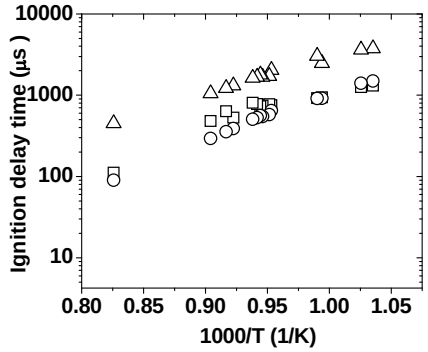


**Figure 95. Toluene/air, P5 = 50 atm, Φ = 1, comparison of experimental ignition delay data of S.S. Vasu et al. [147] and modeling results, [□]- Experiments, [Δ]-High Pressure Toluene Oxidation Model [24], [o]-Updated Toluene Oxidation Model 1.**

Despite the good prediction abilities of the Updated Toluene Oxidation Model 1, before its inclusion in a xylene model would be warranted, further modification of the global steps, R6 and R7 were necessary in view of recent scientific developments. The global reactions R6 and R7 have now been replaced by an elementary mechanism because of a recent computational study by Da Silva et al.[156-158] on the benzyl+$HO_2$ reaction. These researchers have identified benzoxyl radical and OH to be the major products of the reaction for temperatures greater than 800 K. The formation of benzylhydroperoxide molecules was seen to be dominant at lower temperatures and higher pressures. The decomposition kinetics of benzoxyl radical was also studied by the same group with major product channels identified as benzaldehyde and H, benzene and HCO and phenyl and $CH_2O$, in decreasing order of importance. Benzoxyl radical was identified to be the major product in benzyhydroperoxide decay. The reactions R6 and R7 in the Updated Toluene Oxidation Model 1 were consequently replaced by the elementary steps shown in Table 14. Pressure dependent rate constants were included, as available in the references found in Table 14, for the formation of benzylhydroperoxide and benzoxyl radical and their subsequent reactions. For pressures above 1 atm, the high pressure limit rate constants are considered for the formation of benzylhydroperoxide and benzoxyl radical from benzyl+$HO_2$ reaction and subsequent decay of benzylhydroperoxide to benzoxyl radical. The Updated Toluene Oxidation

Model 1 with reactions R6 and R7 replaced with elementary mechanism shown in Table 14, is now referred to as Updated Toluene Oxidation Model 2.

| Reaction Number | Pressure (atm) | Reaction[a] | A | n | $E_a$ | Reference |
|---|---|---|---|---|---|---|
| R22 | 1 | $C_6H_5CH_2+HO_2=C_6H_5CH_2OOH$ | 3.70E+37 | -16.33 | -67470 | 156 |
| R23 | ≥1 | $C_6H_5CH_2+HO_2=C_6H_5CH_2OOH$ | 8.29E+04 | 2.20 | -5130 | 156 |
| R24 | 1 | $C_6H_5CH_2OOH=C_6H_5CH_2O+OH$ | 2.03E+47 | -10.27 | 50710 | 157 |
| R25 | ≥ 1 | $C_6H_5CH_2OOH=C_6H_5CH_2O+OH$ | 3.29E+13 | 0.42 | 39890 | 156 |
| R26 | 1 | $C_6H_5CH_2+HO_2=C_6H_5CH_2O+OH$ | 1.19E+09 | 1.03 | -2250 | 156 |
| R27 | ≥1 (900≤T≤1300 K) | $C_6H_5CH_2+HO_2=C_6H_5CH_2O+OH$ | 1.24E+10 | 0 | -1433 | 156[b] |
| R28 | ≥1 (T<1300 K) | $C_6H_5CH_2+HO_2=C_6H_5CH_2O+OH$ | 3.86E+10 | 0 | 1456 | 156[b] |
| R29 | 1 | $C_6H_5CH_2O=C_6H_5CHO+H$ | 5.26E+28 | -5.081 | 22250 | 158 |
| R30 | 10 | $C_6H_5CH_2O=C_6H_5CHO+H$ | 1.68E+22 | -2.901 | 20760 | 158 |
| R31 | >100 | $C_6H_5CH_2O=C_6H_5CHO+H$ | 5.07E+08 | 1.56 | 16850 | 158 |
| R32 | 1 | $C_6H_5CH_2O=C_6H_5+CH_2O$ | 7.21E+33 | -6.21 | 36850 | 158 |
| R33 | 10 | $C_6H_5CH_2O=C_6H_5+CH_2O$ | 1.32E+27 | -4.009 | 35070 | 158 |
| R34 | >100 | $C_6H_5CH_2O=C_6H_5+CH_2O$ | 1.09E+14 | 0.157 | 31160 | 158 |
| R35 | 1 | $C_6H_5CH_2O=C_6H_6+HCO$ | 2.37E+32 | -6.095 | 28810 | 158 |
| R36 | 10 | $C_6H_5CH_2O=C_6H_6+HCO$ | 3.82E+31 | -5.663 | 29840 | 158 |
| R37 | >100 | $C_6H_5CH_2O=C_6H_6+HCO$ | 1.81E+13 | 0 | 22717 | 158 |

a. $k = AT^n \exp(-Ea/RT)$: rate constant (units: mol, s, $cm^3$, cal).
b. Rate constant estimated utilizing steady state approximation for the benzylhydroperoxide adduct

**Table 14. Reactions R6 and R7 in Updated Toluene Oxidation Model 1 replaced by reactions R22 to R37, now referred to as Updated Toluene Oxidation Model 2.**

The Updated Toluene Oxidation Model 2 is compared against the high pressure oxidation and the ignition delay data in Figure 96 and Figure 97. It can be seen that the model under predicts the toluene consumption and over predicts the ignition delay time. To achieve similar predictions of Updated Toluene Oxidation Model 2 as the Updated Toluene Oxidation Model 1, the rate constant for the formation of benzylhydroperoxide from benzyl+$HO_2$ reaction had to be modified to the value shown in Table 15. The Updated Toluene Oxidation Model 2 with the modified rate constant for the formation of benzylhydroperoxide from the benzyl+$HO_2$ reaction is now referred to a Updated Toluene Oxidation Model 3. The Updated Toluene Oxidation Model 3 shows a closer agreement with the toluene high pressure experimental data and the ignition delay data when compared to the Updated Toluene Oxidation Model 2. To retain the consistency of the original High Pressure Toluene Oxidation Model predictions with the previous high pressure toluene experimental data[26], the Updated Toluene Oxidation Model 3 is considered to be the final version of the revised High Pressure Toluene Oxidation Model and is included in this form in the Xylene oxidation models discussed below.

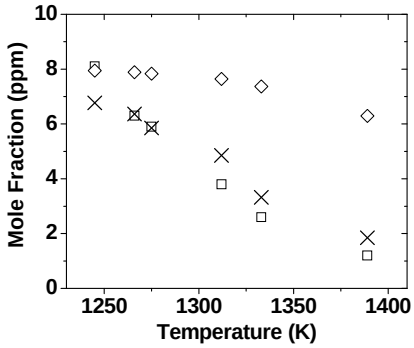


**Figure 96. Comparison of the toluene oxidation experimental data and the modeling results [24], average P5 = 543 atm, Φ = 1, nominal reaction time = 1.4 ms, [□]- Experiments, [◊]- Updated Toluene Oxidation Model 2, [X]-Updated Toluene Oxidation Model 3.**

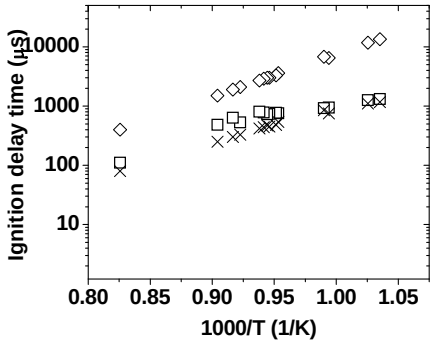


**Figure 97. Toluene/air, P5 = 50 atm, Φ = 1, comparison of the experimental data [147] and the modeling results, [□]- Experiments, [◊]-Updated Toluene Oxidation Model 2, [X]-Updated Toluene Oxidation Model 3.**

| Reaction Number | Pressure (atm) | Reaction[a] | A | n | $E_a$ | Reference |
|---|---|---|---|---|---|---|
| R38 | ≥ 1 | $C_6H_5CH_2+HO_2=C_6H_5CH_2OOH$ | 8.00E+13 | 0.00 | 0 | Estimated |

a. $k = AT^n \exp(-Ea/RT)$: rate constant (units: mol, s, $cm^3$, cal).

**Table 15. Reactions R23 in the Updated Toluene Oxidation Model 2 replaced by reaction R38, now referred to as Updated Toluene Oxidation Model 3.,**

### 5.2.2. The high pressure m-xylene oxidation model

#### *5.2.2.1. The preliminary m-xylene oxidation model (UIC m-xylene oxidation model 1)*

The independent m-xylene oxidation model is built in a hierarchical fashion based on the Updated High Pressure Toluene Oxidation Model 3. The reaction mechanism of m-xylene oxidation was taken from Emdee et al.[27], which was proposed based on the product distribution seen in an atmospheric flow reactor experiments, for a temperature range of 1093-1199 K and an equivalence ratio from 0.4 to 1.7. The oxidation of m-xylene was suggested to take place by

sequential oxidation and removal of the methyl side chains producing, toluene, m-methylbenzyl alcohol, m-tolualdehyde, m-ethyltoluene, m-methylstyrene, methylcyclopentadiene, m-cresol and benzene as intermediates. Due to an absence in the literature of kinetic data for most of the reaction steps, the rate constants for their proposed mechanistic steps were assumed by us to be similar to analogous reactions of toluene[24-26]. The thermochemistry of m-xylene and its oxygenated products was taken from the Gail and Dagaut model. Thermochemistry of dimethylphenoxy radical ($OC_6H_3(CH_3)_2$)T3, dimethylphenol ($HOC_6H_3(CH_3)_2$), methyltolyl (dimethylphenyl) radical ($C_6H_3(CH_3)_2$) and key reaction steps for the formation of methyltolyl were taken from the Battin-Leclerc et al. model.

The m-xylyl+$HO_2$ reactions and their rate constants have been assumed to be analogous to the benzyl+$HO_2$ ones. The m-xylyl+$O_2$ chemistry was included from theoretical study of Murakami et al.[159] on the oxidation of o-, m- and p-xylyl radicals. They proposed pressure dependent rate constants for the formation and decay of o-xylylperoxy radicals ($CH_3C_6H_4CH_2OO$), yielding 2-methylbenzaldehyde ($CH_3C_6H_4CHO$), OH radical and other products. The authors also mentioned that the position of the methyl groups on the aromatic ring had little influence on the heats of reactions and the barrier heights of xylyl+$O_2$ reactions; hence pressure dependent rate expressions for the formation and consumption of m-xylylperoxy radicals were assumed to be same as that of corresponding o-xylylperoxy radical reactions.

Reaction path analyses and sensitivity analyses of the initial assembled model (referred to as Model 1 hereafter), revealed the pathways important to the fuel consumption and formation of the intermediates. The sensitivity analysis of the fuel for 50 atm fuel lean oxidation experiments at a nominal temperature of 1331 K and reaction time of 1.9 ms is shown in Figure 98. Reactions to which m-xylene concentration shows considerable sensitivities have been plotted as a function of the normalized sensitivity coefficient. The fuel decay is sensitive to the formation of m-xylylhydroperoxide, methylbenzaldehyde, m-xylyperoxy radicals, m-xylyl and dimethylphenyl radicals, through the reactions shown in Figure 98. The consumption reactions for m-xylylhydroperoxide and m-xylylperoxy radicals are included in Model 1 and are shown in Table 16. The dimethylphenyl radicals are oxidized to dimethylcresol and dimethylcresoxyl radicals[Error! Reference source not found.]. The dimethylcresoxyl radical reaction mechanism has been assumed to be similar to the reaction mechanism of methylcresoxyl radical. In addition to this, the reaction path analyses of the fuel showed that from $\Phi = 0.53$ to 2.35, most of the fuel decays by hydrogen abstraction reactions forming m-xylyl radicals and the percentage contribution of these reactions increase as the equivalence ratio is increased.

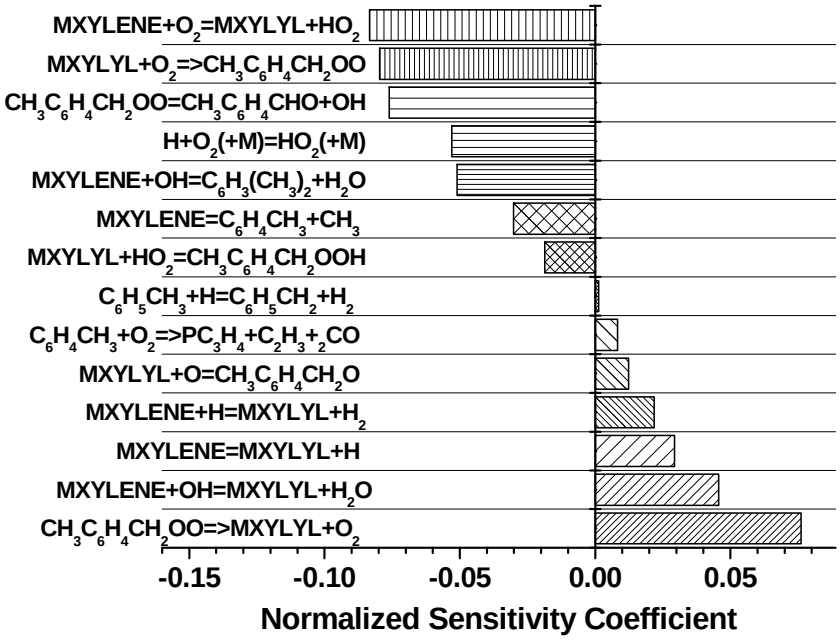


**Figure 98. Sensitivity analysis of m-xylene, P5 = 53 atm, Φ = 0.53, time = 1.9 ms using the UIC m-Xylene Oxidation Model 1.**

| Reaction Number | Reaction[a] | A | n | $E_a$ | Reference |
|---|---|---|---|---|---|
| R39 | $CH_3C_6H_4CH_2+O_2=>CH_3C_6H_4CH_2OO$ | 1.17E+09 | -0.05 | -2414 | 159 |
| R40 | $CH_3C_6H_4CH_2OO=> CH_3C_6H_4CH_2+O_2$ | 1.56E+11 | 0 | 6502 | 159 |
| R41 | $CH_3C_6H_4CH_2OO=CH_3C_6H_4CHO+OH$ | 1.11E+11 | 0 | 9401 | 159 |
| R42 | $CH_3C_6H_4CH_2OO =OC_6H_4CH_3+CH_2O$ | 5.55E+09 | 0 | 17341 | 159 |
| R43 | $CH_3C_6H_4CH_2+HO_2=CH_3C_6H_4CH_2OOH$ | 3.70E+37 | -16.33 | -67470 | 156[b] |
| R44 | $CH_3C_6H_4CH_2OOH=CH_3C_6H_4CH_2O+OH$ | 2.03E+47 | -10.27 | 50710 | 156[b] |
| R45 | $CH_3C_6H_4CH_2+HO_2=CH_3C_6H_4CH_2O+OH$ | 1.19E+09 | 1.03 | -2250 | 157[b] |
| R46 | $CH_3C_6H_4CH_2O=CH_3C_6H_4CHO+H$ | 5.26E+28 | -5.081 | 22250 | 158[b] |
| R47 | $CH_3C_6H_4CH_2O=C_6H_4CH_3+CH_2O$ | 7.21E+33 | -6.21 | 36850 | 158[b] |
| R48 | $CH_3C_6H_4CH_2O=C_6H_5CH_3+HCO$ | 2.37E+32 | -6.095 | 28810 | 158[b] |

a. $k = AT^n \exp(-Ea/RT)$: rate constant (units: mol, s, $cm^3$, cal).

b. Rate constants assumed same as analogous reactions form the benzyl+$HO_2$ mechanism, only the low pressure rate constants are shown in table, detailed reaction mechanism is present in the model.

**Table 16 m-Xylyl+$O_2$ and m-Xylyl+$HO_2$ reactions in UIC m-Xylene Oxidation Model 1.**

The sensitivity analyses and reaction path analyses of the fuel helped us to concentrate on the areas needing further improvement, which were:

(1) The decomposition pathways for cresoxyl radicals

(2) The decomposition pathways for the methylcresoxyl radicals.
(3) The decomposition pathways for the m-xylyl radicals.

#### *5.2.2.2. UIC m-xylene oxidation model 2*

The following sections describe the changes that have been made to UIC m-Xylene Oxidation Model 1 based on the sensitivity analyses and reaction path analyses of the fuel and major intermediates. The UIC m-Xylene Oxidation Model 1 with the added and modified reactions, presented in Table 17 and Table 18 is referred to as the UIC m-Xylene Oxidation Model 2.

| Reaction Number | Reaction[a] | A | n | $E_a$ | Reference |
|---|---|---|---|---|---|
| | *Decomposition of m-Xylyl Radicals* | | | | |
| R49 | $CH_3C_6H_4CH_2=CH_2C_6H_4CH_2+H$ | 3.26E+13 | 0.128 | 70300 | 165 |
| R50 | $CH_3C_6H_4CH_2=C_7H_6+CH_3$ | 4.00E+15 | 0 | 76100 | 165 |
| | *Decomposition of Fulvenallene* | | | | |
| R51 | $C_7H_6+H=>C_6H_5CH_2$ | 1.12E-06 | 6.25 | 6040 | 167 |
| R52 | $C_7H_6+H=>C_5H_5+C_2H_2$ | 8.55E-21 | 10.35 | 12590 | 167 |
| R53 | $C_7H_6+H=>C_5H_5C_2H+H$ | 2.72E-29 | 12.88 | 11510 | 167 |
| R54 | $C_5H_5C_2H+H=>C_5H_5+C_2H_2$ | 4.44E+20 | -1.82 | 14450 | 167 |
| R55 | $C_5H_5+C_2H_2=>C_7H_6+H$ | 1.15E-44 | 17.07 | 22460 | 167 |
| R56 | $C_5H_5C_2H+H=>C_7H_6+H$ | 8.56E-31 | 13.1 | 8670 | 167 |
| R57 | $C_5H_5+C_2H_2=>C_5H_5C_2H+H$ | 7.24E+15 | -0.61 | 34040 | 167 |
| | *Decomposition of p-Xylylene* | | | | |
| R58 | $CH_2C_6H_4CH_2+O=CHOC_6H_4CH_2+H$ | 3.16E+13 | 0 | 0 | **Error! Reference source not found.** |
| R59 | $CHOC_6H_4CH_2+O_2= CHOC_6H_4CHO +OH$ | 6.31E+12 | 0 | 3000 | 169 |
| R60 | $CHOC_6H_4CHO+H=CHOC_6H_4CO+H_2$ | 5.00E+13 | 0 | 4928 | 169 |
| R61 | $CHOC_6H_4CHO+O=CHOC_6H_4CO+OH$ | 9.04E+13 | 0 | 3080 | 169 |
| R62 | $CHOC_6H_4CO+H=CHOC_6H_4CHO$ | 3.00E+13 | 0 | 0 | 169 |
| R63 | $CHOC_6H_4CO=C_6H_4CHO+CO$ | 3.98E+14 | 0 | 29400 | 169 |
| R64 | $C_6H_4CHO+H=C_6H_5CHO$ | 3.98E+15 | 0 | 83701 | 169 |
| R65 | $C_6H_4CHO+O_2=OC_6H_4CHO+O$ | 2.09E+12 | 0 | 7470 | 169 |
| R66 | $CHOC_6H_4CHO+CH_3=CHOC_6H_4CO+CH_4$ | 2.77E+03 | 2.81 | 5773 | 169 |
| R67 | $OC_6H_4CHO=C_5H_4CHO+CO$ | 3.98E+14 | 0 | 29400 | 169 |
| R68 | $C_5H_4CHO=C_5H_5CO$ | 1.00E+12 | 0 | 0 | 169 |
| R69 | $C_5H_5CO=C_5H_5+CO$ | 2.00E+12 | 0 | 0 | 169 |
| | *$OC_6H_4CH_3$→Products* | | | | |
| R70 | $OC_6H_4CH_3=CO+C_5H_4CH_3$ | 2.51E+11 | 0 | 43900 | 160 |
| R71 | $C_5H_4CH_3=C_5H_5CH_2$ | 3.00E+12 | 0 | 50400 | 161 |

| | | | | | |
|---|---|---|---|---|---|
| R72 | $C_5H_4CH_3$=n-$C_6H_7$ | 8.00E+13 | 0 | 50000 | 161 |
| R73 | n-$C_6H_7$=$C_2H_2$+n-$C_4H_5$ | 3.16E+13 | 0 | 43100 | 161 |
| R74 | $C_5H_5CH_2$=c-$C_6H_7$ | 1.40E+13 | 0 | 17400 | 161 |
| R75 | c-$C_6H_7$=$C_6H_6$+H | 7.45E+13 | 0 | 28500 | 161 |
| R76 | c-$C_6H_7$=n-$C_4H_5$+$C_2H_2$ | 2.00E+15 | 0 | 92000 | 161 |
| | *$OC_6H_3(CH_3)_2$→Products* | | | | |
| R77 | $OC_6H_3(CH_3)_2$=CO+$C_5H_3(CH_3)_2$ | 2.51E+11 | 0 | 43900 | 160[b] |
| R78 | $C_5H_3(CH_3)_2$=$C_5H_4CH_3CH_2$ | 6.00E+12 | 0 | 50400 | 161[c] |
| R79 | $C_5H_4CH_3CH_2$=$C_6H_6CH_3$ | 1.40E+13 | 0 | 17400 | Estimated |
| R80 | $CH_3$+$C_6H_6$=>$C_6H_6CH_3$ | 2.60E+03 | 2.84 | 8502 | 163 |
| R81 | $C_6H_6CH_3$=>$CH_3$+$C_6H_6$ | 1.10E+14 | 0 | 22425 | 163 |
| R82 | $C_6H_6CH_3$=>$C_6H_5CH_3$+H | 3.76E+13 | 0 | 27321 | 163 |
| R83 | $C_6H_5CH_3$+H=>$C_6H_6CH_3$ | 1.93E+06 | 2.17 | 4163 | 163 |
| | *m-Xylene+O->Products* | | | | |
| R84 | $C_6H_4(CH_3)_2$+O=$HOC_6H_3(CH_3)_2$ | 1.54E+13 | 0 | 2710 | 169-171[d] |
| R85 | $C_6H_4(CH_3)_2$+O=$C_5H_4(CH_3)_2$+CO | 1.04E+12 | 0 | 2710 | 169-171[d] |
| R86 | $C_6H_6$+O=$C_6H_5OH$ | 5.84E+35 | -5.89 | 34534 | 172 |
| R87 | $C_6H_6$+O=$C_6H_5OH$ | 2.53E+13 | 0 | 6565 | 172 |
| R88 | $C_6H_6$+O=$C_5H_6$+CO | 1.56E+31 | -4.73 | 33568 | 172 |
| R89 | $C_6H_6$+O=$C_5H_6$+CO | 4.83E+03 | 0 | 14929 | 172 |

a. $k = AT^n \exp(-Ea/RT)$: rate constant (units: mol, s, $cm^3$, cal).
b. Rate constants assumed to be same as the analogous reactions of cresoxyl radical
c. Rate constants assumed to be same as the analogous reactions of methylcyclopentadienyl radical
d. Branching ratios for $C_6H_4(CH_3)_2$+O reactions estimated from the analogous reactions of $C_6H_6$+O

**Table 17. Reactions added to UIC m-Xylene Oxidation Model 1.**

| Reaction Number | Reaction[a] | A | n | $E_a$ | Reference |
|---|---|---|---|---|---|
| R89 | $C_6H_4(CH_3)_2$+$O_2$=$CH_3C_6H_4CH_2$+$HO_2$ | 5.23E+07 | 2.5 | 46045 | 173[b] |
| R90 | $C_6H_4(CH_3)_2$+H=$C_6H_5CH_3$+$CH_3$ | 6.47E+00 | 3.98 | 3384 | 147[b] |
| R91 | $C_6H_4(CH_3)_2$+H=$CH_3C_6H_4CH_2$+$H_2$ | 3.90E+08 | 1.25 | 2371 | 147[b] |
| R92 | $C_6H_4(CH_3)_2$+O=$OC_6H_3(CH_3)_2$+H | 1.80E+13 | 0 | 2710 | 169-171[c] |
| R93 | $OC_6H_4CH_3$+H=$HOC_6H_4CH_3$ | 1.00E+14 | 0 | 0 | 174 |
| R94 | $OC_6H_3(CH_3)_2$+H=$HOC_6H_3(CH_3)_2$ | 1.00E+14 | 0 | 0 | 174[b] |
| R95 | $C_6H_6$+O=$C_6H_5O$+H | 3.55E+10 | 0.91 | 6323 | 172 |
| R96 | $C_6H_4(CH_3)_2$+OH=$CH_3C_6H_4CH_2$+$H_2O$ | | 2.39 | -602 | |

| | | |
|---|---|---|
| | 3.62E+05 | 147[b] |

a. $k = AT^n \exp(-Ea/RT)$: rate constant (units: mol, s, $cm^3$, cal).
b. Rate constants estimated from analogous reactions of toluene
c. Branching ratios for $C_6H_4(CH_3)_2$+O reactions estimated from the analogous reactions of $C_6H_6$+O

**Table 18. Reactions whose rate constants were modified in UIC m-Xylene Oxidation Model 1.**

***$OC_6H_4CH_3 \rightarrow$ Products***

The decomposition of cresoxyl radical ($OC_6H_4CH_3$) in UIC m-Xylene Oxidation Model 1 takes place by forming benzene, H and CO in a single step. This reaction has been replaced by a series of reactions, shown as reactions (R70) to (R76) in Table 17. According to this reaction mechanism, the cresoxyl radicals not only produce benzene and CO but also n-$C_4H_5$ and $C_2H_2$ as products.

The decomposition of the phenoxy radical to form CO and cyclopentadienyl radical is the model reaction for the decomposition of cresoxyl radical. The cresoxyl radical decomposes to methyl cyclopentadienyl radical and CO[27]. The rate constant of this step, (R70), was estimated from Emdee et al.[160]

$OC_6H_4CH_3 \leftrightarrow CO + C_5H_4CH_3$ (R70)

Further consumption reactions of methylcyclopentadiene, produce both open chain intermediates (n-$C_4H_5$ and $C_2H_2$) and closed ring compounds ($C_6H_6$), whose rate constants were taken from Lifshitz et al.[161]

***$OC_6H_3(CH_3)_2 \rightarrow$ Products***

The decomposition of dimethylphenoxy radical ($OC_6H_3(CH_3)_2$) in UIC m-Xylene Oxidation Model 1 takes place by forming toluene, H and CO in a single step. This step has been replaced by a series of steps, shown as reactions (R77) to (R83) in Table 17. According to this reaction mechanism, the dimethylphenoxy radicals produce both benzene and toluene as products.

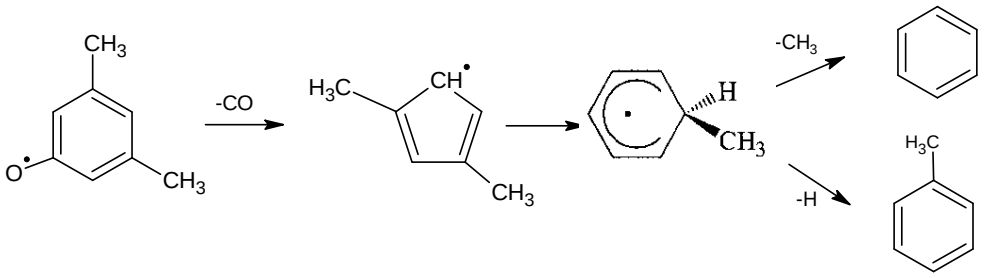


**Figure 99. Reaction mechanism of dimethylphenoxy radical**

This mechanism is similar to the decomposition mechanism proposed by Gregory et al.[162] and is shown in Figure 99. The dimethylphenoxy radical decays to dimethylcyclopentadienyl radical, the rate constant of this reaction was estimated from analogous reaction of phenoxy radical decay to cylcopentadienyl radical[160]. The dimethylcyclopentadienyl radical isomerizes to form a cyclic compound $C_6H_6CH_3$, the rate constant of this reaction was estimated from analogous methylcyclopentadienyl reaction of Lifshitz et al.[161] The rate constants for decay of $C_6H_6CH_3$ to toluene and benzene by fast dehydrogenation and demethylation were taken from the theoretical work of Tokmakov and Lin on the addition of H atoms to toluene and benzene[163].

***Decomposition of m-xylyl radicals***

Emdee et al.[27] suggested two routes for the decay of m-xylyl radicals ($CH_3C_6H_4CH_2$)T3, the oxidation of the methylene side chain and the addition of methyl group to the methylene side chain. These routes have been included in UIC m-Xylene Oxidation Model 1.

Due to the similarities in the chemical structures and decomposition activation energies of m-xylyl and benzyl radicals, later studies hypothesized that these two species decay similarly. Gail and Dagaut[28] hypothesized that the thermal decomposition of m-xylyl radical yields acetylene and methylcylcopentadienyl radical or propargyl radical and 1,3-cyclopentadiene. The rate constants for these two reaction pathways for methylbenzyl radical were assumed to be similar to corresponding reactions of benzyl radical decay forming either cyclopentadiene, acetylene or vinylacetylene, propargyl radical, respectively[164]. Similar reactions have been considered in the Battin-Leclerc et al. model[29] and Narayanaswamy et al. model[144], where m-methylbenzyl decays to form a $C_6H_7$ intermediate and acetylene. In a recent study, Da Silva et al.[165] investigated the kinetics of m-methylbenzyl radicals by high level theoretical calculations and proposed that these radicals decay by forming fulvenallene ($C_7H_6$)T3 and p-xylylene ($CH_2C_6H_4CH_2$)T3 as intermediates at low temperatures. Their estimated rate constant of m-xylyl radical forming p-xylylene+H, was in good agreement with the experimental $C_8H_8$+H measurements of Fernandes et al.[166]. Therefore, these two channels along with their calculated high pressure limit rate parameters were included in the model as taken from Da Silva et al.[165]

The major products of fulvenallene decay were found to be benzyl radical, cyclopentadienyl radical, acetylene and 1-ethynylcylcopentadiene ($C_5H_5C_2H$)T3 by Cavallotti et al.[149] and Da Silva et al.[167]. These steps along with their rate constants were taken from Da Silva et al.[167] and were included in UIC m-Xylene Oxidation Model 1, shown as steps (R51) to (R57) in Table 17. The oxidation of p-xylylene leads, as proposed by Emdee et al.[27], to the formation of p-phthalaldehyde, m-formylphenyl radical ($C_6H_4CHO$)T3, formylcyclopentadiene ($C_5H_4CHO$)T3 and cyclopentadienyl radicals as intermediates. The steps describing these pathways, shown as reactions (R58) to (R69) in Table 17, were included in Model 1 with their rate constants taken from Brezinsky et al.[168] and Dagaut et al.[28]

### 5.2.3. Modeling results and discussion

The UIC m-Xylene Oxidation Model 2 has been validated against a wide range of experimental data. The experimental data can be categorized into high pressure, intermediate pressure and low pressure datasets. The high pressure dataset (40- 50 atm) includes species profiles from our high pressure shock tube m-xylene oxidation experiments and the ignition delay measurements of Shen and Oehlschlaeger[30]. The intermediate pressure range (10 - 25 atm) includes species profiles from our m-xylene oxidation experiments and the ignition delay measurements from Batttin-Leclerc et al.[29] and Shen and Oehlschlaeger[30]. The low pressure datasets (1 atm) include the species profiles measurements of Emdee et al.[27] and Gail and Dagaut[28] in a flow reactor and a jet stirred reactor respectively. The UIC high pressure shock tube m-xylene oxidation experiments complete the species profile spectrum across all pressures and temperatures and play a crucial role in analyzing the fuel behavior over these wide range of experimental conditions.

Ignition delay time measurements were modeled using CHEMKIN 4.1, with an adiabatic constant volume constraint. Maximum slope of the OH concentration traced to the baseline defined the modeling ignition delay time. The plug flow reactor experiments were modeled as isobaric homogenous reactors. The jet stirred reactor experiments were modeled using the PSR code in CHEMKIN 4.1.

#### *5.2.3.1. High pressure experimental datasets*

***Species profiles***

The experimental and modeling profiles for $\Phi$ = 0.53, 1 and 2.35, at nominal reflected shock pressures of 50 atm are shown in Figure 100 through Figure 102. The model shows good agreement with fuel decay for different equivalence ratios. Lower consumption of the $O_2$ and formation of the intermediates is observed for experimental datasets with $\Phi \geq 1$.

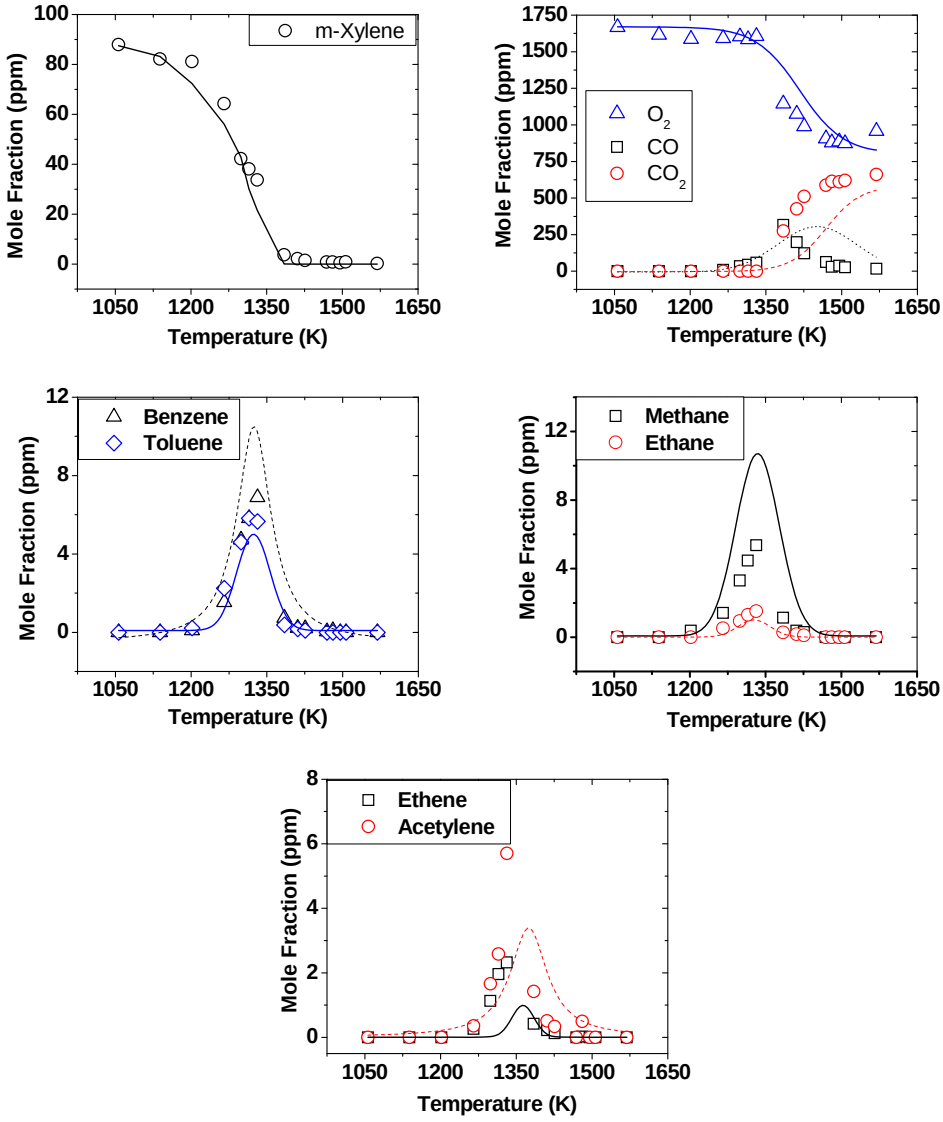

**Figure 100. Comparison of experimental and modeling profiles for m-xylene oxidation, average P5 = 53 atm, Φ = 0.53, nominal reaction time = 1.5 ms, [□]- Experiments, [-]-UIC m-Xylene Model 2.**

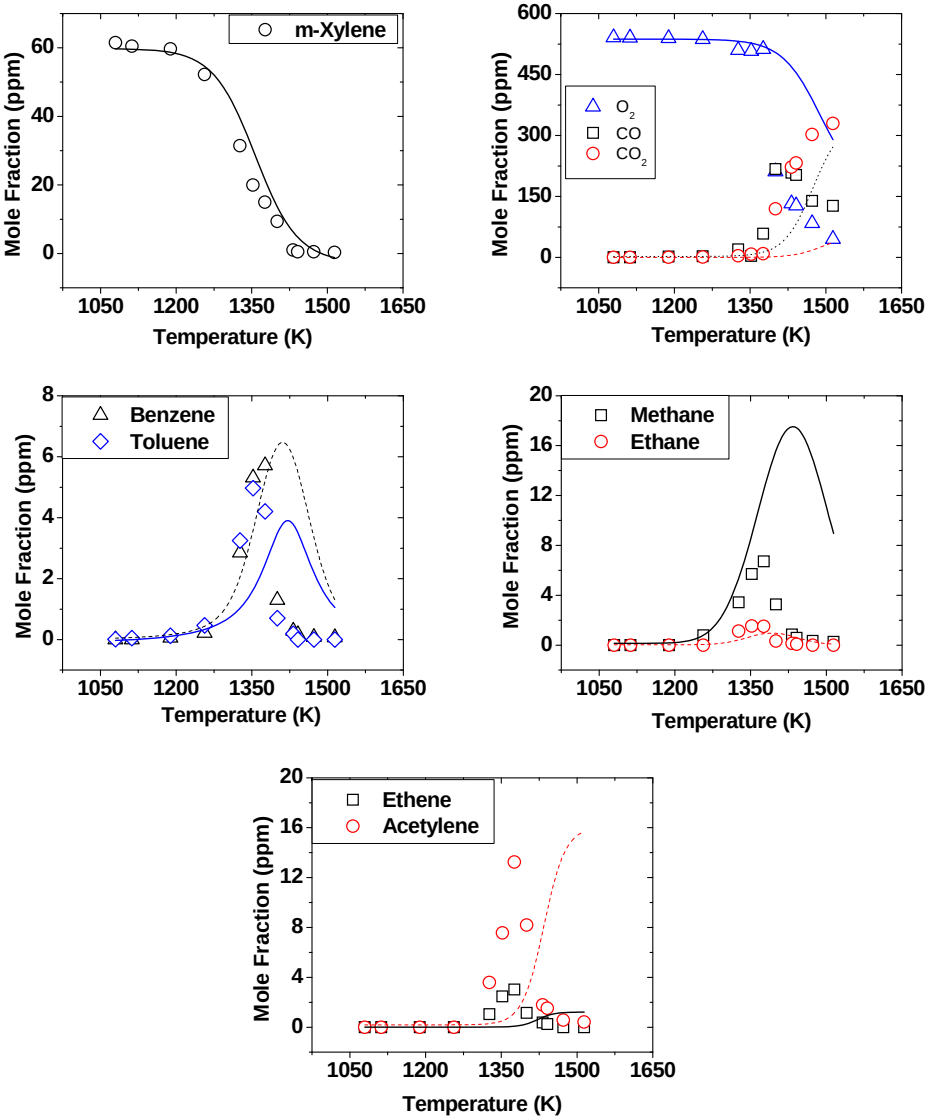


**Figure 101. Comparison of experimental and modeling profiles for m-xylene oxidation, average P5 = 51 atm, Φ = 1.19, nominal reaction time = 1.5 ms, [□]- Experiments, [-]-UIC m-Xylene Model 2.**

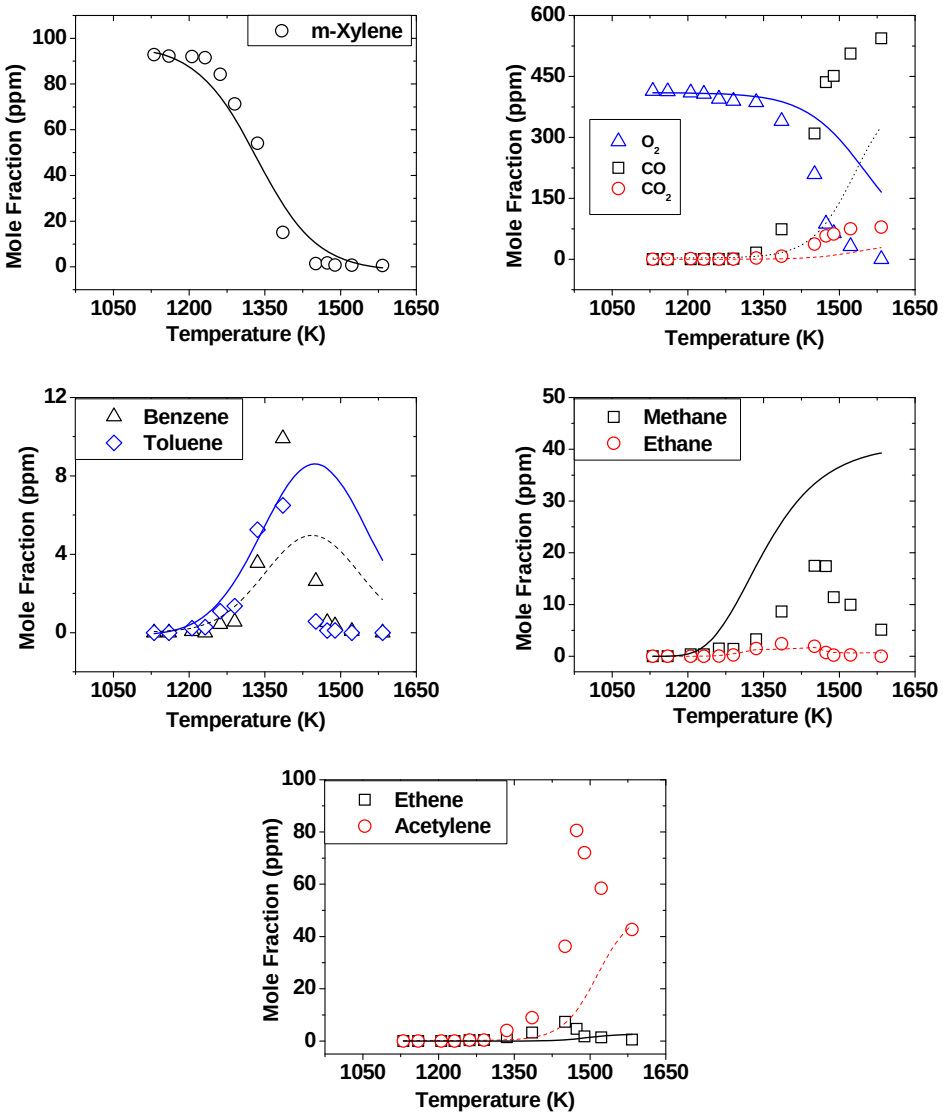


**Figure 102. Comparison of experimental and modeling profiles for m-xylene oxidation, average P5 = 50 atm, Φ = 2.35, P5 = 53 atm, Φ = 0.53, nominal reaction time = 1.5 ms, [□]- Experiments, [-]-UIC m-Xylene Model 2.**

***Ignition delay measurements***

The model has been compared against the ignition delay data of Shen and Oehlschlaeger[30]. These measurements were made at a nominal pressure of 45 atm, for a temperature range from 1023-1269 K and Φ = 0.5 and 1. The model shows excellent agreement with the ignition delay time measurements for the fuel lean data set as shown in Figure 103 (A). It shows fairly good agreement with the experiments for the stoichiometric conditions, Figure 103 (B), with the maximum deviation in the modeling ignition delay times being lower than a factor of 2 at very low temperatures.

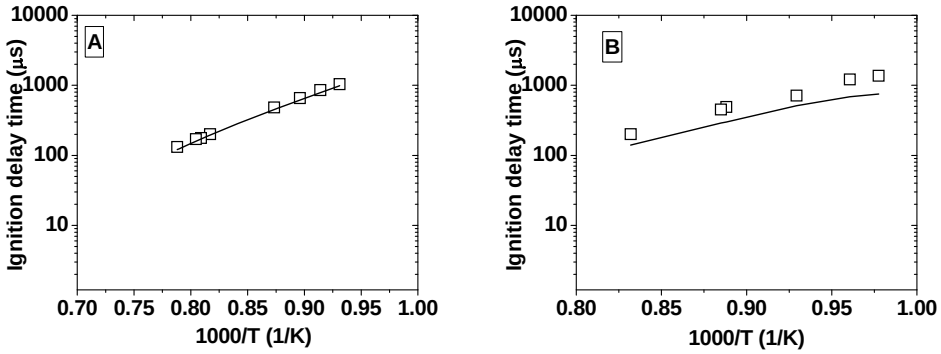


**Figure 103. m-Xylene/air, P = 45 atm, (A) Φ = 0.5, (B) Φ = 1, comparison of experimental ignition delay data of Shen and Oehlschlaeger [30] and modeling results, [□]- Experiments, [-]-UIC m-Xylene Model 2.**

### *5.2.3.2. Intermediate pressure experimental datasets*

***Species profiles***

The experimental and modeling profiles for Φ = 0.5 and 2.1, at nominal reflected shock pressures of 25 atm are shown in Figure 104 and Figure 105. The model shows good agreement with fuel decay for different equivalence ratios. Lower consumption of the $O_2$ and formation of the intermediates is observed for Φ ≥1.

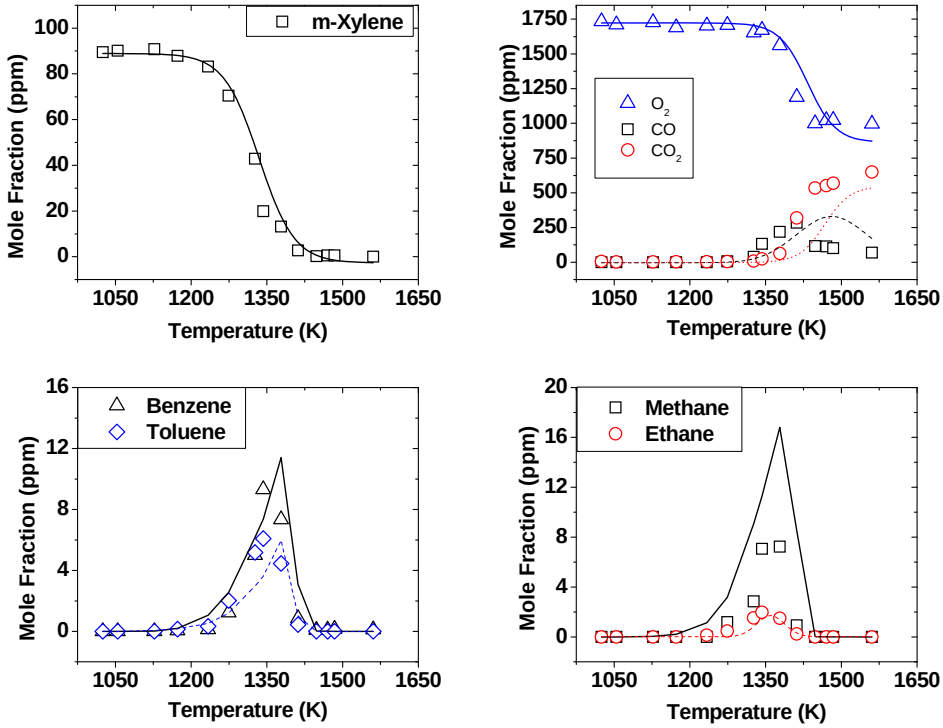

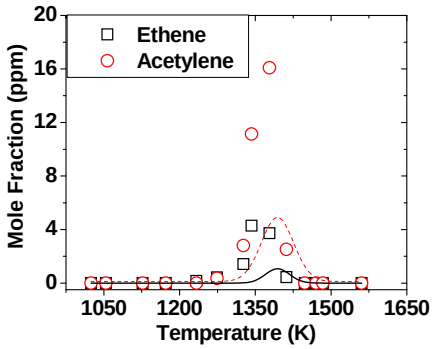


**Figure 104. Comparison of experimental and modeling profiles for m-xylene oxidation, average P5 = 27 atm, Φ = 0.55, nominal reaction time = 1.5 ms, [□]- Experiments, [-]-UIC m-Xylene Model 2.**

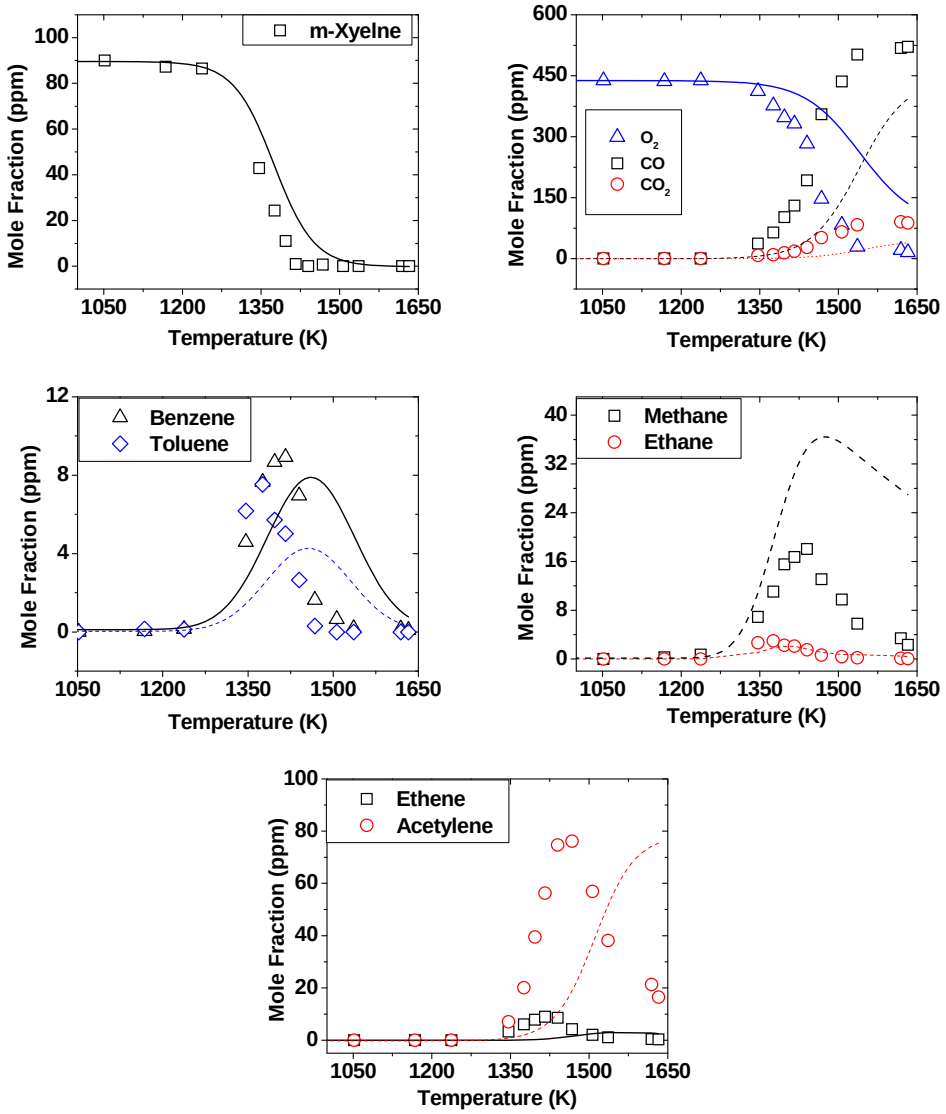

**Figure 105. Comparison of experimental and modeling profiles for m-xylene oxidation, average P5 = 28 atm, Φ = 2.1, nominal reaction time = 1.5 ms, [□]- Experiments, [-]-UIC m-Xylene Model 2.**

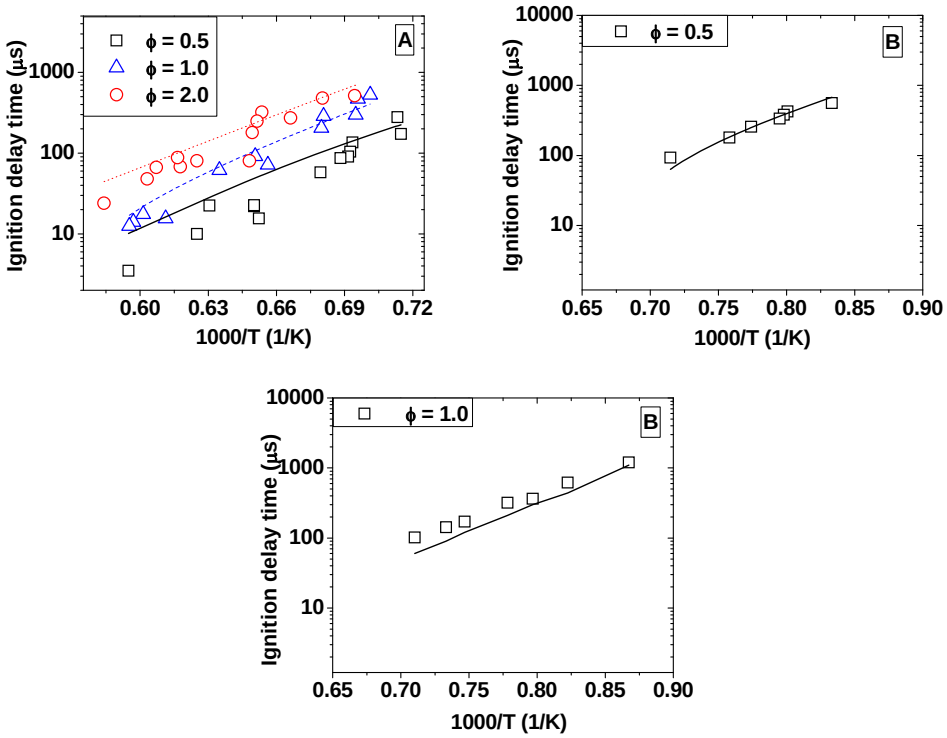


**Figure 106. Comparison of experimental and modeling predictions of the m-xylene ignition delay times, (A) P = 9 atm, Battin-Leclerc et al. [29], (B) P = 9 atm, Shen and Oehlschlaeger [30], [□]- Experiments, [-]-UIC m-Xylene Model 2.**

***Ignition delay measurements***

The model has been compared with the ignition delay measurements of Batttin-Leclerc et al.[29] and Shen and Oehlschlaeger[30]. Ignition measurements by Battin-Leclerc et al. were performed at very high temperature range of 1399 to 1880 K for Φ = 0.5, 1 and 2, for a nominal pressure of 9 atm. Ignition measurements by Shen and Oehlschlaeger[30] were performed for a temperature range of 1153 to 1408 K for a nominal pressure of 10 atm and Φ = 0.5 and 1.

The experimental ignition delay times and the modeling predictions are shown in Figure 106. The model shows excellent agreement with the ignition delay time measurements for the fuel lean data set of Shen and Oehlschlaeger and shows ignition delay times with a maximum deviation by a factor of 3 for temperatures greater than 1590 K for the Battin-Leclerc et al. data sets. For the stoichiometric and fuel rich datasets, the maximum deviation in the modeling ignition delay times are lower by a factor of 2 for both high temperature datasets of Battin-Leclerc et al. and low temperature datasets of Shen and Oehlschlaeger.

### *5.2.3.3. Low pressure datasets*

***Species profiles***

Flow reactor experiments of Emdee et al.[27] were performed for three different equivalence ratios (Φ = 0.5, 1 and 2), an average temperature of 1160 K. The model predictions and the low pressure experimental datasets are shown in Figure 107. For the stoichiometric conditions, the model predicts good profiles for the decay of the fuel, $O_2$ and the formation of intermediates like toluene, benzene, methane, methylstyrene and benzylalcohol. However, it shows twice as much methylbenzaldehyde and much lower amounts of ethyltoluene.

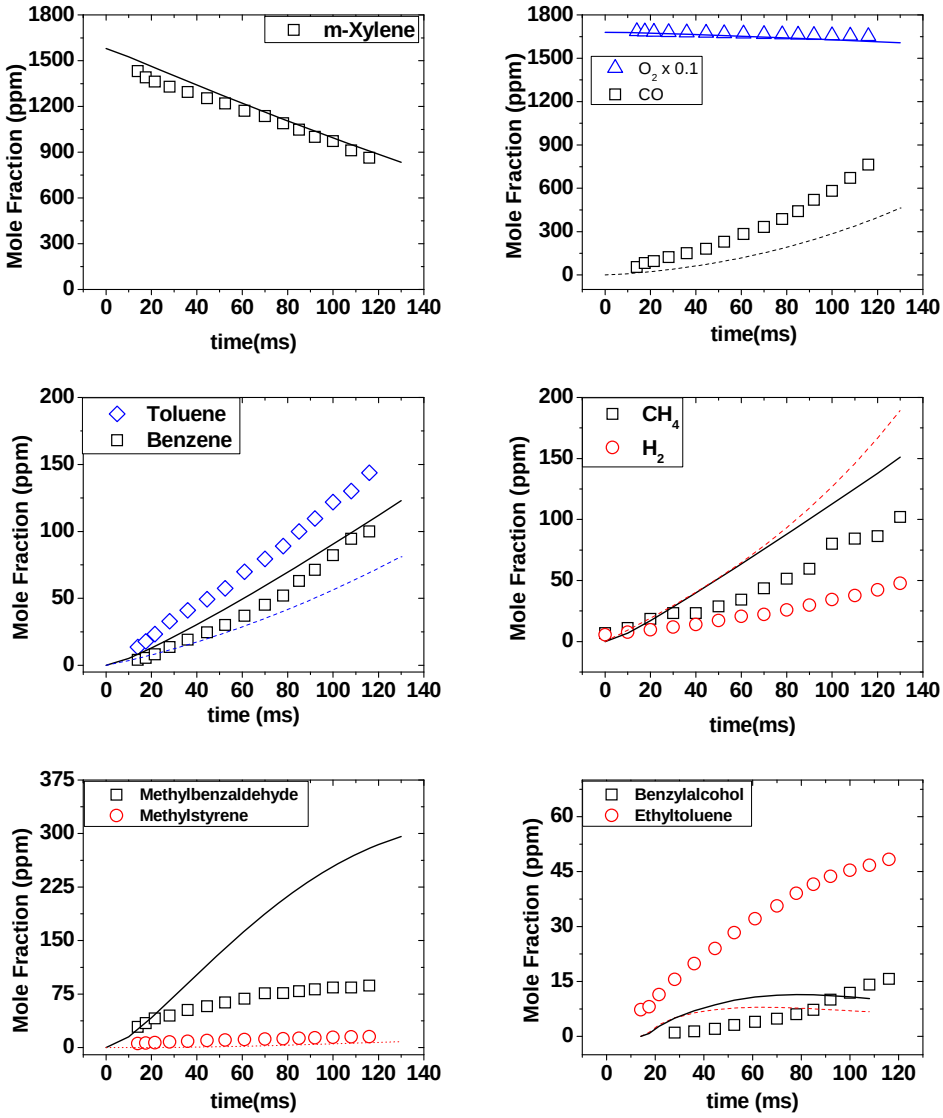


**Figure 107. m-Xylene oxidation flow reactor experiments at atmospheric pressure, Emdee et al. [27] time shift = 10 ms, comparison of experimental and modeling predictions [□]- Experiments, [-]-UIC m-Xylene Model 2**

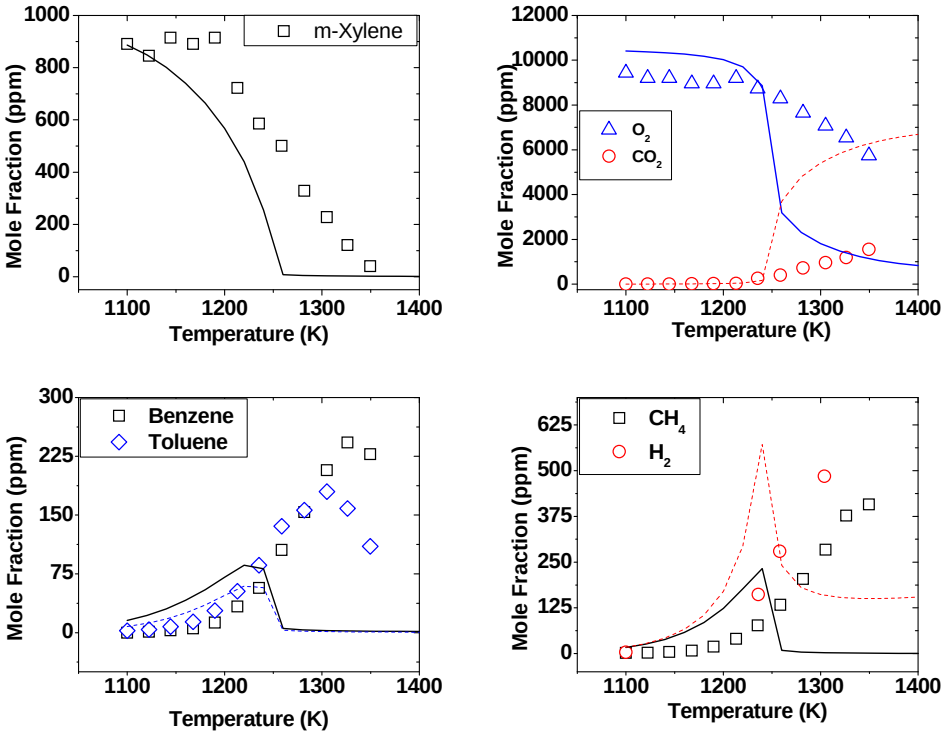


**Figure 108. m-Xylene oxidation jet stirred reactor experiments at atmospheric pressure, Gail and Dagaut. [28], comparison of experimental and modeling predictions [□]- Experiments, [-]-UIC m-Xylene Model 2.**

The jet stirred reactor experiments by Gail and Dagaut[28] were performed for a temperature range of 1049-1399 K and for three different equivalence ratios (Φ = 0.5, 1 and 2). For the jet stirred reactor data at stoichiometric conditions the model shows greater consumption of fuel, oxygen and earlier formation of the intermediates when compared to the experimental data, which is shown in Figure 108.

### 5.2.4. Sensitivity analysis of m-xylene

Sensitivity analyses of the fuel were performed to verify the contribution of the added and modified pathways to the fuel decay. Sensitivity analysis of the fuel was performed at fuel lean conditions for three different cases, which are described in detail below. The analyses were performed using closed homogenous batch reactor subroutine in CHEMKIN 4.1 and the normalized sensitivity coefficients are plotted against the corresponding reaction.

#### *5.2.4.1. High pressure (40-50 atm)*

The sensitivity analysis of the fuel was performed at a temperature of 1265 K, pressure of 45 atm and a reaction time of 1.9ms and is shown in Figure 109. The temperature and pressure of the analysis were chosen such that it encompasses the temperature and pressure range of both high pressure shock tube and ignition delay experiments. The fuel decay is seen to be sensitive to the formation of m-xylyl radical by hydrogen abstraction reactions, followed by the formation of dimethylphenyl radical, methylcresol and methylcresoxyl radicals through reactions of m-xylene

with O, OH and $HO_2$. Reactions of m-xylyl radical with $O_2$ and $HO_2$ leading to the formation of m-xylylperoxy and m-xylylhydroperoxide radicals are also important in this regime. At these temperatures less than 74% of the fuel has been consumed, so these temperatures are low enough and at high enough pressures to see noticeable formation of m-xylylperoxy and m-xylylhydroperoxide in the simulations.

#### *5.2.4.2. Intermediate pressure (10-25 atm)*

The sensitivity analysis of the fuel was performed at a temperature of 1399 K, pressure of 16 atm and a reaction time of 1.9ms. The temperature and pressure of the analysis were chosen such that it encompasses the temperature range of both high pressure shock tube and ignition delay experiments. The pressure chosen was the average pressure for all the experimental datasets. The fuel decay was seen to be sensitive to the formation of m-xylylhydroperoxide, methylphenyl radicals and the consumption of methylphenyl radical with oxygen through reactions shown in Figure 110. At higher temperatures the C-C scission pathway becomes important which explains the fuel decay being sensitive to the consumption reaction of methylphenyl radicals. At these high enough temperatures (100 % fuel decay), the methylphenyl radical chemistry seems to be more important than the m-xylylperoxy radical chemistry.

#### *5.2.4.3. Low pressure (1 atm)*

The sensitivity analysis of the fuel was performed at a temperature of 1161 K, pressure of 1 atm and a reaction time of 0.1s, which are the typical reaction times for complete conversion of the fuel in a plug flow reactor or the residence time in a jet stirred reactor (Figure 111).

The fuel decay is most sensitive to the formation of m-xylylperoxy radicals through m-xylyl+$O_2$ reaction and the formation of methylbenzoxyl radical from the benzyl+$HO_2$ reaction. The fuel decay is also sensitive to the formation of dimethylphenyl radical, methylcresoxy and cresoxyl radical. A significant observation which can be made for the low pressure datasets is the shift in the benzyl+$HO_2$ chemistry. At low pressures the fuel decay is seen to be sensitive to the formation of methylbenzoxyl radical whereas at high pressures it is sensitive to the formation of m-xylylhydroperoxide. The temperatures and the pressures are low enough for this system, for the fuel decay to be dominated by the consumption reactions of methylbenzoxyl and m-xylylperoxy radical reactions. The increased amount of methylbenzaldehyde, shown by the model is due to the formation of methylbenzoxyl and m-xylylperoxy radicals, both of which subsequently form methylbenzaldehyde.

The m-xylene oxidation chemistry is controlled by the formation of m-xylylhydroperoxide and m-xylylperoxy radicals at high pressures and low temperatures. At high pressures and high temperatures the methylphenyl radical oxidation and pyrolytic chemistry becomes important. At low pressures and low temperatures the m-xylyl oxidation chemistry is controlled by the formation of methylbenzoxyl radicals and m-xylylperoxy radicals.

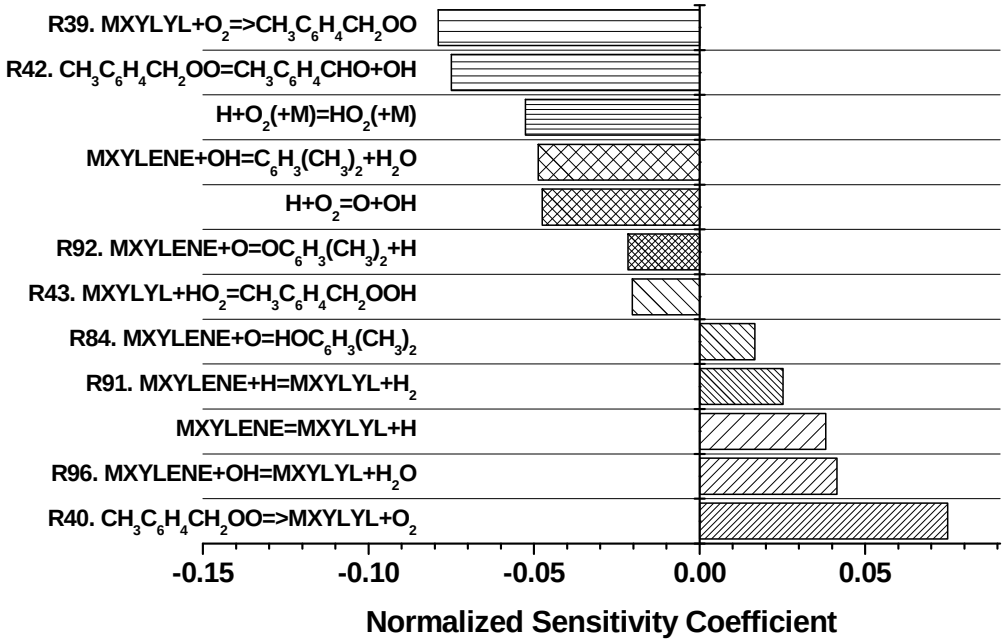


**Figure 109. Sensitivity analysis of m-xylene performed for T = 1265 K, P = 45 atm and time = 1.9 ms, using UIC m-Xylene Oxidation Model 2**

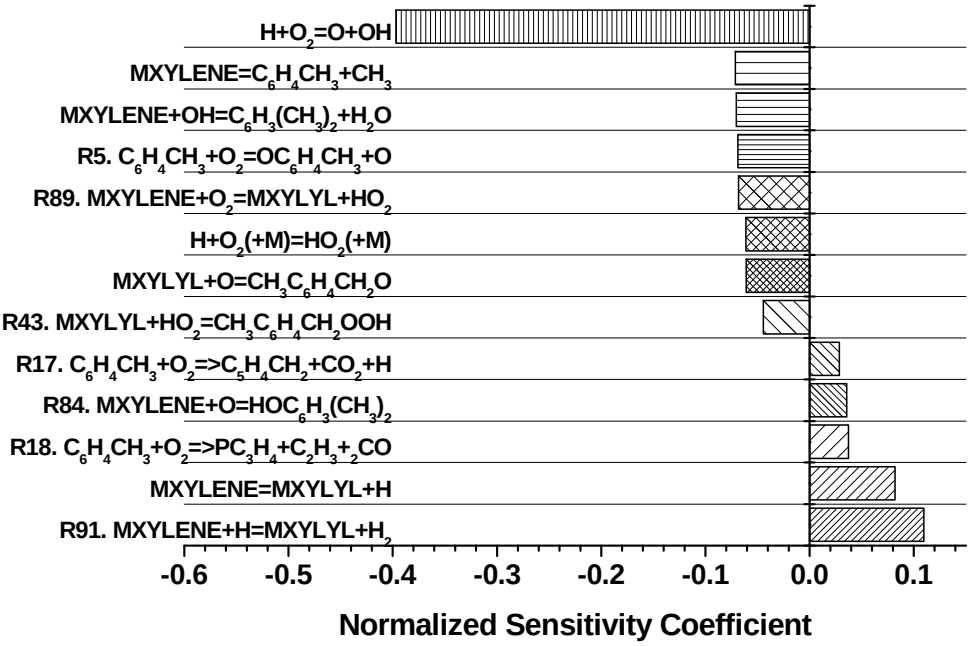


**Figure 110. Sensitivity analysis of m-xylene performed for T = 1399 K, P = 16 atm and time = 1.9 ms, using UIC m-Xylene Oxidation Model 2.**

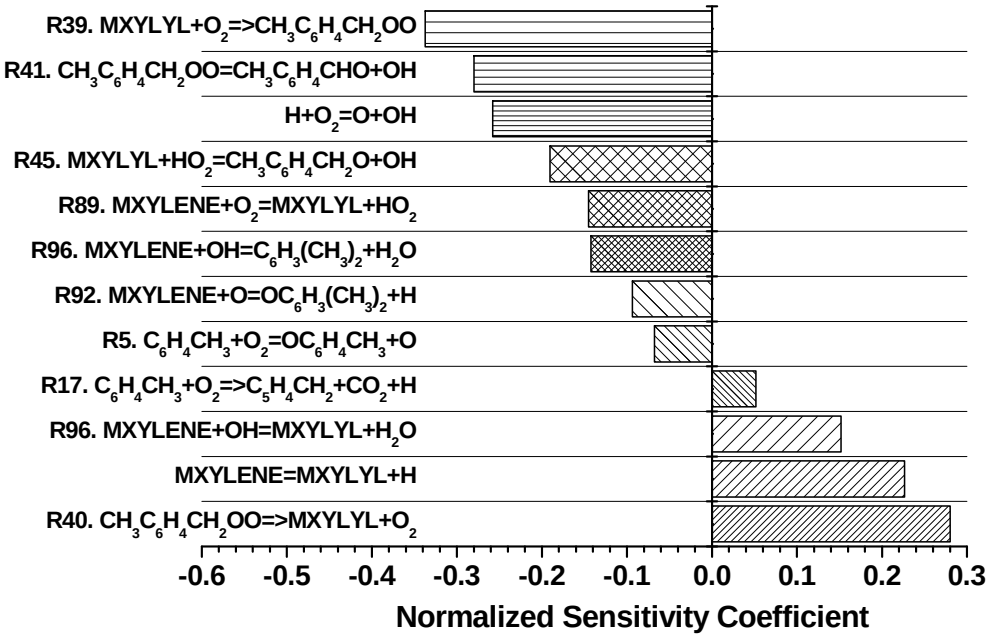


**Figure 111. Sensitivity analysis of m-xylene performed for T = 1161 K, P = 1 atm and time = 0.1s, using UIC m-Xylene Oxidation Model 2.**

#### *5.2.4.4. Implications for soot formation*

The experimental and modeling profiles of $O_2$, CO, $CO_2$, toluene, benzene, methane and acetylene at fuel lean, stoichiometric and fuel rich conditions are shown in Figure 100, Figure 101, Figure 102 and in Figure 104, Figure 105. The model predicts the consumption of oxygen and formation of the intermediates CO and $CO_2$, fairly well for fuel lean conditions. The model shows maximum concentrations of intermediates at the right experimental temperatures. For the fuel rich conditions, the modeling profiles show higher oxygen and correspondingly lower CO and $CO_2$. The modeling profiles show lower consumption of oxygen above 1385 K. For the consumption of the intermediates shown in Figure 102 and Figure 105, there is a shift in the modeling profiles when compared to the experimental data at higher temperatures. The temperatures at which the modeling profiles of intermediates are different from the experiments are the temperatures at which polycyclic aromatic hydrocarbons are being formed and decayed. This suggests that these intermediates play a crucial role in the formation and consumption of the multi-ring compounds. Hence it is important to include in future development, the channels for the formation of polycyclic aromatic hydrocarbons to predict the experimental data more accurately. However, the model at this stage, is sufficiently developed to be combined with a soot model that includes PAH formation and decay, for attempts at simulating the experimentally measured formation of soot from m-xylene. Nevertheless, for better soot modeling an extension of this current work to include pyrolytic experiments on m-xylene is to be performed in future, in order to better identify the pathways leading to the formation of polycyclic aromatic hydrocarbons from the fuel under these shock tube conditions.

# 6. SUMMARY AND CONCLUSIONS

The preliminary experimental work on the phenyl + acetylene reaction showed the necessity to develop a new experimental technique for the measurement of large PAH compounds which are the main focus of the present work. Two different techniques for the recovery and measurement of semi-volatile and non-volatile PAHs present in gas samples have been investigated experimentally using GC analytical techniques. The online technique consists in the direct connection between the analytical apparatus and the high-pressure shock tube at the University of Illinois at Chicago. Treated stainless steel lines and connections were used to build the sampling rig. The new experimental technique was tested on different reaction systems and showed excellent recovery results, within 10% error in the total carbon recovery. The technique allows measurement of large multi-ring compounds, including two-, three-, and four-ring species, which could not be detected by the traditional procedure of sampling and storage in a vessel. The experimental online technique represents, in our opinion, the simplest and optimal, although not always practical, solution to the problems of condensation and adsorption of heavy PAH compounds.

The alternative offline technique, which can be easily implemented with any experimental apparatus, has been experimentally investigated using stainless steel electropolished vessels and a variety of target compounds, i.e. naphthalene and biphenyl as representative PAH species and iodobenzene as representative semi-volatile light compound. The experiments simulate the collection and analyses of gas samples containing ppm levels of these representative compounds. A detailed optimal offline technique for the measurement of heavy compounds has been obtained which includes cooling the vessel at -15 °C, injecting a gas sample into the GC, flushing the vessel with methylene chloride, and finally injecting a liquid sample into the GC. For semi-volatile species such as iodobenzene, a different solution has been proposed which involves the determination of the constant percentage in condensed phase and the application of a correction factor to the gas phase measurement. The experiments have indicated excellent recovery for all the target compounds with a maximum uncertainty of ±7%. Although the offline technique studied in the present investigation constitutes an excellent alternative solution when the online technique can not be implemented, it is not the preferred solution due to its increased procedural complexity compared to the online technique.

Once the new experimental apparatus was tested and implemented, the pyrolysis of the phenyl radical (preliminary to the subsequent reactions with acetylene) and the pyrolytic reactions of the phenyl radical with acetylene were investigated at nominal pressures of 25 and 50 atm and for a temperature range between 900 and 1800 K. The experimental work was performed using GC/GC-MS diagnostic coupled to a high-pressure shock tube apparatus. For the first time it has been possible to detect and accurately measure both small hydrocarbon products including single-ring aromatics and a variety of multi-ring PAH compounds for which mole fraction profiles have been obtained as a function of temperature. A chemical kinetic model has been developed to simulate the experimental results with particular attention to the formation of the PAH products from both reaction systems. The study helped clarify some of the aspects related to the chemistry involved in the formation of large multi-ring compounds.

In particular, the experimental and modeling results on the phenyl radical pyrolysis indicate that the formation of the PAH compounds is strongly influenced by the benzyne chemistry and especially by the reactions involving the o-benzyne radical. Such reactions have been proposed

as relevant for the production of several multi-ring compounds including the terphenyls, acenaphthylene, and the four-ring species. With regards to the acenaphthylene formation a new reaction rate constant expression for the isomerization between cyclopenta[a]indene and acenaphthylene was derived from the experimental profiles, while a new reaction pathway for the isomerization of biphenylene was investigated from a theoretical point of view using ab-initio calculations. In addition, based on the experimental results we revealed the importance of several other reactions such as the reaction between phenyl radical and hydrogen iodide and the reaction between phenyl iodide and phenyl radical to form the iodobiphenyls. Similar reactions should be included in future studies on the phenyl radical derived from phenyl iodide.

The investigation on the phenyl + acetylene system revealed that the formation of PAH compounds is driven by the reaction between phenyl radical and phenylacetylene with regard to phenanthrene and diphenylethyne, while the HACA mechanism plays a key role in the formation of acenaphthylene when high concentrations of acetylene are present in the reactant mixture.

Finally both experimental studies suggest that above a certain temperature the polymerization process becomes dominant. Additional theoretical studies are required in order to clarify the relative high-temperature chemistry. The experimental profiles obtained in this work represent a valuable benchmark for the validation of such future studies.

The presence of considerable amounts of fused-ring compounds from the pyrolysis of the phenyl radical also inspired a theoretical study on non-conventional reaction mechanisms leading to the formation of these important intermediate species. In particular, a comprehensive study of the potential energy surfaces for the radical/π-bond addition reactions between different single-ring aromatic hydrocarbons has been performed for the first time using theoretical calculation techniques. Several pathways leading to the formation of PAH compounds have been proposed as relevant for typical combustion environments.

The ab-initio calculations on the addition between benzene and singlet o-benzyne radical confirm from a theoretical point of view the possibly significant role of o-benzyne in the formation of naphthalene as observed in the experimental work by Friedman and Lindow[94]. The system proceeds through the formation of a benzobicyclo[2,2,2]octatriene intermediate (reaction R1, Figure 58) which subsequently undergoes fragmentation to form naphthalene and acetylene (reaction R2, Figure 58). The high-pressure limit rate constants for the elementary reactions R1 and R2 were estimated based on the calculated properties of the species involved. On the other hand the calculations on the benzene + triplet o-benzyne system confirm the presence of a pathway leading to the formation of a biphenylene-like compound as hypothesized by Friedman and Lindow[94] in their pyrolytic experimental investigation on the system in consideration (Figure 57). Alternative channels for the addition between benzene and triplet o-benzyne lead to the formation of phenyl radicals (H-abstraction) and biphenyl radical + hydrogen (addition + C-H fission).

Further studies on the potential energy surface for the radical/π-bond addition between benzene and phenyl radical reveal that the only products of the reaction are biphenyl and hydrogen, in agreement with previous experimental and theoretical studies. On the other hand the radical/π-bond addition between phenyl radicals proceeds along a variety of pathways on both a singlet and a triplet energy surface. In competition with the expected channels leading to the formation of biphenyl (addition + H-transfer) or biphenyl radical + hydrogen (addition + C-H fission), a new pathway proceeding through the benzobicyclo[2,2,2]octatriene intermediate and leading to the formation of naphthalene and acetylene has been proposed as potentially relevant for the second-ring species formation. Such a pathway can be considered as a prototype for an

aromatic radical adding to the non-radical π-bond site of another aromatic radical leading directly to fused ring structures.

The present investigation supports the idea that the π-bonding could possibly play a significant role in the mechanisms of growth of PAH species and soot. In particular the radical/π-bond addition between aromatic hydrocarbons represents a direct channel for the formation of fused multi-ring compounds as naphthalene. The investigated pathways complement the conventional growth mechanisms involving the reaction of a single aromatic hydrocarbon with small aliphatic compounds as acetylene for the HACA mechanism.

The theoretical investigation was exetended to another radical/π-bond addition reaction, the one between o-benzyne and the cyclic C5 hydrocarbons. In particular, new pathways leading to the formation of the typical PAH compounds relevant to soot formation were proposed.

The ab-initio calculations of the reaction between o-benzyne and cyclopentadiene confirm from a theoretical point of view that the reaction proceeds mainly through concerted 1,4-cycloaddition to form the benzonorbornadiene adduct as observed experimentally[140-**Error! Reference source not found.**]. A novel pathway which involves the fragmentation of benzonorbornadiene has been proposed for the first time as relevant to the formation of indene. The stepwise channels have also been studied and are found to be not favorable from an energetic point of view compared to the concerted pathway to indene.

The additional studies on the potential energy surface of the radical/π-bond addition between o-benzyne and the cyclopentadienyl radical represent to the best of our knowledge the first attempt to investigate this reaction. In competition with the isomerization pathways, a channel which leads to the formation of indenyl radical and acetylene is present on the potential energy surface. At high temperatures this channel could possibly be relevant to the formation of indene-like soot precursors.

The present investigation confirms that the radical/π-bond addition reactions could possibly play a significant role in the mechanisms of growth of PAH species and soot. In this particular case, the reactions between o-benzyne and the cyclic C5 hydrocarbons constitute a direct pathway to the formation of indene which complements the traditional reaction pathways involving the first aromatic ring and small C3 aliphatic hydrocarbons.

In addition to the experimental work performed on the phenyl radical pyrolysis and the phenyl + acetylene reaction, the oxidation of m-xylene has been studied at nominal reflected shock pressures of 25 and 50 atm, for a temperature range of 1050-1584 K at fuel lean, stoichiometric and fuel rich conditions. Species profiles of small hydrocarbons, mono-aromatic and multi-ring aromatic species were obtained as a function of temperature. A model was assembled to describe the decay of m-xylene and the formation of lower carbon number hydrocarbons, as measured from the experiments. The formation of dimethylphenoxy radicals and dimethylphenol are seen to be dominant in modeling the m-xylene decay for fuel lean conditions. The m-xylene oxidation chemistry is seen to be dependent on the consumption of m-xylyl radical through m-xylyl+$O_2$ and m-xylyl+$HO_2$ reactions. The model simulates the fuel decay accurately for all the experimental data sets and fairly good agreement is seen in modeling profiles of the intermediates when compared to the experimental data for fuel lean and stoichiometric conditions. The model has also been tested against experimental data obtained in other laboratories with satisfactory results.

Although the work on the oxidation of m-xylene focused mainly on the formation of single ring and substituted mono-aromatic species from the fuel, work is in progress to include in the

chemical kinetic model the chemistry related to the PAH compounds which have been measured in the experiments.

The extension of the present work would also include the study of the reactions between the benzyl radical ($C_6H_5CH_2$) and acetylene, which has been postulated to be an important pathway for the formation of another intermediate for soot formation processes, indene. Using the experimental technique developed in the present work, the reactions between the benzyl radical and acetylene could be investigated at the high pressure and high temperature conditions typical of modern combustion devices. The results could clarify the mechanisms proposed by the theoretical study by Vereecken and Peeters[175] and possibly highlight the presence of additional reaction channels not considered in previous investigations.

# REFERENCES


1. Von Klot, S.; Woelke, G.; Tuch, T.; Heinrich, J.; Dockery, D. W.; Schwartz, J.; Kreyling, W. G.; Wichmann, H. E.; Peters, A. *European Respiratory Journal* 2002, 20(3), 691-702
2. Pope, III C. A.; Burnett, T. R.; Thurston, D. G.; Thun, J. M.; Calle, E.; Krewski, D.; Ito, K. *Journal of the American Medical Association* 2002, 287, 1132-1141
3. Pope, C. A.; Burnett, R. T.; Thurston, G. D.; Thun, M. J.; Calle, E. E.; Krewski, D.; Godleski, J. J. *Circulation* 109, (2004), 71–77
4. Brook, R. D.; Brook, J.R.; Rajagopalan, S. *Curr. Hypertens. Res.* 5, (2003), 32–39
5. Johnson,R. L. *Circulation* 2004; 109; 5-7
6. Bockhorn, H. Soot Formation in Combustion-Mechanisms and Models, Ed. H. Bockhorn, Springer Series in Chemical Physics, Volume 59, 1994, 3-9
7. Frenklach, M. Phys. *Chem. Chem. Phys.* 2002, 4, 2028-2037
8. Richter H.; Howard, J. B. *Prog. Ener. Comb. Sci.* 2000, 26, 565-608
9. Lindstedt, R. P.; Maurice, L. Q.; Meyer, M. *Faraday Discuss.* 2001, 119, 409-432
10. Lighty, J. S.; Veranth, J. M.; Sarofim, A. F. *J. Air & Waste Manage. Assoc.* 50:1565-1618, 2000
11. Koylu, U . O.; Mcenally, C. S.; Rosner, D. E.; Pfefferle, L. D. *Combustion and Flame*, 110, 494–507, (1997)
12. Di Stasio, S. *Carbon*, 39, 109–118, (2001)
13. Frenklach, M.; Clary, D. W.; Gardiner, W. C.; Stein, S. E. *Proc. Combust. Inst*. 1984, 20, 887
14. Bockhorn, H.; Fetting, F.; Wenz, H. W. *Ber. Bunsen-Ges. Phys. Chem*. 1983, 97, 1067
15. Fahr, A.; Stein S. E. *Proc. Combust. Inst.* 1988, 22, 1023-1029
16. Yu, T.; Lin, M. C.; Melius, C. F. *Int. J. Chem. Kin.* 1994, 26, 1095-1104
17. Wang, H. Frenklach, M. *J. Phys. Chem*. 1994, 98, 11465-11489.
18. Heckmann, E.; Hippler, H. Troe, J. *Proc. Combust. Inst.* 1996, 26, 543-550
19. Richter, H. ; Mazyar, O. A. ; Sumathi, R. ; Green, W. H. ; Howard, J. B. ; Bozzelli, J. W. *J. Phys. Chem. A* 2001, 105, 1561-1573
20. Tokmakov, I. V.; Lin, M. C. *J. Am. Chem. Soc.* 2003, 125, 11397-11408
21. W.J. Pitz, N.P. Cernansky, F.L. Dryer, F.N. Egolfopoulos, J.T. Farrell, D.G. Friend, H. Pitsch, Development of an Experimental Database and Chemical Kinetic Models for Surrogate Gasoline Fuels, SAE International, 2007.
22. J.T. Farrell, N.P. Cernansky, F.L. Dryer, D.G. Friend, C.A. Hergart, C.K. Law, R. M. McDavid, C.J. Mueller, A. K. Patel, H. Pitsch, SAE International, 2007.
23. M. Colket, T. Edwards, S. Williams, N.P. Cernansky, D.L. Miller, F.N. Egolfopoulos, P. Lindstedt, K. Seshadri, F.L. Dryer, C.K. Law, D.G. Friend, D.B. Lenhert, H. Pitsch, A. Sarofim, M. Smooke, W. Tsang, 45th AIAA Aerospace Sciences Meeting and Exhibit, 2007.
24. R. Sivaramakrishnan, R. S. Tranter, K. Brezinsky, Combust. Flame 139 (2004) 340-350.
25. R. Sivaramakrishnan, R. S. Tranter, K. Brezinksy, J. Phys. Chem. A 110 (2006) 9388-9399.
26. R. Sivaramakrishnan, R. S. Tranter, K. Brezinsky, J. Phys. Chem. A 110 (2006) 9400-9404.
27. J. L. Emdee, K. Brezinsky, I. Glassman, J. Phys. Chem. 96 (1992) 2151-2161.
28. S. Gail, P. Dagaut, Combust. Sci. Technol. 179 (2007) 813-844.
29. F. Battin-Leclerc, R. Bounaceur, N. Belmekki, P. A. Glaude, Int. J. Chem. Kinet. 38 (2006) 284-302.
30. H.-P. S. Shen, M. A. Oehlschlaeger, Combust. Flame 156 (2009) 1053-1062.

31. A. Roubaud, R. Minetti, L. R. Sochet, Combust. Flame 121 (2000) 535-541.
32. R. J. Johnston, J. T. Farrell, Proc. Combust. Inst. 30 (2005) 217-224.
33. Frenklach, M.; Wang, H. *Proc. Combust. Inst.* **1990**, 23, 1559–1566.
34. Shukla, B.; Koshi, M. *Phys. Chem. Chem. Phys.* **2010**, 12, 2427–2437.
35. Shukla, B.; Koshi, M. *Combust. Flame* **2011**, 158, 369–375.
36. Park, J.; Lin, M. C. *J. Phys. Chem. A* **1997**, 101, 14–18.
37. Tranter, R. S.; Klippenstein, S. J.; Harding, L. B.; Giri, B. R.; Yang, X.; Kiefer, J. H. *J. Phys. Chem. A* **2010**, 114, 8240–8261.
38. Tranter, R. S.; Fulle, D.; Brezinsky, K. *Rev. Sci. Inst.* **2001**, 72, 3046–3054.
39. Tranter, R. S.; Sivaramakrishnan, R.; Srinivasan, N.; Brezinsky, K. *Int. J. Chem. Kinet.* **2001**, 33, 722–731.
40. Lifshitz, A.; Shweky, I.; Kiefer, J. H.; Sidhu, S. S. Shock Waves; *Proceedings of the 18th International Symposium on Shock Waves*, Sendia, Japan (**1991**); K. Takayama, Ed.; Springer–Verlag: Berlin (**1992**) 825.
41. Tsang, W.; Lifshitz, A. *Int. J. Chem. Kinet.* **1998**, 30, 621–628.
42. Saito, K.; Toriyama, Y.; Yokubo, T.; Higashihara, T.; Murakami, I. *Bull. Chem. Soc.* **1980**, 53, 1437–1438.
43. Tang, W.; Brezinsky, K. *Int. J. Chem. Kinet.* **2006**, 38, 75–97.
44. *Method 429 - Determination of Polycyclic Aromatic Hydrocarbon (PAH) Emissions from Stationary Sources* (California Environmental Protection Agency – State of California Air Resources Board, Sacramento, 1997).
45. A. R. Collier, C. A. Jemma, B. Wedekind, D. E. Hall, and P. Heinze, "Sampling and Analysis of Vapor-Phase and Particulate-Bound PAH From Vehicle Exhaust", SAE paper No. 982727, 1998.
46. W. T. Winberry, Jr., and G. Jungclaus, *Compendium Method TO-13A - Determination of Polycyclic Aromatic Hydrocarbons (PAHs) in Ambient Air Using Gas Chromatography/Mass Spectrometry (GC/MS)*, (U.S. Environmental Protection Agency, Cincinnati, 1999).
47. H. N. Berko, *Technical Report No. 2: Polycyclic aromatic hydrocarbons (PAHs) in Australia*, (Environment Australia - Department of the Environment and Heritage, Perth, Western Australia, 1999).
48. C. C. Cheng, Polycyclic Arom. Comp. **23**, 315 (2003).
49. A. Comandini, T. Malewicki, and K. Brezinsky, *Chemistry of PAHs Formation from Phenyl Radical Pyrolysis and Phenyl + Acetylene Reaction*, submitted to J. Phys. Chem. A (2011).
50. S. Gudiyella, T. Malewicki, A. Comandini, and K. Brezinsky, Combust. Flame **158**, 687 (2011).
51. S. Gudiyella, and K. Brezinsky, *High Pressure Study of n-Propylbenzene Oxidation*, submitted to Combust. Flame (2011).
52. W. Tang, R. S. Tranter, and K. Brezinsky, J. Phys. Chem. A **109**, 6056 (2005).
53. S. Garner, R. Sivaramakrishnan, K. Brezinsky, Proc. Combust. Inst. **32**, 461 (2009)
54. Kee, R. J.; Rupley, F. M.; Miller, J. A.; Coltrin, M. E.; Grcar, J. F.; Meeks, E.; Moffat, H. K.; Lutz, A. E.; Dixon-Lewis, G.; Smooke, M. D.; Warnatz, J.; Evans, G. H.; Larson, R. S.; Mitchell, R. E.; Petzold, L. R.; Reynolds, W. C.; Caracotsios, M.; Stewart, W. E.; Glarborg, P.; Wang, C.; Adigun, O. CHEMKIN Collection, 3.6 ed., Reaction Design Inc., San Diego, CA, 2000.

55. Kee, R. J.; Rupley, F. M.; Miller, J. A.; Coltrin, M. E.; Grcar, J. F.; Meeks, E.; Moffat, H. K.; Lutz, A. E.; Dixon-Lewis, G.; Smooke, M. D.; Warnatz, J.; Evans, G. H.; Larson, R. S.; Mitchell, R. E.; Petzold, L. R.; Reynolds, W. C.; Caracotsios, M.; Stewart, W. E.; Glarborg, P.; Wang, C.; McLellan, C. L.; Adigun, O.; Houf, W. G.; Chou, C. P.; Miller, S. F.; Ho, P.; Young, P. D.; Young, D. J.; Hodgson, D. W.; Petrova, M. V.; Puduppakkam, K. V. CHEMKIN Release 4.1, Reaction Design, San Diego, CA, 2006.
56. Burcat, A.; Ruscic, B. Ideal Gas Thermochemical Database with updates from Active Thermochemical Tables. ftp://ftp.technion.ac.il/pub/supported/aetdd/thermodynamics.
57. Wang, H.; Dames, E.; Sirjean, B.; Sheen, D. A.; Tangko, R.; Violi, A.; Lai, J. Y. W.; Egolfopoulos, F. N.; Davidson, D. F.; Hanson, R. K.; Bowman, C. T.; Law, C. K.; Tsang, W.; Cernansky, N. P.; Miller, D. L.; Lindstedt, R. P. A high-temperature chemical kinetic model of n-alkane (up to n-dodecane), cyclohexane, and methyl-, ethyl-, n-propyl and n-butyl-cyclohexane oxidation at high temperatures, JetSurF version 2.0, September 19, 2010 (http://melchior.usc.edu/JetSurF/JetSurF2.0).
58. Richter, H.; Granata, S.; Green, W. H.; Howard, J. B. *Proc. Comb. Inst.* **2005**, 30, 1397–1405 (http://web.mit.edu/anish/www/MITcomb.html)
59. Kee, R. J.; Rupley, F. M.; Miller, J. A.; Coltrin, M. E.; Grcar, J. F.; Meeks, E.; Moffat, H. K.; Lutz, A. E.; Dixon-Lewis, G.; Smooke, M. D.; Warnatz, J.; Evans, G. H.; Larson, R. S.; Mitchell, R. E.; Petzold, L. R.; Reynolds, W. C.; Caracotsios, M.; Stewart, W. E.; Glarborg, P.; Wang, C.; Adigun, O.; Houf, W. G.; Chou, C. P.; Miller, S. F. Chemkin Collection, Release 3.7.1, Reaction Design, Inc., San Diego, CA, 2003.
60. Sivaramakrishnan, R.; Tranter, R. S.; Brezinsky, K. *J. Phys. Chem. A* **2005**, 109, 1621–1628.
61. Becke, A. D. *J. Chem. Phys.* **1993**, 98, 5648–5652.
62. Lee, C.; Yang, W.; Parr, R. G. *Phys. Rev. B* **1988**, 37, 785–789.
63. Krishnan, R.; Binkley, J. S.; Seeger, R.; Pople, J. A. *J. Chem. Phys.* **1980**, 72, 650–654.
64. Godbout, N.; Salahub, D. R.; Andzelm, J.; Wimmer, E. *Can. J. Chem.* **1922**, 70, 560–571.
65. Frisch, M. J.; Trucks, G. W.; Schlegel, H. B.; Scuseria, G. E.; Robb, M. A.; Cheeseman, J. R.; Montgomery, J. A., Jr.; Vreven, T.; Kudin, K. N.; Burant, J. C.; Millam, J. M.; Iyengar, S. S.; Tomasi, J.; Barone, V.; Mennucci, B.; Cossi, M.; Scalmani, G.; Rega, N.; Petersson, G. A.; Nakatsuji, H.; Hada, M.; Ehara, M.; Toyota, K.; Fukuda, R.; Hasegawa, J.; Ishida, M.; Nakajima, T.; Honda, Y.; Kitao, O.; Nakai, H.; Klene, M.; Li, X.; Knox, J. E.; Hratchian, H. P.; Cross, J. B.; Bakken, V.; Adamo, C.; Jaramillo, J.; Gomperts, R.; Stratmann, R. E.; Yazyev, O.; Austin, A. J.; Cammi, R.; Pomelli, C.; Ochterski, J. W.; Ayala, P. Y.; Morokuma, K.; Voth, G. A.; Salvador, P.; Dannenberg, J. J.; Zakrzewski, V. G.; Dapprich, S.; Daniels, A. D.; Strain, M. C.; Farkas, O.; Malick, D. K.; Rabuck, A. D.; Raghavachari, K.; Foresman, J. B.; Ortiz, J. V.; Cui, Q.; Baboul, A. G.; Clifford, S.; Cioslowski, J.; Stefanov, B. B.; Liu, G.; Liashenko, A.; Piskorz, P.; Komaromi, I.; Martin, R. L.; Fox, D. J.; Keith, T.; Al-Laham, M. A.; Peng, C. Y.; Nanayakkara, A.; Challacombe, M.; Gill, P. M. W.; Johnson, B.; Chen, W.; Wong, M. W.; Gonzalez, C.; Pople, J. A. *Gaussian 03*, revision D.01; Gaussian, Inc.: Wallingford, CT, 2004.
66. Robaugh, D.; Tsang, W. *J. Phys. Chem.* **1986**, 90, 5363–5367.
67. Kumaran, S. S. ; Su, M. C. ; Michael, J. V. *Chem. Phys. Lett.* **1997**, 269, 99–106.
68. Kominar, R. J.; Krech, M. J.; Price, S. J. W. *Can. J. Chem.* **1976**, 54, 2981–2984.
69. Butler, E. T.; Polanyi, M. *Trans. Faraday Soc.* **1943**, 39, 19–35.
70. Moskaleva, L. V.; Madden, L. K.; Lin, M. C. *Phys. Chem. Chem. Phys.* **1999**, 1, 3967–3972.
71. Giri, B. R.; Bentz, T.; Hippler, H.; Olzmann, M. *Z. Phys. Chem.* **2009**, 223, 539–549.

72. Rodgers, A. S.; Golden, D. M.; Benson, S. W. *J. Am. Chem. Soc.* **1967**, 89, 4578–4583.
73. Wang, H.; Frenklach, M. *Combust. Flame* **1997**, 110, 173–221.
74. Park, J.; Burova, S.; Rodgers, A. S.; Lin, M. C. *J. Phys. Chem. A* **1999**, 103, 9036–9041.
75. Brooks, C. T.; Peacock, S. J.; Reuben, B. G. *J. Chem. Soc. Faraday Trans. I* **1979**, 75, 652–662.
76. Zhang, L.; Cai, J.; Zhang , T.; Qi, F. *Combust. Flame* **2010**, 157, 1686–1697.
77. Lifshitz, A.; Tamburu, C.; Dubnikova, F. *J. Phys. Chem. A* **2009**, 113, 10446–10451.
78. Richter, H.; Benish, T. G.; Mazyar, O. A.; Green, W. H.; Howard, J. B. *Proc. Combust. Inst.* **2000**, 28, 2609–2618.
79. Shukla, B.; Tsuchiya, K.; Koshi, M. *J. Phys. Chem. A* **2011**, 115, 5284–5293.
80. Brown, R. F. C.; Choi, N.; Coulston, K. J.; Eastwood, F. W.; Wiersum, U. E.; Jenneskens, L. W. *Tetrahedron Letters* **1994**, 35:25, 4405–4408.
81. Brown, R. F. C.; Eastwood, F. W. *Pure & Appl. Chem.* **1996**, 68:2, 261–166.
82. Wiersum, U. E.; Jenneskens, L. W. *Tetrahedron Letters* **1993**, 34:41, 6615–6618.
83. Blake, M. E.; Bartlett, K. L.; Jones Jr., M. *J. Am. Chem. Soc.* **2003**, 125, 6485–6490.
84. Eyring, H. J. *J. Chem. Phys.* **1935**, 3, 107–115.
85. Evans, M. G.; Polanyi, M. *Trans. Faraday Soc.* **1935**, 31, 875–894.
86. Wigner, E. *Trans. Faraday Soc.* **1938**, 34, 29–41.
87. Shavitt, I. *J. Phys. Chem.* **1959**, 31, 1359–1367.
88. Scott, L. T. *Pure & Appl. Chem.* **1996**, 68:2, 291–300.
89. Raghavachari, K.; Trucks, G. W.; Pople, J. A.; Head-Gordon, M. *Chem. Phys. Lett.* **1989**, 157, 479–483.
90. Dunning Jr., T. H. *J. Chem. Phys.* **1989**, 90, 1007–1023.
91. Comandini, A.; Brezinsky, K. *J. Phys. Chem. A* **2011**, 115, 5547–5559.
92. Poster, D. L.; Schantz, M. M.; Sander, L. C.; Wise, S. A. *Anal. Bioanal. Chem*. **2006**, 386, 859–881.
93. Jacobelli, C.; Perez, G.; Polcaro, C.; Possagno, E.; Bassanelli, R.; Lilla, E. *J. Anal. Appl. Pyrol.* **1983**, 5, 237–243.
94. Friedman, L.; Lindow, D. F. *J. Am. Chem. Soc.* **1968**, 90:9, 2324–2328.
95. Copeland, P. G.; Dean, R. E.; McNeil, D. *J. Chem. Soc.* **1960**, 1687–1689.
96. Fields, E. K.; Meyerson, S. *Chem. Commun.* **1965**, 20, 474–476.
97. Fields, E. K.; Meyerson, S. *J. Org. Chem.* **1966**, 31, 3307–3309.
98. Lindow, D. F.; Friedman, L. *J. Am. Chem. Soc.* **1967**, 89:5, 1271–1272.
99. Wang, H.; Laskin, A.; Moriarty, N. W.; Frenklach, M. *Proc. Combust. Inst.* **2000**, 28, 1545–1555.
100. Laskin, A.; Lifshitz, A. *Proc. Combust. Inst.* **1996**, 26, 669–675.
101. Wang, H.; Frenklach, M. *Combust. Flame* **1997**, 110, 173–221.
102. Gao, Y.; Fessel, K.; McLeod, C.; Marshall, P. *Chem. Phys. Lett.* **2008**, 451, 8–13.
103. Aguilera-Iparraguirre, J.; Klopper, W. *J. Chem. Theory Comput.* **2007**, 3, 139–145.
104. Hertzler, J.; Frank, P. *Ber. Bunsenges. Phys. Chem.* **1992**, 96, 1333–1338.
105. Kislov, V. V.; Islamova, N. I.; Kolker, A. M.; Lin, S. H.; Mebel, A. M. *J. Chem. Theory Comput.* **2005**, 1, 908–924.
106. a) Kruse, T.; Roth, P. *J. Phys. Chem. A* **1997**, 101, 2138–2146; b) Kern, R. D.; Xie, K.; Chen, H.; Kiefer, J. H. *23th International Symposium on Combustion*, The Combustion Institute (**1990**) 69–75; c) Frank, P.; Just, T. *Combust. Flame* **1980**, 38, 231–248.
107. Colket III, M. B.; Seery, D. J.; Palmer, H. B. *Combust. Flame* **1989**, 75, 343–366.

108. Dooley, S.; Won, S. H.; Chaos, M.; Heyne, J.; Ju, Y.; Dryer, F. L.; Kumar, K.; Sung, C. J.; Wang, H.; Oehlschlaeger, M. A.; Santoro, R. J.; Litzinger, T. A. *Combust. Flame* **2010**, 157, 2333–2339.
109. Choi, Y. M.; Park, J.; Lin, M. C. *J. Phys. Chem. A* **2003**, 107, 7755–7761.
110. Seetula, J. A.; Russell, J. J.; Gutman, D. *J. Am. Chem. Soc.* **1990**, 112, 1347–1353.
111. Appel, J.; Bockhorn, H.; Frenklach, M. *Combust. Flame* **2000**, 121, 122.
112. Fascella, S.; Cavallotti, C.; Rota, R.; Carrà, S. *J. Phys. Chem. A* **2004**, 108, 3829.
113. Goldaniga, A.; Faravelli, T.; Ranzi, E. *Combust. Flame* **2000**, 122, 350.
114. Dean, A. M. *J. Phys. Chem.* **1990**, 94, 1432.
115. Marinov, N. M.; Pitz, W. J.; Westbrook, C. K.; Castaldi, M. J.; Senkan, S. M. *Combust. Sci. Technol.* **1996**, 116, 211.
116. Marinov, N. M.; Pitz, W. J.; Westbrook, C. K.; Vincitore, A. M.; Castaldi, M. J.; Senkan, S. M.; Melius, C. F. *Combust. Flame* **1998**, 114, 192.
117. Bryce, M. R.; Vernon, J. M. *Advances in Heterogeneous Chemistry* **1981**, 28, 183.
118. Miller, R. G.; Stiles, M. *J. Amer. Chem. Soc.* **1963**, 85, 1798.
119. Fields, E. K.; Meyerson, S. *J. Amer. Chem. Soc.* **1966**, 88, 21.
120. Scaiano, J. C.; Stewart, L. C. *J. Amer. Chem. Soc.* **1983**, 105, 3609.
121. Manion, J. A.; Tsang, W. *Proceedings of Chemical and Physical Processes in Combustion*, **1996** Fall Technical Meeting, 527.
122. Wang, H. *Proc. Combust. Inst.* **2010**, 33, 41.
123. Cain, J. P.; Gassman, P. L.; Wang, H.; Laskin, A. *Phys. Chem. Chem. Phys.* **2010**, 12, 5206.
124. Schlegel, H. B. *J. Comp. Chem.* **1982**, 3, 214.
125. Peng, C.; Schlegel, H. B. *Isr. J. Chem.* **1993**, 33, 449.
126. Gonzalez, C.; Schlegel, H. B. *J. Chem. Phys.* **1989**, 90, 2154.
127. Beno, B. R.; Sheu, C.; Houk, K. N.; Warmuth, R.; Cram, D. J. *Chem. Commun.* **1998**, 301.
128. Friedman L. *J. Amer. Chem. Soc.* **1967**, 89, 3071.
129. Lee, T. J.; Taylor, P. R. *Int. J. Quantum Chem.* **1989**, S23, 199.
130. Davico, G. E.; Bierbaum, V. M.; DePuy, C. H.; Ellison, G. B.; Squires, R. R. *J. Am. Chem. Soc.* **1995**, 117, 2590.
131. Madden, L. K.; Moskaleva, L. V.; Kristyan, S.; Lin, M. C. *J. Phys. Chem. A* **1997**, 101, 6790.
132. Xu, C.; Braun-Unkhoff, M.; Naumann, C.; Frank, P. *Proc. Combust. Inst.* **2007**, 31, 231.
133. García-Cruz, I.; Martínez-Magadán, J. M.; Bofill; J. M.; Illas, F. *J. Phys. Chem. A* **2004**, 108, 5111.
134. Miller, J. A.; Klippenstein, S. J. *J. Phys. Chem. A* **2003**, 107, 7783.
135. Harrison, A. G.; Honnen, L. R.; Dauben, H. J.; Lossing, F. P. *J. Am. Chem. Soc.* **1960**, 82, 5593–5598.
136. Lovell, A. B.; Brezinsky, K.; Glassman, I. *Proc. Combust. Inst.* **1988**, 22, 1063–1074.
137. Kislov, V. V.; Mebel, A. M. *J. Phys. Chem. A* **2008**, 112, 700–716.
138. Butler, R. G.; Glassman, I. *Proc. Combust. Inst.* **2009**, 32, 395–402.
139. Kim, D. H.; Mulholland, J. A.; Wang, D.; Violi, A. *J. Phys. Chem. A* **2010**, 114, 12411–12416.
140. Wittig, G.; Knauss, E. *Chem. Ber.* **1958**, 91, 895–907.

141. Mich, T. F.; Nienhouse, E. J.; Farina, T. E.; Tufariello, J. J. *J. Chem. Educ.* **1968**, 45, 272.
142. Meinwald, J.; Gruber, G. W. *J. Am. Chem. Soc.* **1971**, 93, 3802–3803.
143. A. Kazakov, H. Wang, M. Frenklach, Combust. Flame 100 (1995) 111-120.
144. K. Naraynaswamy, G. Blanquart, H. Pitsch, Combust. Flame 157 (2010) 1879-1898.
145. R.S. Tranter, A. Raman, R. Sivaramakrishnan, K. Brezinsky, Int. J. Chem. Kinet. 37 (2005) 306-331.
146. R. Sivaramakrishnan, A. Comandini, R. S. Tranter, K. Brezinsky, S. G. Davis, H. Wang, Proc. Combust. Inst. 31 (2007) 429-437.
147. S. S. Vasu, D. F. Davidson, R. K. Hanson, J. Propul. Power, 26 (2010) 776-783.
148. G. Da Silva, J. A. Cole, J. W. Bozzelli, J. Phys. Chem., 113 (2009) 6111-6120.
149. C. Cavallotti, M. Derudi, R. Rota, Proc. Combust. Inst. 32 (2009) 115-121.
150. J. C. G. Andrae, P. Bjornbom, R. F. Carcknell, G. T. Kalghatgi, Combust. Flame, 149 (2007) 2-24.
151. Y. Sakai, A. Miyoshi, M. Koshi, W. J. Pitz, Proc. Combust. Inst., 32 (2009) 411-418.
152. J. C. G. Andrea, T. Brink, G. T. Kalghatgi, Combust. Flame, 155 (2008) 696-712.
153. G. Mittal, C. J. Sung, Combust. Flame, 150 (2007) 355-368.
154. Y. Murakami, T. Oguchi, K. Hashimoto and Y. Nosaka, J. Phys. Chem. A 111 (2007) 13200-13208.
155. G. Da Silva, C. C. Chen and J. W. Bozzelli, J. Phys. Chem. A, 111(2007) 8663-8676.
156. G. Da Silva, J. W. Bozzelli, Proc. Combust. Inst., 32 (2009) 287-294.
157. G. Da Silva, M. R. Hamdan and J. W. Bozzelli, J. Chem. Theory Comput., 5 (2009) 3185-3194.
158. G. Da Silva and J. W. Bozzelli, J. Phys. Chem. A 113(2009) 6979-6986.
159. Y. Murakami, T. Oguchi, K. Hashimoto and Y. Nosaka, J. Phys. Chem. A. 113 (2009) 10652-10666.
160. J. L. Emdee, K. Brezinsky and I. Glassman, J. Phys. Chem., 96 (1992) 2151-2161.
161. A. Lifshitz, C. Tamburu, A. Suslensky, F. Dubnikova, Proc. Combust. Inst. 30 (2005) 1039-1047.
162. D. Gregory, R. A. Jackson, P. J. Bennett, Combust. Flame 118 (1999) 459-468.
163. I. V. Tokmakov, M. C. Lin, Int. J. Chem. Kinet. 33 (2001) 633-653.
164. M. B. Colket and D. J. Seery, Proc. Combust. Inst. 25 (1994) 883-891.
165. G. Da Silva, E. E. Moore, J. W. Bozzelli, J. Phys. Chem. A. 113 (2009) 10264-10278.
166. R. X. Fernandes, A. Gebert, H. Hippler, Proc. Combust. Inst. 29 (2002) 1337-1343.
167. G. Da Silva, J. A. Cole, J. W. Bozzelli, J. Phys. Chem. A. 114 (2010) 2275-2283.
168. K. Brezinsky, T. A. Litzinger, I. Glassman, Int. J. Chem. Kinet., 16 (1984) 1053-1074.
169. R. Atkinson, J. N. Pitts, J. Phys. Chem 78 (1974) 1780-1784.
170. J. M. Nicovich, C. A. Gump, A. R. Ravishankara, J. Phys. Chem. 86 (1982) 1690-1694.
171. H. Frerichs, V. Schliephake, M. Tappe, H. G. Wagner, Z. Phys. Chem. 165 (1989) 9-22.
172. C. A. Taatjes, D. L. Osborn, T. M. Selby, G. Meloni, A. J. Trevitt, E. Epifanovsky, A. I. Krylov, B. Sirjean, E. Dames, H. Wang, J. Phys. Chem. A. 114 (2010) 3355-3370.
173. M. A. Oehlschlaeger, D. F. Davidson, R. K. Hanson, Combust. Flame 147 (2006) 195-208.
174. H. Wang, M. Colket, SERDP PAH MODEL version 0.1, June 2007.
175. Vereecken, L.; Peeters, J. *Phys. Chem. Chem. Phys.* 2003, 5, 2807-2817.

# JOURNAL PUBLICATIONS

S. Gudiyella, T. Malewicki, A. Comandini, K. Brezinsky: "High Pressure Study of m-Xylene Oxidation", Combustion and Flames 158, Issue 4, 687-704, 2011

A. Comandini, K. Brezinsky: "Theoretical Study of the Formation of Naphthalene from the Radical/π-Bond Addition between Single-Ring Aromatic Hydrocarbons", Journal of Physical Chemistry A 115, Issue 22, 5547-5559, 2011

A. Comandini, T. Malewicki, K. Brezinsky: "Chemistry of PAHs Formation from Phenyl Radical Pyrolysis and Phenyl + Acetylene Reaction", journal article submitted to J. Phys. Chem. A

A. Comandini, K. Brezinsky: "Radical/π-Bond Addition between o-Benzyne and Cyclic C5 Hydrocarbons", journal article submitted to J. Phys. Chem. A

A. Comandini, T. Malewicki, K. Brezinsky: "Online and Offline Experimental Techniques for PAHs Recovery and Measurement", journal article submitted to Rev. Sci. Instrum.

S. H. Dürrstein, A. Comandini, T. Bentz, K. Brezinsky, M. Olzmann: "Iodobenzene pyrolysis and the phenyl + acetylene reaction – collaborative shock-tube studies and kinetic modeling", journal article, in preparation